AKADEMIA GÓRNICZO-HUTNICZA IM. STANISŁAWA STASZICA W KRAKOWIE

DZIEDZINA NAUK INŻYNIERYJNO-TECHNICZNYCH

DYSCYPLINA: INŻYNIERIA MATERIAŁOWA

ROZPRAWA DOKTORSKA

Analiza odpowiedzi komórkowych na właściwości elektroprzędzonych włókien polimerowych i rusztowań do zastosowań w inżynierii tkanki kostnej

Autor: mgr inż. Martyna Polak

Promotor rozprawy: prof. dr hab. inż. Urszula Stachewicz
Drugi promotor lub Promotor pomocniczy: dr inż. Joanna Karbowniczek

Praca wykonana: Akademia Górniczo-Hutnicza im. Stanisława Staszica w Krakowie, Wydział Inżynierii Metali i Informatyki Przemysłowej

Kraków, 2025

AKADEMIA GÓRNICZO-HUTNICZA IM. STANISŁAWA STASZICA W KRAKOWIE

FIELD OF SCIENCE: ENGINEERING AND TECHNICAL SCIENCES

SCIENTIFIC DISCIPLINE: MATERIALS ENGINEERING

DOCTORAL DISSERTATION

Analysis of cellular responses to the properties of electrospun polymer fibers and scaffolds for bone tissue engineering applications

Author: mgr inż. Martyna Polak

First supervisor: prof. dr hab. inż. Urszula Stachewicz
Auxiliary supervisor: dr inż. Joanna Karbowniczek

Completed at: AGH University of Krakow, Faculty of Metals Engineering and Industrial Computer Science

Kraków, 2025

This research was conducted with funding from the OPUS 17 project granted by the National Science Centre in Poland, No 2019/33/B/ST5/01311, and supported by the ERC-2020-STG project (BioCom4SavEn), under ERC grant agreement no. 948840, funded by the European Research Council within the EU's Horizon 2020 Framework Programme and by the program „Excellence initiative – research university" for the AGH University of Krakow in Poland.

Acknowledgments

I extend my deepest thanks to prof. dr hab. inż. Urszula Stachewicz for the opportunity to be part of her research group, for the immense time and help, for all the doors opened to me, and for the faith in my abilities.

I want to thank my research group, the Electrospun Fibers Group, for every day spent together, for every helping hand, for all our shared trips, and for our daily lunches. My special thanks go to the postdocs from whom I learned so much: Piotr, Krzysztof, Zuza, Daniel, and Asia. Without you, this would not have been possible.

I thank all my collaborators and co-authors who helped shape this dissertation.

I am thankful to prof. Eyal Zussman and the NanoEngineering Group at the Technion for their hospitality and the knowledge they shared during my research stays.

I thank my friends. To Sylwia, whom I met at the beginning of our studies in Kraków and who had a key influence on my decision to begin a PhD. I also thank the friends I met only thanks to my doctoral path. A special thank you to Patrick, my lab mate and tutor during my research stay at the Technion, who also became a friend.

I am grateful to my parents and siblings for their support, encouragement, and for always being just a phone call away. To Kuba, Iza, and Emilka—for being my safe haven in Kraków.

To everyone who cheered me on and believed in me—thank you.

Table of contents

List of Figures

List of Tables

Abstract

The regeneration of bone tissue requires scaffolds that not only mimic the extracellular matrix (ECM) on the structural level but also provide biofunctional cues that actively guide osteoblast activity. This dissertation addresses this challenge by investigating how electrospun polymer scaffolds can be engineered to control fiber surface properties and how these material features regulate bone cell interactions. Electrospinning was employed as the fabrication strategy due to its capacity to create fibrous architectures with tunable morphology, surface chemistry, and electroactivity, all of which are critical for bone tissue engineering.

The research pursued three main objectives. Firstly, it was determined how applied voltage polarity during electrospinning governs the surface potential and piezoelectric response of PLLA fibers, and how these effect influences osteoblast adhesion, focal adhesion formation, proliferation, and collagen production. Secondly, it was verified how the blending of polymers in core–shell PC–PMMA fibers affects surface potential, chemistry, wettability, and mechanical properties. It was established how osteoblasts respond to these changes at the single cell and single fiber level, including the development of a confocal protocol for paxillin immunostaining and quantitative focal adhesion analysis. Lastly, the research aimed to compare reduced graphene oxide (rGO) and MXene nanofillers in PLLA fibers, quantifying their influence on fiber surface charge, filler dispersion in the scaffolds, and their mechanical performance. Again, these properties were correlated with osteoblast attachment and focal adhesion formation at the single fiber and single cell scales, considering filler-enriched fiber regions.

To achieve this, multiscale materials characterization was combined with advanced biological evaluation. Techniques such as Kelvin probe force microscopy (KPFM), zeta potential, and X-ray photoelectron spectroscopy (XPS) were used for surface and electrostatic analysis, while confocal laser scanning microscopy (CLSM) and scanning electron microscopy (SEM) enabled detailed assessment of osteoblast morphology and adhesion.

The results demonstrate that electrospun scaffolds can be precisely tuned through electrospinning parameters, fiber design, and incorporation of functional fillers to control

their surface characteristics. These scaffold modifications affect osteoblast responses, including focal adhesion formation.

This research shows that controlling surface properties of fibers provides a powerful handle for modulating osteoblast behavior. By integrating scaffold design with cell biology, this thesis presents a framework for developing electrospun scaffolds tailored to specific cell responses.

List of Abbreviations

2D	two-dimensional
3D	three-dimensional
AFM	atomic force microscopy
ANOVA	analysis of variance
ATP	adenosine triphosphate
Au	gold
CPD	contact potential difference
CLSM	confocal laser scanning microscopy
DAPI	4’,6-diamidino-2-phenylindole
DBSCAN	Density-Based Spatial Clustering of Applications with Noise
DMAC	N,N-dimethylacetamide
DMEM	Dulbecco’s Modified Eagle Medium
DMF	N,N-dimethylformamide
DSC	differential scanning calorimetry
EDS	energy-dispersive spectroscopy
ECM	extracellular matrix
FBS	fetal bovine serum
FA / FAs	focal adhesion / focal adhesions
FIB	focused ion beam
FTIR	Fourier transform infrared spectroscopy
FWHM	full width at half maximum
HCl	hydrochloric acid
HMDS	hexamethyldisilazane
HOPG	highly ordered pyrolytic graphite
ITO	indium tin oxide (glass)
KCl	potassium chloride
KPFM	Kelvin probe force microscopy

MG-63	human osteoblast-like cell line MG-63
MXene	two-dimensional transition-metal carbide/nitride (e.g., $Ti_3C_2T_x$)
MTS	3-(4,5-dimethylthiazol-2-yl)-2,5-diphenyltetrazolium bromide
MTT	3-(4,5-dimethylthiazol-2-yl)-5-(3-carboxymethoxyphenyl)-2-(4-sulfophenyl)-2H-tetrazolium
NaOH	sodium hydroxide
NN	nearest neighbor
PCL	polycaprolactone
PC	polycarbonate
PC-PMMA	polycarbonate–poly(methyl methacrylate)
PBS	phosphate-buffered saline
PFM	piezoresponse force microscopy
PLGA	poly(lactic-co-glycolic acid)
PLLA	poly(L-lactide)
PMMA	poly(methyl methacrylate)
PVA	poly(vinyl alcohol)
PVDF	poly(vinylidene fluoride)
rGO	reduced graphene oxide
RH	relative humidity
SEM	scanning electron microscopy
TCPS	tissue culture polystyrene
$Ti_3C_2T_X$	titanium carbide MXene (surface-terminated)
WF	work function
XPS	X-ray photoelectron spectroscopy

1. Biomaterials – Scaffold Requirements and Challenges in the Design for Tissue Regeneration

Tissue engineering combines principles of biology, engineering, and materials science to restore, maintain, or improve tissue function by integrating living cells with biomaterial scaffolds and signaling factors [1]. The central concept is to recreate or enhance the body's natural ability to regenerate tissues either *in vivo* (within the body) or *in vitro* (outside the body for transplantation) [2]. Globally, millions of bone grafting procedures are performed each year (with estimates exceeding 2 million procedures annually worldwide), making bone the second most transplanted tissue after blood [3–5]. Autografts and allografts, though clinically established, are associated with significant drawbacks such as donor site morbidity, limited supply, risk of disease transmission, and immune rejection. Current synthetic and natural biomaterials used as bone grafts often face challenges in matching the mechanical strength, biocompatibility, and complex biological signaling of native bone tissue [6,7].

Bone is a hierarchically organized tissue that combines mechanical strength with critical biological functions. It provides structural support and protects internal organs. This tissue consists of compact bone, which forms the dense outer layer and resists fractures, and spongy bone, a porous interior that reduces weight [8]. Bone growth and remodeling depend on the regulation of osteoclasts, which resorb bone matrix, and osteoblasts, which secrete extracellular components [9]. Its structure spans multiple scales: at the microscale level, bone displays a complex architecture of osteons, which are cylindrical units 100–300 µm wide and 3–5 mm long, made of concentric lamellae [10,11]. These surround Haversian canals that carry blood vessels and nerves. Further, at progressively smaller scales, these structures are built from collagen fibrils (mainly type I collagen) with hydroxyapatite crystals, creating a composite. This mineralized matrix is composed also of water, noncollagenous proteins and proteoglycans [12]. The organization of these elements at multiple scales is responsible for their mechanical strength [13]. The hierarchical structure of bone is schematically presented in **Figure 1A**. Importantly, bone exhibits piezoelectric properties due to the highly organized structure of collagen [14]. The piezoelectric effect helps to drive regeneration by converting mechanical stress into localized electrical signals in the tissue, as presented in **Figure 1B**. These signals are stimulating cellular activity involved in repair and remodeling [14,15].

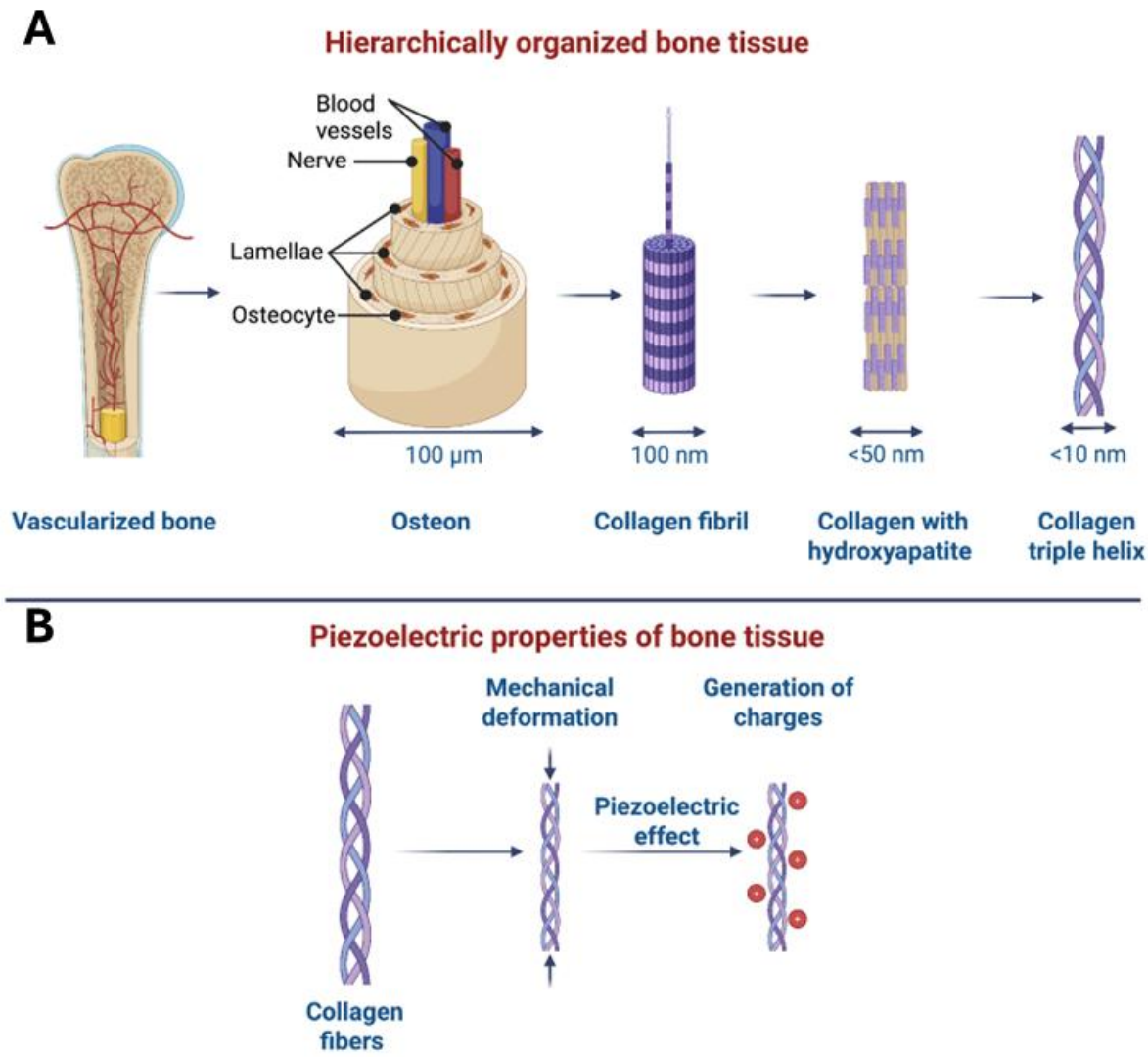

Figure 1. Scheme presenting: A) the hierarchical organization of bone tissue, illustrating structural levels from vascularized bone to osteons, collagen fibrils, collagen-hydroxyapatite composites, and the collagen triple helix. B) the piezoelectric properties of bone tissue, where mechanical deformation of collagen fibers induces a piezoelectric effect, leading to the generation of surface charges.

Biomaterials serve as the foundation of modern tissue engineering by providing structural and biochemical support to guide cell attachment, proliferation, and differentiation [16–18]. Among them, scaffolds are temporary 3D architectures designed to replicate the ECM, enabling cell colonization and bone tissue formation until the scaffold degrades, being entirely replaced by native tissue [19,20]. The ideal scaffold must satisfy a complex set of requirements that bridge materials science, cell biology, and clinical application [21,22].

Key functional demands placed on scaffolds include biocompatibility, mechanical integrity, tunable degradation rates, and a porous structure that facilitates nutrient transport and cell infiltration [23,24]. Surface properties, such as chemistry, charge, and topography, play a particularly critical role in mediating early cell responses, including adhesion and spreading [25–27]. These initial interactions can significantly impact longer-term outcomes, including bone tissue integration and remodeling. Therefore, scaffold design must go beyond bulk properties and incorporate surface features that mimic or modulate natural biological signals.

These various design factors are summarized in **Figure 2**, which illustrates the core parameters that influence scaffold performance in tissue engineering. As shown, scaffold performance is dictated not only by bulk properties such as mechanical strength and degradation rate, but also by specific factors including surface potential, chemistry, roughness, and pore architecture. Moreover, electroactivity, as mentioned in this context, refers to the scaffold's ability to conduct or mediate electrical signals, thereby mimicking the natural bioelectrical environment of excitable tissues, such as bone, nerve, or muscle. This property has been shown to influence cell behavior by promoting adhesion, proliferation, and differentiation via electrically driven mechanisms, thereby contributing to improved regenerative outcomes [28].

Despite extensive advances in scaffold fabrication techniques, several challenges remain in engineering constructs to ensure that all functional criteria are met simultaneously. High porosity, necessary for cell infiltration and vascularization, can reduce mechanical strength [29,30]. Polymers with excellent mechanical properties can lack sufficient bioactivity. Biodegradable materials must degrade at a rate compatible with tissue healing. If it is too fast, then mechanical support is lost; if it is too slow, chronic inflammation may occur [31,32]. Additionally, surface modifications that enhance cell attachment can sometimes alter degradation behavior or introduce unintended immunogenicity [33–35].

A major design challenge lies in controlling the surface properties of scaffolds to promote desirable biological responses. These properties are influenced not only by material selection but also by the fabrication technique. Among numerous manufacturing methods, electrospinning has emerged as a versatile platform for generating fibrous scaffolds with high

surface area and tunable morphology [36]. However, the dense fiber packing typical of electrospun materials often limits cell infiltration, and surface potential remains an underexplored but critical parameter for modulating cell–material interactions [29]. In the following sections, two often underappreciated design parameters are examined in detail: surface potential and scaffold porosity.

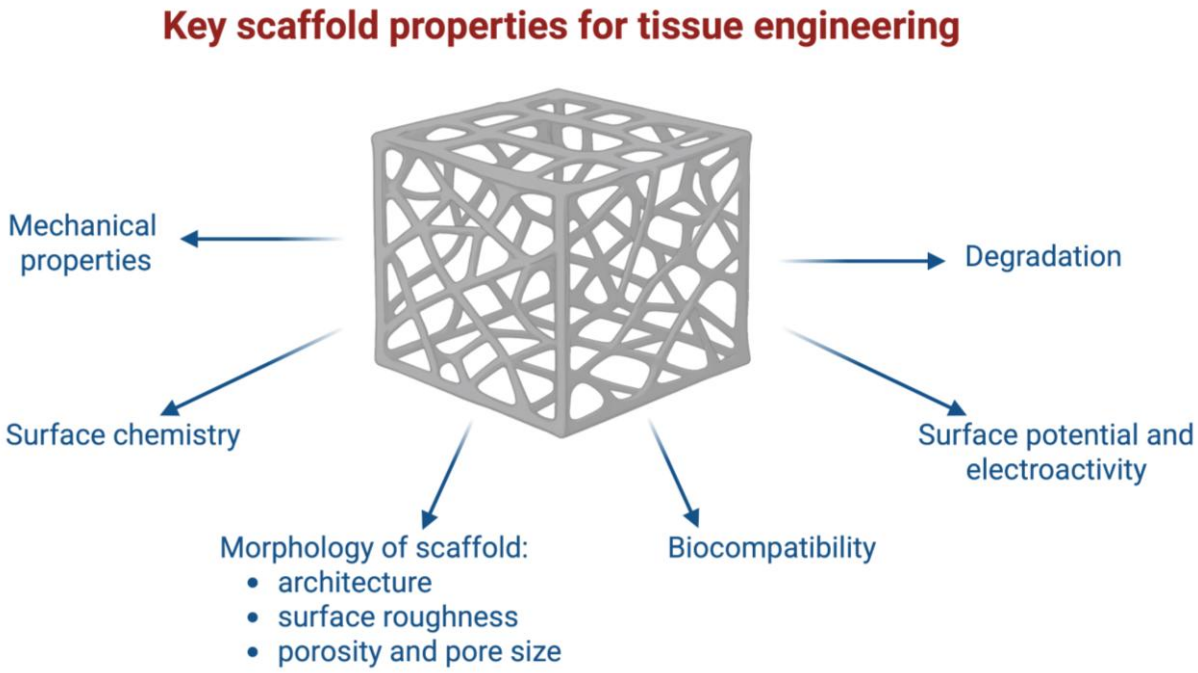

Figure 2. Schematic illustration of key scaffold properties that influence bone tissue engineering outcomes. The interplay between these factors governs scaffold bioactivity and cell–material interactions.

1.1. Surface Potential of Biomaterials

From a biological standpoint, the cell membrane is naturally electroactive and maintains a net negative charge under physiological conditions. This negative potential arises from the asymmetric distribution of ions, primarily sodium (Na^+) and potassium (K^+), as well as the presence of anionic phospholipids and glycoproteins on the membrane surface [25,37,38]. This naturally negative charge enables electrostatic interactions with the positively charged domains of ECM proteins such as collagen and fibronectin [39–41]. The electrostatic character of the membrane influences how cells sense and respond to their environment. In the context of tissue engineering, when cells encounter a scaffold, electrostatic interactions

occur between the negatively charged membrane and the material's surface, influencing protein adsorption, integrin binding, and the assembly of focal adhesions [42,43].

Surface potential, defined by the electrostatic charge distribution at the material–environment interface, plays a critical role in regulating early cell responses. Despite its importance, surface potential remains a relatively underexplored factor in biomaterial design, partly due to challenges in its measurement and the complexity of decoupling it from other surface properties [25,44,45].

Tuning the surface potential of biomaterials becomes a biologically meaningful strategy to modulate cellular behavior in a controlled and non-chemical manner. **Figure 3** presents a schematic illustration of native tissue, highlighting the electrochemical nature of the cell membrane.

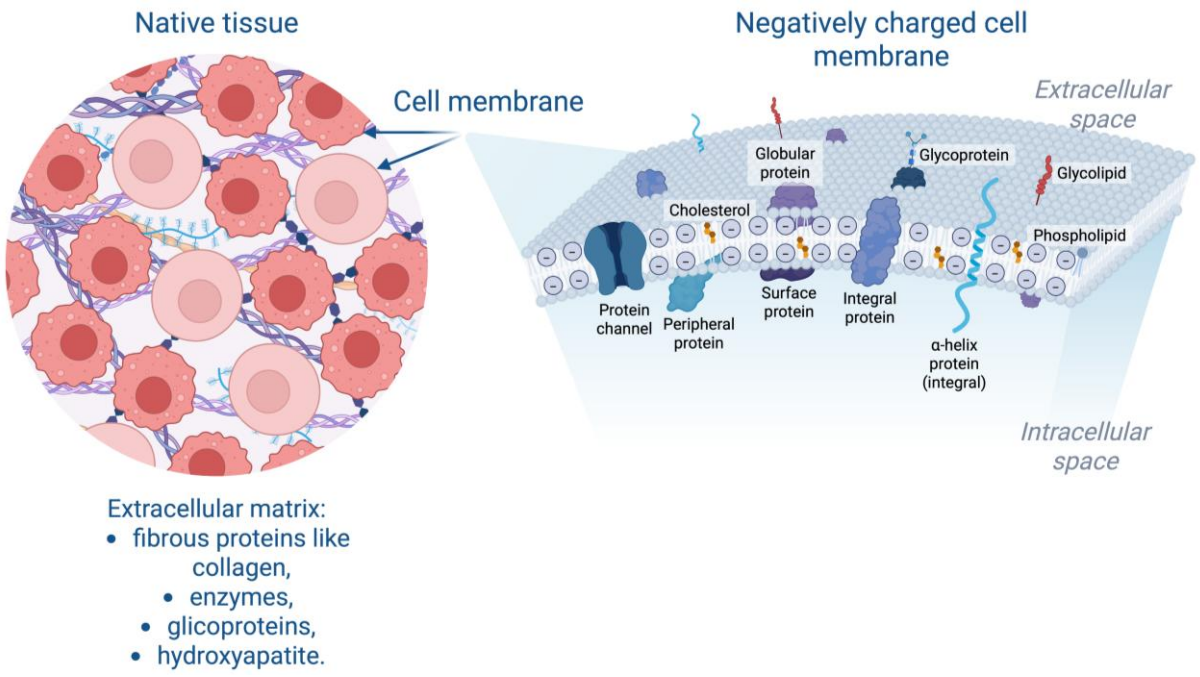

Figure 3. A schematic illustration of native tissue with its characteristic elements for hard tissues like bone, and a focused image of a negatively charged cell membrane.

1.2. Selected Methods of Surface Charge Evaluation

To understand and engineer these essential electrostatic interactions at the cell–material interface, it is crucial to accurately characterize the surface potential and charge of biomaterials, which can be achieved using advanced techniques such as atomic force microscopy (AFM) and zeta potential measurements.

AFM is a powerful technique widely used in nanotechnology and biomaterials research for its ability to probe surface properties with exceptionally high spatial resolution. Beyond imaging surface topography, AFM enables the measurement of local mechanical properties, adhesion forces, and molecular interactions at biomaterial interfaces. Depending on the operational mode, contact, tapping (non-contact), or intermittent, the AFM tip interacts differently with the sample surface, allowing tailored analysis of various physical parameters [46–48]. In contact mode, the tip maintains constant contact with the surface, while in tapping mode, it oscillates near its resonant frequency without physically dragging across the sample. Intermittent contact mode combines aspects of both, enabling sensitive detection of repulsive and attractive interactions [44].

Among advanced AFM modalities, KPFM stands out as a particularly valuable technique for mapping surface potential at the micro- and nanoscale. KPFM operates by detecting electrostatic forces between a conductive AFM tip and the sample surface, which arise due to differences in their Fermi energy levels [49,50]. By applying an oscillating AC voltage along with a compensating DC bias, the system can nullify the electrostatic force, and the resulting DC value directly reflects the local contact potential difference (CPD) [51,52]. This enables precise surface potential mapping, which is particularly relevant for biomaterials, where bioactivity is influenced by electrostatic cues. Recent studies have extended the application of KPFM to a variety of biomaterials, including polymers, hydroxyapatite-based surfaces, and nanocomposites used in tissue engineering [26,53,54]. Notably, KPFM can be conducted in non-contact mode, making it suitable for delicate biological samples and allowing imaging in both ambient and liquid environments [55]. In this thesis, KPFM was applied to electrospun scaffolds to evaluate surface potential and correlate these variations with early osteoblast responses, such as focal adhesion formation and initial cell attachment.

Zeta potential is another widely used parameter for characterizing the electrokinetic properties of material surfaces, particularly in liquid environments. Unlike KPFM, which

provides localized, high-resolution maps of surface potential, zeta potential offers an average assessment of surface charge by examining how a material interacts with its ionic surroundings when in contact with a liquid medium [56]. When a solid material is immersed in an electrolyte solution, its surface interacts with ions in the fluid, forming an electrical double layer [57]. This double layer consists of a tightly bound inner layer of counterions, attracted to charged surface groups such as protonated or ionized functional moieties, and a more diffuse outer layer of loosely associated ions. The zeta potential is measured at the shear plane, located at the boundary between these two layers, where liquid begins to flow during electrophoretic movement [58]. The resulting electrostatic potential depends on multiple factors, including the surface chemistry, ionic strength, pH of the surrounding medium, and temperature [25,59]. In the field of biomaterials, zeta potential is used to infer the presence and nature of surface functional groups and indirectly assess surface charge behavior under physiological conditions [25,59–61]. Although it lacks the spatial resolution of techniques like KPFM, zeta potential remains a valuable tool for evaluating the average electrochemical profile of scaffold surfaces and their likely interactions with proteins, cells, or other biomolecules in aqueous environments [27,56].

In summary, surface potential is a dynamic and influential property of biomaterials that governs early stages of cell–material interaction. It demonstrates that electrostatic cues at the material surface modulate collagen formation and osteoblast adhesion, underscoring the biological relevance of surface potential beyond traditional topographical or chemical effects [26,62]. Its impact on protein adsorption, adhesion site formation, and cellular signaling makes it a critical yet underutilized factor in scaffold design. Incorporating surface potential analysis into scaffold development may provide new pathways for optimizing and improving outcomes in regenerative medicine or disease modelling.

1.3. The Importance of Scaffold Porosity and Pore Size

Porosity and pore size are among the most critical physical parameters in the design of scaffolds for tissue engineering [63–65]. They directly affect nutrient and oxygen diffusion, waste removal, and the ability of cells to adhere, migrate, and infiltrate into the material [66,67]. As discussed in the review article included in this dissertation, while electrospun

scaffolds are inherently porous due to their fibrous structure, the scale and accessibility of these pores are often insufficient for supporting deep cellular infiltration and vascularization. Vascularization is the formation of blood vessels within a tissue or scaffold. In bone tissue engineering, insufficient vascularization can lead to poor scaffold integration, delayed healing, or even necrosis, making the development of vascular networks essential for successful and functional tissue regeneration [68–71]. Electrospun fibers typically assemble into dense mats with small inter-fiber pores, often around 10 μm, which limits their ability to support cell penetration beyond the surface [72,73]. This is particularly problematic in applications such as bone tissue regeneration, where pore sizes of up to 100 μm are generally favorable for enabling osteoblast infiltration and vascular ingrowth. For fibroblasts and epithelial cells, smaller pores (20–60 μm) can be sufficient, but pore interconnectivity remains equally important [74].

Several strategies have been proposed to improve porosity in electrospun scaffolds. These include the use of sacrificial fibers, cryogenic electrospinning, wet electrospinning, patterned collectors, or multi-jet systems [75–77]. These approaches aim to increase inter-fiber spacing and introduce macro-porosity while maintaining fiber integrity and mechanical properties. Importantly, porosity should not be viewed as a static morphological trait but rather as a tunable design feature with direct biological consequences. The inclusion of porosity-enhancing techniques should therefore be carefully matched to the intended application, cell type, and mechanical requirements of the target tissue [74].

To contextualize the typical pore size ranges achieved by different scaffold fabrication techniques, **Figure 4** compares various approaches used in tissue engineering. While gas foaming and 3D printing offer large and controllable pores (40–800 μm), electrospinning remains one of the few methods that enables nanoscale porosity (100 nm–10 μm), though at the cost of limited infiltration depth. This highlights both the advantages and the challenges of electrospun scaffolds in meeting specific biological demands.

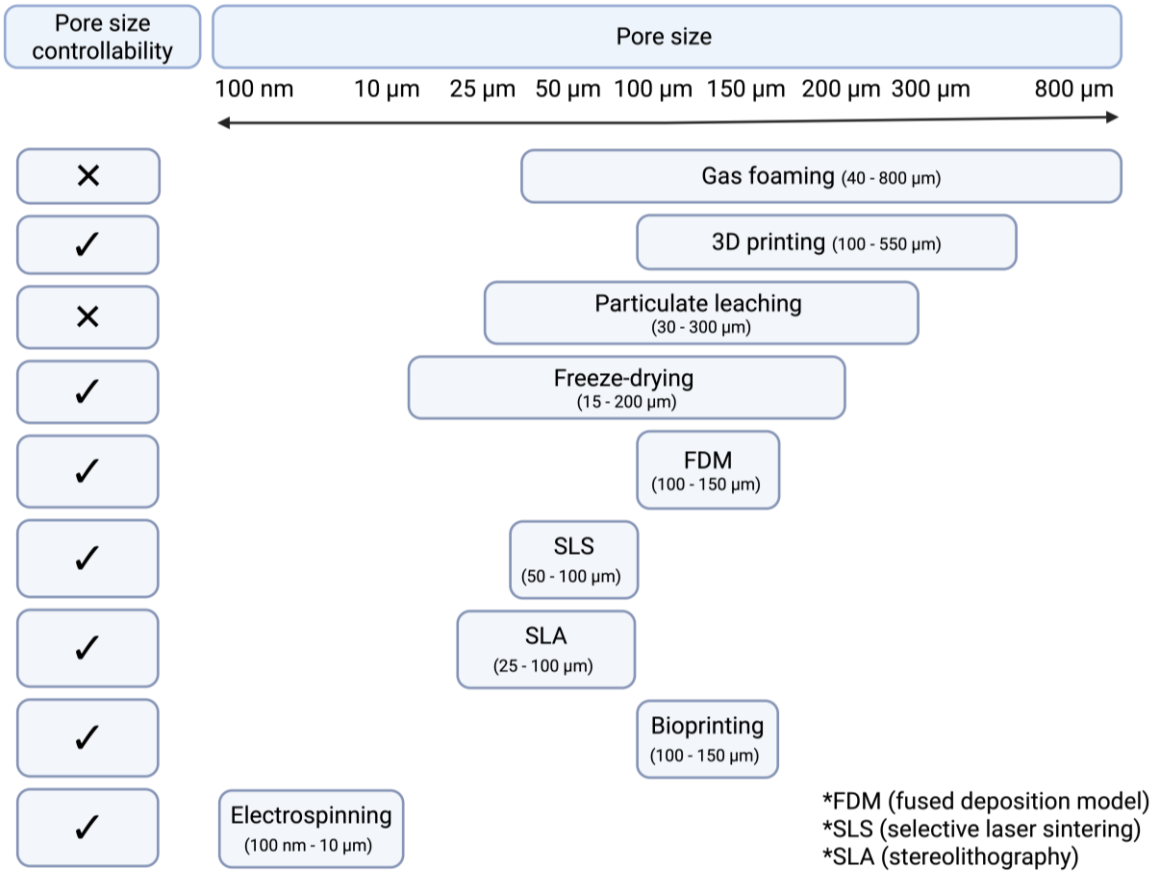

Figure 4. Comparison of pore size ranges and pore size controllability among various scaffold fabrication methods. While electrospinning allows for nanoscale control and produces fibers in diameters resembling ECM fibers, it typically results in the smallest pores [75–77].

Scaffold porosity and pore size assessment follow scaffold fabrication, as they dictate functionalities that affect cell behavior, as mentioned above. The evaluation should be precise and nondestructive to the initial state of the scaffold. Micro-CT (microcomputed tomography) is an often chosen method for 3D quantification of pore size and connectivity [78,79]. Micro-CT results can serve as input for CFD (computational fluid dynamics) or permeability models, giving many possibilities for porosity investigation [80]. Other commonly used approaches involve mercury intrusion and flow porosimetry techniques, gas pycnometry, and gas adsorption analysis provided alone or in combination with theoretical modeling [81–83]. Microscopy analysis using SEM can deliver high-resolution surface topography and cross-sectional views when careful and aware sample preparation preserves scaffold architecture, enabling reliable assessment. Moreover, FIB-SEM (focused ion beam–SEM) is particularly well

suited to this requirement. Beyond that, confocal microscopy is a powerful and widely used imaging technique for analyzing scaffold geometry at high resolution. By exploiting either intrinsic autofluorescence or fluorescent staining, CLSM enables 3D visualization of scaffold architecture with minimal sample preparation [67,84]. This is particularly advantageous for hydrogel-based scaffolds, which present significant imaging challenges due to their high water content, optical transparency, and mechanical fragility. Traditional imaging methods like SEM or micro-CT often require dehydration, fixation, or contrast agents that can distort the native structure of soft materials, especially used in tissue engineering applications [85]. In contrast, CLSM enables non-destructive imaging under hydrated conditions, thereby preserving the geometry and microstructural integrity of the scaffold [84,86]. Furthermore, CLSM can be integrated with fluorescent markers for specific biological components or functional assays, allowing simultaneous assessment of scaffold architecture and cell-material interactions.

2. Cell Responses to the Properties of Biomaterials

Understanding how cells respond to biomaterials is central to the development of functional scaffolds for tissue engineering. Once in contact with a biomaterial, cells undergo a sequence of events, beginning with initial adhesion and spreading, followed by proliferation, migration, and ultimately differentiation or integration with the surrounding tissue. These processes are governed by a complex interplay of physical, chemical, and mechanical cues presented by the scaffold [87–89].

To evaluate these interactions, researchers employ a wide range of *in vitro* techniques**.** Cell adhesion is often assessed at early time points using staining of focal adhesion proteins (e.g., paxillin, vinculin), coupled with fluorescence or confocal microscopy to observe cytoskeletal organization and adhesion point formation [90,91]**.** Viability and proliferation are typically quantified using colorimetric or fluorometric assays (e.g., MTT, MTS, Live/Dead), while migration can be studied through time-lapse imaging, transwell assays, or scratch wound models [92,93]. High-resolution imaging tools such as SEM or CLSM are further used to visualize cell morphology and interaction with scaffold topography.

In recent years, quantitative image analysis has become increasingly important for assessing focal adhesion size, distribution, and density as a proxy for how cells interpret material surfaces. In parallel, techniques such as gene expression profiling, western blotting,

or ELISA enable the monitoring of cell signaling pathways activated in response to specific material cues. Together, these methods provide a comprehensive toolkit for studying cell–material interactions and their implications for scaffold biofunctionality. The following sections focus on key early-stage cell responses such as adhesion, viability, and migration, and cell morphology.

2.1. Initial Adhesion and Focal Adhesion Point Analysis

Initial cell adhesion is a critical first step in the interaction between biomaterials and cells. Within minutes of seeding, cells begin probing the surface through filopodia and lamellipodia, initiating contact that determines their ability to attach and spread [25]. This process is primarily mediated by integrins—transmembrane receptors that serve as mechanical and biochemical linkers between the ECM or biomaterial surface and the cell's actin cytoskeleton [94,95]**.**

Integrins interact with adsorbed to the biomaterial's surface proteins, such as fibronectin, vitronectin, and collagen, that spontaneously coat the surface due to exposure to biological fluids [96]. Upon ligand binding, integrins cluster into specialized regions of the membrane known as focal adhesions**.** These adhesion complexes recruit intracellular adaptor proteins such as talin, paxillin, and vinculin**,** which connect to actin filaments and trigger mechanotransduction pathways [97,98]. This signaling cascade enables the cell to sense surface stiffness, topography, and chemical composition, thereby regulating their behavior [94].

In the research work presented in this dissertation, early cell adhesion was evaluated through two types of experiments: analysis of adhered cells after 1-5 h of cell culture on scaffolds and focal adhesion point staining after 3 days of cell culture**,** targeting paxillin to visualize integrin engagement. Quantitative analysis performed using CLSM included cluster size, distribution, and signal density—metrics that provide insights into the strength and organization of cell attachment to the scaffold. The schemes presenting the protocols for initial adhesion and focal adhesion point analysis are shown in **Figure 5**.

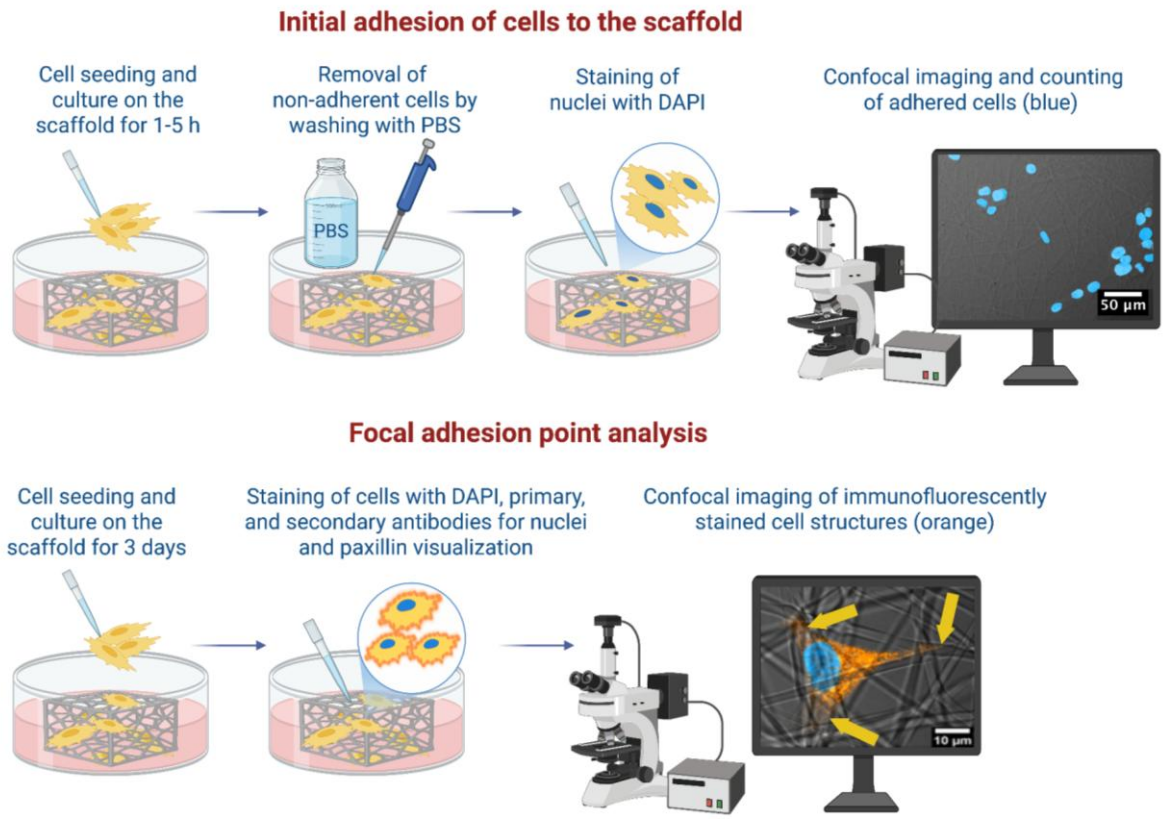

Figure 5. Schematics presenting protocols for cell culture, staining, and imaging of desired cell structures, allowing the analysis of initial adhesion and focal adhesion points.

2.2. Cell Viability and Migration

Following initial adhesion, two critical aspects of a successful scaffold–cell interface are cell viability and migration**.** These processes not only reflect the cytocompatibility of the material but also its ability to support dynamic cellular behavior necessary for tissue regeneration. A scaffold that supports adhesion but compromises viability, or that allows cell survival without enabling movement and tissue integration, cannot fulfill its role in regenerative applications.

Cell viability refers to the ability of cells to maintain metabolic activity and structural integrity in response to contact with the biomaterial. As mentioned in the previous section, it is commonly assessed using quantitative assays such as MTS, MTT**,** or resazurin-based tests**,** which measure metabolic enzyme activity, giving the number of living cells [99]. However, it is important to note that increased metabolic activity or proliferation does not always equate

to a positive biological response. Cells under stress can exhibit compensatory proliferation or altered metabolism, which may mask cytotoxic or pro-inflammatory effects of the material [100,101]. Therefore, proliferation alone can be misleading if not interpreted in the context of other indicators of cell behavior. To overcome this limitation, a more comprehensive approach is required that combines viability and proliferation assays with additional techniques. This multi-parameter evaluation enables a more accurate understanding, allowing for differentiation between true bioactivity and stress-induced proliferation or survival.

Cell migration**,** on the other hand, is a highly dynamic and coordinated process driven by actin remodeling, integrin turnover, and the disassembly and reformation of focal adhesions [102,103]. For a scaffold to facilitate tissue regeneration, it must allow cells not only to attach and survive but also to infiltrate into its 3D architecture. As already mentioned, migration is often assessed via scratch assays, transwell migration tests, or live-cell imaging [104,105]; however, in the case of fibrous scaffolds, z-stack confocal imaging or SEM cross-sections help determine the penetration depth. An overview of these complementary assays is schematically illustrated in **Figure 6**.

The scratch assay is a straightforward 2D method used to measure collective cell migration. A uniform gap is created in a cell monolayer, and the rate of gap closure indicates the cells' migratory ability. However, this assay does not replicate the conditions of 3D fibrous tissue environments. The scratch assay is particularly useful for evaluating drug delivery systems in wound healing applications. For example, cell migration significantly increased in the presence of hyaluronic acid released from electrospun poly(3-hydroxybutyrate-co-3-hydroxyvalerate) (PHBV) fibers, proving the effect of accelerated wound closure [93].

Furthermore, Wu et al. used a standard transwell migration assay in which rat bone marrow mesenchymal stem cells (BMSCs) were seeded in the upper insert and silk fibroin electrospun scaffolds, either coated with polydopamine (PDA) or peptide-grafted (E7 peptide), were placed in the lower chamber in Dulbecco's modified Eagle's medium (DMEM) [106]. After 12 h, BMSCs that traversed the porous membrane were fixed and stained. Then, migrated cells were counted, providing a quantitative result of scaffold-induced effect. Cells migrate downward because the functionalized scaffolds generate chemotactic and affinity cues, where

PDA improves cell–material interactions, and the E7 peptide presents BMSC-binding motifs that attract cells.

To verify that cells truly infiltrate a fibrous scaffold (not just migrate on the surface), the research presented in this dissertation combines CLSM and SEM investigation. For CLSM, fixed samples with stained actin filaments and nuclei were scanned as Z-stacks, and the images were acquired with consistent excitation/detection settings across samples. Depth profiles were computed by averaging the fluorescence intensity through the stack. The first plane from the top of the sample with in-focus nuclei marks the scaffold surface layer, and the breadth and tail of the depth profile show the extent of cell infiltration. SEM provides complementary information about cell penetration into scaffolds. Samples after fixation, graded ethanol dehydration, hexamethyldisilazane (HMDS) drying, and a thin conductive coating (~8 nm Au), were imaged from the top and bottom of the scaffold; cross-sections were prepared by scalpel cutting of the scaffold midline before coating. The presence of cells on the top surface, within cross-sections, and on the bottom allows for confirmation of penetration and corroborates CLSM depth profiles. In addition, CLSM enables high-resolution 3D live imaging of cells on electrospun fibers. It is reported that by combining CLSM with resonance scanning and fluorescent dyes, it is possible to visualize, in real time, the spatial distribution, morphology, and dynamic intracellular calcium activity of live cells cultured on electrospun poly(lactic-co-glycolic acid) (PLGA) scaffolds [107].

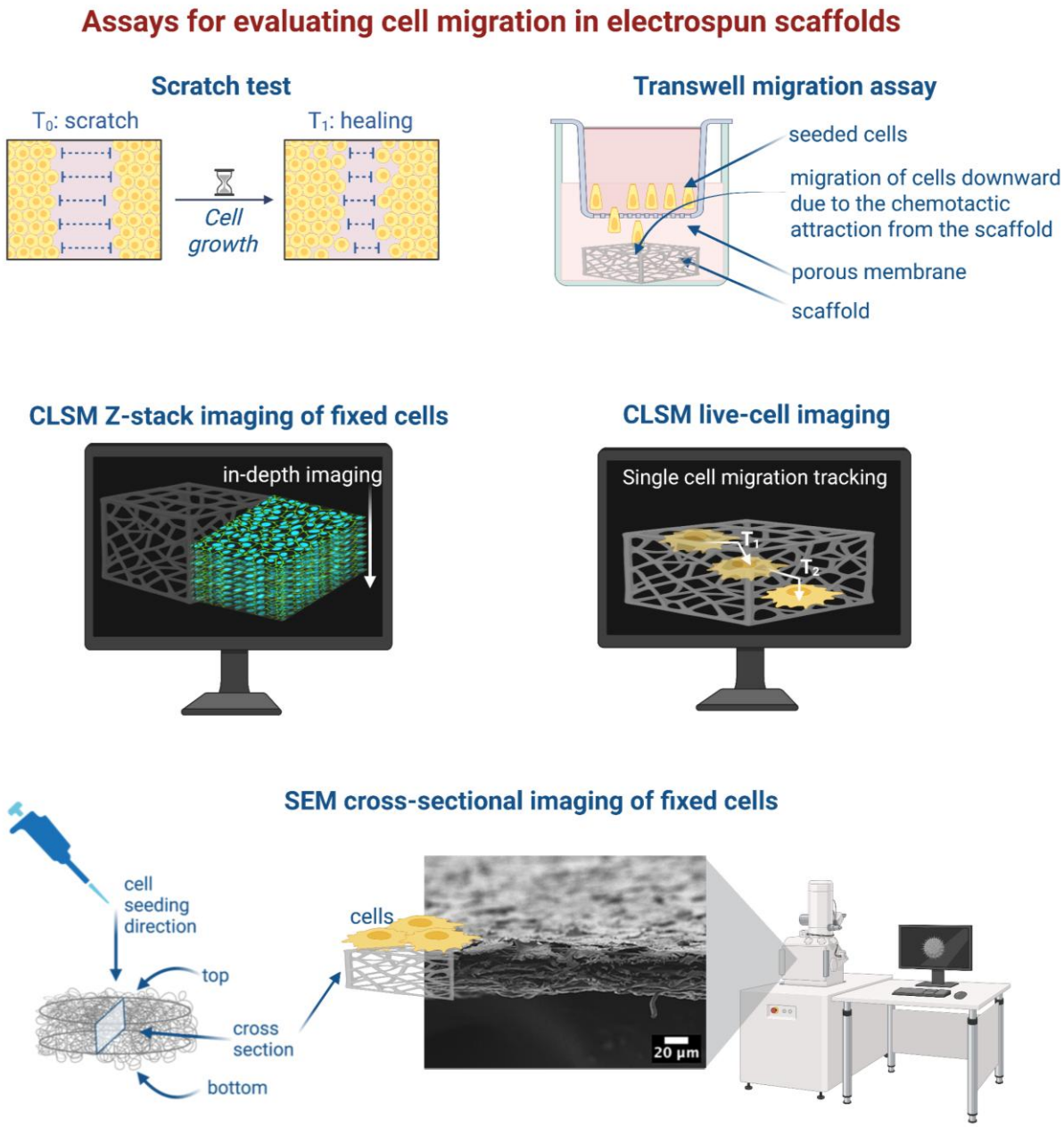

Figure 6. Illustration of cell migration assays used in tissue engineering of electrospun scaffolds: scratch test, transwell migration assay, in-depth CLSM of the scaffold (z-direction imaging), live-cell CLSM, and SEM cross-sectional imaging of the scaffold.

2.3. Cell Morphology Assessment via SEM and CLSM

Beyond migration, the assessment of cell morphology provides insights into how cells interact with electrospun scaffolds. Cell shape and cytoskeletal organization are indicators in cell condition investigations. As already mentioned, SEM enables the visualization of fixed

cells; however, when performed at multiple time points, it provides a valuable overview of cytoskeleton and filopodia development. When cells are spread and stretched on the fibers, using them to communicate with other cells, it can be concluded that the material is favorable for cell development. Moreover, with SEM, it is possible to connect specific material topography characteristics and cell response simultaneously, which is the main advantage compared to other imaging techniques. Metwally et al. presented a study in which electrospun polycaprolactone (PCL) fibers with smooth and porous surfaces were analyzed in the context of cell-material interaction. It was shown that cells growing on the porous scaffolds formed a higher number of filopodia, indicating a preference for rough surfaces for their attachment [27]. Beyond that, SEM together with energy-dispersive spectroscopy (EDS) allows for precise indication of the changes in chemical composition, for instance, the formation of calcium apatite in osteoblast cells, as it was performed after 7 days of cell culture on poly(vinylidene fluoride) (PVDF) fibers [26].

CLSM is a primary tool for visualizing the actin cytoskeleton and cell shape on biomaterials. With fluorescent phalloidin for F-actin and nuclear counterstains, CLSM reveals filopodia and cell spreading. Airyscan (a super-resolution CLSM mode) further sharpens these results, revealing cell–material interfaces through focal adhesion markers (e.g., paxillin, vinculin) imaged together with actin [108]. Berniak et al. presented that Airyscan enabled quantification of nanoscale adhesion organization on fibers versus glass. They uncovered that paxillin and vinculin form numerous, smaller, more elongated clusters on fibers, with systematic shifts between their intensity maxima, which is evidence for material-dependent adhesion. These distributions were extracted using intensity profiling and nearest-neighbor analysis, which transformed CLSM images into quantitative data. CLSM also interrogates function, not just structure. For example, it was shown that keratinocytes grown on cholesterol-enriched electrospun scaffolds take up a fluorescent cholesterol and transport it to the perinuclear region [109]. In the same samples, cell replication was quantified by 5-ethynyl-2’-deoxyuridine (EdU) incorporation. These results led to a link between molecular delivery from the scaffold and a measurable cellular response *in situ*.

To summarize, SEM and CLSM offer complementary views of cell–material interactions. SEM gives high-resolution surface images that reveal cell shape, spreading, filopodia formation, and how cells physically anchor to individual fibers. Cross-sections can

confirm whether cells have penetrated the scaffold. CLSM provides depth-resolved, 3D information by staining nuclei, the actin cytoskeleton, and focal-adhesion proteins, enabling the quantification of cell distribution and infiltration throughout the scaffold thickness. Additionally, it can track functional responses that affect cell morphology, such as cellular uptake of fluorescent molecules.

3. Electrospinning of Scaffolds for Tissue Engineering

One of the most promising fabrication techniques for scaffolds is electrospinning, due to its unique ability to produce fibers with diameters ranging from a few nanometers to several micrometers—comparable to the native ECM components such as collagen (~500 nm), elastin (~400 nm), or fibronectin (~2 nm) [27,110]. These fiber dimensions enable electrospun materials to closely replicate the structural and topographical cues of the natural ECM, which are known to regulate key cell behaviors [29]. Unlike 3D printing or salt-leaching techniques, electrospinning enables the continuous formation of interconnected fibrous networks that can be functionalized with bioactive agents and tuned in terms of mechanical properties, degradation rate, or surface chemistry.

Electrospinning is a fiber fabrication process that employs electrostatic forces to generate fine polymer fibers. It involves applying a high voltage between a polymer solution (or melt) held in a syringe, which ends with a nozzle and a grounded collector, as presented in **Figure 7**, where the scheme of the electrospinning set-up is schematically introduced. Once the electrostatic force overcomes the surface tension of the droplet at the nozzle tip, a charged jet forms and extends in the direction of the electric field, resulting in fiber formation. As the solvent evaporates during the polymer jet stretching, solid fibers are deposited on the collector [111,112]. The process parameters, such as voltage, flow rate, polymer concentration, nozzle–collector distance, and ambient conditions, significantly influence fiber morphology, diameter, and surface features [113]. Electrospinning also allows the fabrication of complex fiber designs, such as core–shell, Janus, composite, or porous fibers, enabling controlled delivery of biological agents and advanced scaffold functionality [114–117]. Hence, the following sections discuss electrospinning modifications that were applied and further

presented in detail in the experimental part of this dissertation, in **Chapter 6**. These modifications include:

- investigation on the influence of voltage polarity on fiber surface charges,
- core-shell fiber design for the modulation of mechanical and surface properties of fibers,
- fabrication of composite polymer fibers with incorporated conductive fillers.

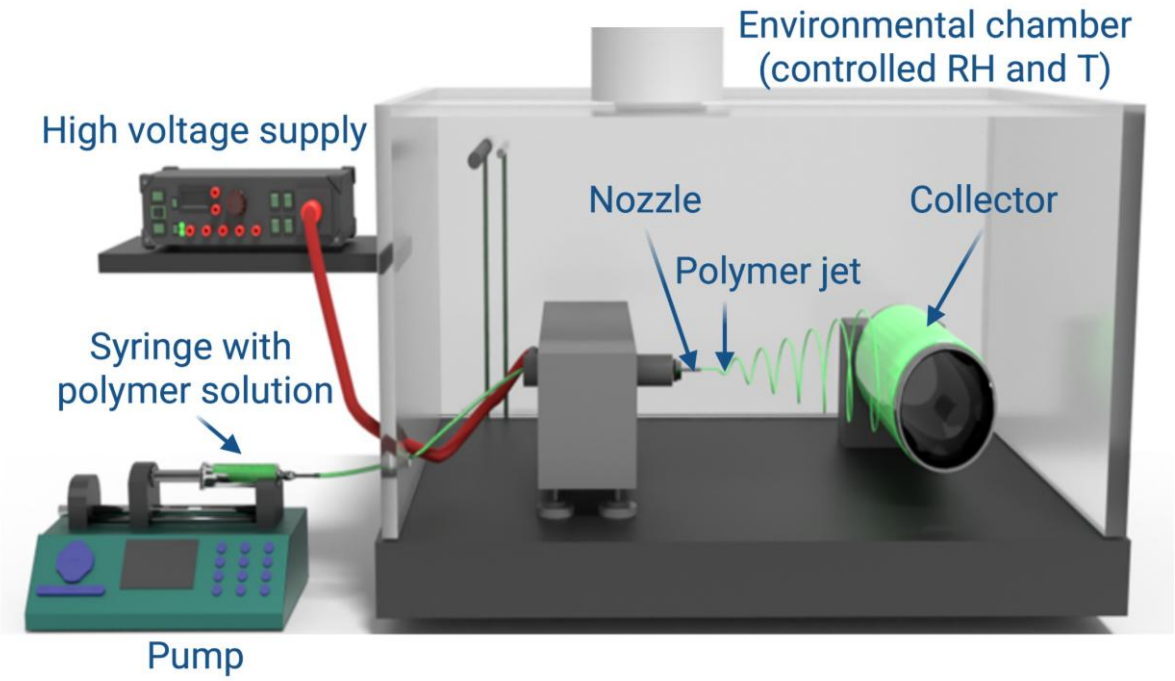

Figure 7. Schematic of the electrospinning set-up. A high-voltage supply is applied to a nozzle. A syringe pump controls the flow rate of the polymer solution. An environmental chamber with controlled relative humidity (RH) and temperature (T), where the electrospinning takes place, allows for reproducibility of the produced fibers. A polymer solution is pushed from the syringe through the tubing, which ends with a nozzle through which the polymer solution is exerted, and creates a jet due to electric field forces. A grounded collector is placed in front of the nozzle to collect polymer fibers.

3.1. Voltage Polarity Effect in Electrospinning

As noted above, electrospinning is driven by a high-voltage electric field between the needle and collector [118]. When a polymer solution forms a droplet at the end of the nozzle,

it proceeds through deformation of the pendant droplet into a cone–jet, driven by the accumulated surface charge. This is followed by the creation of a straight jet, and later, jet thinning is accompanied by bending (whipping) instabilities. Lastly, solidification and deposition of the jet take place as solid fibers on a grounded collector [119]. Here, the electrical potential difference between the nozzle and the collector causes the transport of charges, positive or negative, depending on the electrical polarity applied to the nozzle [120]. It is crucial at the stage when the polymer solution is unsolidified. Polar polymers, which contain permanent dipole moments due to their molecular structure, respond by attempting to align their dipoles in reaction to surrounding external charges. It has already been reported for polymers such as nylon 6 (PA6) [121], polycarbonate (PC) [122], PCL [36], poly(methyl methacrylate) (PMMA) [123], PVDF [124]. For instance, for a positively charged nozzle, positive charges dominate the jet surface. Electronegative groups (e.g., oxygen or fluorine atoms within polymer chains) are attracted toward the surface, driven by the field's direction. Conversely, with a negatively charged nozzle, negative charges on the jet surface repel these electronegative segments, realigning them toward the jet's interior, while more electropositive segments orient toward the surface [113]. Significantly, not only will polar polymers be affected by the applied voltage polarity, but also widely used polyelectrolytes, natural ones such as alginates, and synthetic ones like polyacrylic acid [120,121]. This physical phenomenon occurring during electrospinning of polymers is schematically illustrated in **Figure 8**, where a negative voltage polarity is shown as an example.

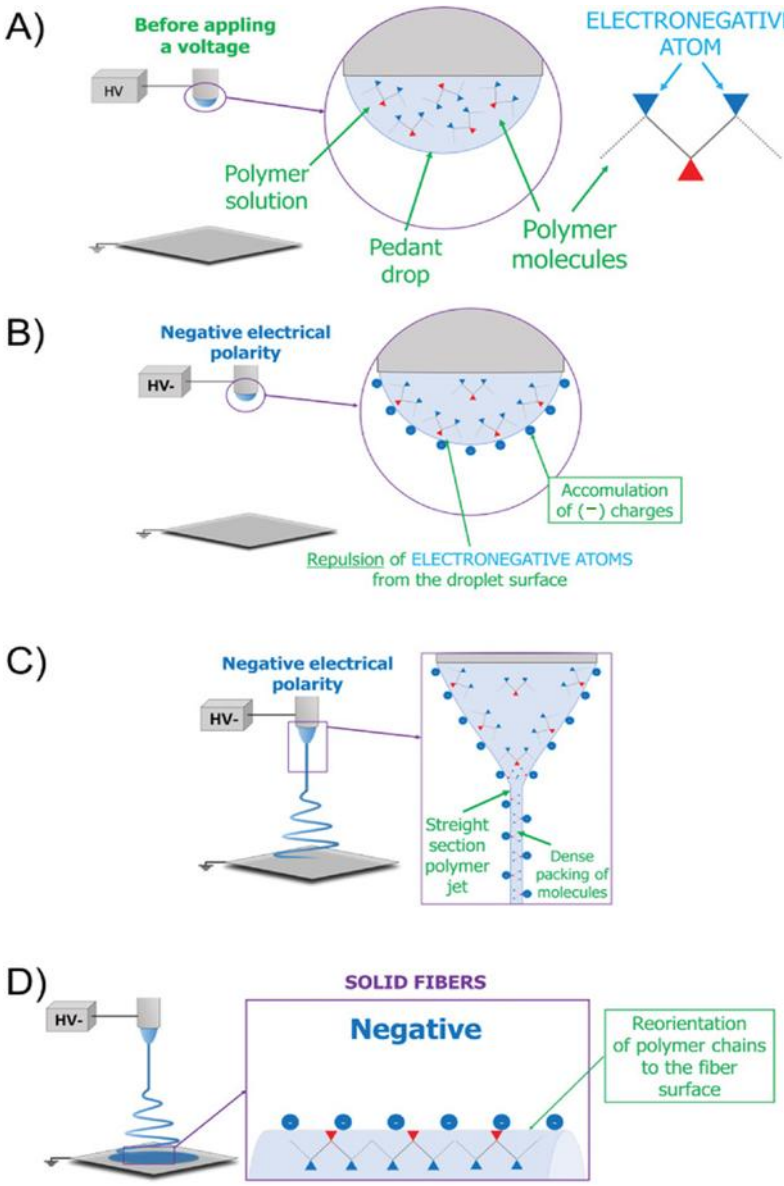

Figure 8. Schematic of polymer chain reorientation during electrospinning under negative voltage polarity. A) Pendant drop at the nozzle tip. B) Surface charge accumulation on the droplet. C) Formation of the jet. D) Deposition of fibers on the grounded collector (counter electrode) with polymer chains reoriented at the fiber surface. Reproduced from the Ref. [113].

Moreover, the surface potential of fibers discussed in Sections 1.1 and 1.2 arises from a combination of intrinsic polymer properties, such as dipole orientation and chemical functional groups, and processing conditions during fiber fabrication [27,36,62,122]. Parameters such as solvent selection, applied voltage, and polarity during electrospinning can

induce surface charge accumulation and molecular polarization [114,123,124]. These modifications do not necessarily affect the scaffold morphology, yet they create substantial differences in electrostatic properties that can strongly influence cellular responses.

In the later discussed studies, it was investigated how one of the most commonly used polymers in tissue engineering, poly(L-lactide) (PLLA), behaves when electrospun with positive and negative voltage polarities. The effect of polarity was linked to the surface potential and the piezoelectric properties of fibers, as well as insights into osteoblast cell response to these effects.

3.2. Core-Shell Fibers

Several challenges in tissue engineering can be overcome by the application of core–shell fibers. This distinctive electrosinning modification, where two concentric fluid streams form a single polymer cone and a continuous core–shell jet, enables the use of different materials in the inner core of the fiber and an outer shell. The functionality of this type of fiber can be used in drug delivery systems [125]. The shell serves as a diffusional and/or degradable barrier that protects from the burst release of substances loaded in the core [126,127]. However, it is highly challenging to control the release rate and diffusion mechanisms because these processes are influenced by numerous variables, both environmental when applied but also dictated by the fiber's properties themselves. A compelling example of advanced drug delivery design was demonstrated by Tiwari et al., who utilized coaxial-electrospinning to fabricate core–shell fibers for partition-controlled release of hydrophilic drugs [128]. It was explored how the combination of a hydrophilic drug-loaded polymer core and a hydrophobic polymer shell can be leveraged to modulate release kinetics. Metoclopramide hydrochloride, encapsulated within a polyvinyl alcohol (PVA) core and surrounded by different shell polymers, such as PCL, PLLA, or poly(lactide-co-glycolide) (PLGA), was investigated. The results showed that shell composition and porosity are critical determinants of the release profile.

Interestingly, specifically for bone tissue engineering, besides the possibility of loading core-shell fibers with active biomolecules in the core for sustained release, this system can also be used for incorporating particles into the outer layer of fibers. Karbowniczek et al. have

shown that core-shell fibers, where the core of poly(3-hydroxybutyrate-co-3-hydroxyvalerate) (PHBV) was coated with TiO_2 (cPHBV+TiO_2) nanoparticles in the shell, promoted better osteoblast proliferation and collagen production than both pristine PHBV and blend electrospun PHBV/TiO_2 (bPHBV+TiO_2) scaffolds [115]. The co-axial electrospinning ensured the uniform distribution of nanoparticles in the shell layer, as illustrated by EDS mapping in **Figure 9b,d**. To compare, in **Figure 9a,c**, it is evident that for blend fibers, bPHBV+TiO_2, formation of embedded in the bulk agglomerations of TiO_2 took place. Importantly, the average diameter of all the fibers was kept constant, allowing for a comparison of the mechanical properties of the scaffolds. Additionally, particle distribution analysis showed that blend electrospinning resulted in a heterogeneous TiO_2 distribution along the fibers, with frequent large aggregates (> 5 μm^2), where co-axial electrospinning yielded composite fibers with uniformly surface-localized nanoparticles, and the mean aggregate area remained ≤ 0.3 μm^2 (violin plot presenting the results is in **Figure 9e**. This uniform nanoparticle distribution strategy within the core-shell design enhanced osteoblast responses, characterized by increased proliferation and collagen expression, suggesting promising outcomes for bone tissue engineering.

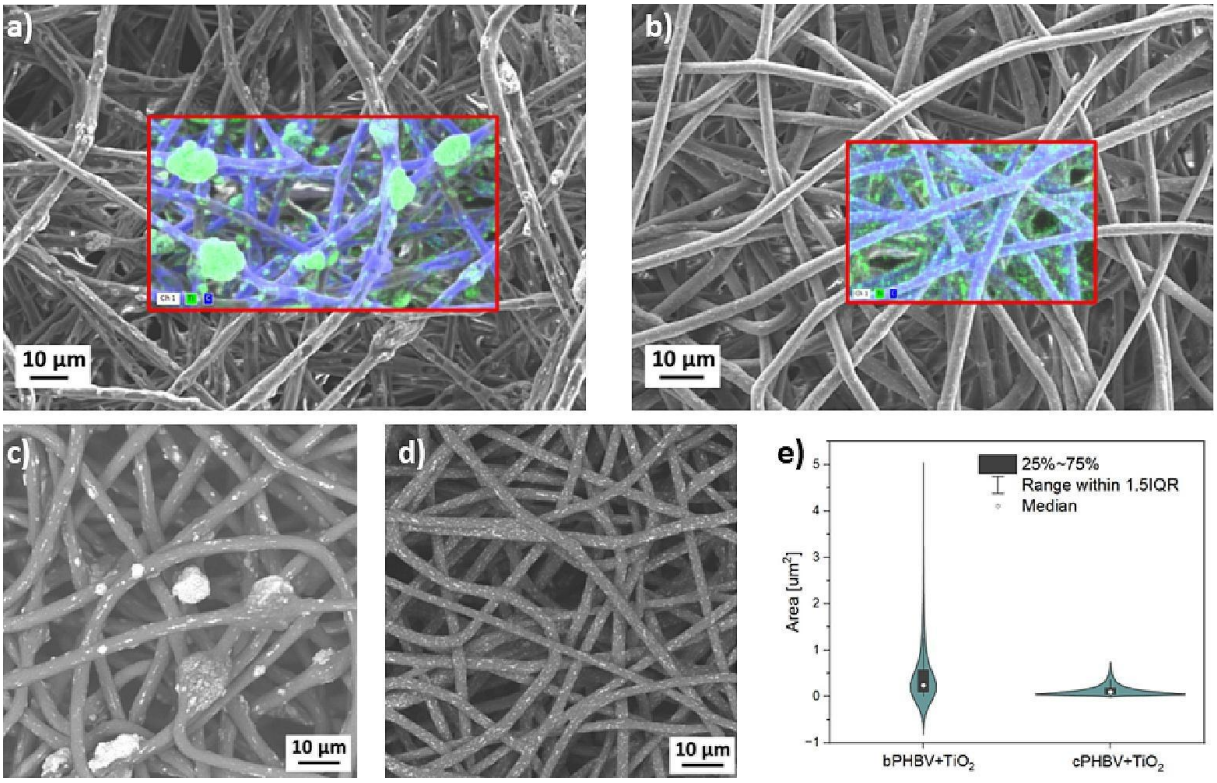

Figure 9. Particle distribution in composite electrospun fibers. a), b) SE-SEM (SE-Secondary Electron) images with EDS maps for bPHBV+TiO_2 and cPHBV+sTiO_2, respectively, showing

carbon (blue) and titanium (green). BSE-SEM (BSE-Backscattered Electron) images of c) bPHBV+TiO_2, d) cPHBV+sTiO_2, highlighting TiO_2 aggregate contrast. e) Violin plot of TiO_2 aggregate areas in blend and core-shell fibers. Reproduced from the Ref. [115].

Nonetheless, in core-shell design, the problem of miscibility between two polymeric materials used in the core and shell has been overlooked in the literature, resulting in a lack of analysis on the surface properties of this type of fibers. This knowledge gap was addressed in this thesis through an analysis of the broad spectrum of properties, including both single fibers and mats. For the experimental part of this thesis, the core-shell PC-PMMA system was chosen. These materials were selected because PMMA is known for its biocompatibility, but the brittleness of this polymer makes it challenging to apply in tissue engineering. While PC shows outstanding mechanical properties, it was selected as a core material for the fibers. Two materials with dissimilar mechanical properties were paired to reduce the intrinsic brittleness of PMMA. Surface potential, topography, chemistry, wettability, and mechanical properties were integrated to provide a comprehensive picture of cell–material interactions, as further discussed in detail.

3.3. Composite Fibers

Bioactivity can be introduced into electrospun fibers through several strategies. One common approach involves blending synthetic polymers with other natural ones, such as collagen, gelatin, or chitosan, which provide cell-binding motifs by affecting the fiber surface properties [129]. Another method incorporates bioactive inorganic components, such as hydroxyapatite, calcium phosphates, or silica nanoparticles, to promote osteogenesis and mechanical stiffness or antibacterial properties of scaffolds [130,131]. Additionally, growth factors, peptides, and drugs can be encapsulated within fibers to offer sustained delivery of biological signals over time [126,127,132,133]. Recent advances have explored the use of electroactive fillers, such as reduced graphene oxide (rGO), carbon nanotubes (CNTs), or MXenes, which impart conductivity or piezoelectricity to the scaffold, enabling electrical stimulation or mechanotransduction-based signaling [30,134–138]. As noted in Chapter 2, the piezoelectric properties of the scaffold are specifically crucial for bone tissue engineering, and composite fibers with enhanced electrical properties appear to be a promising option.

Although rGO and Mxene have been investigated as fillers incorporated into polymer scaffolds for tissue engineering, their effect on the surface properties of fibers has not been explored. Moreover, a comprehensive analysis of the two was never given. These observations motivated an analysis of filler-dependent surface charge and single-fiber/single-cell interactions. PLLA was selected as the matrix polymer for these composite scaffolds, which was already well characterized in previous studies.

4. Aim of the Study

The study aimed to investigate fundamental aspects of cell–material interactions in electrospun scaffolds for bone tissue engineering, with a particular focus on the role of surface charge and its modulation through fiber design and electrospinning parameters.

The research combined design and fabrication of scaffolds, including single-material, composite, and core–shell fibers, with comprehensive multi-scale characterization and biological evaluation. The thesis objectives were defined as follows:

1. Determine how applied voltage polarity during electrospinning governs the surface potential and piezoelectric response of electrospun PLLA fibers, and establish how the resulting electrostatic cues regulate osteoblast adhesion, focal adhesion sites formation, cell proliferation, and collagen formation.
2. Verify whether polymer miscibility in core-shell PC-PMMA electrospun fibers alters surface potential, surface chemistry, wettability, and mechanical properties, and how osteoblasts will respond to those variations at the single-fibre and single-cell scale. To achieve this, develop and apply a confocal microscopy protocol for paxillin immunostaining in osteoblasts, along with quantitative measurements of focal adhesion signal intensity.
3. Compare reduced rGO and MXene as 2D conductive nanofillers in PLLA fibers, quantifying how each alters the surface characteristics of fibers, including surface potential, filler dispersion, mechanical properties of scaffolds, and establishing the resulting effects on osteoblast attachment. Study comprehensive biological responses with the focus on focal adhesion point formation in the fiber regions enriched with fillers via CLSM.

5. Articles Included in the Publication Cycle of the Dissertation

I. **M. Polak**, J.E. Karbowniczek, U. Stachewicz, *Strategies in Electrospun Polymer and Hybrid Scaffolds for Enhanced Cell Integration and Vascularization for Bone Tissue Engineering and Organoids*, WIREs Nanomedicine and Nanobiotechnology, 2024, vol. 16, e2022, pp. 1–35. https://doi.org/10.1002/wnan.2022

II. **M. Polak**, K. Berniak, P.K. Szewczyk, J.E. Karbowniczek, M.M. Marzec, U. Stachewicz, *PLLA Scaffolds with Controlled Surface Potential and Piezoelectricity for Enhancing Cell Adhesion in Tissue Engineering*, Applied Surface Science, 2023, vol. 621, 156835. https://doi.org/10.1016/j.apsusc.2023.156835

III. **M. Polak**, D.P. Ura, K. Berniak, P.K. Szewczyk, M.M. Marzec, U. Stachewicz, *Interfacial Blending in Co-axially Electrospun Polymer Core–Shell Fibers and Their Interaction with Cells via Focal Adhesion Point Analysis*, Colloids and Surfaces B: Biointerfaces, 2024, vol. 237, 113864. https://doi.org/10.1016/j.colsurfb.2024.113864

IV. **M. Polak**, K. Berniak, P.K. Szewczyk, J. Knapczyk-Korczak, M.M. Marzec, M.A.K. Purbayanto, A.M. Jastrzębska, U. Stachewicz, *Modulating Cell Adhesion and Infiltration in Advanced Scaffold Designs Based on PLLA Fibers with rGO and MXene ($Ti_3C_2T_x$)*, Materials Today Bio, 2025, vol. 32, 101785. https://doi.org/10.1016/j.mtbio.2025.101785

Table 1. Summary of bibliographic data included in the dissertation based on Scopus (28.08.2025).

Publication number	IF	Scores MNSiW 2024	Scores divided by the number of co-authors	Citation number (Scopus)
I	8.2	100	33.3	7
II	6.9	140	23.33	47
III	5.6	100	16.66	9
IV	10.2	20	2.5	1

6. Summary of the Articles Included in the Publication

6.1. Strategies in Electrospun Polymer and Hybrid Scaffolds for Enhanced Cell Integration and Vascularization for Bone Tissue Engineering and Organoids

To establish a solid foundation for the experimental phase of my research, I conducted a comprehensive review of strategies for electrospun polymers and hybrid scaffolds that enhance cell integration and vascularization, particularly in bone tissue engineering and organoid systems. Importantly, the review integrates both engineering and biological perspectives, providing a structured discussion on how scaffold properties can be optimized to support the formation of vascularized tissue. It includes numerous examples and comparative analyses of systems tested *in vitro* and *in vivo*, providing a practical guide for future scaffold design in regenerative medicine.

This review analyzed the hierarchical structure of bone, the importance of neovascularization in tissue regeneration, and the limitations of conventional scaffolding methods regarding porosity and oxygen delivery. It explored recent advances in electrospinning modifications to improve scaffold architecture and vascularization potential. Among the electrospinning techniques discussed are air-based fiber focusing, where coaxial airflow is applied at the nozzle to manipulate fiber trajectory and reduce stacking density, and air impedance electrospinning, which utilizes perforated collectors to control fiber deposition through modulated airflow. Other methods include the incorporation of sacrificial fibers or porogens into the scaffold matrix, which can be later dissolved or removed to leave behind pores. Additionally, cryogenic electrospinning involves depositing fibers onto a dry ice-filled collector to maintain loose, open structures. Wet electrospinning into a liquid bath also prevents the formation of tight fiber compaction, supporting the creation of more porous networks. Additionally, patterned collectors and reduced nozzle-to-collector distances in near-field electrospinning are employed to control fiber alignment and inter-fiber spacing with higher precision. These architectural modifications, illustrated in **Figure 10**, reflect the evolving capabilities of electrospinning to address one of its primary challenges—insufficient fiber spacing—while preserving fiber continuity and microscale morphology.

Moreover, challenges in pre-vascularization strategies, selection of cell types, evaluation methods for vascular network formation, and the integration of scaffolds with

bone organoid models were also discussed. This literature study inspired my experimental work, which focused on the fabrication of electrospun scaffolds with controlled properties, with a special emphasis on tuning the surface charge and evaluating osteoblast responses to the physicochemical characteristics of the fibers.

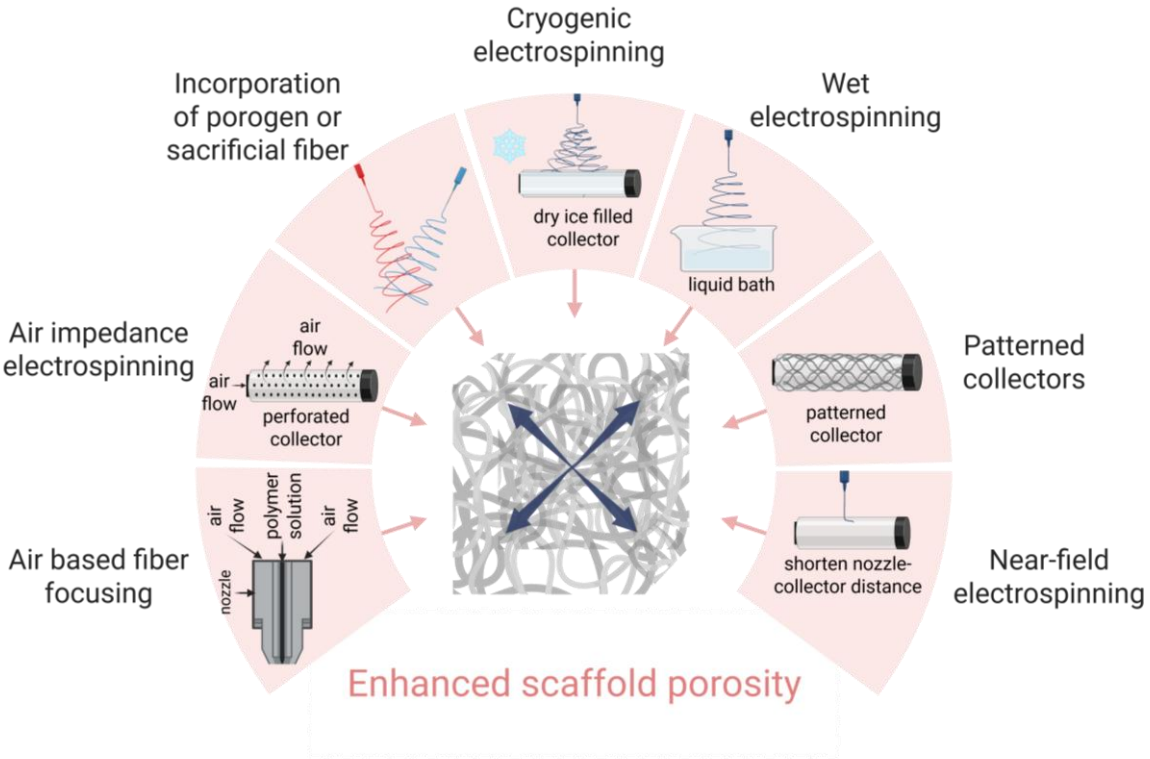

Figure 10. Schematic illustration of electrospinning-based scaffold fabrication strategies and approaches to improve scaffold porosity for promoting better vascularization in tissue regeneration processes.

6.2. PLLA Scaffolds with Controlled Surface Potential and Piezoelectricity for Enhancing Cell Adhesion in Tissue Engineering

The electroactive properties of biomaterials, such as surface potential and piezoelectricity, have emerged as promising physical cues to regulate cell behavior in tissue engineering [25,139–141]. These properties can influence protein adsorption and cell–material interactions, thereby affecting processes such as adhesion, proliferation, and differentiation [142–144]. Among synthetic biodegradable polymers, PLLA is particularly attractive due to its inherent piezoelectricity, which arises from its chiral molecular structure

[145]. However, conventional fabrication methods do not optimize this functionality. In electrospinning, the application of a high-voltage electric field provides a unique opportunity to align polymer chains at the molecular level, potentially enhancing the electroactive response of the resulting fibers [146]. By modifying the polarity of the applied voltage, it is possible to influence both the surface charge distribution and piezoelectric performance of the scaffold, offering a possibility to tune cell–material interactions without additional chemical modification [147–149]. This study investigated the influence of the polarity of the applied voltage during electrospinning on the surface potential and piezoelectric behavior of PLLA fibers, as well as how these properties affect early osteoblast adhesion.

Two types of PLLA scaffolds were fabricated using identical electrospinning conditions, with the only variable being the polarity of applied voltage: positive (PLLA+) and negative (PLLA-). Both scaffold types displayed comparable fiber morphology, diameter, and random orientation, ensuring that observed differences were due to electrostatic factors rather than other variation. KPFM revealed a significant difference in surface potential: PLLA+ fibers exhibited a surface potential of 589 ± 109 mV, while PLLA- 294 ± 62 mV, presented in **Figure 11A** as maps of single fibers confirming similar fiber topography and differences in surface charge. This two-fold increase in surface potential for PLLA+ scaffolds was attributed to reorientation of polymer chains induced by the voltage polarity during fiber formation. Complementary piezoresponse force microscopy (PFM) measurements confirmed that PLLA+ also had a higher piezoelectric coefficient, reinforcing the correlation between voltage polarity and fiber properties. To evaluate the biological relevance of these differences, MG-63 osteoblast-like cells were seeded on both scaffold types and, after 5 hours of incubation, fixed and stained with DAPI to visualize cell nuclei. CLSM was used to capture images of the scaffolds, and the number of adhered cells was quantified by counting DAPI-stained nuclei. The results showed that PLLA+ scaffolds supported significantly more adherent cells than PLLA- (**Figure 11B**), confirming that increased surface potential and piezoelectric response contribute to improved early-stage osteoblast adhesion.

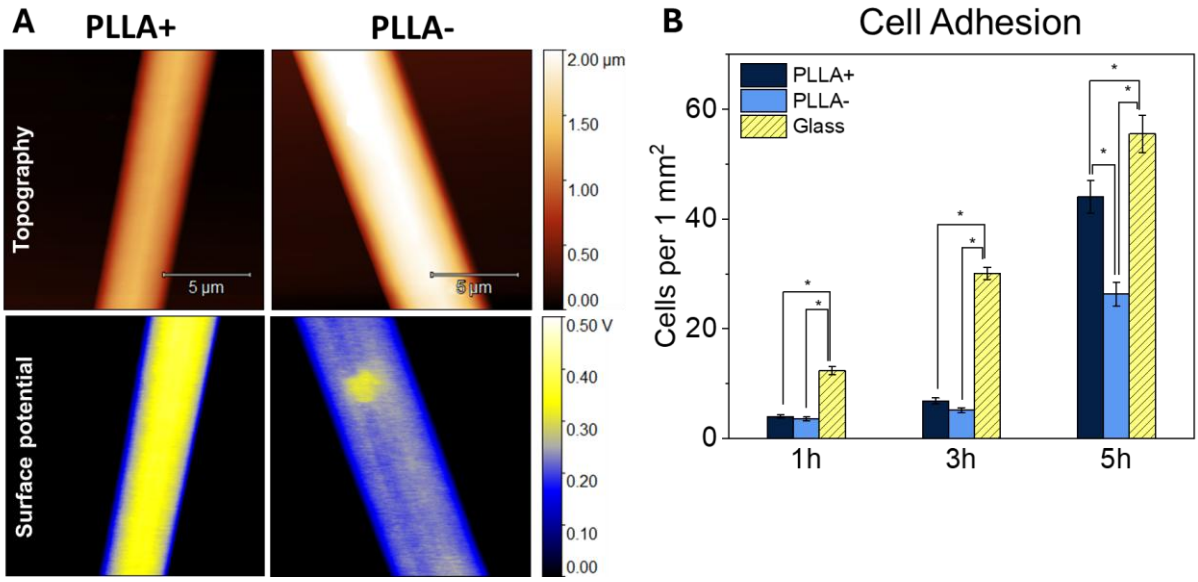

Figure 11. A) Topographical and surface potential characterization of electrospun PLLA fibers produced under opposite voltage polarities. B) Graph presenting the number of adhered MG-63 cells on the scaffolds after 5 hours of cell culture, based on DAPI-stained nuclei counted from CLSM images. Statistical analysis was performed using one-way ANOVA; results show a significant difference ($p < 0.05$) between groups.

This work established that electrospinning polarity is a powerful tool for engineering surface charge and piezoelectricity in polymer scaffolds, without requiring additional chemical modification. These insights laid the groundwork for subsequent studies in this dissertation, where the modulation of surface charge was further expanded using different approaches.

6.3. Interfacial Blending in Co-axially Electrospun Polymer Core–Shell Fibers and Their Interaction with Cells via Focal Adhesion Point Analysis

Coaxial electrospinning is widely utilized in biomedical applications, particularly in drug delivery systems, where the primary objective is often to control the diffusion of core-loaded agents over time [115,126,132]. While considerable effort has been devoted to tailoring the release kinetics through core–shell architecture, the actual composition and surface chemistry of co-axially electrospun fibers immediately after fabrication have remained poorly investigated [150–152]. Despite the common assumption that the outer shell governs initial cell–material interactions, no prior study has directly demonstrated whether and to what extent the core material diffuses through the shell during electrospinning, and whether this

diffusion is sufficient to alter surface chemistry and electrostatic properties. Critically, the question of whether such interfacial blending affects surface potential, or whether cells can detect and respond to these subtle chemical changes, has never been experimentally verified. This study addresses this fundamental gap by characterizing the surface composition and charge in core-shell fibers and investigating their influence on osteoblast adhesion via focal adhesion point formation. **Figure 12** presents the conceptual framework of this study.

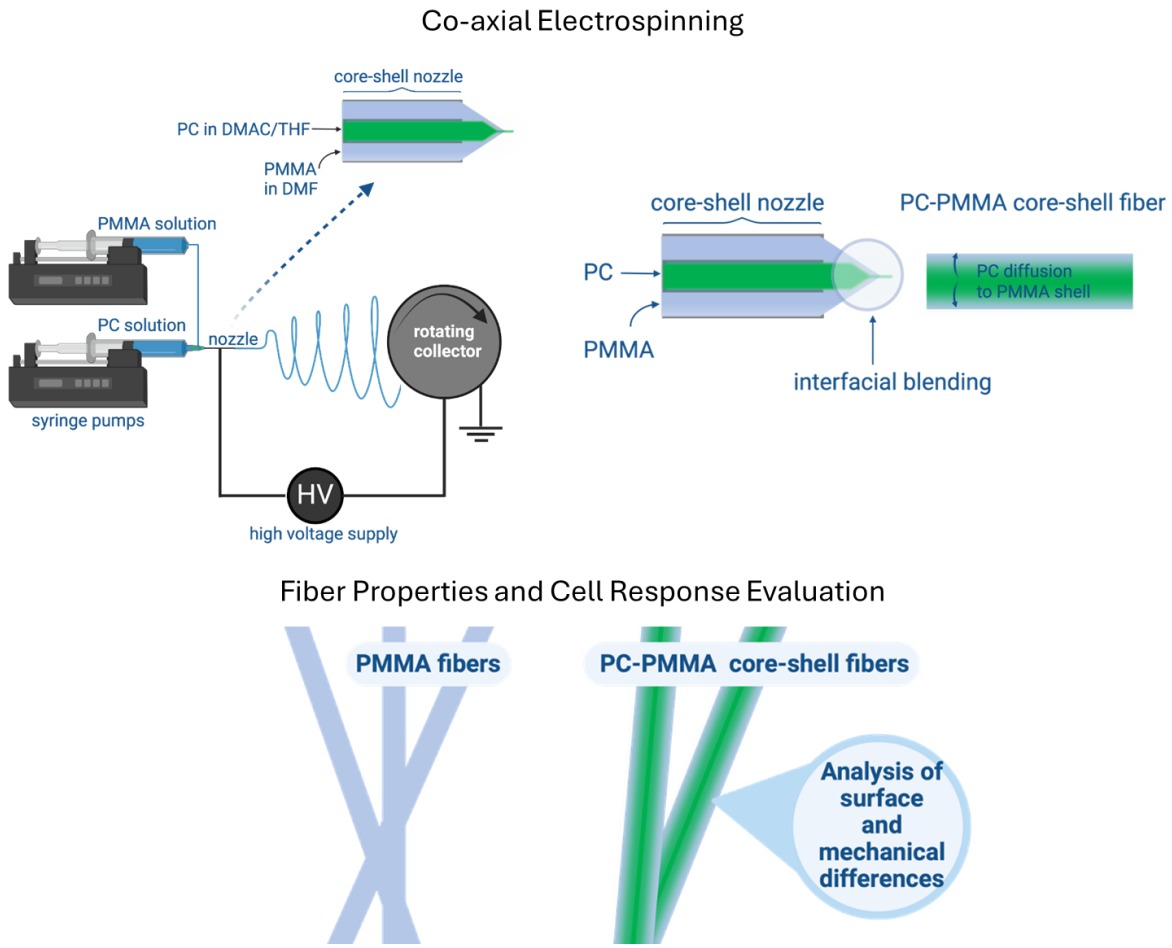

Figure 12. Graphical presentation of the conceptual framework of the study, illustrating core-shell design of fibers, surface property modulation, and the resulting cell–material interactions. Full names of the polymers and solvents used for polymer solutions: PMMA - poly(methyl methacrylate, PC – polycarbonate, DMAC - N,N-dimethylacetamide, DMF - N,N-dimethylformamide.

In this study, PMMA and PC-PMMA core–shell fibers were fabricated to investigate how interfacial blending, caused by polymer diffusion during electrospinning, affects the surface properties, mechanical properties, and cellular response of the resulting scaffolds. SEM analysis confirmed uniform, bead-free morphologies with average fiber diameters of 2 ± 0.35 µm for PMMA and 4.94 ± 0.88 µm for PC-PMMA. Contact angle measurements indicated that both scaffolds remained hydrophobic (~121° for PMMA and ~125° for PC-PMMA). FTIR and DSC confirmed the presence of both polymers in the core–shell structure, while XPS analysis revealed the diffusion of PC into the outer surface of the fibers. Notably, this diffusion altered the fiber surface chemistry, reducing the surface potential from ~650 mV (PMMA) to ~500 mV (PC-PMMA), as measured by KPFM. Mechanical testing revealed that PC-PMMA fibers exhibited toughness over 50 times greater and an elongation at break more than 10 times higher than PMMA mats, demonstrating enhanced ductility due to the PC core.

Cell culture studies with MG-63 osteoblasts were conducted to assess how these surface and mechanical differences influenced cell proliferation and focal adhesion formation. After 7 days, PMMA fibers supported 28% higher cell viability than PC-PMMA. SEM and CLSM imaging corroborated these findings: osteoblasts on PMMA formed dense, confluent layers, while those on PC-PMMA were more elongated and sparse.

To gain deeper insight into the biological interaction, focal adhesion sites were immunostained for paxillin and imaged using super-resolution Airyscan confocal microscopy. Here, single-cell and individual fiber analysis were performed, allowing for the decoupling of the mechanical properties of the whole scaffold from those of the fiber surface. Quantitative analysis revealed that the paxillin signal on PC-PMMA fibers was around 7 times lower than on PMMA fibers, indicating a significant decrease in the number and density of focal adhesion points, as presented in **Figure 13**. This difference was attributed to the altered surface potential and chemical composition caused by PC diffusion through the shell during the coaxial electrospinning process. Although focal adhesion formation on the glass was similar for both samples (as internal controls), the interaction with the fibers differed substantially, highlighting the surface-specific cell response.

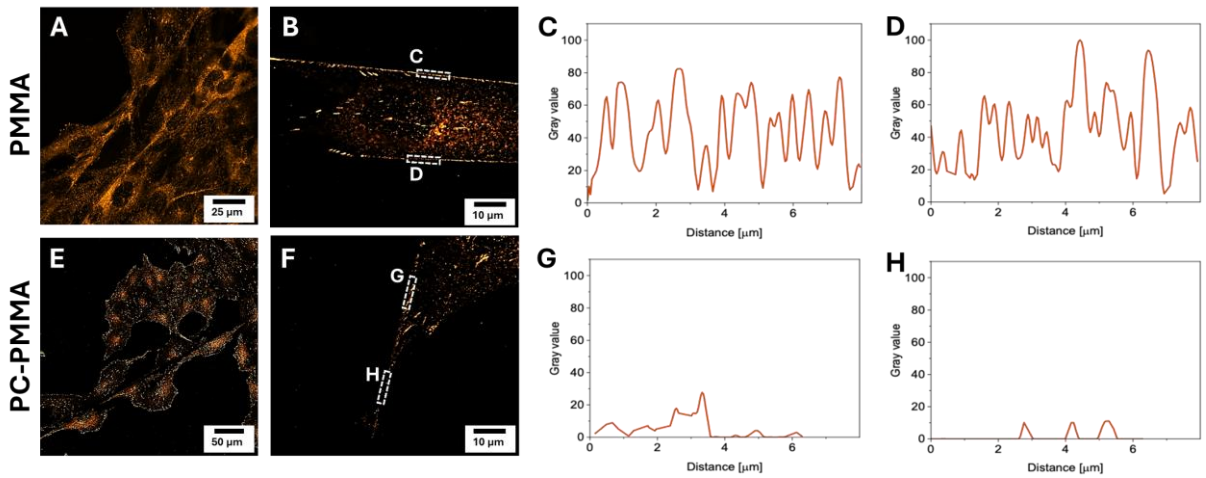

Figure 13. Representative images of paxillin-stained MG-63 osteoblasts cultured on PMMA A)–D) and PC-PMMA E)–H) fibers. A), E) Wide-field Airyscan super-resolution microscopy images showing the overall distribution of focal adhesion points. B), F) Higher magnification views of individual cells on single fibers. C)–D), G)–H) Intensity profiles of paxillin signal across selected regions (white boxes). PMMA-cell interaction exhibits dense and continuous focal adhesion clustering C)–D), while cells on PC-PMMA fibers show sparse and less structured signal patterns G)–H), indicating reduced adhesion site formation.

These results emphasize that even minor interfacial blending in coaxial fibers can drastically alter cellular interactions through modifications in surface charge and chemistry. Therefore, while core–shell designs offer a route to tailor scaffold properties, careful control of core–shell miscibility is crucial to preserve desired surface bioactivity for tissue engineering applications.

6.4. Modulating Cell Adhesion and Infiltration in Advanced Scaffold Designs Based on PLLA Fibers with rGO and MXene ($Ti_3C_2T_X$)

As already discussed, electrospun scaffolds are increasingly used in tissue engineering due to their fibrous architecture and tunable microstructure. However, their dense networks often limit cell infiltration and restrict spatial integration [153,154]. In recent years, two-dimensional (2D) nanomaterials, such as rGO and MXenes (particularly $Ti_3C_2T_x$), have garnered increasing interest for biomedical applications due to their exceptional conductivity, potential for surface functionalization, and bioactive interfaces [155–160]. Although both materials

have been independently explored in tissue engineering contexts, their direct incorporation into polymeric scaffolds, and especially their comparative effects on scaffold electroactivity and architecture, were unexplored. rGO is known for increasing surface roughness and supporting protein adsorption [161], while MXenes offer high surface charge density and hydrophilicity due to their termination groups [162–164]. The novelty of this study lies in using these two 2D fillers in electrospun PLLA fibers to verify how their presence alters the physical and electrostatic properties of scaffolds and how these changes modulate osteoblast adhesion and infiltration. This direct comparison provides insight into how physicochemical properties and distribution of fillers influence cell–material interaction and scaffold performance.

The conceptual framework of this research is presented in **Figure 14**, illustrating how conductive fillers modulate surface charge, thereby impacting osteoblast infiltration. Incorporating fillers into PLLA resulted in distinct changes in fiber arrangement, as repulsion forces induced by the filler surface charge increased inter-fiber spacing and introduced irregularities in fiber packing. This architectural transformation is particularly evident in PLLA-$Ti_3C_2T_X$ scaffolds, where $Ti_3C_2T_X$ agglomerates created the most open and porous scaffold's structure due to their high inherent surface charge and fiber-fiber repulsion effect [121].

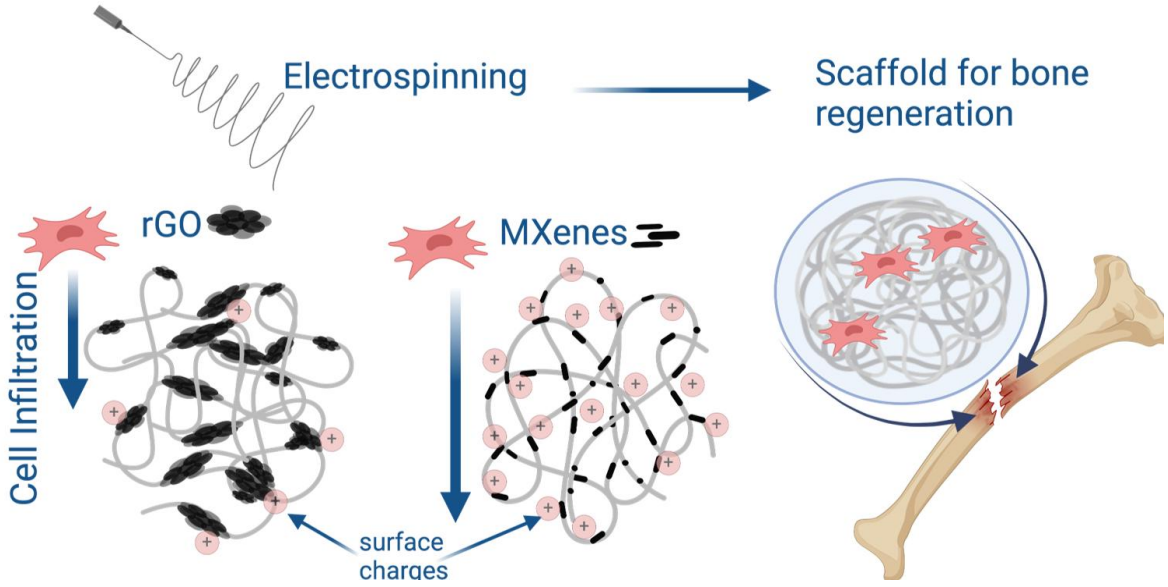

Figure 14. Conceptual scheme of the study on the effect of conductive fillers (rGO and $Ti_3C_2T_X$) on PLLA electrospun fiber surface charge, architecture, and resulting osteoblast response of cell infiltration throughout the scaffold.

KPFM analysis showed that PLLA-$Ti_3C_2T_X$ fibers exhibited a surface potential shift exceeding 400 mV, significantly higher than the ~50 mV shift observed with rGO addition compared to PLLA fibers. It is a direct effect of filler incorporation in the fibers. These substantial differences in surface potential directly affect cell–material interactions, supporting the hypothesis that local charge environment plays a pivotal role in guiding early osteoblast behavior. Mechanical testing demonstrated that the incorporation of fillers compromised the tensile strength and toughness of the scaffolds, with tensile strength decreasing by 55% with rGO and by 81% with $Ti_3C_2T_X$, while toughness declined by 57% and 88%, respectively. Confocal microscopy and z-stack analysis (**Figure 15**) demonstrated that $Ti_3C_2T_X$ scaffolds supported the deepest and most uniform osteoblast infiltration (~125 μm), followed by PLLA-rGO (~100 μm), while pristine PLLA limited infiltration to ~70 μm. The enhanced infiltration in $Ti_3C_2T_X$ scaffolds correlates with both their higher surface potential and changed scaffold architecture. High-resolution confocal imaging further revealed differences in focal adhesions. PLLA-$Ti_3C_2T_X$ scaffolds promoted the formation of large, elongated adhesion clusters, while PLLA-rGO increased the density of localized focal adhesion points. These results highlight how filler type not only modulates surface charge but also dictates the spatial organization of cell–material anchoring structures, which are crucial for stable adhesion. SEM cross-sectional analysis confirmed the confocal results, showing dense layers of cells that penetrate deeper into PLLA-Ti_3C_2TX scaffolds, in contrast to the more superficial colonization observed in pristine PLLA. The improved infiltration and robust adhesion structures in modified scaffolds are directly linked to surface charge differences in filler-containing fibers, which create larger inter-fiber gaps and more accessible paths for cell migration.

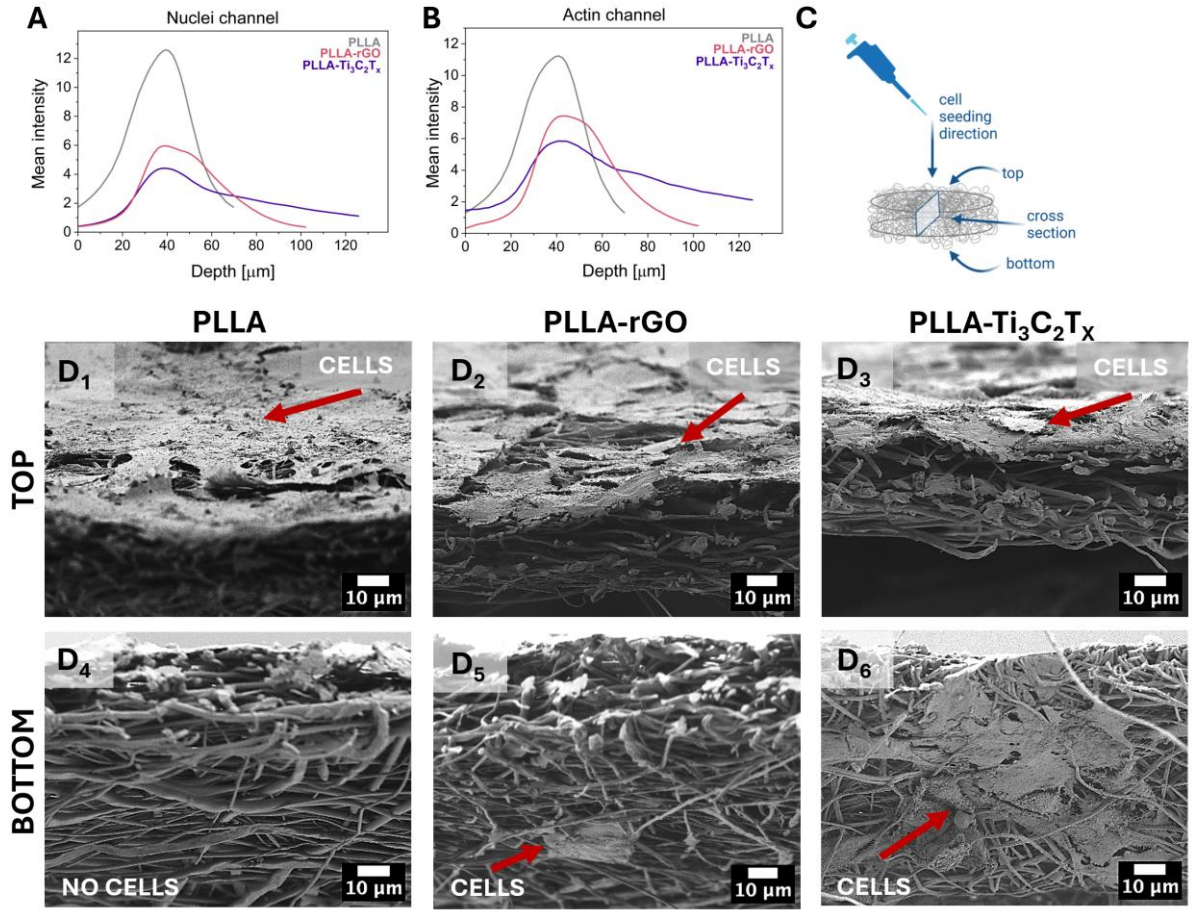

Figure 15. Analysis of osteoblast nuclei and actin signal intensity at different z-stack depths on PLLA, PLLA-rGO, and PLLA-$Ti_3C_2T_X$ scaffolds after 7 days of culture, with 0 µm corresponding to the scaffold surface. A) Graph of nuclei channel (DAPI) signal and B) actin channel (Alexa Fluor 488 Phalloidin) signal, obtained from confocal laser scanning microscopy (CLSM) of stained samples. C) Illustration showing the experimental setup for top and bottom imaging of the samples. D1)-D6) SEM images depicting osteoblast distribution on PLLA (D_1, D_4), PLLA-rGO (D_2, D_5), and PLLA-$Ti_3C_2T_X$ (D_3, D_6) scaffolds, with D1)-D3) representing the top and D4-D6 the bottom view, highlighting differences in cell infiltration among the scaffolds.

To summarize, this study demonstrates that controlling the type and distribution of fillers within electrospun fibers is an effective strategy to modulate scaffold surface charge and architecture, which in turn dictate osteoblast adhesion, focal adhesion cluster formation, and infiltration depth. While challenges remain regarding mechanical strength and long-term biocompatibility of conductive fillers, these findings establish a crucial link between electrospinning parameters, local surface properties, and biological performance.

7. Concluding Remarks and Future Directions

This thesis advances the design of scaffolds for bone tissue engineering and the understanding of cell–material interactions by identifying surface property as a key physical parameter that can be modulated through fiber design and electrospinning conditions. Using a combination of single-material, composite, and core–shell electrospun fibers, I demonstrated that scaffold properties, controlled via voltage polarity, filler incorporation, and core–shell design, have a measurable impact on osteoblast adhesion, focal adhesion organization, and infiltration depth. Importantly, these findings are broadly transferable beyond bone tissue engineering; they provide insights for the development of engineered scaffolds for a variety of tissues and across diverse biomedical contexts. Moreover, the observation that interfacial blending of polymers can occur in core–shell fiber systems has significant implications for drug delivery platforms, where such fibers are widely used, often without a complete understanding of the potential for core–shell mixing to influence release profiles and material performance. Thus, this work underlines critical considerations for the broader application of electrospun fibers in biomedical engineering and therapeutic systems.

The findings presented in this dissertation demonstrate that surface properties are a powerful, tunable parameter in scaffold design, influencing critical early cellular events. By applying positive versus negative voltage polarity during electrospinning of PLLA, fibers with surface potential of 589 ± 109 mV (PLLA+) and 294 ± 62 mV (PLLA-) were fabricated, with the PLLA+ supporting significantly greater osteoblast adhesion within 5h (40% higher), as shown by DAPI-stained nuclei counts.

Co-axial electrospinning was employed to fabricate core–shell PC-PMMA fibers. Characterization via XPS and KPFM revealed that the diffusion of PC into the PMMA shell significantly altered the surface composition, reducing the surface potential from ~650 mV to ~500 mV. This seemingly minor chemical shift resulted in a nearly 7-fold reduction in focal adhesion signal intensity and a 28% decrease in osteoblast viability on PC-PMMA compared to PMMA scaffolds.

Additionally, the incorporation of conductive 2D nanomaterials (rGO and MXene) into PLLA scaffolds induced distinct shifts in surface potential. $Ti_3C_2T_X$ shifted the potential by over

400 mV, compared to ~50 mV for rGO, and altered the scaffold architecture, resulting in enhanced cell infiltration depths of ~125 µm and ~100 µm, respectively, versus only ~70 µm in neat PLLA. Notably, MXene-filled scaffolds promoted the formation of larger, elongated focal adhesion clusters, while rGO-modified fibers enhanced the density of smaller adhesion sites. Both effects are attributable to differences in filler chemistry and resulting charge distribution.

To summarize, in accordance with the research objectives, I developed three types of modifications of electrospun scaffolds, demonstrating that surface potential is a programmable property that links fiber design to early osteoblast behavior. First, I demonstrated that adjusting the electrospinning polarity tunes the surface potential and piezoelectric response of PLLA fibers, thereby regulating the adhesion of osteoblasts. Second, I proved that polymer diffusion from the core to the shell in core–shell fibers occurs, further altering the surface potential of the fibers. This was followed by cell response analysis, which involved quantifying osteoblast adhesion using a single-cell and single-fiber confocal assay with paxillin immunostaining, a technique developed specifically for this work. Third, I compared electroactive nanofillers in composite fibers and elucidated how their physiochemical properties and dispersion alter the surface potential of fibers, their mechanical performance, and scaffold architecture, leading to distinct focal adhesion point analysis on the single-cell scale and cellular infiltration results.

Collectively, these studies establish a coherent framework that links processing, surface properties, and cellular responses, alongside a validated imaging strategy for quantifying interactions between cells and materials at multiple scales. The outcome is a set of practical design rules for tuning electrospun scaffolds through surface charge, core and shell chemistry, and filler selection to direct osteoblast behavior relevant to bone tissue engineering.

Future work should focus on translating these findings into *in vivo* systems to determine the long-term consequences of charge-modulated scaffolds on tissue remodeling, immune response, and vascularization. The development of dynamically responsive scaffolds, capable of modulating surface charge in response to mechanical or environmental stimuli, represents a promising avenue for controlling cell behavior. Finally, expanding this framework

to additional cell types and tissue models, and integrating computational modeling to predict charge–protein–cell interactions, could further accelerate the rational design of next generation bioactive scaffolds.

8. References

[1] N. Ashammakhi, A. Ghavaminejad, R. Tutar, A. Fricker, I. Roy, X. Chatzistavrou, E. Hoque Apu, K.L. Nguyen, T. Ahsan, I. Pountos, E.J. Caterson, Highlights on Advancing Frontiers in Tissue Engineering, Tissue Eng Part B Rev 28 (2022) 633–664. https://doi.org/10.1089/ten.teb.2021.0012.

[2] N. Pallua, C. V. Suschek, Tissue engineering: From lab to clinic, Springer-Verlag Berlin Heidelberg, 2011. https://doi.org/10.1007/978-3-642-02824-3.

[3] B.J. Spanninga, T.-C.A. Hoelen, S. Johnson, B. Cheng, T.J. Blokhuis, P.C. Willems, J.J.C. Arts, Clinical efficacy and safety of P-15 peptide enhanced bone graft substitute in surgical bone regenerative procedures in adult maxillofacial, spine, and trauma patients a systematic literature review, Bone Joint Res 14 (2025) 77–92. https://doi.org/10.1302/2046-3758.

[4] J. Zhang, W. Zhang, W. Yue, W. Qin, Y. Zhao, G. Xu, Research Progress of Bone Grafting: A Comprehensive Review, Int J Nanomedicine 20 (2025) 4729–4757. https://doi.org/10.2147/IJN.S510524.

[5] L. Sapoznikov, M. Humphrey, Progress in Dentin-Derived Bone Graft Materials: A New Xenogeneic Dentin-Derived Material with Retained Organic Component Allows for Broader and Easier Application, Cells 13 (2024). https://doi.org/10.3390/cells13211806.

[6] M.P. Ferraz, Bone Grafts in Dental Medicine: An Overview of Autografts, Allografts and Synthetic Materials, Materials 16 (2023). https://doi.org/10.3390/ma16114117.

[7] E. Steijvers, A. Ghei, Z. Xia, Manufacturing artificial bone allografts: a perspective, Biomaterials Translational 3 (2022) 65–80. https://doi.org/10.12336/biomatertransl.2022.01.007.

[8] P. Fratzl, R. Weinkamer, Nature's hierarchical materials, Prog Mater Sci 52 (2007) 1263–1334. https://doi.org/10.1016/j.pmatsci.2007.06.001.

[9] A.A. Al-Bari, A. Al Mamun, Current advances in regulation of bone homeostasis, FASEB Bioadv 2 (2020) 668–679. https://doi.org/10.1096/fba.2020-00058.

[10] J.G. Skedros, G.C. Clark, S.M. Sorenson, K.W. Taylor, S. Qiu, Analysis of the effect of osteon diameter on the potential relationship of osteocyte lacuna density and osteon wall thickness, Anatomical Record 294 (2011) 1472–1485. https://doi.org/10.1002/ar.21452.

[11] P. Zawadzki, R. Talar, K. Grochalski, M. Dąbrowski, The Influence of Osteon Orientation on Surface Topography Parameters after Machining of Cortical Bone Tissue, Materials 16 (2023). https://doi.org/10.3390/ma16124293.

[12] H.S. Gupta, U. Stachewicz, W. Wagermaier, P. Roschger, H.D. Wagner, P. Fratzl, Mechanical modulation at the lamellar level in osteonal bone, J Mater Res 21 (2006) 1913–1921. https://doi.org/10.1557/jmr.2006.0234.

[13] D.J. Buss, R. Kröger, M.D. McKee, N. Reznikov, Hierarchical organization of bone in three dimensions: A twist of twists, J Struct Biol X 6 (2022). https://doi.org/10.1016/j.yjsbx.2021.100057.

[14] A. Carter, K. Popowski, K. Cheng, A. Greenbaum, F.S. Ligler, A. Moatti, Enhancement of Bone Regeneration through the Converse Piezoelectric Effect, A Novel Approach for Applying Mechanical Stimulation, Bioelectricity 3 (2021) 255–271. https://doi.org/10.1089/bioe.2021.0019.

[15] B. Tandon, J.J. Blaker, S.H. Cartmell, Piezoelectric materials as stimulatory biomedical materials and scaffolds for bone repair, Acta Biomater 73 (2018) 1–20. https://doi.org/10.1016/j.actbio.2018.04.026.

[16] F.M. Chen, X. Liu, Advancing biomaterials of human origin for tissue engineering, Prog Polym Sci 53 (2016) 86–168. https://doi.org/10.1016/j.progpolymsci.2015.02.004.

[17] A. Mishra, U. Modi, R. Sharma, D. Bhatia, R. Solanki, Biochemical and biophysical cues of the extracellular matrix modulates stem cell fate: Progress and prospect in extracellular matrix mimicking biomaterials, Biomedical Engineering Advances 9 (2025) 100143. https://doi.org/10.1016/j.bea.2024.100143.

[18] A. Roi, L.C. Ardelean, C.I. Roi, E.R. Boia, S. Boia, L.C. Rusu, Oral bone tissue engineering: Advanced biomaterials for cell adhesion, proliferation and differentiation, Materials 12 (2019). https://doi.org/10.3390/ma12142296.

[19] P.D. Dalton, T.B.F. Woodfield, V. Mironov, J. Groll, Advances in Hybrid Fabrication toward Hierarchical Tissue Constructs, Advanced Science 7 (2020). https://doi.org/10.1002/advs.201902953.

[20] P.D. Dalton, C. Vaquette, B.L. Farrugia, T.R. Dargaville, T.D. Brown, D.W. Hutmacher, Electrospinning and additive manufacturing: Converging technologies, Biomater Sci 1 (2013) 171–185. https://doi.org/10.1039/c2bm00039c.

[21] L. Parisi, A. Toffoli, G. Ghiacci, G.M. Macaluso, Tailoring the interface of biomaterials to design effective scaffolds, J Funct Biomater 9 (2018). https://doi.org/10.3390/jfb9030050.

[22] S.J. Lee, A. Atala, Scaffold technologies for controlling cell behavior in tissue engineering, Biomedical Materials (Bristol) 8 (2013). https://doi.org/10.1088/1748-6041/8/1/010201.

[23] J.L. Hernandez, K.A. Woodrow, Medical Applications of Porous Biomaterials: Features of Porosity and Tissue-Specific Implications for Biocompatibility, Adv Healthc Mater 11 (2022). https://doi.org/10.1002/adhm.202102087.

[24] S. Norouzi, N. Saveh Shemshaki, E. Norouzi, M. Latifi, B. Azimi, S. Danti, X. Qiao, Y. Miao, S. Yang, M. Gorji, V. Petrovic, M.A. Aboudzadeh, R. Bagherzadeh, Recent advances in biomaterials for tissue-engineered constructs: Essential factors and engineering techniques, Mater Today Chem 37 (2024). https://doi.org/10.1016/j.mtchem.2024.102016.

[25] S. Metwally, U. Stachewicz, Surface potential and charges impact on cell responses on biomaterials interfaces for medical applications, Materials Science and Engineering C 104 (2019). https://doi.org/10.1016/j.msec.2019.109883.

[26] P.K. Szewczyk, S. Metwally, J.E. Karbowniczek, M.M. Marzec, E. Stodolak-Zych, A. Gruszczyński, A. Bernasik, U. Stachewicz, Surface-Potential-Controlled Cell Proliferation and Collagen Mineralization on Electrospun Polyvinylidene Fluoride (PVDF) Fiber Scaffolds for Bone Regeneration, ACS Biomater Sci Eng 5 (2019) 582–593. https://doi.org/10.1021/acsbiomaterials.8b01108.

[27] S. Metwally, S. Ferraris, S. Spriano, Z.J. Krysiak, Ł. Kaniuk, M.M. Marzec, S.K. Kim, P.K. Szewczyk, A. Gruszczyński, M. Wytrwal-Sarna, J.E. Karbowniczek, A. Bernasik, S. Kar-Narayan, U. Stachewicz, Surface potential and roughness controlled cell adhesion and collagen formation in electrospun PCL fibers for bone regeneration, Mater Des 194 (2020). https://doi.org/10.1016/j.matdes.2020.108915.

[28] Y. Zhang, Z. Zheng, S. Zhu, L. Xu, Q. Zhang, J. Gao, M. Ye, S. Shen, J. Xing, M. Wu, R.X. Xu, Electroactive Electrospun Nanofibrous Scaffolds: Innovative Approaches for Improved Skin Wound Healing, Advanced Science 12 (2025). https://doi.org/10.1002/advs.202416267.

[29] M. Polak, J.E. Karbowniczek, U. Stachewicz, Strategies in Electrospun Polymer and Hybrid Scaffolds for Enhanced Cell Integration and Vascularization for Bone Tissue Engineering and Organoids, Wiley Interdiscip Rev Nanomed Nanobiotechnol 16 (2024). https://doi.org/10.1002/wnan.2022.

[30] M. Polak, K. Berniak, P.K. Szewczyk, J. Knapczyk-Korczak, M.M. Marzec, M.A.K. Purbayanto, A.M. Jastrzębska, U. Stachewicz, Modulating Cell Adhesion and Infiltration in Advanced Scaffold Designs based on PLLA Fibers with rGO and MXene (Ti3C2T), Mater Today Bio (2025) 101785. https://doi.org/10.1016/j.mtbio.2025.101785.

[31] M. Mohseni, S. Cometta, L. Klein, M.L. Wille, C. Vaquette, D.W. Hutmacher, F. Medeiros Savi, In vitro and in vivo degradation studies of a dual medical-grade scaffold design for guided soft tissue regeneration, Biomater Sci 13 (2025) 2115–2133. https://doi.org/10.1039/d4bm01132e.

[32] H. Mndlovu, P. Kumar, L.C. du Toit, Y.E. Choonara, A review of biomaterial degradation assessment approaches employed in the biomedical field, Npj Mater Degrad 8 (2024). https://doi.org/10.1038/s41529-024-00487-1.

[33] M.I. Echeverria Molina, K.G. Malollari, K. Komvopoulos, Design Challenges in Polymeric Scaffolds for Tissue Engineering, Front Bioeng Biotechnol 9 (2021). https://doi.org/10.3389/fbioe.2021.617141.

[34] N.R. Richbourg, N.A. Peppas, V.I. Sikavitsas, Tuning the biomimetic behavior of scaffolds for regenerative medicine through surface modifications, J Tissue Eng Regen Med 13 (2019) 1275–1293. https://doi.org/10.1002/term.2859.

[35] H. Rashidi, J. Yang, K.M. Shakesheff, Surface engineering of synthetic polymer materials for tissue engineering and regenerative medicine applications, Biomater Sci 2 (2014) 1318–1331. https://doi.org/10.1039/c3bm60330j.

[36] S. Metwally, J.E. Karbowniczek, P.K. Szewczyk, M.M. Marzec, A. Gruszczyński, A. Bernasik, U. Stachewicz, Single-Step Approach to Tailor Surface Chemistry and Potential on Electrospun PCL

Fibers for Tissue Engineering Application, Adv Mater Interfaces 6 (2019). https://doi.org/10.1002/admi.201801211.

[37] S. Eisenberg, E. Haimov, G.F.W. Walpole, J. Plumb, M.M. Kozlov, S. Grinstein, Mapping the electrostatic profiles of cellular membranes, Mol Biol Cell 32 (2021) 301–310. https://doi.org/10.1091/MBC.E19-08-0436.

[38] V.V. Galassi, N. Wilke, On the coupling between mechanical properties and electrostatics in biological membranes, Membranes (Basel) 11 (2021). https://doi.org/10.3390/membranes11070478.

[39] S. Ahn, K.Y. Lee, K.K. Parker, K. Shin, Formation of Multi-Component Extracellular Matrix Protein Fibers, Sci Rep 8 (2018). https://doi.org/10.1038/s41598-018-20371-8.

[40] S. Eisenberg, E. Haimov, G.F.W. Walpole, J. Plumb, M.M. Kozlov, S. Grinstein, Mapping the electrostatic profiles of cellular membranes, Mol Biol Cell 32 (2021) 301–310. https://doi.org/10.1091/MBC.E19-08-0436.

[41] S. Ahn, A. Jain, K.C. Kasuba, M. Seimiya, R. Okamoto, B. Treutlein, D.J. Müller, Engineering fibronectin-templated multi-component fibrillar extracellular matrices to modulate tissue-specific cell response, Biomaterials 308 (2024). https://doi.org/10.1016/j.biomaterials.2024.122560.

[42] F. Wang, X. Cai, Y. Shen, L. Meng, Cell–scaffold interactions in tissue engineering for oral and craniofacial reconstruction, Bioact Mater 23 (2023) 16–44. https://doi.org/10.1016/j.bioactmat.2022.10.029.

[43] P. Nitti, A. Narayanan, R. Pellegrino, S. Villani, M. Madaghiele, C. Demitri, Cell-Tissue Interaction: The Biomimetic Approach to Design Tissue Engineered Biomaterials, Bioengineering 10 (2023). https://doi.org/10.3390/bioengineering10101122.

[44] H. Lee, W. Lee, J.H. Lee, D.S. Yoon, Surface potential analysis of nanoscale biomaterials and devices using Kelvin probe force microscopy, J Nanomater 2016 (2016). https://doi.org/10.1155/2016/4209130.

[45] Y. Li, Y. Luo, S. Xiao, C. Zhang, C. Pan, F. Zeng, Z. Cui, B. Huang, J. Tang, T. Shao, X. Zhang, J. Xiong, Z.L. Wang, Visualization and standardized quantification of surface charge density for triboelectric materials, Nat Commun 15 (2024). https://doi.org/10.1038/s41467-024-49660-9.

[46] H.J. Butt, B. Cappella, M. Kappl, Force measurements with the atomic force microscope: Technique, interpretation and applications, Surf Sci Rep 59 (2005) 1–152. https://doi.org/10.1016/j.surfrep.2005.08.003.

[47] B. Cappella, G. Dietler, Force-distance curves by atomic force microscopy, n.d.

[48] Y.F. Dufrêne, Atomic force microscopy, a powerful tool in microbiology, J Bacteriol 184 (2002) 5205–5213. https://doi.org/10.1128/JB.184.19.5205-5213.2002.

[49] D.S. Jakob, N. Li, H. Zhou, X.G. Xu, Integrated Tapping Mode Kelvin Probe Force Microscopy with Photoinduced Force Microscopy for Correlative Chemical and Surface Potential Mapping, Small 17 (2021). https://doi.org/10.1002/smll.202102495.

[50] H.O. Jacobs, H.F. Knapp, A. Stemmer, Practical aspects of Kelvin probe force microscopy, Review of Scientific Instruments 70 (1999) 1756–1760. https://doi.org/10.1063/1.1149664.

[51] U. Zerweck, C. Loppacher, T. Otto, S. Grafström, L.M. Eng, Accuracy and resolution limits of Kelvin probe force microscopy, Phys Rev B Condens Matter Mater Phys 71 (2005). https://doi.org/10.1103/PhysRevB.71.125424.

[52] M. Checa, A.S. Fuhr, C. Sun, R. Vasudevan, M. Ziatdinov, I. Ivanov, S.J. Yun, K. Xiao, A. Sehirlioglu, Y. Kim, P. Sharma, K.P. Kelley, N. Domingo, S. Jesse, L. Collins, High-speed mapping of surface charge dynamics using sparse scanning Kelvin probe force microscopy, Nat Commun 14 (2023). https://doi.org/10.1038/s41467-023-42583-x.

[53] C. Yang, H. Wang, K. Wang, Z. Cao, F. Ren, G. Zhou, Y. Chen, B. Sun, Silk Fibroin-Based Biomemristors for Bionic Artificial Intelligence Robot Applications, ACS Nano 19 (2025) 17173–17198. https://doi.org/10.1021/acsnano.5c02480.

[54] W. Liu, H. Zhao, C. Zhang, S. Xu, F. Zhang, L. Wei, F. Zhu, Y. Chen, Y. Chen, Y. Huang, M. Xu, Y. He, B.C. Heng, J. Zhang, Y. Shen, X. Zhang, H. Huang, L. Chen, X. Deng, In situ activation of flexible magnetoelectric membrane enhances bone defect repair, Nat Commun 14 (2023). https://doi.org/10.1038/s41467-023-39744-3.

[55] T. Hackl, G. Schitter, P. Mesquida, AC Kelvin Probe Force Microscopy Enables Charge Mapping in Water, ACS Nano 16 (2022) 17982–17990. https://doi.org/10.1021/acsnano.2c07121.

[56] X. Yin, J. Drelich, Surface charge microscopy: Novel technique for mapping charge-mosaic surfaces in electrolyte solutions, Langmuir 24 (2008) 8013–8020. https://doi.org/10.1021/la801269z.

[57] S. Kamble, S. Agrawal, S. Cherumukkil, V. Sharma, R.V. Jasra, P. Munshi, Revisiting Zeta Potential, the Key Feature of Interfacial Phenomena, with Applications and Recent Advancements, ChemistrySelect 7 (2022). https://doi.org/10.1002/slct.202103084.

[58] D. Cho, S.G. Lee, M.W. Frey, Characterizing zeta potential of functional nanofibers in a microfluidic device, J Colloid Interface Sci 372 (2012) 252–260. https://doi.org/10.1016/j.jcis.2012.01.007.

[59] Ł. Kaniuk, S. Ferraris, S. Spriano, T. Luxbacher, Z. Krysiak, K. Berniak, A. Zaszczynska, M.M. Marzec, A. Bernasik, P. Sajkiewicz, U. Stachewicz, Time-dependent effects on physicochemical and surface properties of PHBV fibers and films in relation to their interactions with fibroblasts, Appl Surf Sci 545 (2021). https://doi.org/10.1016/j.apsusc.2021.148983.

[60] S. Ferraris, M. Cazzola, V. Peretti, B. Stella, S. Spriano, Zeta potential measurements on solid surfaces for in Vitro biomaterials testing: Surface charge, reactivity upon contact with fluids and protein absorption, Front Bioeng Biotechnol 6 (2018). https://doi.org/10.3389/fbioe.2018.00060.

[61] S. Spriano, V. Sarath Chandra, A. Cochis, F. Uberti, L. Rimondini, E. Bertone, A. Vitale, C. Scolaro, M. Ferrari, F. Cirisano, G. Gautier di Confiengo, S. Ferraris, How do wettability, zeta potential and hydroxylation degree affect the biological response of biomaterials?, Materials Science and Engineering C 74 (2017) 542–555. https://doi.org/10.1016/j.msec.2016.12.107.

[62] M. Polak, K. Berniak, P.K. Szewczyk, J.E. Karbowniczek, M.M. Marzec, U. Stachewicz, PLLA scaffolds with controlled surface potential and piezoelectricity for enhancing cell adhesion in tissue engineering, Appl Surf Sci 621 (2023). https://doi.org/10.1016/j.apsusc.2023.156835.

[63] S. Preethi Soundarya, A. Haritha Menon, S. Viji Chandran, N. Selvamurugan, Bone tissue engineering: Scaffold preparation using chitosan and other biomaterials with different design and fabrication techniques, Int J Biol Macromol 119 (2018) 1228–1239. https://doi.org/10.1016/j.ijbiomac.2018.08.056.

[64] U. Stachewicz, P.K. Szewczyk, A. Kruk, A.H. Barber, A. Czyrska-Filemonowicz, Pore shape and size dependence on cell growth into electrospun fiber scaffolds for tissue engineering: 2D and 3D analyses using SEM and FIB-SEM tomography, Materials Science and Engineering C 95 (2019) 397–408. https://doi.org/10.1016/j.msec.2017.08.076.

[65] U. Stachewicz, T. Qiao, S.C.F. Rawlinson, F.V. Almeida, W.Q. Li, M. Cattell, A.H. Barber, 3D imaging of cell interactions with electrospun PLGA nanofiber membranes for bone regeneration, Acta Biomater 27 (2015) 88–100. https://doi.org/10.1016/j.actbio.2015.09.003.

[66] A.G. Abdelaziz, H. Nageh, S.M. Abdo, M.S. Abdalla, A.A. Amer, A. Abdal-hay, A. Barhoum, A Review of 3D Polymeric Scaffolds for Bone Tissue Engineering: Principles, Fabrication Techniques, Immunomodulatory Roles, and Challenges, Bioengineering 10 (2023). https://doi.org/10.3390/bioengineering10020204.

[67] Q.L. Loh, C. Choong, Three-dimensional scaffolds for tissue engineering applications: Role of porosity and pore size, Tissue Eng Part B Rev 19 (2013) 485–502. https://doi.org/10.1089/ten.teb.2012.0437.

[68] N. Goonoo, Vascularization and angiogenesis in electrospun tissue engineered constructs: Towards the creation of long-term functional networks, Biomed Phys Eng Express 4 (2018). https://doi.org/10.1088/2057-1976/aaab03.

[69] F. Diomede, G.D. Marconi, L. Fonticoli, J. Pizzicanella, I. Merciaro, P. Bramanti, E. Mazzon, O. Trubiani, Functional relationship between osteogenesis and angiogenesis in tissue regeneration, Int J Mol Sci 21 (2020). https://doi.org/10.3390/ijms21093242.

[70] C. Correia, W.L. Grayson, M. Park, D. Hutton, B. Zhou, X.E. Guo, L. Niklason, R.A. Sousa, R.L. Reis, G. Vunjak-Novakovic, In vitro model of vascularized bone: Synergizing vascular development and osteogenesis, PLoS One 6 (2011). https://doi.org/10.1371/journal.pone.0028352.

[71] H. Zhang, J.L. Liesveld, L.M. Calvi, B.C. Lipe, L. Xing, M.W. Becker, E.M. Schwarz, S.C.A. Yeh, The roles of bone remodeling in normal hematopoiesis and age-related hematological malignancies, Bone Res 11 (2023). https://doi.org/10.1038/s41413-023-00249-w.

[72] N.İ. Büyük, D. Aksu, G. Torun Köse, Effect of different pore sizes of 3D printed PLA-based scaffold in bone tissue engineering, International Journal of Polymeric Materials and Polymeric Biomaterials 72 (2023) 1021–1031. https://doi.org/10.1080/00914037.2022.2075869.

[73] M.N. Collins, G. Ren, K. Young, S. Pina, R.L. Reis, J.M. Oliveira, Scaffold Fabrication Technologies and Structure/Function Properties in Bone Tissue Engineering, Adv Funct Mater 31 (2021). https://doi.org/10.1002/adfm.202010609.

[74] F. Mukasheva, L. Adilova, A. Dyussenbinov, B. Yernaimanova, M. Abilev, D. Akilbekova, Optimizing scaffold pore size for tissue engineering: insights across various tissue types, Front Bioeng Biotechnol 12 (2024). https://doi.org/10.3389/fbioe.2024.1444986.

[75] J. Rnjak-Kovacina, A.S. Weiss, Increasing the pore size of electrospun scaffolds, Tissue Eng Part B Rev 17 (2011) 365–372. https://doi.org/10.1089/ten.teb.2011.0235.

[76] J.M. Ameer, P.R. Anil Kumar, N. Kasoju, Strategies to tune electrospun scaffold porosity for effective cell response in tissue engineering, J Funct Biomater 10 (2019). https://doi.org/10.3390/jfb10030030.

[77] K.P. Feltz, E.A. Growney Kalaf, C. Chen, R.S. Martin, S.A. Sell, A review of electrospinning manipulation techniques to direct fiber deposition and maximize pore size, Electrospinning 2 (2017) 46–61. https://doi.org/10.1515/esp-2017-0002.

[78] R. Podgórski, M. Wojasiński, A. Małolepszy, J. Jaroszewicz, T. Ciach, Fabrication of 3D-Printed Scaffolds with Multiscale Porosity, ACS Omega 9 (2024) 29186–29204. https://doi.org/10.1021/acsomega.3c09035.

[79] Y. Satapathy, V. Nikitin, J. Hana, K.R. Venkatesan, F. Tran, S. Chen, P. Shevchenko, F. De Carlo, R. Kettimuthu, S. Zekriardehani, J. Mapkar, A. Krishnamurthy, A. Tekawade, Multiscale porosity characterization in additively manufactured polymer nanocomposites using micro-computed tomography, Addit Manuf 86 (2024). https://doi.org/10.1016/j.addma.2024.104199.

[80] L. Vásárhelyi, Z. Kónya, Kukovecz, R. Vajtai, Microcomputed tomography–based characterization of advanced materials: a review, Mater Today Adv 8 (2020). https://doi.org/10.1016/j.mtadv.2020.100084.

[81] S. Scaglione, L. Ceseracciu, M. Aiello, L. Coluccino, F. Ferrazzo, P. Giannoni, R. Quarto, A Novel Scaffold Geometry for Chondral Applications: Theoretical Model and in Vivo Validation, Biotechnol. Bioeng 111 (2014) 2107–2119. https://doi.org/10.1002/bit.25255/abstract.

[82] P.R. Cortez Tornello, P.C. Caracciolo, T.R. Cuadrado, G.A. Abraham, Structural characterization of electrospun micro/nanofibrous scaffolds by liquid extrusion porosimetry: A comparison with other techniques, Materials Science and Engineering C 41 (2014) 335–342. https://doi.org/10.1016/j.msec.2014.04.065.

[83] H.J. Haugen, S. Bertoldi, Characterization of morphology-3D and porous structure, in: Characterization of Polymeric Biomaterials, Elsevier, 2017: pp. 21–53. https://doi.org/10.1016/B978-0-08-100737-2.00002-9.

[84] L.T. Choong, P. Yi, G.C. Rutledge, Three-dimensional imaging of electrospun fiber mats using confocal laser scanning microscopy and digital image analysis, J Mater Sci 50 (2015) 3014–3030. https://doi.org/10.1007/s10853-015-8834-2.

[85] K. Keklikoglou, C. Arvanitidis, G. Chatzigeorgiou, E. Chatzinikolaou, E. Karagiannidis, T. Koletsa, A. Magoulas, K. Makris, G. Mavrothalassitis, E.D. Papanagnou, A.S. Papazoglou, C. Pavloudi, I.P. Trougakos, K. Vasileiadou, A. Vogiatzi, Micro-ct for biological and biomedical studies: A comparison of imaging techniques, J Imaging 7 (2021). https://doi.org/10.3390/jimaging7090172.

[86] A.L. Marquez, I.E. Gareis, F.J. Dias, C. Gerhard, M.F. Lezcano, Methods to Characterize Electrospun Scaffold Morphology: A Critical Review, Polymers (Basel) 14 (2022). https://doi.org/10.3390/polym14030467.

[87] S. Wang, S. Hashemi, S. Stratton, T.L. Arinzeh, The Effect of Physical Cues of Biomaterial Scaffolds on Stem Cell Behavior, Adv Healthc Mater 10 (2021). https://doi.org/10.1002/adhm.202001244.

[88] C.F. Guimarães, A.P. Marques, R.L. Reis, Pushing the Natural Frontier: Progress on the Integration of Biomaterial Cues toward Combinatorial Biofabrication and Tissue Engineering, Advanced Materials 34 (2022). https://doi.org/10.1002/adma.202105645.

[89] P. Nitti, A. Narayanan, R. Pellegrino, S. Villani, M. Madaghiele, C. Demitri, Cell-Tissue Interaction: The Biomimetic Approach to Design Tissue Engineered Biomaterials, Bioengineering 10 (2023). https://doi.org/10.3390/bioengineering10101122.

[90] C. Von Bilderling, M. Caldarola, M.E. Masip, A. V. Bragas, L.I. Pietrasanta, Monitoring in real-time focal adhesion protein dynamics in response to a discrete mechanical stimulus, Review of Scientific Instruments 88 (2017). https://doi.org/10.1063/1.4973664.

[91] B. Zimerman, T. Volberg, B. Geiger, Early molecular events in the assembly of the focal adhesion-stress fiber complex during fibroblast spreading, Cell Motil Cytoskeleton 58 (2004) 143–159. https://doi.org/10.1002/cm.20005.

[92] J. Xue, D. Pisignano, Y. Xia, Maneuvering the Migration and Differentiation of Stem Cells with Electrospun Nanofibers, Advanced Science 7 (2020). https://doi.org/10.1002/advs.202000735.

[93] Ł. Kaniuk, K. Berniak, A. Lichawska-Cieślar, J. Jura, J.E. Karbowniczek, U. Stachewicz, Accelerated wound closure rate by hyaluronic acid release from coated PHBV electrospun fiber scaffolds, J Drug Deliv Sci Technol 77 (2022). https://doi.org/10.1016/j.jddst.2022.103855.

[94] K. Katoh, Integrin and Its Associated Proteins as a Mediator for Mechano-Signal Transduction, Biomolecules 15 (2025). https://doi.org/10.3390/biom15020166.

[95] R.E. Bridgewater, J.C. Norman, P.T. Caswell, Integrin trafficking at a glance, J Cell Sci 125 (2012) 3695–3701. https://doi.org/10.1242/jcs.095810.

[96] P. Dhavalikar, A. Robinson, Z. Lan, D. Jenkins, M. Chwatko, K. Salhadar, A. Jose, R. Kar, E. Shoga, A. Kannapiran, E. Cosgriff-Hernandez, Review of Integrin-Targeting Biomaterials in Tissue Engineering, Adv Healthc Mater 9 (2020). https://doi.org/10.1002/adhm.202000795.

[97] X. Pang, X. He, Z. Qiu, H. Zhang, R. Xie, Z. Liu, Y. Gu, N. Zhao, Q. Xiang, Y. Cui, Targeting integrin pathways: mechanisms and advances in therapy, Signal Transduct Target Ther 8 (2023). https://doi.org/10.1038/s41392-022-01259-6.

[98] M. Ripamonti, B. Wehrle-Haller, I. de Curtis, Paxillin: A Hub for Mechano-Transduction from the β3 Integrin-Talin-Kindlin Axis, Front Cell Dev Biol 10 (2022). https://doi.org/10.3389/fcell.2022.852016.

[99] L. Khalef, R. Lydia, K. Filicia, B. Moussa, Cell viability and cytotoxicity assays: Biochemical elements and cellular compartments, Cell Biochem Funct 42 (2024). https://doi.org/10.1002/cbf.4007.

[100] Y. Fan, A. Bergmann, Apoptosis-induced compensatory proliferation. The Cell is dead. Long live the Cell!, Trends Cell Biol 18 (2008) 467–473. https://doi.org/10.1016/j.tcb.2008.08.001.

[101] C.E. Fogarty, A. Bergmann, Killers creating new life: Caspases drive apoptosis-induced proliferation in tissue repair and disease, Cell Death Differ 24 (2017) 1390–1400. https://doi.org/10.1038/cdd.2017.47.

[102] A. Huttenlocher, A.R. Horwitz, Integrins in cell migration, Cold Spring Harb Perspect Biol 3 (2011) 1–16. https://doi.org/10.1101/cshperspect.a005074.

[103] D.J. Webb, J.T. Parsons, A.F. Horwitz, Adhesion assembly, disassembly and turnover in migrating cells-over and over and over again, 2002. http://cellbio.nature.comE97.

[104] N. Kramer, A. Walzl, C. Unger, M. Rosner, G. Krupitza, M. Hengstschläger, H. Dolznig, In vitro cell migration and invasion assays, Mutat Res Rev Mutat Res 752 (2013) 10–24. https://doi.org/10.1016/j.mrrev.2012.08.001.

[105] J. Pijuan, C. Barceló, D.F. Moreno, O. Maiques, P. Sisó, R.M. Marti, A. Macià, A. Panosa, In vitro cell migration, invasion, and adhesion assays: From cell imaging to data analysis, Front Cell Dev Biol 7 (2019). https://doi.org/10.3389/fcell.2019.00107.

[106] J. Wu, L. Cao, Y. Liu, A. Zheng, D. Jiao, D. Zeng, X. Wang, D.L. Kaplan, X. Jiang, Functionalization of Silk Fibroin Electrospun Scaffolds via BMSC Affinity Peptide Grafting through Oxidative Self-Polymerization of Dopamine for Bone Regeneration, ACS Appl Mater Interfaces 11 (2019) 8878–8895. https://doi.org/10.1021/acsami.8b22123.

[107] K. Venkateswarlu, G. Suman, V. Dhyani, S. Swain, L. Giri, S. Samavedi, Three-dimensional imaging and quantification of real-time cytosolic calcium oscillations in microglial cells cultured on electrospun matrices using laser scanning confocal microscopy, Biotechnol Bioeng 117 (2020) 3108–3123. https://doi.org/10.1002/bit.27465.

[108] K. Berniak, D.P. Ura, A. Piórkowski, U. Stachewicz, Cell–Material Interplay in Focal Adhesion Points, ACS Appl Mater Interfaces (2024). https://doi.org/10.1021/acsami.3c19035.

[109] K. Berniak, A. Moradi, A. Lichawska-Cieslar, W. Szukala, J. Jura, U. Stachewicz, Controlled therapeutic cholesterol delivery to cells for the proliferation and differentiation of keratinocytes, J Mater Chem B 12 (2024) 11110–11122. https://doi.org/10.1039/d4tb01015a.

[110] M. Li, M.J. Mondrinos, M.R. Gandhi, F.K. Ko, A.S. Weiss, P.I. Lelkes, Electrospun protein fibers as matrices for tissue engineering, Biomaterials 26 (2005) 5999–6008. https://doi.org/10.1016/j.biomaterials.2005.03.030.

[111] G.C. Rutledge, S. V. Fridrikh, Formation of fibers by electrospinning, Adv Drug Deliv Rev 59 (2007) 1384–1391. https://doi.org/10.1016/j.addr.2007.04.020.

[112] U. Stachewicz, J.F. Dijksman, D. Burdinski, C.U. Yurteri, J.C.M. Marijnissen, Relaxation times in single event electrospraying controlled by nozzle front surface modification, Langmuir 25 (2009) 2540–2549. https://doi.org/10.1021/la8021408.

[113] D.P. Ura, U. Stachewicz, The Significance of Electrical Polarity in Electrospinning: A Nanoscale Approach for the Enhancement of the Polymer Fibers' Properties, Macromol Mater Eng 307 (2022). https://doi.org/10.1002/mame.202100843.

[114] M. Polak, D.P. Ura, K. Berniak, P.K. Szewczyk, M.M. Marzec, U. Stachewicz, Interfacial blending in co-axially electrospun polymer core-shell fibers and their interaction with cells via focal adhesion point analysis, Colloids Surf B Biointerfaces 237 (2024) 113864. https://doi.org/10.1016/j.colsurfb.2024.113864.

[115] J.E. Karbowniczek, K. Berniak, J. Knapczyk-Korczak, G. Williams, J.A. Bryant, N.D. Nikoi, M. Banzhaf, F. de Cogan, U. Stachewicz, Strategies of nanoparticles integration in polymer fibers to achieve antibacterial effect and enhance cell proliferation with collagen production in tissue engineering scaffolds, J Colloid Interface Sci 650 (2023) 1371–1381. https://doi.org/10.1016/j.jcis.2023.07.066.

[116] J. Knapczyk-Korczak, J. Zhu, D.P. Ura, P.K. Szewczyk, A. Gruszczyński, L. Benker, S. Agarwal, U. Stachewicz, Enhanced Water Harvesting System and Mechanical Performance from Janus Fibers with Polystyrene and Cellulose Acetate, ACS Sustain Chem Eng 9 (2021) 180–188. https://doi.org/10.1021/acssuschemeng.0c06480.

[117] T. Kowalczyk, Functional micro- and nanofibers obtained by nonwoven post-modification, Polymers (Basel) 12 (2020). https://doi.org/10.3390/POLYM12051087.

[118] M.M. Hohman, M. Shin, G. Rutledge, M.P. Brenner, Electrospinning and electrically forced jets. I. Stability theory, Physics of Fluids 13 (2001) 2201–2220. https://doi.org/10.1063/1.1383791.

[119] A. Greiner, J.H. Wendorff, Electrospinning: A fascinating method for the preparation of ultrathin fibers, Angewandte Chemie - International Edition 46 (2007) 5670–5703. https://doi.org/10.1002/anie.200604646.

[120] P. Martin, E. Zussman, Charge transport in electrospinning of polyelectrolyte solutions, Soft Matter 20 (2024) 5572–5582. https://doi.org/10.1039/d4sm00605d.

[121] C.A. Bonino, K. Efimenko, S.I. Jeong, M.D. Krebs, E. Alsberg, S.A. Khan, Three-dimensional electrospun alginate nanofiber mats via tailored charge repulsions, Small 8 (2012) 1928–1936. https://doi.org/10.1002/smll.201101791.

[122] B. Niemczyk-Soczynska, A. Gradys, P. Sajkiewicz, Hydrophilic surface functionalization of electrospun nanofibrous scaffolds in tissue engineering, Polymers (Basel) 12 (2020) 1–20. https://doi.org/10.3390/polym12112636.

[123] T. Busolo, D.P. Ura, S.K. Kim, M.M. Marzec, A. Bernasik, U. Stachewicz, S. Kar-Narayan, Surface potential tailoring of PMMA fibers by electrospinning for enhanced triboelectric performance, Nano Energy 57 (2019) 500–506. https://doi.org/10.1016/j.nanoen.2018.12.037.

[124] N. Lavielle, A. Hébraud, G. Schlatter, L. Thöny-Meyer, R.M. Rossi, A.M. Popa, Simultaneous electrospinning and electrospraying: A straightforward approach for fabricating hierarchically structured composite membranes, ACS Appl Mater Interfaces 5 (2013) 10090–10097. https://doi.org/10.1021/am402676m.

[125] A.L. Yarin, Coaxial electrospinning and emulsion electrospinning of core-shell fibers, Polym Adv Technol 22 (2011) 310–317. https://doi.org/10.1002/pat.1781.

[126] G.R.R.-A.B.T.L.C.J. Williams, Nanofibres in Drug Delivery, UCL Press, 2018. https://doi.org/10.14324/111.9781787350182.

[127] X. Liu, Y. Yang, D.G. Yu, M.J. Zhu, M. Zhao, G.R. Williams, Tunable zero-order drug delivery systems created by modified triaxial electrospinning, Chemical Engineering Journal 356 (2019) 886–894. https://doi.org/10.1016/j.cej.2018.09.096.

[128] S.K. Tiwari, R. Tzezana, E. Zussman, S.S. Venkatraman, Optimizing partition-controlled drug release from electrospun core-shell fibers, Int J Pharm 392 (2010) 209–217. https://doi.org/10.1016/j.ijpharm.2010.03.021.

[129] W. Han, L. Wang, Q. Li, B. Ma, C. He, X. Guo, J. Nie, G. Ma, A Review: Current Status and Emerging Developments on Natural Polymer-Based Electrospun Fibers, Macromol Rapid Commun 43 (2022). https://doi.org/10.1002/marc.202200456.

[130] J.E. Karbowniczek, D.P. Ura, U. Stachewicz, Nanoparticles distribution and agglomeration analysis in electrospun fiber based composites for desired mechanical performance of poly(3-hydroxybuty-rate-co-3-hydroxyvalerate (PHBV) scaffolds with hydroxyapatite (HA) and titanium dioxide (TiO2) towards medical applications, Compos B Eng 241 (2022) 110011. https://doi.org/10.1016/j.compositesb.2022.110011.

[131] J.E. Karbowniczek, Ł. Kaniuk, K. Berniak, A. Gruszczyński, U. Stachewicz, Enhanced Cells Anchoring to Electrospun Hybrid Scaffolds With PHBV and HA Particles for Bone Tissue Regeneration, Front Bioeng Biotechnol 9 (2021). https://doi.org/10.3389/fbioe.2021.632029.

[132] C. Yang, D.G. Yu, D. Pan, X.K. Liu, X. Wang, S.W.A. Bligh, G.R. Williams, Electrospun pH-sensitive core-shell polymer nanocomposites fabricated using a tri-axial process, Acta Biomater 35 (2016) 77–86. https://doi.org/10.1016/j.actbio.2016.02.029.

[133] E. Zoneff, Y. Wang, C. Jackson, O. Smith, S. Duchi, C. Onofrillo, B. Farrugia, S.E. Moulton, R. Williams, C. Parish, D.R. Nisbet, L.M. Caballero-Aguilar, Controlled oxygen delivery to power tissue regeneration, Nat Commun 15 (2024). https://doi.org/10.1038/s41467-024-48719-x.

[134] A.A. Kohestani, Z. Xu, F.E. Baştan, A.R. Boccaccini, F. Pishbin, Electrically conductive coatings in tissue engineering, Acta Biomater 186 (2024) 30–62. https://doi.org/10.1016/j.actbio.2024.08.007.

[135] Z. Zhang, L.H. Klausen, M. Chen, M. Dong, Electroactive Scaffolds for Neurogenesis and Myogenesis: Graphene-Based Nanomaterials, Small 14 (2018). https://doi.org/10.1002/smll.201801983.

[136] B. Gürbüz, F. Ciftci, Bio-electric-electronics and tissue engineering applications of MXenes wearable materials: A review, Chemical Engineering Journal 489 (2024). https://doi.org/10.1016/j.cej.2024.151230.

[137] K. Krukiewicz, D. Putzer, N. Stuendl, B. Lohberger, F. Awaja, Enhanced osteogenic differentiation of human primary mesenchymal stem and progenitor cultures on graphene oxide/poly(methyl methacrylate) composite scaffolds, Materials 13 (2020) 1–12. https://doi.org/10.3390/ma13132991.

[138] M. Kopacz, P.K. Szewczyk, E. Długoń, K. Berniak, J. Nizioł, P. Jeleń, M. Sitarz, U. Stachewicz, Multifunctional, Flexible and Interactive PVDF Fibers with Tunable Conductivity via CNT Coatings for Sensing and Smart Textile Applications, Adv Funct Mater (2025). https://doi.org/10.1002/adfm.202515157.

[139] C. Ribeiro, V. Sencadas, D.M. Correia, S. Lanceros-Méndez, Piezoelectric polymers as biomaterials for tissue engineering applications, Colloids Surf B Biointerfaces 136 (2015) 46–55. https://doi.org/10.1016/j.colsurfb.2015.08.043.

[140] D. Khare, B. Basu, A.K. Dubey, Electrical stimulation and piezoelectric biomaterials for bone tissue engineering applications, Biomaterials 258 (2020). https://doi.org/10.1016/j.biomaterials.2020.120280.

[141] N.A. Kamel, Bio-piezoelectricity: fundamentals and applications in tissue engineering and regenerative medicine, Biophys Rev 14 (2022) 717–733. https://doi.org/10.1007/s12551-022-00969-z.

[142] A.H. Rajabi, M. Jaffe, T.L. Arinzeh, Piezoelectric materials for tissue regeneration: A review, Acta Biomater 24 (2015) 12–23. https://doi.org/10.1016/j.actbio.2015.07.010.

[143] M. Levin, Bioelectric mechanisms in regeneration: Unique aspects and future perspectives, Semin Cell Dev Biol 20 (2009) 543–556. https://doi.org/10.1016/j.semcdb.2009.04.013.

[144] P.K. Szewczyk, K. Berniak, J. Knapczyk-Korczak, J.E. Karbowniczek, M.M. Marzec, A. Bernasik, U. Stachewicz, Mimicking natural electrical environment with cellulose acetate scaffolds enhances collagen formation of osteoblasts, Nanoscale 15 (2023) 6890–6900. https://doi.org/10.1039/d3nr00014a.

[145] Y. Tai, S. Yang, S. Yu, A. Banerjee, N. V. Myung, J. Nam, Modulation of piezoelectric properties in electrospun PLLA nanofibers for application-specific self-powered stem cell culture platforms, Nano Energy 89 (2021). https://doi.org/10.1016/j.nanoen.2021.106444.

[146] U. Stachewicz, C.A. Stone, C.R. Willis, A.H. Barber, Charge assisted tailoring of chemical functionality at electrospun nanofiber surfaces, J Mater Chem 22 (2012) 22935–22941. https://doi.org/10.1039/c2jm33807f.

[147] D.P. Ura, U. Stachewicz, The Significance of Electrical Polarity in Electrospinning: A Nanoscale Approach for the Enhancement of the Polymer Fibers' Properties, Macromol Mater Eng 307 (2022). https://doi.org/10.1002/mame.202100843.

[148] D.P. Ura, J. Knapczyk-Korczak, P.K. Szewczyk, E.A. Sroczyk, T. Busolo, M.M. Marzec, A. Bernasik, S. Kar-Narayan, U. Stachewicz, Surface Potential Driven Water Harvesting from Fog, ACS Nano 15 (2021) 8848–8859. https://doi.org/10.1021/acsnano.1c01437.

[149] D.P. Ura, J. Rosell-Llompart, A. Zaszczyńska, G. Vasilyev, A. Gradys, P.K. Szewczyk, J. Knapczyk-Korczak, R. Avrahami, A.O. Šišková, A. Arinstein, P. Sajkiewicz, E. Zussman, U. Stachewicz, The role of electrical polarity in electrospinning and on the mechanical and structural properties of as-spun fibers, Materials 13 (2020). https://doi.org/10.3390/ma13184169.

[150] R. Longo, L. Vertuccio, F. Aliberti, A. Mariconda, M. Raimondo, P. Longo, L. Guadagno, Coaxial Electrospinning of PCL-PVA Membranes Loaded with N-Heterocyclic Gold Complex for Antitumoral Applications, Fibers 12 (2024). https://doi.org/10.3390/fib12120101.

[151] Š. Zupančič, Core-shell nanofibers as drug delivery systems, Acta Pharmaceutica 69 (2019) 131–153. https://doi.org/10.2478/acph-2019-0014.

[152] U. Nisha, C. Merline, L. Ragupathy, D. Painuly, Tunable Release of Combined Contraceptive Steroids from Core-shell Gelatin/PCL Fibers, Fibers and Polymers 21 (2020) 1906–1916. https://doi.org/10.1007/s12221-020-9932-6.

[153] E. Kaniuk, A. Lechowska-Liszka, M. Gajek, A. Nikodem, A. Ścisłowska-Czarnecka, A. Rapacz-Kmita, E. Stodolak-Zych, Correlation between porosity and physicochemical and biological properties of electrospinning PLA/PVA membranes for skin regeneration, Biomaterials Advances 152 (2023). https://doi.org/10.1016/j.bioadv.2023.213506.

[154] G. L. Bowlin, Enhanced Porosity without Compromising Structural Integrity: The Nemesis of Electrospun Scaffolding, J Tissue Sci Eng 02 (2011). https://doi.org/10.4172/2157-7552.1000103e.

[155] K. Rasool, M. Helal, A. Ali, C.E. Ren, Y. Gogotsi, K.A. Mahmoud, Antibacterial Activity of Ti3C2Tx MXene, ACS Nano 10 (2016) 3674–3684. https://doi.org/10.1021/acsnano.6b00181.

[156] K. Diedkova, A.D. Pogrebnjak, S. Kyrylenko, K. Smyrnova, V. V. Buranich, P. Horodek, P. Zukowski, T.N. Koltunowicz, P. Galaszkiewicz, K. Makashina, V. Bondariev, M. Sahul, M. Caplovicova, Y. Husak, W. Simka, V. Korniienko, A. Stolarczyk, A. Blacha-Grzechnik, V. Balitskyi, V. Zahorodna, I. Baginskiy, U. Riekstina, O. Gogotsi, Y. Gogotsi, M. Pogorielov, Polycaprolactone-Mxene nanofibrous scaffolds for tissue engineering, ACS Appl Mater Interfaces 15 (2023) 14033–14047. https://doi.org/10.1021/acsami.2c22780.

[157] J.J. Grant, S.C. Pillai, S. Hehir, M. McAfee, A. Breen, Biomedical Applications of Electrospun Graphene Oxide, ACS Biomater Sci Eng 7 (2021) 1278–1301. https://doi.org/10.1021/acsbiomaterials.0c01663.

[158] A. Zarepour, Ç. Karasu, Y. Mir, M.H. Nematollahi, S. Iravani, A. Zarrabi, Graphene- and MXene-based materials for neuroscience: diagnostic and therapeutic applications, Biomater Sci 11 (2023) 6687–6710. https://doi.org/10.1039/d3bm01114c.

[159] E. Mostafavi, S. Iravani, MXene-Graphene Composites: A Perspective on Biomedical Potentials, Nanomicro Lett 14 (2022). https://doi.org/10.1007/s40820-022-00880-y.

[160] P. Iravani, S. Iravani, R.S. Varma, MXene-Chitosan Composites and Their Biomedical Potentials, Micromachines (Basel) 13 (2022). https://doi.org/10.3390/mi13091383.

[161] X.Q. Wei, L.Y. Hao, X.R. Shao, Q. Zhang, X.Q. Jia, Z.R. Zhang, Y.F. Lin, Q. Peng, Insight into the Interaction of Graphene Oxide with Serum Proteins and the Impact of the Degree of Reduction and Concentration, ACS Appl Mater Interfaces 7 (2015) 13367–13374. https://doi.org/10.1021/acsami.5b01874.

[162] K. Maleski, V.N. Mochalin, Y. Gogotsi, Dispersions of Two-Dimensional Titanium Carbide MXene in Organic Solvents, Chemistry of Materials 29 (2017) 1632–1640. https://doi.org/10.1021/acs.chemmater.6b04830.

[163] M. Naguib, M. Kurtoglu, V. Presser, J. Lu, J. Niu, M. Heon, L. Hultman, Y. Gogotsi, M.W. Barsoum, Two-dimensional nanocrystals produced by exfoliation of Ti 3AlC 2, Advanced Materials 23 (2011) 4248–4253. https://doi.org/10.1002/adma.201102306.

[164] G. Li, S. Lian, J. Wang, G. Xie, N. Zhang, X. Xie, Surface chemistry engineering and the applications of MXenes, Journal of Materiomics 9 (2023) 1160–1184. https://doi.org/10.1016/j.jmat.2023.08.003.

Appendix: Articles Included in the Publication Cycle of the Dissertation

Wiley Interdisciplinary Reviews: Nanomedicine and Nanobiotechnology

WILEY

WIREs NANOMEDICINE AND NANOBIOTECHNOLOGY

ADVANCED REVIEW

Strategies in Electrospun Polymer and Hybrid Scaffolds for Enhanced Cell Integration and Vascularization for Bone Tissue Engineering and Organoids

Martyna Polak | Joanna Ewa Karbowniczek | Urszula Stachewicz

Faculty of Metals Engineering and Industrial Computer Science, AGH University of Krakow, Kraków, Poland

Correspondence: Urszula Stachewicz (ustachew@agh.edu.pl)

Received: 13 July 2024 | **Revised:** 5 November 2024 | **Accepted:** 25 November 2024

Associate Editor: Gareth Williams | **Co-Editor-in-Chief:** Qiaobing Xu

Funding: The literature review was part of the OPUS 17 project funded by the National Science Center in Poland, project no. 2019/33/B/ST5/01311 and supported by the program "Excellence Initiative—Research University" for the AGH University of Krakow in Poland.

Keywords: angiogenesis | bone tissue engineering | electrospun fibers | polymer scaffolds | vascularization

ABSTRACT

Addressing the demand for bone substitutes, tissue engineering responds to the high prevalence of orthopedic surgeries worldwide and the limitations of conventional tissue reconstruction techniques. Materials, cells, and growth factors constitute the core elements in bone tissue engineering, influencing cellular behavior crucial for regenerative treatments. Scaffold design, including architectural features and porosity, significantly impacts cellular penetration, proliferation, differentiation, and vascularization. This review discusses the hierarchical structure of bone and the process of neovascularization in the context of biofabrication of scaffolds. We focus on the role of electrospinning and its modifications in scaffold fabrication to improve scaffold properties to enhance further tissue regeneration, for example, by boosting oxygen and nutrient delivery. We highlight how scaffold design impacts osteogenesis and the overall success of regenerative treatments by mimicking the extracellular matrix (ECM). Additionally, we explore the emerging field of bone organoids—self-assembled, three-dimensional (3D) structures derived from stem cells that replicate native bone tissue's architecture and functionality. While bone organoids hold immense potential for modeling bone diseases and facilitating regenerative treatments, their main limitation remains insufficient vascularization. Hence, we evaluate innovative strategies for pre-vascularization and discuss the latest techniques for assessing and improving vascularization in both scaffolds and organoids presenting the most commonly used cell lines and biological models. Moreover, we analyze cutting-edge techniques for assessing vascularization, evaluating their advantages and drawbacks to propose complex solutions. Finally, by integrating these approaches, we aim to advance the development of bioactive materials that promote successful bone regeneration.

Abbreviations: ALP, alkaline phosphatase; ATP, adenosine triphosphate; BMP-2, bone morphogenetic protein-2; BMP-7, bone morphogenetic protein-7; BMSCs, bone marrow stromal cells; CAM, chorioallantoic membrane; CD31, cluster of differentiation 31; CLSM, confocal laser scanning microscopy; CyQUANT, CyQUANT cell proliferation assay kit; DAPI, 4′,6-diamidino-2-phenylindole; DMEM, Dulbecco's modified eagle medium; ECM, extracellular matrix; ECs, endothelial cells; EHS, Engelbreth-Holm–Swarm; ELISA, enzyme-linked immunosorbent assay; EPCs, endothelial progenitor cells; FBS, fetal bovine serum; GFP, green fluorescent protein; HIF-1α, hypoxia-inducible factor-1α; hMSCs, human mesenchymal stem cells; HUVECs, human umbilical vein endothelial cells; LDH, lactate dehydrogenase; LIVE/DEAD, LIVE/DEAD viability/cytotoxicity kit; MicroCT, microcomputed tomography; MRI, magnetic resonance imaging; MSCs, mesenchymal stem cells; MTS, 3-(4,5-dimethylthiazol-2-yl)-5-(3-carboxymethoxyphenyl)-2-(4-sulfophenyl)-2*H*-tetrazolium; MTT, 3-(4,5-dimethylthiazole-2-yl)-2,5-diphenyltetrazolium bromide; PBS, phosphate-buffered saline; PCL, polycaprolactone; PCR, polymerase chain reaction; PDMS, polydimethylsiloxane; PEEK, polyether ether ketone; PEG, polyethylene glycol; PEGDA, poly(ethylene glycol) diacrylate; PLA, polylactic acid; PLCL, poly(L-lactide-co-ε-caprolactone); PLGA, poly(lactic-co-glycolic acid); PLLA, poly(L-lactic acid); PTFE, polytetrafluoroethylene; RT-PCR, real-time quantitative PCR; Runx2, runt-related transcription factor 2; SEM, scanning electron microscopy; SPIONs, superparamagnetic iron oxide nanoparticles; TGF-β, transforming growth factor-β; TNF-α, tumor necrosis factor-α; VEGF, vascular endothelial growth factor; VEGF-A, vascular endothelial growth factor A; VSMCs, vascular smooth muscle cells; WST-1, 2-(4-iodophenyl)-3-(4-nitrophenyl)-5-(2,4-disulfophenyl)-2*H*-tetrazolium.

1 | Introduction

Diseased or damaged bone tissue creates a significant demand for bone substitutes for transplantation, making it the second most transplanted tissue each year. Hard tissue engineering is employed for patients who do not respond to conventional techniques like free flaps for tissue reconstruction. These defects could arise from tumor removal, trauma, or congenital conditions (Seppänen-Kaijansinkko 2019). In 2017, approximately 22.3 million orthopedic surgery procedures were conducted worldwide (Collins et al. 2021). Bone fracture healing is challenging in large-size defects due to slow and insufficient tissue repair, often leading to nonunion, graft rejection, high-cost implantation, and chronic pain. Advances in tissue engineering offer promising solutions, with biomaterials accelerating regeneration, activating osteoblastic cells, and enhancing bone remodeling. These biocompatible, bioresorbable, and biodegradable materials promote osteoconductive and osteoinductive properties. Bone tissue engineering aims to achieve rapid and optimal functional bone regeneration using a combination of biomaterials, growth factors, cells, and other agents or stimuli (Kontogianni et al. 2023). Moreover, several studies indicate that organoids are crucial for various tissue repair and biofunction reconstruction, offering high clinical relevance compared to traditional stem cell therapies (Aykora and Uzun 2024). However, conventional methods have limited their clinical use. Bone organoids, created through the three-dimensional (3D) self-assembly of bone-associated stem cells, mimic native bone tissue's properties and have gained significant experimental support (D. Zhao et al. 2024).

In the realm of bone tissue engineering, scaffolds, cells, and growth factors stand as the fundamental building blocks. Scaffolds not only mimic the extracellular matrix (ECM) but also function as carriers for cells and growth factors. They significantly impact the behavior of seeded cells, influencing attachment, migration, and proliferation, thereby determining the effectiveness of regenerative treatments. Scaffolds, made from natural or synthetic materials or their combinations, offer a myriad of advantages. They can incorporate bone progenitor cells and growth factors, showcasing osteoconductive and osteoinductive properties, ultimately aiding in the replacement and repair of bone defects (Abdelaziz et al. 2023; K. Zhang et al. 2018). Nonetheless, the capacity for cells to penetrate, proliferate, differentiate, and migrate is influenced by the size and geometry of the scaffold's pores and the extent of vascularization (Abbasi et al. 2020; Efraim et al. 2019). Architectural scaffold design, porosity, and pore size must possess an interconnected structure and high porosity to facilitate cellular penetration and ensure proper diffusion of nutrients to the cells or waste removal within the construct (Loh and Choong 2013; Preethi Soundarya et al. 2018).

Manufacturing highly porous supportive scaffolds for bone tissue regeneration requires consideration of desired architecture, mechanical stability, and bioactivity (Chen, Dong, et al. 2022; Metwally and Stachewicz 2019). Various methods are explored, including 3D printing, bioprinting, electrospinning, freeze-drying, sol–gel, polymer replica, and so forth. Electrospinning is an especially versatile method among the mentioned ones as it enables the process of natural and synthetic polymers as well as their blends and organic–inorganic hybrids (Y. Chen, Fu, et al. 2022). Additionally, it is an excellent platform for growth factors and incorporation of other biologically active molecules for targeted release and osteoinduction. The fast development of multi-nozzle systems and careful control of process parameters, it enables crating desired architecture and tailoring properties of the entire scaffold as well as designing individual fibers' surface charge, roughness, porosity, and availability of bioactive compounds (Metwally et al. 2019; Metwally and Stachewicz 2019; Polak et al. 2023; Stachewicz et al. 2019).

Here, similar design requirements are assigned to classical tissue-engineered scaffolds and modern bone organoids. Bone organoids are 3D tissue constructs cultivated and designed to replicate the structural and functional characteristics of native bone tissue. Typically derived from stem cells, organoids undergo culture under conditions conducive to their differentiation into bone-specific cell types, notably osteoblasts and osteocytes (S. Chen et al. 2020). By establishing an environment that mimics the microenvironment present during natural bone development, it is possible to generate organoids that faithfully mimic fundamental features of bone tissue, encompassing cellular composition, architectural arrangement, and physiological attributes (D. Zhao et al. 2024). Bone organoids offer significant potential for investigating bone development processes, modeling diseases affecting bone, conducting drug screening studies, and potentially serving as platforms for regenerative medicine interventions to repair or replace bone structures (J. Huang, Zhang, et al. 2023).

Bone organoids serve as valuable models for replicating the intricate processes of osteogenesis, resorption, mineralization, and remodeling observed in real bone tissue. To effectively mimic these mechanisms, it is crucial to construct bone organoids in strict accordance with bone morphology. However, it is essential to note that only mineralized bone possesses unique biomechanical properties necessary for support, load-bearing, and strain functions. Mineralization, the inorganic deposition of elements such as calcium and phosphorus, was previously viewed as a passive process (Akiva et al. 2021). Yet, recent research has revealed it to be a programmed process regulated by multiple factors. In vitro bone mineralization within organoids is closely linked to forming the ECM, a complex network of macromolecules surrounding cells (Y. Park et al. 2021). The ECM not only acts as a scaffold for cellular embedding but also regulates various cellular activities crucial for bone development and disease progression. Collagen, a major component of the ECM, provides the bone matrix with tensile strength and is secreted by cells like osteoblasts, chondrocytes, and fibroblasts. The interplay between cells and the ECM profoundly influences bone organoid development and functionality, with ECM-derived matrix derivatives playing a significant role in bone organoid regeneration and maturation in different contexts (C. Li, Zhang, et al. 2023). Notwithstanding, organoids can be built by cell self-organization; it is worth mentioning that bioactive materials supporting organoid biofabrication hold great promise for better stimulation of cell differentiation and imitation of ECM (S. Chen, Chen, et al. 2022; C. Li, Zhang, et al. 2023; D. Zhao et al. 2024). Although many studies report the utilization of hydrogels and decellularized natural ECM as scaffold-based organoids, polymer fibrous scaffolds attract attention due to

their unique properties of possible cell stimulation and ECM imitation (Joddar et al. 2022; D. Kim et al. 2023; Ritzau-Reid et al. 2023). The main challenge assigned to polymer scaffolds used for classical bone tissue engineering is insufficient vascularization of the construct, which also applies to the development of fully functional organoids (S. Chen, Chen, et al. 2022). Therefore, this review discusses the limitations of current scaffolding techniques with the following strategies for modifying scaffold fabrication, leading to improved vascularization. We focus on the problematics of insufficient scaffold porosity and oxygen delivery. Moreover, we point out possible solutions like pre-vascularization with different types of cells that increase the chances of creating a fully functioning tissue. Finally, the most advanced techniques of vascularization analysis, along with their advantages and drawbacks, are communicated.

2 | Bone Tissue Regeneration and Neovascularization

Bones are part of the skeletal system, serving as mechanical and structural support in the human body and protecting vital organs. Within bone tissue, we distinguish compact bone constituting bone exteriors, ensuring their strength and crack resistance, and spongy bone—a highly porous internal structure, decreasing the overall weight (Fratzl and Weinkamer 2007). In the process of growth, remodeling, and maintenance of healthy bone tissue, it is crucial to precisely regulate the activities of osteoclasts, which resorb the existing matrix, and osteoblasts, which secrete compounds of the ECM (Al-Bari and Al Mamun 2020). Hence, the vascular system in bones is of utmost importance, ensuring proper nutrition and oxygenation and facilitating cellular signaling, high regenerative capacity, and the performance of other vital functions, such as mineral homeostasis, hematopoiesis, and an endocrine role (H. Zhang, Liesveld, et al. 2023; R. Zhou et al. 2021). The bone scheme in Figure 1 presents an advanced network of arteries that enable the tissue to maintain optimal biological conditions by supplying all the necessary substances to the cells that build the bone structure and the building blocks of the tissue (Watanabe et al. 2023). The fundamental structural units of cortical bone tissue consist of osteons, characterized as elliptical cylinders measuring between 100 and 300 μm in diameter and spanning a length of 3–5 mm (Skedros et al. 2011). Osteons consist of 5–30 concentric lamellae with varying orientations of collagen fibrils. These lamellae encircle Haversian canals, which facilitate sufficient blood supply and innervation to the bone tissue (Lefèvre et al. 2019; Zawadzki et al. 2023). The chemical composition of the mineralized ECM primarily comprises carbonate-substituted hydroxyapatite, Type I collagen fibrils, water, and noncollagenous organic constituents (primarily proteins and small proteoglycans) (Gupta et al. 2006). The 3D arrangement of these components at each length scale confers upon bone its exceptional mechanical characteristics (Buss et al. 2022).

In the event of bone injury, tissue has its own healing mechanisms that strive to restore the proper structure. The situation becomes more complicated if we are dealing with critical size defects, for example, after tumor resection of complex fractures with bone loss (Schemitsch 2017). The medical gold standard in such cases is autologous grafts since they perfectly match biological and mechanical properties (Schmidt 2021). However, the limited available volume of bone for grafting and the risk of donor site morbidity or other complications evoke the necessity of exploring biomaterials-based solutions. In recent years, much effort has been dedicated to research materials that can effectively augment missing tissue and support bone regeneration, including neovascularization of implanted scaffolds (Simunovic and Finkenzeller 2021). Initially, the vascularized scaffold must provide the proper structure—interconnected porosity for the circulatory system to be developed within. Following scaffold implantation, neovascularization induced by inflammation occurs spontaneously as a part of the wound-healing mechanism. However, the new blood vessel infiltration rate into the scaffold is very slow (insufficient). Lack of a functional vascular system results in a limited supply of nutrients and oxygen, slowing down the regeneration process and accumulation of scaffold degradation products and metabolites, leading to a prolonged inflammatory response (Goonoo 2018), which can eventually cause necrosis of cells spread in the scaffold structure, preventing intended tissue development.

The circulatory system is formed during embryonic development in the process of vasculogenesis. This process is not limited to the embryonic period and can occur in adults through the recruitment and participation of bone marrow–derived

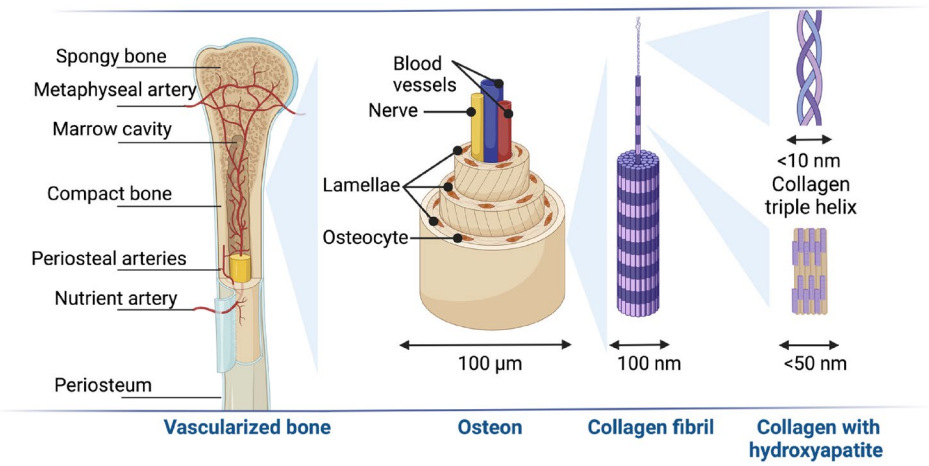

FIGURE 1 | Scheme of the hierarchical structure of bone tissue presenting vascularized bone, osteon, collagen fibril, and collagen triple helix.

endothelial progenitor cells (EPCs). In most post-injury regenerations, the new blood vessel formation is mostly by angiogenesis—the formation of new branches from existing ones with the leading role of endothelial cells (ECs) (Afzal et al. 2007; Bae et al. 2012; Mastrullo et al. 2020). Neovascularization as a process with the leading role in angiogenesis and vasculogenesis, in which ECs proliferate and migrate, is mediated by many angiogenic inducers like growth factors, chemokines, angiogenic enzymes, endothelial-specific receptors, and adhesion molecules. Moreover, angiogenesis is an intricate process characterized by extensive interactions among cells, soluble substances, and ECM components (Liekens, De Clercq, and Neyts 2001; Saberianpour et al. 2018). Thereby, perivascular macrophages play an important role in vessel formation and angiogenesis. They contribute to this process by secreting various growth factors and cytokines that promote the proliferation and migration of ECs, which are the building blocks of blood vessels. Additionally, perivascular macrophages regulate the recruitment and function of other immune cells involved in angiogenesis. Their presence and activity are essential for developing and remodeling blood vessels during angiogenesis (Fantin et al. 2010). Another function of perivascular macrophages is to uphold tight junctions among ECs, controlling vessel permeability. Additionally, they engage in the phagocytosis of potential pathogens before they can enter tissues from the bloodstream, thereby curbing undue inflammation (Lapenna, De Palma, and Lewis 2018). The new vessel growth process is schematically shown in Figure 2.

Vascularization coupled with osteogenesis is essential to foster a supportive environment for bone cells and enhances scaffold integration (Safari et al. 2024; Yan et al. 2022; T. Zhao et al. 2022). It is also crucial in bone development and osseointegration, enabling the delivery of growth factors that sustain cell survival and promote cellular interactions (Correia et al. 2011; Diomede et al. 2020). Moreover, vascular endothelial growth factor (VEGF), a key driver of angiogenesis, promotes EC migration and proliferation while indirectly enhancing osteogenesis by modulating osteogenic growth factor release and activating paracrine signaling pathways (Diomede et al. 2020). Many studies report the potential of electrospun fibers to induce osteogenic differentiation (Hashemi et al. 2020) as composite fibers incorporating inorganic fillers can strongly improve osteointegration and target specific osteogenic cell signaling (Pesaran Afsharian et al. 2023). For instance, electrospun polycaprolactone (PCL) fibers containing nano-hydroxyapatite and nano-zinc oxide showed improved angiogenic and osteogenic gene expression (Rahmani et al. 2019). Other investigated strategies include also the encapsulation of growth factors, like VEGF, and surface modifications of fibers (Martine et al. 2017; C. Wang, Lu, and Wang 2020; L. Wu et al. 2020).

3 | Fabrication of 3D Scaffolds for Bone Tissue Engineering

3.1 | Scaffolding Techniques and Pore Size Controllability

Techniques used in scaffold fabrication play a crucial role in determining implanted biomaterials' ultimate structural, mechanical properties, and biological responses. Generally, the fabrication of 3D porous scaffolds can be divided into two groups: conventional, such as solvent casting and particulate leaching, gas foaming, phase separation, freeze-drying, or sol–gel method and rapid prototyping (RP) techniques known as additive manufacturing, relying on layer-by-layer addition of material to create a 3D scaffold (Abdelaziz et al. 2023; Loh and Choong 2013). We can distinguish 3D printing, selective laser sintering, fused deposition modeling, stereolithography, and electrospinning in the RP group.

While conventional techniques do not allow complete control of scaffold architecture, pore shape, and size, RP techniques enable the design of the shape, dimensions, and mechanical properties of 3D biomimetic scaffold (Abdelaziz et al. 2023; Loh and Choong 2013; Preethi Soundarya et al. 2018). Among many advantages of RP techniques, like reproducibility and controllability of designed scaffolds, the main limitation is the narrow group

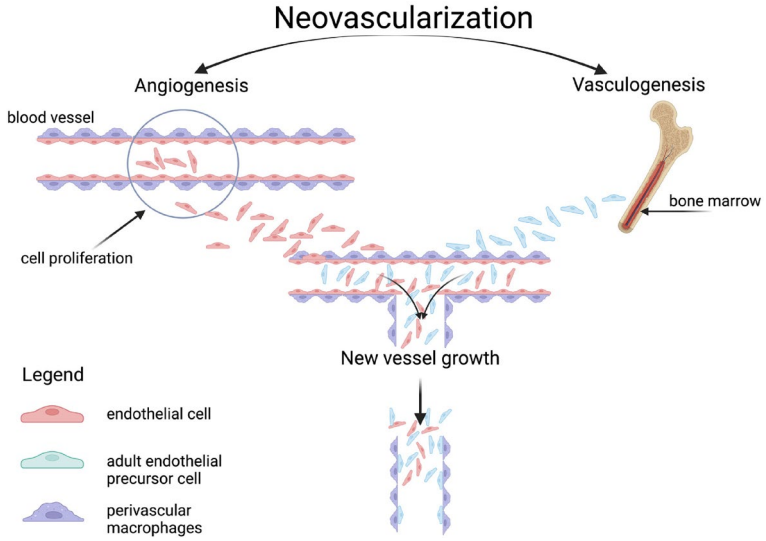

FIGURE 2 | Schematic representation of new blood vessel formation. Angiogenesis—endothelial cell proliferation and reperfusion to areas of ischemia with new vessel growth. Vasculogenesis—adult endothelial precursor cells enter the circulation in response to injury.

of biomaterials that can be used for processing. As shown in Figure 3, conventional production of scaffolds results with generally large pores, but the difficulty is the controllability of pore size and pore interconnection (Preethi Soundarya et al. 2018). Here, electrospinning enables the creation of scaffolds with a porosity between 100 nm and 10 μm, effectively improving cell adhesion. On the contrary, higher porosity of scaffolds, in the range of 100–550 μm, can be obtained by 3D printing. The combination of electrospinning and 3D printing offers strong adhesion through electrospun fibers while providing mechanical support and nutrient flow due to the scaffold's high porosity and free spaces.

In addition to the most promising scaffold fabrication techniques, the following step is the correct evaluation of pore size and scaffold architecture, which gives crucial insight into the functional properties. An ideal evaluation should be rapid, precise, and nondestructive, while offering a thorough analysis of both morphological and architectural properties. Commonly used assessment methods include theoretical modeling (Scaglione et al. 2014), scanning electron microscopy (SEM) (Stachewicz et al. 2015, 2019), mercury intrusion and flow porosimetry, gas pycnometry, gas adsorption analysis (Cortez Tornello et al. 2014; Haugen and Bertoldi 2017), and microcomputed tomography (Micro-CT) (Cengiz, Oliveira, and Reis 2018). Among the others, Micro-CT is one of the most widely used techniques enabling high-resolution visualization of pore size, distribution, and interconnectivity (Podgórski et al. 2024; Satapathy et al. 2024). Lastly, confocal laser scanning microscopy (CLSM) is an excellent tool to investigate scaffold geometry using material staining or autofluorescence properties (Choong, Yi, and Rutledge 2015), especially in the case of hydrogel materials that are difficult to analyze with different methods without affecting scaffold geometry (Bagherzadeh et al. 2013; Kang et al. 2024; E. Liu et al. 2007; Marquez et al. 2022). The following sections focus on electrospinning and 3D printing as the best candidates for scaffolds with improved tissue vascularization.

3.2 | Electrospinning

In this section, our attention is directed toward the electrospinning process and its modifications, which result in various changes, including an enhancement in the porosity of the produced scaffolds. Since the leading role of polymer scaffolds used in tissue engineering is to mimic the ECM, the properties of this natural structure are worth noting. The ECM consists of a complex network of interlinked macromolecules, including proteins and polysaccharides like collagen, elastin, fibronectin, or laminin, which create 3D structures between the cells. These macromolecules are secreted by cells, allowing them to build surrounding mesh. Moreover, the average diameter of fibrous ECM components was investigated, showing the lowest average fiber diameter for fibronectin (2 nm), larger for laminin (57 nm) and elastin (400 nm), and the largest diameter for collagen fibers (500 nm) (M. Li et al. 2005; Metwally and Stachewicz 2020; Neal et al. 2009; Shoulders and Raines 2009). Of the previously mentioned scaffold fabrication techniques, electrospinning is the only one that allows the production of fibers with diameters similar in size to those of natural fibers (Stachewicz et al. 2015).

3.2.1 | Process of Electrospinning

Electrospinning refers to a category of fiber-forming methods where electrostatic forces are utilized to control fiber production, which are typically continuous with the possibility of also obtaining short fibers with a controlled length (Ura and

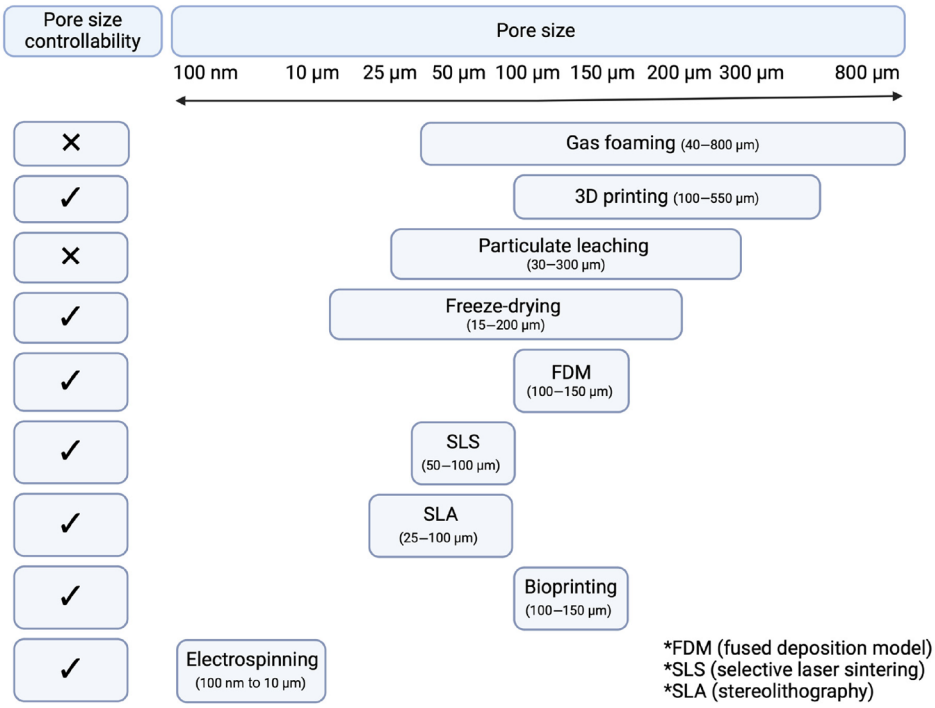

FIGURE 3 | The pore size in the scaffolds prepared by different manufacturing techniques (Büyük, Aksu, and Torun Köse 2023; Collins et al. 2021).

Stachewicz 2024). It is an electrohydrodynamic process in which a polymer solution exerts the nozzle under high voltage (Rosell-Llompart, Grifoll, and Loscertales 2018). The liquid droplet is surrounded by charges (positive or negative, depending on the voltage polarity of the voltage generator) (Rutledge and Fridrikh 2007; Ura and Stachewicz 2022). Surface tension is overcome by the repulsion of charges at the free surface of the liquid droplet that further deforms into a cone (Stachewicz et al. 2007). When charge density is critical, the cone is unstable, and the jet is created (Stachewicz et al. 2009, 2012). The polymer solution is accelerated and stretched by the electric Maxwell stresses (Z. Sun et al. 2003; Yarin 2011), and fibers are collected on the ground collector. The spinnability of the polymer solution depends on parameters such as polymer concentration, molecular weight, and chosen solvent. Basic parameter alternations of electrospinning include applied voltage, polymer solution flow rate, nozzle–collector distance, and ambient conditions like temperature and humidity (Szewczyk and Stachewicz 2020; Ura and Stachewicz 2022). Correctly selected parameters allow for a stable and reproducible fiber manufacturing process (Y. Li et al. 2021). Manipulating the above parameters makes it possible to obtain fibers with different properties. For example, ambient conditions like temperature and humidity strongly affect the morphology of fibers (Putti et al. 2015; Stachewicz et al. 2015; Ura et al. 2019). Managing environmental conditions during electrospinning significantly reduces result variability and greatly influences fiber properties, which is essential for the reproducibility of results. Using PCL as a model, it was shown how temperature, humidity, collector rotation, and solvent composition influence the architecture of the mat, advancing potential application (Putti et al. 2015). Another study on PCL fibers presents that increased humidity and the use of a solvent system designed to cause phase separation during electrospinning allowed the production of porous fibers for application as carriers of oils in atopic dermatitis treatments (Metwally et al. 2021).

3.2.2 | Bioactive Electrospun Scaffolds

Scaffolds are designed to support cellular processes from the initial adhesion to tissue development by creating an entire microenvironment evoking the sequence of biological reactions. The versatility of the electrospinning process allows us to control the scaffold's properties at multiple levels. Starting from chemical composition, whereby simple selection of the natural or synthetic polymers (Khajavi, Abbasipour, and Bahador 2016; Lai et al. 2014; Sharifi et al. 2018), their blends (Lai et al. 2014; Sharifi et al. 2018), or organic–inorganic composites (Augustine et al. 2019; Karbowniczek et al. 2021), it is possible to tailor the degradation rate, mechanical properties and guide cellular responses. Electrospinning of blend fibers, where additional chemicals are added for uniform incorporation in the composite mat at the stage of polymer solution preparation, serves in many biomedical applications (Kaniuk, Podborska, and Stachewicz 2022; Karbowniczek et al. 2021; Kontogianni et al. 2024; Krysiak and Stachewicz 2022; Szewczyk et al. 2023). In co-axial electrospinning, core–shell fibers are produced by utilizing a multichannel nozzle, allowing the use of different materials in the core and shell. Various functionalities can be integrated into the core and shell, such as combining mechanical strength from the core with bioactivity from the shell (Krysiak and Stachewicz 2023; Polak et al. 2024; Ura, Berniak, and Stachewicz 2021). Hierarchical fibrous scaffolds can be prepared by a multi-nozzle approach or by combining fiber bonding processes to generate microfibers and electrospinning to incorporate nanofibers (Santos et al. 2008). Adjusting solvent composition and humidity makes it possible to produce porous fibers, creating additional cell attachment points (Celebioglu and Uyar 2011). Directly during the electrospinning, we can control the surface charge of manufactured fibers by applying positive or negative voltage polarity to the nozzle (Ura and Stachewicz 2022); such tailoring of surface properties allows the regulation of cell attachment, proliferation, and ECM formation visualized for example, by built fibrous collagen structures (Polak et al. 2023, 2024; Szewczyk et al. 2019). Another type of electrospinning utilizes a side-nozzle system in which two different materials can be combined to create Janus fibers. For instance, this variant allows us to use two materials with antagonistic properties like hydrophilicity and hydrophobicity in a single fiber, providing opposite functions simultaneously (Knapczyk-Korczak et al. 2021). Z. Zhang et al. (2024) produced side-by-side fibers composed of polylactic acid (PLA)/PCL and gelatin for enhanced hydrophilicity and improved fibroblast cell adhesion. Moreover, encapsulating bioactive molecules, particles, and drugs is possible in two ways: loading substances in the core for prolonged release or isolation from the environment; or the opposite by exposing them in the shell of fibers for immediate direct interaction with the surrounding (Karbowniczek, Ura, and Stachewicz 2022; Karbowniczek et al. 2023). The use of electrospun fibers in drug delivery systems is attributed to their versatility in process modifications. These modifications not only facilitate the production of blended fibers but also enable the development of more advanced designs, offering enhanced control over drug release rates (Y. Liu et al. 2024). Furthermore, this approach effectively addresses key challenges such as poor drug solubility and the need for controlled release (Williams, Raimi-Abraham, and Luo 2018; C. Yang et al. 2016). Studies shows that VEGF incorporated in fibers improves angiogenic response due to controlled release during tissue regeneration (Y. Chen et al. 2023; S. He et al. 2022; C. Wang, Lu, and Wang 2020). Interestingly, modified triaxial electrospinning has been shown to precisely control drug release in nanoscale formulations. In this method, two non-spinnable solutions are used to create a coating around the spinnable core. The cellulose acetate coating protects the fibers from rapid drug release, and, importantly, the thickness of the coating can be controlled by adjusting the solution flow rate (X. Liu et al. 2019).

3.2.3 | Modifications for Enhanced Porosity

Moreover, it is possible to distinguish a separate group of electrospinning modifications that increase porosity; these include air impedance electrospinning, incorporation of porogen or sacrificial fiber, cryo-electrospinning, electrospinning in wet media, or using patterned collectors. All the techniques are schematically presented in Figure 4 (Ameer, Anil Kumar, and Kasoju 2019; Feltz et al. 2017; Rnjak-Kovacina and Weiss 2011). In air-impedance electrospinning, fibers are deposited on collectors, which are porous plates. The airflow that goes through the pores in the plate creates areas of low and high fiber deposition in the electrospun mat (McClure et al. 2012; Selders et al. 2016). Another technique based on porogen or sacrificial fiber showed

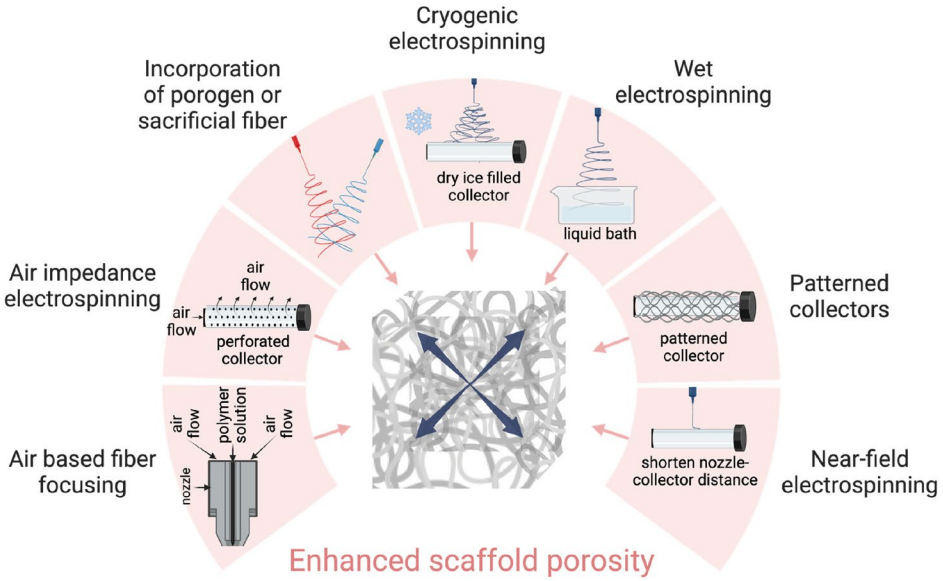

FIGURE 4 | The schematics representing the methods used in electrospinning to increase the porosity of scaffolds. The methods are related to the controlling of environment via cryogenic and wet electrospinning, using different type of collectors or set up including near-field electrospinning and multi-nozzle system or air-based fiber focusing.

effectively increased porosity of the scaffold. For example, sacrificial polyethylene oxide (PEO) microparticles incorporated in the polyglycolic acid (PGA), poly(lactic-co-glycolic acid) (PLGA), and PCL scaffolds by electrospraying resulted in a porosity increase of around 20% (J. Hodge and Quint 2019). It was shown that the sacrificial particles enhanced porosity better than sacrificial fiber in PLGA electrospun scaffolds (J. G. Hodge and Quint 2022). Electrospinning/spraying the subsequent discussed modification that increases the scaffold's porosity is cryogenic electrospinning (cryo-electrospinning) (Simonet et al. 2007). This method employs a collector system filled with dry ice to facilitate the formation of ice crystals during fiber collection. This process increases the distance between fibers, and the resulting inter-fiber spacing persists after sublimation (Crouch et al. 2023; Khorshidi et al. 2016; Leong et al. 2009). Simonet et al. showed that employing a low-temperature fiber collection device in a humidity-controlled environment enables the effective integration of ice particles within polymer fibers, forming pore templates. This method significantly influences the mesh porosity after drying, as the degree of water condensation directly affects the interfiber distance and overall porosity (Simonet et al. 2007, 2014). Thus, precise control of environmental conditions during fiber collection is essential for tailoring the structural properties of the resulting fibrous meshes. Chinnakorn et al. (2024) presented a study in which a modified electrospinning set-up and controlled fabrication allowed the production of a 3D PCL scaffold, also underlying the role of additives, such as phosphoric acid, in the wetting properties of fibers. Moreover, it is possible to influence the porosity of the scaffolds by using collectors with different geometries or patterned collectors (Palomares et al. 2021). Finally, wet electrospinning has been identified as a viable method to enhance pore size (Wilson et al. 2022; Yokoyama et al. 2009). In this process, electrospun fibers enter a liquid coagulation bath and remain suspended within the liquid, resulting in a porous, 3D structure. It was shown that electrospun nanoyarn scaffold made by twisting electrospun nanofibers into yarns within a water vortex, created with the purpose of enhancing cell infiltration and vascularization, was favorable for cell infiltration and capillary-like network formation compared to classic electrospun nanofiber scaffold (J. Wu et al. 2014). There are also methods that allow for better control of the deposition of fibers on the collector. One of them uses the magnetic field to deflect the deposition direction of fibers in the intended direction. Another one relies on air-based fiber focusing, where the electrospinning nozzle is surrounded by a specialized air sheath that focuses air parallel to the stream of the polymer jet (C. Chen et al. 2016; Feltz et al. 2017). This air assistant technique is also used to increase the porosity of the whole scaffold by better deposition control.

The challenge in bone tissue scaffold design is the translation from the laboratory scale to the manufacturing of large-scale scaffolds meeting the dimensions of the critical size bone defects exceeding several cm in thickness (Lowen and Leach 2020; Stoddard et al. 2016). The majority of research regarding electrospun meshes involves in vitro testing of thin scaffolds (below 1 mm in thickness) where nutrients and oxygen delivery are assured by diffusion (Walther et al. 2022). Large-scale scaffolds require effective and fast neovascularization to ensure proper tissue formation, avoiding cell necrosis within the material network (Fleischer, Tavakol, and Vunjak-Novakovic 2020). One of the parameters necessary for neovascularization is the interconnected system of large pores, which can be achieved while manufacturing.

In conventional electrospinning (far-field electrospinning [FFES]), fibers are generated with the chaotic jet motion without precise deposition of fibers on the collector. However, in 2006, near-field electrospinning (NFES) was introduced as a method where the nozzle–collector distance is shorter, and the applied voltage can be reduced compared to the conventional technique (Nazemi, Khodabandeh, and Hadjizadeh 2022; Y. S. Park et al. 2020; D. Sun et al. 2006). While NFES offers several benefits, including low-voltage deposition, accurate

fiber patterning, minimal material consumption, and precise positioning control, its application is usually confined to generating 2D patterns on flat surfaces (B. Zhang et al. 2016). However, it is possible to create 3D mesh structures through layer-by-layer additive printing using highly viscous polymer melts in NFES (Brown, Dalton, and Hutmacher 2011; J. He, Xia, and Li 2016). Fiber patterning design is controlled by a computer program with advanced precision of collector and nozzle movement. The speed of this movement is crucial for the designed architecture of the fibers, which can be straight but also wavy, spiral, or helical (X. Li et al. 2016; Zheng et al. 2010). The diameters of produced fibers by NFES are in the range of 0.05–200 μm (Middleton et al. 2018; D. Sun et al. 2006), while in conventional electrospinning, it is 0.01–10 μm (Fridrikh et al. 2003). A key advantage of NFES is its better ability to control pore sizes and shapes (Nazemi, Khodabandeh, and Hadjizadeh 2022). Nevertheless, researchers report that controlling the alignment, directionality, and distribution of fibers in NFES is challenging. Thus, the electrostatic jet deflection can be incorporated into a standard NFES setup. The conventional setup uses a thin nozzle, a syringe pump, an XY motorized stage, a high-voltage power supply, and a control system. Jet-deflection modification adds two auxiliary electrodes and amplifiers to modify the electric field and generate a jet deflection signal during the production of the fibers. It was demonstrated to overcome the drawback of noncontrolled unstable jet whipping (Liashenko et al. 2022).

3.2.4 | Hierarchical Structure of Electrospun Scaffolds

Overcoming the drawbacks of insufficient porosity in electrospun scaffolds for tissue engineering applications is possible by using various post-processing methods, such as 3D expansion methods (Kamaraj et al. 2023). Expansion of electrospun mat can be achieved by immersion in $NaBH_4$ solution, but it brings with it several significant disadvantages like suitability only for hydrophobic polymers, the necessity of freeze-drying, and finally, the reaction of $NaBH_4$, which is a strong reducing agent, with components and bioactive molecules incorporated into the fibers (S. Chen et al. 2020). The second reported method of 3D expansion of electrospun fibers is via depressurization of subcritical CO_2 fluid. Jiang et al. showed that cellular infiltration and tissue formation were promoted in developed scaffolds compared to traditional electrospun mats. Moreover, an in vivo study revealed blood vessel formation in expanded scaffolds and a lack of neovascularization in conventionally electrospun ones (Jiang et al. 2018). Interestingly, a completely different approach to creating a hierarchical structure of scaffolds is using short fibers, which can be used alone but also in combination with hydrogels (Niemczyk-Soczynska et al. 2023; Ning et al. 2023; J. Wang, Lin, et al. 2022). S. Qian et al. (2022) developed a Janus electrospun short fiber scaffold for wound healing, showing an improved healing process, collagen deposition, and neovascularization. Recently, it was shown that PCL short fibers modified with nano-hydroxyapatite and loaded with alkaline phosphatase (ALP) were successfully tested in vivo to treat 3D osteoporotic defects (Y. Yang et al. 2024). These short fibers can be produced by optimizing the process of electrospinning and direct collection of short fibers on the collector or by cutting standard electrospun fibrous mat by shear stress fluid flow, UV cutting, mechanical cutting, and electric spark-induced cutting (Fathona and Yabuki 2013; Y. Huang, Zhan, et al. 2023; Raja et al. 2023; Stoiljkovic and Agarwal 2008). Another study presents coaxially electrospun fibers loaded with protoporphyrin IX (PpIX) in the shell for sonodynamic therapy to damage giant cell tumors of bone selectively. Core–shell fibers were shattered into nano-scaled short fibers for further incorporation in PEO and hyaluronan, and preparation of 3D printing inks for scaffold-derived osteochondral defects treatment (W. He et al. 2024). In vitro studies showed osteogenic and chondrogenic differentiation of bone marrow stromal cells (BMSCs), while in vivo experiments in nude mice models revealed antitumor activity and good support for bone and cartilage tissue repair. Another strategy used to fabricate scaffolds with enhanced porosity is a combination of electrospinning and electrospraying. Both methods rely on the interaction of electric fields with polymer solutions, but their combination can yield even more advanced structures. Lavielle et al. (2013) demonstrated creating micropatterned nonwoven composite membranes by simultaneously electrospraying microparticles and electrospinning nanofibers onto a common collector. The process promotes self-organization between fibers and particles, forming honeycomb-like hierarchical structures. Similar studies show that by alternating electrospraying and electrospinning on a micropatterned collector, a cooperative effect between the electric field and charges allows for precise control over pore size, ranging from tens to hundreds of microns. The result is a robust 3D scaffold with cylindrical pores, exhibiting strong mechanical properties suitable for easy handling (Wittmer et al. 2014).

3.2.5 | Hierarchical Structure of Additive-Manufactured Scaffolds

Another promising strategy is the combination of 3D printing and electrospinning, which allows for obtaining multiscale, hierarchical structures with increased porosity and overall scaffold size compared to solely electrospun materials (Dalton et al. 2020; Hrynevich et al. 2018; Muerza-Cascante et al. 2015; Xu et al. 2024). Additionally, it allows for tailoring mechanical properties and degradation rate by optimizing the polymer's choice and manufacturing properties (Gonzalez-Pujana et al. 2022; Y. Yu et al. 2016). 3D printing is an additive manufacturing process that creates various shapes based on computer designs, prepared by segmenting, and selecting the filling percentage. Additionally, nozzle size and speed of printing help to adjust the resolution of the final product, with the diameter of the extruded filament in the range of hundreds of micrometers. In a typical approach, the process is performed from a solid polymer filament that is heated to the right temperature to soften and further is extruded through the nozzle to be finally deposited on the platform in the manner specified by the computer design (S. Park et al. 2022). Therefore, additive manufacturing allows the preparation of a larger scaffold structure that can be personally designed based on magnetic resonance imaging (MRI) to match the size and shape of the patient's tissue defect, a vital issue in bone regeneration (Cámara-Torres et al. 2023). Interestingly, already introduced above, electrospun Janus fibers can also be translated into 3D

printing technology to produce Janus scaffolds. Researchers demonstrate that dynamic additive-manufactured Janus scaffolds can be remotely activated by ultrasound to induce mechanical nano vibrations, enhancing cell proliferation, matrix deposition, and osteogenic differentiation of human bone marrow–derived stromal cells. These scaffolds, made from phase-segregated PCL and PLA blends, effectively function as ultrasound transducers. The remote stimulation activates voltage-gated calcium ion channels in cells, suggesting a promising noninvasive approach for future in vivo applications to modulate cellular functions (Camarero-Espinosa and Moroni 2021).

Traditional nozzle-based 3D printing methods are highly versatile but are hindered by limited printing speed and resolution. These techniques depend on mechanical stages to shape the geometry, which reduces their efficiency and precision. Recent advancements in this technique utilize EHD jetting, allowing submicrometer jets to be generated at speeds above 1 m/s. This method overcomes the limitations of slow mechanical stages by allowing the precise collection of jets and high-resolution printing. Additionally, the electrostatic control of jet trajectory allows printing patterns on a micrometer scale and using various materials, including polymers, metals, ceramics, wood, and biological tissues, preventing the risk of nozzle clogging while printing (Liashenko, Rosell-Llompart, and Cabot 2020).

Several strategies of electrospun fibers integration into the 3D-printed scaffolds were developed and described, beginning with the two-step system of simple coating of printed structure with ultrathin fibers generated by elctrospinning (Ejiohuo 2023). This approach was used to create PCL scaffolds enriched with hydroxyapatite and multiwalled carbon nanotubes (PCL/nHA/MWCNTs) by extrusion-based 3D printing followed by electrospinning resulting in enhanced cell–cell interactions and osteogenic differentiation (Y. Cao et al. 2023) In another work, 3D-printed PLLA scaffolds were functionalized with gelatin electrospun fibers loaded with osteogenon drug improving bioactivity and cell adhesion (Rajzer et al. 2018). The drawback of using electrospinning as post processing modification of printed structures is the presence of fibers only on the topmost layer, not inside the scaffold. Therefore, another solution is the integration of two devices allowing sequential 3D printing and electrospinning to create multiscale structures with alternating layers. Manufactured macro/micro-PCL porous scaffolds by combination of two technologies in the same fabrication platform were found to promote the expression of early and late osteogenic markers (Gonzalez-Pujana et al. 2022). Moreover, hybrid printing process combining screw-assisted additive manufacturing and rotational electrospinning allowing to create PCL dual-scale anisotropic scaffolds for bone tissue engineering was described (Ejiohuo 2023). The higher rotational velocity in electrospinning process promoted nanofibers alignment leading to more elongated and stretched cell morphologies. Although various configurations of both processes are described in the literature, there are still areas that require improvement, especially to ensure the proper adhesion between individual layers.

4 | Vascularization Strategies in Bone Tissue Engineering With a Focus on Electrospun Scaffolds

The main effort of tissue engineering research is focused on creating a fully functional, living cellular structure to replace damaged tissues. Tissue regeneration requires a continuous supply of oxygen and nutrients through diffusion, ensuring cells develop correctly. This primary transport mechanism allows cells to be nourished at a maximum distance of about 200 μm from the existing capillaries (Shafiee and Atala 2017; G. Yang et al. 2020). Hence, the leading challenge in fabricating scaffolds is engineering vascularized tissue for further translation to clinical application. Figure 5. presents selected publications focusing on the vascularization of electrospun scaffolds showing proposed in vitro and in vivo models.

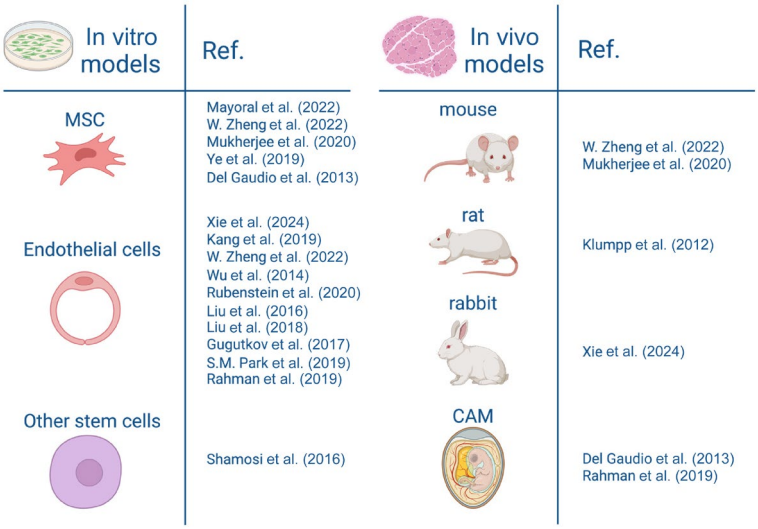

FIGURE 5 | Types of in vitro and in vivo models for the investigation of vascularization in electrospun scaffolds based on arbitrarily chosen 15 references: Mayoral et al. (2022), Xie et al. (2024), Kang et al. (2019), W. Zheng et al. (2022), J. Wu et al. (2014), Rubenstein, Greene, and Yin (2020), Mukherjee et al. (2020), Ye et al. (2019), Shamosi et al. (2017), Liu et al. (2018), Gugutkov et al. (2017), Del Gaudio et al. (2013), S. M. Park et al. (2019), Klumpp et al. (2012), and Rahmani et al. (2019).

4.1 | In Vitro Pre-Vascularization Strategies

One of the leading strategies for building blood vessel networks in cellular scaffolds involves using cell sources that exhibit primary angiogenic behavior. The advantage of using vascular ECs is that they can create a functional vascular network that, when implanted, will anastomose to the existing vascular network in the tissue surrounding the scaffold. We distinguish three main groups of cells, including somatic cells, stem cells, and induced pluripotent stem cells (Saberianpour et al. 2018). Nevertheless, these cells require isolation from the patient, which greatly complicates the procedure and carries additional risks (G. Yang et al. 2020). Moreover, these cells may lose their functionality in in vitro cultures. Utilizing stem cells, characterized by their unique ability for unlimited self-renewal and differentiation, holds promise in overcoming the limitations associated with primary cell acquisition. Initial efforts to generate regenerative cells for in vitro expansion involved isolating and expanding EPCs obtained either from peripheral blood or through the spontaneous differentiation of stem cells into embryoid bodies. However, owing to their restricted availability in the blood and unregulated specification as embryoid bodies, attention has shifted toward investigating controlled, directed differentiation approaches (Y. Wang, Keshavarz, et al. 2022). Table 1 presents examples of cell types used as a source of ECs in vascular tissue engineering with their main function in the vascularization process. It is indicated that the use of ECs alone is insufficient to reconstruct vascularization, and a promising solution is the parallel use of the pericytes, fibroblasts, or human vascular smooth muscle cells (VSMCs) (G. Yang et al. 2020). For example, it was shown that using a co-culture of ECs (human umbilical vein endothelial cells [HUVECs]) with human mesenchymal stem cells (hMSCs) on electrospun fibers resulted in improved proliferation and osteogenic differentiation in vitro (Carvalho et al. 2019). Regarding co-cultures, it is worth noticing that there is a communication mechanism between ECs and osteoblasts defined by different paths: through membrane molecules or cytoplasmic connections of two adjacent cells and secretion of factors in the ECM environment (Cenni, Perut, and Baldini 2011). These paths can be affected by the material properties of the used scaffold, making it crucial for cell–material interaction and angiogenic behavior.

4.2 | Hypoxia-Induced Angiogenesis

Hypoxia is a state characterized by reduced oxygen levels within the tissue or its surrounding microenvironment. Oxygen is pivotal for numerous cellular processes, encompassing metabolism, proliferation, differentiation, and cell survival. When oxygen levels decline below physiological thresholds, cells encounter stress and initiate adaptive mechanisms to mitigate the effects of hypoxic conditions (Araldi and Schipani 2010; Hannah et al. 2021; Maes, Carmeliet, and Schipani 2012; Potier et al. 2007). Oxygen levels regulate signaling pathways like the hypoxia-inducible factor (HIF) pathway, essential for cellular responses to hypoxia. HIFs, crucial mediators in this context, orchestrate adaptive mechanisms that enable hypoxic cells to survive and differentiate, with VEGF as a key downstream target in angiogenesis (Maes, Carmeliet, and Schipani 2012). There is a growing interest in hypoxia-mimicking scaffolds for induced angiogenesis. However, controlling the reduced oxygen level is difficult, especially since each tissue type requires specific levels varying between 14% and 1% O_2 concentration (Krock, Skuli, and Simon 2011). For instance, preferable oxygen pressure for avascular tissues is between 1% and 5% O_2, while vascularized ones, like bone, require higher levels of 5%–12% O_2 (Fu et al. 2021). Moreover, hypoxia-based strategies in tissue engineering can be divided into two groups. The first one uses hypoxia as an in vitro tool for preconditioning tissue-engineered scaffolds before transplantation, and the second aims to induce angiogenic pathways in vivo (Hadjipanayi and Schilling 2013). Chemical regulation from the scaffolds is the most popular approach in tissue engineering to induce angiogenesis by hypoxia. We can distinguish several chemicals commonly used to regulate the expression of HIF, such as dimethoxyallyl glycine (DMOG), deferoxamine (DFO), metal ions, small molecule drugs, and nitric oxide (NO) (Fu et al. 2021; M. Zhou et al. 2019). Electrospun scaffolds, known as excellent carriers in drug delivery as mentioned in the previous sections, can be used as hypoxia-mimicking materials

TABLE 1 | Examples of the most common cells used as a source of endothelial cells in vascularization tissue engineering.

Type of cells	Function/in vitro or in vivo study	Ref.
Endothelial progenitor cells (EPCs)	Injected into the ischemic hindlimbs of a mouse model, it enhanced neovascularization and seamlessly integrated into the walls of capillary vessels. The in vitro study also confirmed good integration of cells with electrospun scaffolds.	(Asahara et al. 1997; Jiménez-Beltrán et al. 2022; Rubenstein, Greene, and Yin 2020)
Human pluripotent stem cells (HPSCs)	Ethical concerns related to the isolation of cells.	(Y. Wang, Keshavarz, et al. 2022)
Human-induced pluripotent stem cells (hiPSCs)	hiPSCs can proliferate extensively and subsequently undergo differentiation into specialized human brain capillary endothelial cells, and further functional blood–brain barrier using electrospun scaffold in the in vitro study.	(Rohde et al. 2022)
Human mesenchymal stem cells (hMSCs)	MSCs showed capability in vessel formation and angiogenic effect in a mouse ischemic hind-limb in vivo model.	(Z. Yao et al. 2020)

by incorporation of chemicals that regulate HIF expression (Nazarnezhad et al. 2020). Cui et al. (2022) showed electrospun core–shell PCL fibers loaded with DFO in the shell and dexamethasone (DEX) loaded in the core of the fiber as a promising system for parallel enhancement of angiogenesis and osteogenesis. Another group studied the exposure of cells to the hypoxic conditions seeded onto electrospun fibers and standard 2D controls. Studies indicated significantly better cellular responses by observing *HIF-1A* gene expression upregulation in PCL-nHA electrospun scaffolds (Frontini-López et al. 2023). Rafique et al. fabricated DMOG-loaded PCL grafts via electrospinning, achieving sustained DMOG release for up to 2 weeks and enhancing proliferation, migration, and VEGF and NO release from HUVECs in vitro through HIF-1α stabilization. Moreover, in vivo implantation of these DMOG-loaded PCL grafts into rat abdominal arteries facilitated vascular regeneration, including cellularization and capillary formation (Rafique et al. 2021). Also, bioactive glass, is extensively used to stimulate vascularization and bone regeneration (Ghorbani et al. 2023). Incorporated in electrospun PCL fibers stimulated the HIF pathway by releasing cobalt, which led to hypoxic conditions in the scaffold (Solanki et al. 2021). To summarize, the hypoxic microenvironment, particularly prevalent in injured bone tissues due to limited vascularization, poses challenges for cell survival and tissue regeneration. Culturing cells under hypoxic conditions may enhance their survival and regenerative potential postimplantation in conditions such as bone fractures, where oxygen levels can drop close to anoxic levels (<1% oxygen). This approach holds promise for improving the efficacy of cell-based therapies aimed at bone repair, regeneration, and vascularization.

4.3 | Oxygen Delivery

One major barrier in tissue engineering is providing an adequate oxygen supply to implanted tissue scaffolds. Oxygen diffusion from surrounding vasculature in vivo is limited to the periphery of the scaffolds, leading to insufficient oxygen reaching the inner regions of the engineered tissues. This limitation can result in necrosis or apoptosis of cells in the core of the scaffold, impacting cell viability and tissue functionality.

The requisites for scaffolds to facilitate oxygen delivery to cells encompass several key aspects. First is the interconnected porosity in scaffolds, so the interconnected pores enable the diffusion of oxygen-enriched media throughout the construct. Another is the mechanical strength to achieve an optimal balance between high porosity for effective oxygen transport and maintaining mechanical resilience. It is essential, especially in scenarios where rigid or sturdy scaffold structures are required. Importantly, the interconnected vascular channels should biomimic naturally occurring in the tissues thus allowing media perfusion, thereby ensuring sustained oxygen supply critical for supporting cell viability and promoting successful tissue growth (Augustine et al. 2023).

To overcome current barriers in scaffolds for oxygen delivery in tissue engineering applications, hyperbaric oxygen therapy (HBOT) and oxygen-generating materials are explored by researchers. HBOT involves exposing patients to 100% oxygen at pressures greater than atmospheric pressure. This therapy has been traditionally used to treat conditions like decompression sickness in divers but is now being investigated for tissue engineering applications. HBOT can increase oxygen concentration in tissues, promoting cell survival, enhancing metabolic activity, and supporting tissue regeneration (Y. Zhang, Zhou, et al. 2023). Another option is hemoglobin-based oxygen carriers (HbOCs) derived from hemoglobin extracted from red blood cells, show potential for controlled oxygen delivery in tissue scaffolds. These carriers mimic the oxygen-binding properties of natural hemoglobin, releasing oxygen selectively in hypoxic environments where oxygen demand is high (M. Cao et al. 2021). Incorporating HbOCs into biomaterials could offer a safe and effective method for supplying oxygen to engineered tissues. The most recent is oxygen-releasing biomaterials (ORBs) for providing sustained oxygen supply to engineered tissues, both in vitro and in vivo. These materials release oxygen through diffusion or chemical generation, aiming for controlled, gradual release to avoid cell death from high oxygen concentrations. Common ORBs include sodium percarbonate, calcium peroxide, magnesium peroxide, hydrogen peroxide, and fluorinated materials. Incorporating ORBs into tissue engineering constructs in various forms, such as microspheres, films, nanofibers, and scaffolds, allows for prolonged oxygen release. However, some ORBs produce reactive oxygen species, like hydrogen peroxide, which can be cytotoxic. To mitigate this, catalase, an antioxidant enzyme, can be incorporated into scaffolds to decompose hydrogen peroxide into oxygen and water. Microencapsulation techniques, such as using PLGA and alginate layers, enable controlled release of oxygen from hydrogen peroxide while minimizing cytotoxic effects (Gholipourmalekabadi et al. 2016). Thus, peroxides and inorganic peroxide salts release oxygen through controlled degradation processes. These materials can provide a continuous oxygen supply to tissue-engineered constructs, overcoming oxygen diffusion limitations in large scaffolds. These materials include solid peroxides like magnesium peroxide and calcium peroxide, as well as liquid hydrogen peroxide. Solid peroxides, such as CaO_2 and MgO_2, offer sustained oxygen release compared to liquid H_2O_2. They generate oxygen by reacting with water, forming H_2O_2, which then decomposes into water and oxygen. Perfluorocarbons (PFC) are also used as oxygen carriers. The choice of oxygen-generating material depends on factors like cell density, scaffold size, and tissue regeneration requirements. Optimization of oxygen release kinetics is crucial for specific tissue engineering applications (Gholipourmalekabadi et al. 2016). By incorporating oxygen-generating materials into scaffolds, researchers aim to ensure sufficient oxygen levels reach all regions of the engineered tissues, promoting cell viability and functionality. Incorporating OGBs into hydrophobic polymers, such as cell scaffolds, hydrogels, and electrospun meshes, enables sustained oxygen release until early neovascularization occurs. OGBs hold the potential for regenerating not only bone tissue but vital organs like the brain and heart, where oxygen supply is crucial for tissue health and function. However, concerns about the production of toxic byproducts like hydrogen peroxide and reactive oxygen species need to be addressed. Factors affecting oxygen release, such as hydration rate, pH, and environmental catalysts, require careful consideration. Research efforts are underway to optimize oxygen delivery systems and develop novel strategies, particularly in advancing 3D scaffold-based organ regeneration using biological and synthetic materials (Hosseini et al. 2023).

4.4 | Vascularization in Organoids

Organoids are 3D clusters of self-organized cells derived from stem cells, replicating the functions and diversity of their original organs. Stem cells obtained from human cells are cultured in vitro or in vivo. The first organoid was developed in 2009 to model various differentiated cells of the intestine in vivo (Sato et al. 2009). To date, among the brain, retina, kidney, liver, lung, and prostate, also bone organoids have been established (J. Huang, Zhang, et al. 2023). As discussed in terms of classical bone tissue–engineered scaffolds, vascularization is an indispensable aspect of culture cells as 3D structures that properly perform their functions. Again, similarly, we recognize bone organoid vascularization as the main challenge to overcome (Strobel, Moss, and Hoying 2023). Among the methods of organoid vascularization, we can distinguish strategies of incorporating into the organoid structure: ECs, typically HUVECs (Wenger et al. 2004), other cells like MSCc, pericytes, or fibroblasts that help to increase microvessel complexity and contribute to ECs development (Hsu et al. 2021; Kook et al. 2022; Lee, Han, and Lee 2016), and lastly, stem cells which induce the process of vascularization (Homan et al. 2019; Pitaktong et al. 2020).

Incorporating individual cell types such as ECs, fibroblasts, MSCs, or pericytes has shown utility, but they do not fully replicate the complexity of native microvessels. Native microvessels interact continuously with diverse cells and matrix types, modulating functions within the vessel and surrounding tissue. This cellular complexity is crucial for forming perfused microvascular networks capable of adapting and remodeling in response to hemodynamic and metabolic cues, ensuring networks are well suited for specific tissue environments and meet essential perfusion requirements (J. Kim et al. 2015; Kosyakova et al. 2020; Lin and Melero-Martin 2012; Rambøl, Han, and Niklason 2020). To overcome the insufficient complexity of the incorporation of individual cell types, Strobel et al. successfully applied an approach to vascularize tissue organoids using isolated microvessel fragments combined with MSCs. These fragments formed a neovascular network that invaded and vascularized the surrounding matrix. They developed vascularized adipose organoids through a staged differentiation approach, demonstrating that the presence of microvasculature enhanced insulin receptor expression in adipocytes. This suggests that microvessels may play a functional role even without perfusion; therefore, further research is needed to understand these interactions and their implications for tissue engineering fully (Strobel, Gerton, and Hoying 2021).

Scaffolds improve nutrient diffusion and waste removal, addressing challenges associated with traditional organoid systems where limited accessibility can lead to necrosis at the core of larger organoids. The porosity of scaffolds enables better access to nutrients and mechanical stimuli, promoting longer culture lifespans (Hofer and Lutolf 2021; D. Kim et al. 2023; H. Liu et al. 2023). Electrospun membranes are excellent for application in organoids/spheroids but also as a construction platform in tissue barrier models (D. Kim et al. 2023).

Poling et al. (2024) presented study where they verify whether incorporating piezoelectric materials into organoid development could promote earlier organoid formation and support their further stimulation using external ultrasound for tissue engineering applications. It was presented that electrospun nanofiber matrices fasten the organoid formation 3 days earlier than in the control group. Moreover, ultrasound stimulation enhanced cell proliferation, proving that piezoelectric fibrous materials can stimulate organoid development.

5 | Vascularization Analysis Techniques In Vitro, In Vivo, and Ex Vivo

This section focuses on techniques to analyze biomaterials for biocompatibility and angiogenesis potential. The tools commonly used by scientists are presented in Figure 6. Proliferation, migration, and viability tests are the basic techniques for testing a material's biocompatibility. This is the first step in evaluating the material's potential for use as a scaffold in tissue engineering. This is no different for electrospun fibers used in vascularization during bone tissue regeneration, which are meticulously verified in vitro before being tested in vivo. The most common proliferation tests are based on the following:

I. Cell metabolism assays which include MTT (3-[4,5-dimethylthiazole-2-yl]-2,5-diphenyltetrazolium bromide), MTS (3-[4,5-dimethylthiazol-2-yl]-5-[3-carboxymethoxyphenyl]-2-[4-sulfophenyl]-2*H*-tetrazolium), WST-1 (2-[4-iodophenyl]-3-[4-nitrophenyl]-5-[2,4-disulfophenyl]-2*H*-tetrazolium), and water-soluble tetrazolium.
II. Nuclei acid, such as PicoGreen and CyQUANT.
III. Other methods, such as ATP (adenosine triphosphate) measurements, counting nuclei or immunolabeled cells, flow cytometry, and TEER (transepithelial/transendothelial electrical resistance) measurements (Fischer and Aparicio 2020).

Importantly, cell viability tells us whether the cells are alive or dead, in contrast to cell proliferation, which measures cell division. To measure cell viability, we can apply the following tests: LIVE/DEAD, cytoplasmic enzyme lactate dehydrogenase (LDH), or transmembrane potential, which are based on the breakdown of the cell and nuclear membrane (Fischer and Aparicio 2020).

Other in vitro tests focus on crucial aspects of cell migration. In the context of vascularization in electrospun fibers, researchers are usually concentrating on EC's behavior. A relatively easy and popular technique to examine the migration of cells is the scratch test, which can also be modified. Ahmed et al. (2018) investigated the ECs migration on electrospun PLGA fibers with different diameters to verify geometry as a factor affecting cellular response. Their scratch test consisted of preventing cells from migrating through a physical barrier for a specified period of time and later subsequent confocal imaging of the rate of cell movement through the unpopulated scaffold area after barrier removal. This experiment is useful in determining which scaffold's geometry and other surface properties are preferable for certain types of cells.

A separate group of experiments allows the quantification of pro-angiogenic factors. Here, we can perform western blotting that can be employed to assess various biological

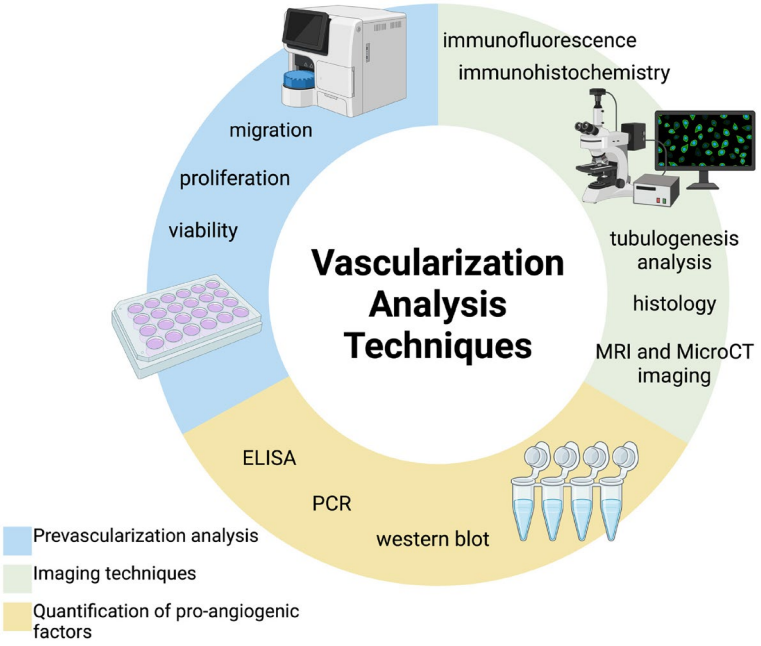

FIGURE 6 | Scheme of typical techniques applied in scaffold vascularization analysis divided to three categories: pre-vascularization, imaging, and quantification of pro-angiogenic factors.

processes and protein expressions. For instance, evaluation of osteoblast differentiation in hMSCs to detect the expression levels of ALP and runt-related transcription factor 2 (*Runx2*). This application helps understand osteoblast's differentiation process derived from hMSCs, providing insights into bone formation and remodeling. Additionally, by utilizing a western blot, we can assess the angiogenic activity of cells, as shown for HUVECs seeded on electrospun PLA scaffolds (Bhattarai et al. 2020). This application allows researchers to investigate the signaling pathways involved in angiogenesis. Furthermore, ELISA (enzyme-linked immunosorbent assay) is a useful tool for measuring the presence of commonly used growth factors like angiogenic factor VEGF-A (vascular endothelial growth factor A) as a substance incorporated in the scaffolds, but it is also possible to quantify the secretion of these enzymes from cells (S. Chen et al. 2020; Gritsch et al. 2020). Typically, it measures the levels of specific proteins or factors involved in the biological processes (C. Qian et al. 2020; Shimazaki et al. 2021; Xi et al. 2020). Lastly, PCR (polymerase chain reaction) is a widely used technique in biology that focuses on specific segments of DNA and allows the analysis of gene expression levels. PCR can be used to assess the biocompatibility and osteoconductive properties of scaffolds. By analyzing gene expression profiles of cells cultured on different scaffolds, it is possible to determine the scaffold's ability to support specific cellular behavior, like osteogenic differentiation or angiogenic gene expression (Y. C. Chen, Fu, et al. 2022; R. Yang et al. 2022; H. Yu et al. 2023). Zhan et al. (2021) presented a study of osteogenesis and angiogenesis potential in electrospun PLLA fibers enriched with liquid crystals and hydroxyapatite, which created a novel composite supporting bone regeneration. They implemented real-time quantitate PCR (RT-PCR) experiments to analyze osteogenic and vascularization-related gene expression, specifically the angiogenic CD31 gene, proving their composite to accelerate the angiogenic activity of cells.

The neovascularization potential in biomaterials can be assessed using several imaging techniques ex vivo and in vivo, such as microscopy study of histological sections with immunostained ECs, CLSM, microcomputed tomography (MicroCT), high-frequency ultrasound, optoacoustic imaging, or MRI. Among the others, the most popular is histological assessment (Woloszyk et al. 2019). However, its main drawbacks are the 2D analysis and difficulty evaluating blood vessel functionality (Kiessling, Razansky, and Alves 2010). The vessel network and interaction of cells with the biomaterial cannot be verified in the real 3D model (Woloszyk et al. 2019). Here, MicroCT, as a technique that allows the transformation of scans into 3D vessel trees, enables the investigation of vascularization patterning. Using this technique to quantify scaffold vascularization, it was reported that electrospun PCL/collagen-blend fibers with different geometries influenced the number of vessels (Klumpp et al. 2012). Moreover, MicroCT, in combination with MRI, allows to verify in vivo neovascularization in bone regeneration, visualizing both biomaterial and the tissue. Ribot et al. (2017) successfully used these two techniques to investigate neovascularization in biomaterials implanted in a femoral defect in rats. However, as in vivo animal experiments are time-consuming and challenging to carry out, requiring specialized infrastructure and bioethical approvals, an increasingly common alternative for analyzing angiogenesis in biomaterials is using a chick chorioallantoic membrane (CAM) model (Vimalraj, Renugaa, and Dhanasekaran 2023). According to the European Parliament Directive 2010/63/EU and the 3Rs concept (the concept of reduction, refinement, and replacement of animal models), it is strongly recommended to strive for more ethical biological models than standard animal ones, where the CAM model is found as one of the most attractive and ethical (Mapanao and Voliani 2020; Sarogni et al. 2021). We are seeing increasing use of chicken-embryo assay in the study of angiogenesis and vasculogenesis in electrospun scaffolds for the regeneration of

various tissues (D. Li, Zhang, et al. 2023; Oliinyk et al. 2023; T. Yao et al. 2023): urethral tissue (Abbas et al. 2024), wound healing (Amiri et al. 2024; Koohzad and Asoodeh 2024; Pamu et al. 2024; Patole et al. 2024), and bone regeneration (de Oliveira et al. 2022; Dhinasekaran et al. 2021; Näf et al. 2024). Woloszyk et al. (2019) present a study of vascularization in scaffolds for bone regeneration using MicroCT, MRI, and CAM assay as a model instead of an animal one. They report using a CAM assay as an efficient bioreactor that is a cost and time-effective model for angiogenesis studies in biomaterials. Figure 7 shows the application, advantages, and disadvantages of the used techniques, proving that the comprehensive combination of them in vivo and ex vivo gives full information about the functionality of blood vessel formation.

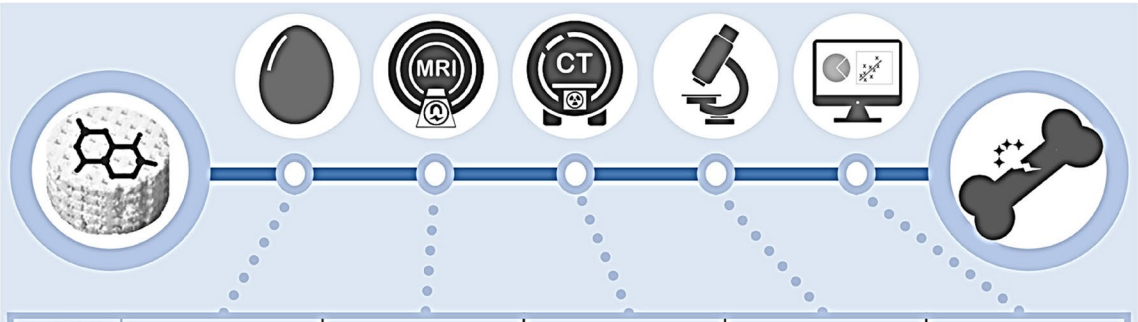

	In vivo CAM assay	In vivo MRI	Ex vivo MicroCT	Ex vivo Histology	Comprehensive Analysis
	• Surface area: ingrown vessels visible	• Total scaffold • Interface area • Middle area • Surface area	• Total scaffold: Microcalcification dependent on scaffold type • Interface area • Middle area • Surface area: Microcalcification dependent on scaffold type	• Total scaffold: depending on tissue size • Interface area • Middle area • Surface area	Comprehensive functional, structural and cellular in vivo and ex vivo analysis of blood vessels
	• Immature immune system • Cost-effective in vivo method • No animal licence necessary • Newly developed pump-assisted perfusion technology	• 3D in vivo imaging • Quantitative functional analysis (e.g., perfusion capacity) • Suitable for time course studies • Not destructive to target tissue • No radiation exposure	• 3D in vivo / ex vivo imaging • High resolution • Quantitative analysis (e.g., vessel length, branches) • Representation of vascular architecture • Not destructive to target tissue	• Analysis of tissue structure at cellular level • Use of specific stainings and antibodies possible • Software solutions for semi-automated analysis available	
	• Scaffold size is limited • Incubation period limited to 7 days	• Resolution is limited • Use of Gadolinium contrast agent • Injection of contrast agent requires knowledge in microsurgery • Requires good IT infrastructure and data pipeline	• X-ray radiation • Use of MicroFil contrast agent is linked to an end-point measurement • Injection of contrast agent requires knowledge in microsurgery • A non-continuous filling of the vasculature by MicroFil® may occur • Requires good IT infrastructure and data pipeline	• 2D ex vivo endpoint analysis • Artifacts based on insufficient fixation and preparation techniques • Complete analysis of larger samples or organs is time- and cost-consuming	

FIGURE 7 | The scheme presents a comprehensive blood vessel analysis through a combined in vivo CAM assay, advanced magnetic resonance imaging (MRI), microcomputed tomography (MicroCT), and histology, with advantages and disadvantages. Reprinted with permission from Woloszyk et al. (2019).

Following further analysis of the vascularization of scaffolds in vitro and in vivo in addition to the CAM model, we often come across the use of the Matrigel model (Dikici, Claeyssens, and MacNeil 2020; Hasmad et al. 2022). Matrigel is a substance derived from the basement membranes found in normal tissues, which are thin sheets of ECM serving various roles in the body. These membranes are highly insoluble, making extracting and studying their components difficult. However, the EHS tumor in mice (named after Dr. Engelbreth-Holm, who isolated it) has provided a significant amount of basement membrane material, enabling researchers to characterize its components structurally and functionally. Due to its components, Matrigel, an extract derived from the EHS tumor, forms a solid gel at body temperature (37°C). This gel replicates the structure of basement membranes and has been extensively utilized in cell culture and in vivo experiments. It is reported that up to 2021, more than 12,000 scientific publications presented studies with embryonic, normal, stem, or malignant cells using Matrigel as a model for experiments (Passaniti, Kleinman, and Martin 2022). This in vivo basement membrane mimics the ECM and allows experiments to be conducted focusing on different aspects of vascularization in scaffolds (Laschke et al. 2008). For example, it was shown that ECs started to create capillary-like tubes on the membrane within 12 h of culture (Benton et al. 2011). Cui et al. claim that the tubular formation of ECs is an in vivo gold standard in bone tissue engineering, leading to a comprehensive evaluation of angiogenesis critical for tissue regeneration. They produced electrospun core–shell fibers with programmed drug release to boost vascularized bone regeneration. It was observed that HUVECs cultured on Matrigel created tubular formation after 6 h (Cui et al. 2022). Another group produced electrospun PLA fibers with sequential release of tauroursodeoxycholic acid (TUDCA) and bone morphogenic protein 2 (BMP2), which were tested for potential stimulation of angiogenesis. Also, in this study, HUVECs tubular formation on Matrigel was analyzed, showing more extended tube formation and more than three times better cellular migration on scaffolds containing bioactive substances compared to pure PLA fibers (Bhattarai et al. 2020).

6 | Conclusions

Conventional scaffold fabrication methods such as solvent casting and particulate leaching, gas foaming, phase separation, freeze-drying, or sol–gel methods can produce scaffolds with large pores, but controlling pore size and interconnectivity remains challenging. Electrospinning can uniquely create scaffolds with porosity ranging from 100 nm to 10 μm, enhancing cell adhesion. In contrast, 3D printing achieves higher scaffold porosity, from 100 to 550 μm, facilitating adequate nutrient flow. Combining electrospinning and 3D printing yields scaffolds that offer both excellent cell adhesion and robust mechanical support, with appropriate free spaces for nutrient flow. This synergy makes them ideal candidates for scaffolds aimed at improving tissue vascularization.

Effective vascularization often requires co-culturing ECs with other cell types like pericytes and fibroblasts. Additionally, the scaffold's material properties significantly impact cell communication and angiogenesis, making the choice of scaffold material crucial for successful vascular network formation. Reviewing vascularization assessment, histological analysis remains the most popular method for evaluating neovascularization in biomaterials despite its limitations. MicroCT presents a promising alternative, offering a 3D perspective and overcoming traditional histology constraints. Integrating MicroCT with MRI holds significant potential for enhancing our understanding of vascularization dynamics and improving tissue engineering strategies, particularly in bone regeneration applications.

While hypoxia has been proposed as a viable strategy for inducing vascularization, the opposite approach of utilizing oxygen-delivering scaffolds presents a promising avenue for ensuring adequate oxygen supply, particularly in large scaffolds where the risk of cell necrosis is heightened. This alternative method offers potential advantages in mitigating the challenges associated with extremely low oxygen levels in regenerating regions and underscores the importance of tailored strategies in tissue engineering and regenerative medicine. Further research and development in this direction hold significant promise for improving the efficacy and viability of tissue.

The field of organoid fabrication has significantly advanced, yet fully modeling native tissues remains challenging. A major hurdle is enhancing tissue complexity, especially through vascularization, without complicating the process. Promising approaches include stem cell co-differentiation, incorporating whole microvessels, and adding tissue-specific cells and matrices. Stem cell–based fabrication of vascularized organoids offers significant advantages over methods using primary cells, such as greater proliferation and regeneration capacities and the potential for patient-specific models. Despite these benefits, challenges remain, particularly in co-culturing different cell types and achieving consistent differentiation results. Ongoing improvements and advancements in stem cell differentiation protocols are essential to overcome these limitations and enhance the reproducibility and practicality of vascularized organoids in in vitro models. Future research should focus on mimicking in vivo complexity, emphasizing cell signaling and mechanical cues like intravascular perfusion. In summary, multi-stimuli research combining material properties, growth factors, oxygen level manipulation, and biomechanical stimulation in designed bioreactors with the following complex vascularization assessment is necessary to overcome insufficient vascularization in currently used approaches.

The future of bone tissue engineering holds great promise in addressing the need for bone substitutes, particularly in improving scaffold design and enhancing vascularization and focusing on better replicating the complexity of native tissues. Advances in electrospinning and biofabrication must focus on optimizing scaffold porosity and mimicking the ECM to improve oxygen and nutrient diffusion, which is critical for successful tissue regeneration. The advantage of electrospinning is the application of high electric field strength to create fibers with controlled surface properties; however, combined with other manufacturing techniques, it will enable precise control over pore size and robust 3D scaffolds with enhanced porosity and mechanical properties. Bone organoids show promise for disease modeling and treatments but struggle with poor vascularization, so future

research should focus on developing better pre-vascularization strategies. Moving forward, scaling up the fabrication techniques from lab-scale to large-scale manufacturing will be essential for clinical applications, bringing us closer to effective, functional bone regeneration therapies. Nevertheless, to reach effective bone regeneration solutions, the integration of bioactive materials and functional tissue constructs still needs new scaffold designs.

Author Contributions

Martyna Polak: conceptualization (equal), validation (equal), visualization (lead), writing – original draft (equal), writing – review and editing (equal). **Joanna Ewa Karbowniczek:** conceptualization (equal), validation (equal), visualization (supporting), writing – original draft (supporting), writing – review and editing (supporting). **Urszula Stachewicz:** conceptualization (equal), funding acquisition (lead), project administration (lead), resources (lead), supervision (lead), validation (equal), visualization (supporting), writing – original draft (equal), writing – review and editing (equal).

Conflicts of Interest

The authors declare no conflicts of interest.

Data Availability Statement

Data Availability StatementData sharing is not applicable to this article as no new data were created or analyzed in this study.

Related WIREs Articles

Biominerals-hierarchical nanocomposites: the example of bone

Nanotechnology for bone materials

Nanostructured polymer scaffolds for tissue engineering and regenerative medicine

References

Abbas, T. O., H. Parangusan, H. C. Yalcin, et al. 2024. "Trilayer Composite Scaffold for Urethral Reconstruction: In Vitro Evaluation of Mechanical, Biological, and Angiogenic Properties." *Biomedical Materials* 19, no. 2: 1–13. https://doi.org/10.1088/1748-605X/ad1c9c.

Abbasi, N., S. Hamlet, R. M. Love, and N. T. Nguyen. 2020. "Porous Scaffolds for Bone Regeneration." *Journal of Science: Advanced Materials and Devices* 5, no. 1: 1–9. https://doi.org/10.1016/j.jsamd.2020.01.007.

Abdelaziz, A. G., H. Nageh, S. M. Abdo, et al. 2023. "A Review of 3D Polymeric Scaffolds for Bone Tissue Engineering: Principles, Fabrication Techniques, Immunomodulatory Roles, and Challenges." *Bioengineering* 10, no. 2: 1–43. https://doi.org/10.3390/bioengineering10020204.

Afzal, A., L. C. Shaw, A. V. Ljubimov, M. E. Boulton, M. S. Segal, and M. B. Grant. 2007. "Retinal and Choroidal Microangiopathies: Therapeutic Opportunities." *Microvascular Research* 74, no. 2–3: 131–144. https://doi.org/10.1016/j.mvr.2007.04.011.

Ahmed, M., T. Ramos, P. Wieringa, C. Van Blitterswijk, J. De Boer, and L. Moroni. 2018. "Geometric Constraints of Endothelial Cell Migration on Electrospun Fibres." *Scientific Reports* 8, no. 1: 1–10. https://doi.org/10.1038/s41598-018-24667-7.

Akiva, A., J. Melke, S. Ansari, et al. 2021. "An Organoid for Woven Bone." *Advanced Functional Materials* 31, no. 17: 1–9. https://doi.org/10.1002/adfm.202010524.

Al-Bari, A. A., and A. Al Mamun. 2020. "Current Advances in Regulation of Bone Homeostasis." *FASEB Bioadvances* 2, no. 11: 668–679. https://doi.org/10.1096/fba.2020-00058.

Ameer, J. M., P. R. Anil Kumar, and N. Kasoju. 2019. "Strategies to Tune Electrospun Scaffold Porosity for Effective Cell Response in Tissue Engineering." *Journal of Functional Biomaterials* 10, no. 3: 1–21. https://doi.org/10.3390/jfb10030030.

Amiri, Z., A. M. Molavi, A. Amani, et al. 2024. "Fabrication, Characterization and Wound-Healing Properties of Core–Shell SF@Chitosan/ZnO/*Astragalus arbusculinus* Gum Nanofibers." *Nanomedicine* 19, no. 6: 499–518. https://doi.org/10.2217/nnm-2023-0311.

Araldi, E., and E. Schipani. 2010. "Hypoxia, HIFs and Bone Development." *Bone* 47, no. 2: 190–196. https://doi.org/10.1016/j.bone.2010.04.606.

Asahara, T., T. Murohara, A. Sullivan, et al. 1997. "Isolation of Putative Progenitor Endothelial Cells for Angiogenesis." *Science* 275, no. 5302: 964–967. https://doi.org/10.1126/science.275.5302.964.

Augustine, R., Y. B. Dalvi, V. K. Yadu Nath, et al. 2019. "Yttrium Oxide Nanoparticle Loaded Scaffolds With Enhanced Cell Adhesion and Vascularization for Tissue Engineering Applications." *Materials Science and Engineering C* 103: 1–13. https://doi.org/10.1016/j.msec.2019.109801.

Augustine, R., M. Gezek, N. S. Bostanci, A. Nguyen, and G. Camci-Unal. 2023. "Oxygen-Generating Scaffolds: One Step Closer to the Clinical Translation of Tissue Engineered Products." *Chemical Engineering Journal* 455: 1–19. https://doi.org/10.1016/j.cej.2022.140783.

Aykora, D., and M. Uzun. 2024. "Bone Tissue Engineering for Osteointegration: Where Are We Now?" *Polymer Bulletin* 81: 8595–8605. https://doi.org/10.1007/s00289-024-05153-9.

Bae, H., A. S. Puranik, R. Gauvin, et al. 2012. "Building Vascular Networks." *Science Translational Medicine* 4, no. 160: 160ps23. https://doi.org/10.1126/scitranslmed.3003688.

Bagherzadeh, R., M. Latifi, S. S. Najar, M. A. Tehran, and L. Kong. 2013. "Three-Dimensional Pore Structure Analysis of Nano/Microfibrous Scaffolds Using Confocal Laser Scanning Microscopy." *Journal of Biomedical Materials Research. Part A* 101, no. 3: 765–774. https://doi.org/10.1002/jbm.a.34379.

Benton, G., H. K. Kleinman, J. George, and I. Arnaoutova. 2011. "Multiple Uses of Basement Membrane-Like Matrix (BME/Matrigel) In Vitro and In Vivo With Cancer Cells." *International Journal of Cancer* 128, no. 8: 1751–1757. https://doi.org/10.1002/ijc.25781.

Bhattarai, D. P., M. H. Kim, H. Park, W. H. Park, B. S. Kim, and C. S. Kim. 2020. "Coaxially Fabricated Polylactic Acid Electrospun Nanofibrous Scaffold for Sequential Release of Tauroursodeoxycholic Acid and Bone Morphogenic Protein2 to Stimulate Angiogenesis and Bone Regeneration." *Chemical Engineering Journal* 389: 1–14. https://doi.org/10.1016/j.cej.2019.123470.

Brown, T. D., P. D. Dalton, and D. W. Hutmacher. 2011. "Direct Writing by Way of Melt Electrospinning." *Advanced Materials* 23, no. 47: 5651–5657. https://doi.org/10.1002/adma.201103482.

Buss, D. J., R. Kröger, M. D. McKee, and N. Reznikov. 2022. "Hierarchical Organization of Bone in Three Dimensions: A Twist of Twists." *Journal of Structural Biology: X* 6: 1–10. https://doi.org/10.1016/j.yjsbx.2021.100057.

Büyük, N. İ., D. Aksu, and G. Torun Köse. 2023. "Effect of Different Pore Sizes of 3D Printed PLA-Based Scaffold in Bone Tissue Engineering." *International Journal of Polymeric Materials and Polymeric Biomaterials* 72, no. 13: 1021–1031. https://doi.org/10.1080/00914037.2022.2075869.

Cámara-Torres, M., P. Fucile, R. Sinha, C. Mota, and L. Moroni. 2023. "Boosting Bone Regeneration Using Augmented Melt-Extruded

Additive-Manufactured Scaffolds." *International Materials Reviews* 68, no. 7: 755–785. https://doi.org/10.1080/09506608.2022.2153219.

Camarero-Espinosa, S., and L. Moroni. 2021. "Janus 3D Printed Dynamic Scaffolds for Nanovibration-Driven Bone Regeneration." *Nature Communications* 12, no. 1: 1–12. https://doi.org/10.1038/s41467-021-21325-x.

Cao, M., G. Wang, H. He, et al. 2021. "Hemoglobin-Based Oxygen Carriers: Potential Applications in Solid Organ Preservation." *Frontiers in Pharmacology* 12: 1–21. https://doi.org/10.3389/fphar.2021.760215.

Cao, Y., L. Sun, Z. Liu, et al. 2023. "3D Printed-Electrospun PCL/Hydroxyapatite/MWCNTs Scaffolds for the Repair of Subchondral Bone." *Regenerative Biomaterials* 10: 1–12. https://doi.org/10.1093/rb/rbac104.

Carvalho, M. S., J. C. Silva, R. N. Udangawa, et al. 2019. "Co-Culture Cell-Derived Extracellular Matrix Loaded Electrospun Microfibrous Scaffolds for Bone Tissue Engineering." *Materials Science and Engineering C* 99: 479–490. https://doi.org/10.1016/j.msec.2019.01.127.

Celebioglu, A., and T. Uyar. 2011. "Electrospun porous cellulose acetate fibers from volatile solvent mixture." *Materials Letters* 65, no. 14: 2291–2294. https://doi.org/10.1016/j.matlet.2011.04.039.

Cengiz, I. F., J. M. Oliveira, and R. L. Reis. 2018. "Micro-CT—A Digital 3D Microstructural Voyage Into Scaffolds: A Systematic Review of the Reported Methods and Results." *Biomaterials Research* 22: 1–11. https://doi.org/10.1186/s40824-018-0136-8.

Cenni, E., F. Perut, and N. Baldini. 2011. "In Vitro Models for the Evaluation of Angiogenic Potential in Bone Engineering." *Acta Pharmacologica Sinica* 32, no. 1: 21–30. https://doi.org/10.1038/aps.2010.143.

Chen, C., B. T. Mehl, S. A. Sell, and R. Scott Martin. 2016. "Use of Electrospinning and Dynamic Air Focusing to Create Three-Dimensional Cell Culture Scaffolds in Microfluidic Devices." *Analyst* 141, no. 18: 5311–5320. https://doi.org/10.1039/c6an01282e.

Chen, S., X. Chen, Z. Geng, and J. Su. 2022. "The Horizon of Bone Organoid: A Perspective on Construction and Application." *Bioactive Materials* 18: 15–25. https://doi.org/10.1016/j.bioactmat.2022.01.048.

Chen, S., D. Galusková, H. Kaňková, et al. 2020. "Electrospun PCL Fiber Mats Incorporating Multi-Targeted B and Co Co-Doped Bioactive Glass Nanoparticles for Angiogenesis." *Materials* 13, no. 18: 1–15. https://doi.org/10.3390/ma13184010.

Chen, Y., X. Dong, M. Shafiq, G. Myles, N. Radacsi, and X. Mo. 2022. "Recent Advancements on Three-Dimensional Electrospun Nanofiber Scaffolds for Tissue Engineering." *Advanced Fiber Materials* 4, no. 5: 959–986. https://doi.org/10.1007/s42765-022-00170-7.

Chen, Y., Z. Yuan, W. Sun, et al. 2023. "Vascular Endothelial Growth Factor-Recruiting Nanofiber Bandages Promote Multifunctional Skin Regeneration via Improved Angiogenesis and Immunomodulation." *Advanced Fiber Materials* 5, no. 1: 327–348. https://doi.org/10.1007/s42765-022-00226-8.

Chen, Y. C., Y. S. Fu, S. W. Tsai, et al. 2022. "IL-1b in the Secretomes of MSCs Seeded on Human Decellularized Allogeneic Bone Promotes Angiogenesis." *International Journal of Molecular Sciences* 23, no. 23: 1–14. https://doi.org/10.3390/ijms232315301.

Chinnakorn, A., Y. Soi-Ngoen, O. Weeranantanapan, et al. 2024. "Fabrication of 3D Polycaprolactone Macrostructures by 3D Electrospinning." *American Chemical Society Biomaterials Science and Engineering*: 5336–5351. https://doi.org/10.1021/acsbiomaterials.4c00302.

Choong, L. T., P. Yi, and G. C. Rutledge. 2015. "Three-Dimensional Imaging of Electrospun Fiber Mats Using Confocal Laser Scanning Microscopy and Digital Image Analysis." *Journal of Materials Science* 50, no. 8: 3014–3030. https://doi.org/10.1007/s10853-015-8834-2.

Collins, M. N., G. Ren, K. Young, S. Pina, R. L. Reis, and J. M. Oliveira. 2021. "Scaffold Fabrication Technologies and Structure/Function Properties in Bone Tissue Engineering." *Advanced Functional Materials* 31, no. 21: 1–22. https://doi.org/10.1002/adfm.202010609.

Correia, C., W. L. Grayson, M. Park, et al. 2011. "In Vitro Model of Vascularized Bone: Synergizing Vascular Development and Osteogenesis." *PLoS One* 6, no. 12: 1–9. https://doi.org/10.1371/journal.pone.0028352.

Cortez Tornello, P. R., P. C. Caracciolo, T. R. Cuadrado, and G. A. Abraham. 2014. "Structural Characterization of Electrospun Micro/Nanofibrous Scaffolds by Liquid Extrusion Porosimetry: A Comparison With Other Techniques." *Materials Science and Engineering C* 41: 335–342. https://doi.org/10.1016/j.msec.2014.04.065.

Crouch, D. J., C. M. Sheridan, J. G. Behnsen, R. A. D'Sa, and L. A. Bosworth. 2023. "Cryo-Electrospinning Generates Highly Porous Fiber Scaffolds Which Improves Trabecular Meshwork Cell Infiltration." *Journal of Functional Biomaterials* 14, no. 10: 1–15. https://doi.org/10.3390/jfb14100490.

Cui, J., X. Yu, B. Yu, et al. 2022. "Coaxially Fabricated Dual-Drug Loading Electrospinning Fibrous Mat With Programmed Releasing Behavior to Boost Vascularized Bone Regeneration." *Advanced Healthcare Materials* 11, no. 16: 1–20. https://doi.org/10.1002/adhm.202200571.

Dalton, P. D., T. B. F. Woodfield, V. Mironov, and J. Groll. 2020. "Advances in Hybrid Fabrication Toward Hierarchical Tissue Constructs." *Advanced Science* 7, no. 11: 1–15. https://doi.org/10.1002/advs.201902953.

de Oliveira, N. K., E. P. Ferraz, F. C. P. Rosin, L. Correa, and M. C. Z. Deboni. 2022. "Poly-ε-Caprolactone/Poly(Rotaxane) Seeded With Human Dental Pulp Stem Cells or Osteoblasts Promotes Angiogenesis: A Chorioallantoic Membrane Assay." *Journal of Biomaterials Science. Polymer Edition* 33, no. 16: 2051–2066. https://doi.org/10.1080/09205063.2022.2091372.

Del Gaudio, C., S. Baiguera, M. Boieri, et al. 2013. "Induction of Angiogenesis Using VEGF Releasing Genipin-Crosslinked Electrospun Gelatin Mats." *Biomaterials* 34, no. 31: 7754–7765. https://doi.org/10.1016/j.biomaterials.2013.06.040.

Dhinasekaran, D., S. Vimalraj, A. R. Rajendran, S. Saravanan, B. Purushothaman, and B. Subramaniam. 2021. "Bio-Inspired Multifunctional Collagen/Electrospun Bioactive Glass Membranes for Bone Tissue Engineering Applications." *Materials Science and Engineering C* 126: 1–15. https://doi.org/10.1016/j.msec.2020.111856.

Dikici, S., F. Claeyssens, and S. MacNeil. 2020. "Bioengineering Vascular Networks to Study Angiogenesis and Vascularization of Physiologically Relevant Tissue Models In Vitro." *American Chemical Society Biomaterials Science and Engineering* 6, no. 6: 3513–3528. https://doi.org/10.1021/acsbiomaterials.0c00191.

Diomede, F., G. D. Marconi, L. Fonticoli, et al. 2020. "Functional Relationship Between Osteogenesis and Angiogenesis in Tissue Regeneration." *International Journal of Molecular Sciences* 21, no. 9: 1–14. https://doi.org/10.3390/ijms21093242.

Efraim, Y., B. Schoen, S. Zahran, et al. 2019. "3D Structure and Processing Methods Direct the Biological Attributes of ECM-Based Cardiac Scaffolds." *Scientific Reports* 9, no. 1: 1–13. https://doi.org/10.1038/s41598-019-41831-9.

Ejiohuo, O. 2023. "A Perspective on the Synergistic Use of 3D Printing and Electrospinning to Improve Nanomaterials for Biomedical Applications." *Nano Trends* 4: 100025. https://doi.org/10.1016/j.nwnano.2023.100025.

Fantin, A., J. M. Vieira, G. Gestri, et al. 2010. "Tissue Macrophages Act as Cellular Chaperones for Vascular Anastomosis Downstream of VEGF-Mediated Endothelial Tip Cell Induction." *Blood* 116, no. 5: 829–840. https://doi.org/10.1182/blood-2009-12-257832.

Fathona, I. W., and A. Yabuki. 2013. "One-Step Fabrication of Short Electrospun Fibers Using an Electric Spark." *Journal of Materials Processing Technology* 213, no. 11: 1894–1899. https://doi.org/10.1016/j.jmatprotec.2013.05.013.

Feltz, K. P., E. A. Growney Kalaf, C. Chen, R. S. Martin, and S. A. Sell. 2017. "A Review of Electrospinning Manipulation Techniques to Direct Fiber Deposition and Maximize Pore Size." *Electrospinning* 2, no. 1: 46–61. https://doi.org/10.1515/esp-2017-0002.

Fischer, N. G., and C. Aparicio. 2020. "On the Proliferation of Cell Proliferation Tests." In *Handbook of Biomaterials Biocompatibility*, 175–193. Amsterdam, Netherlands: Elsevier. https://doi.org/10.1016/B978-0-08-102967-1.00010-4.

Fleischer, S., D. N. Tavakol, and G. Vunjak-Novakovic. 2020. "From Arteries to Capillaries: Approaches to Engineering Human Vasculature." *Advanced Functional Materials* 30, no. 37: 1–23. https://doi.org/10.1002/adfm.201910811.

Fratzl, P., and R. Weinkamer. 2007. "Nature's Hierarchical Materials." *Progress in Materials Science* 52, no. 8: 1263–1334. https://doi.org/10.1016/j.pmatsci.2007.06.001.

Fridrikh, S. V., J. H. Yu, M. P. Brenner, and G. C. Rutledge. 2003. "Controlling the Fiber Diameter During Electrospinning." *Physical Review Letters* 90, no. 14: 4. https://doi.org/10.1103/PhysRevLett.90.144502.

Frontini-López, Y. R., L. Rivera, A. A. Aldana, et al. 2023. "Human Adipose Mesenchymal Stromal Cells Growing Into PCL-nHA Electrospun Scaffolds Undergo Hypoxia Adaptive Ultrastructural Changes." *Biotechnology Journal* 18, no. 4: 1–9. https://doi.org/10.1002/biot.202200413.

Fu, L., L. Zhang, X. Zhang, L. Chen, Q. Cai, and X. Yang. 2021. "Roles of Oxygen Level and Hypoxia-Inducible Factor Signaling Pathway in Cartilage, Bone and Osteochondral Tissue Engineering." *Biomedical Materials* 16, no. 2: 1–20. https://doi.org/10.1088/1748-605X/abdb73.

Gholipourmalekabadi, M., S. Zhao, B. S. Harrison, M. Mozafari, and A. M. Seifalian. 2016. "Oxygen-Generating Biomaterials: A New, Viable Paradigm for Tissue Engineering?" *Trends in Biotechnology* 34, no. 12: 1010–1021. https://doi.org/10.1016/j.tibtech.2016.05.012.

Ghorbani, F., T. Reiter, L. Liverani, D. W. Schubert, A. R. Boccaccini, and J. A. Roether. 2023. "Progress on Electrospun Composite Fibers Incorporating Bioactive Glass: An Overview." *Advanced Engineering Materials* 25, no. 6: 1–26. https://doi.org/10.1002/adem.202201103.

Gonzalez-Pujana, A., T. Carranza, E. Santos-Vizcaino, et al. 2022. "Hybrid 3D Printed and Electrospun Multi-Scale Hierarchical Polycaprolactone Scaffolds to Induce Bone Differentiation." *Pharmaceutics* 14, no. 12: 1–15. https://doi.org/10.3390/pharmaceutics14122843.

Goonoo, N. 2018. "Vascularization and Angiogenesis in Electrospun Tissue Engineered Constructs: Towards the Creation of Long-Term Functional Networks." *Biomedical Physics & Engineering Express* 4, no. 3: 1–14. https://doi.org/10.1088/2057-1976/aaab03.

Gritsch, L., L. Liverani, C. Lovell, and A. R. Boccaccini. 2020. "Polycaprolactone Electrospun Fiber Mats Prepared Using Benign Solvents: Blending With Copper(II)-chitosan Increases the Secretion of Vascular Endothelial Growth Factor in a Bone Marrow Stromal Cell Line." *Macromolecular Bioscience* 20, no. 3: 1–14. https://doi.org/10.1002/mabi.201900355.

Gugutkov, D., J. Gustavsson, M. Cantini, M. Salmeron-Sánchez, and G. Altankov. 2017. "Electrospun Fibrinogen-PLA Nanofibres for Vascular Tissue Engineering." *Journal of Tissue Engineering and Regenerative Medicine* 11, no. 10: 2774–2784. https://doi.org/10.1002/term.2172.

Gupta, H. S., U. Stachewicz, W. Wagermaier, P. Roschger, H. D. Wagner, and P. Fratzl. 2006. "Mechanical Modulation at the Lamellar Level in Osteonal Bone." *Journal of Materials Research* 21, no. 8: 1913–1921. https://doi.org/10.1557/jmr.2006.0234.

Hadjipanayi, E., and A. F. Schilling. 2013. "Hypoxia-Based Strategies for Angiogenic Induction: The Dawn of a New Era for Ischemia Therapy and Tissue Regeneration." *Organogenesis* 9, no. 4: 261–272. https://doi.org/10.4161/org.25970.

Hannah, S. S., S. McFadden, A. McNeilly, and C. McClean. 2021. "'Take My Bone Away?' Hypoxia and Bone: A Narrative Review." *Journal of Cellular Physiology* 236, no. 2: 721–740. https://doi.org/10.1002/jcp.29921.

Hashemi, J., G. Barati, S. E. Enderami, and M. Safdari. 2020. "Osteogenic Differentiation of Induced Pluripotent Stem Cells on Electrospun Nanofibers: A Review of Literature." *Materials Today Communications* 25: 1–9. https://doi.org/10.1016/j.mtcomm.2020.101561.

Hasmad, H. N., R. Bt Hj Idrus, N. Sulaiman, and Y. Lokanathan. 2022. "Electrospun Fiber-Coated Human Amniotic Membrane: A Potential Angioinductive Scaffold for Ischemic Tissue Repair." *International Journal of Molecular Sciences* 23, no. 3: 1–15. https://doi.org/10.3390/ijms23031743.

Haugen, H. J., and S. Bertoldi. 2017. "Characterization of Morphology-3D and Porous Structure." In *Characterization of Polymeric Biomaterials*, 21–53. Amsterdam, Netherlands: Elsevier. https://doi.org/10.1016/B978-0-08-100737-2.00002-9.

He, J., P. Xia, and D. Li. 2016. "Development of Melt Electrohydrodynamic 3D Printing for Complex Microscale Poly (ε-Caprolactone) Scaffolds." *Biofabrication* 8, no. 3: 1–11. https://doi.org/10.1088/1758-5090/8/3/035008.

He, S., J. Fang, C. Zhong, M. Wang, and F. Ren. 2022. "Spatiotemporal Delivery of pBMP2 and pVEGF by a Core–Sheath Structured Fiber-Hydrogel Gene-Activated Matrix Loaded With Peptide-Modified Nanoparticles for Critical-Sized Bone Defect Repair." *Advanced Healthcare Materials* 11, no. 21: 1–11. https://doi.org/10.1002/adhm.202201096.

He, W., C. Li, S. Zhao, et al. 2024. "Integrating Coaxial Electrospinning and 3D Printing Technologies for the Development of Biphasic Porous Scaffolds Enabling Spatiotemporal Control in Tumor Ablation and Osteochondral Regeneration." *Bioactive Materials* 34: 338–353. https://doi.org/10.1016/j.bioactmat.2023.12.020.

Hodge, J., and C. Quint. 2019. "The Improvement of Cell Infiltration in an Electrospun Scaffold With Multiple Synthetic Biodegradable Polymers Using Sacrificial PEO Microparticles." *Journal of Biomedical Materials Research. Part A* 107, no. 9: 1954–1964. https://doi.org/10.1002/jbm.a.36706.

Hodge, J. G., and C. Quint. 2022. "Improved Porosity of Electrospun Poly (Lactic-co-Glycolic) Scaffolds by Sacrificial Microparticles Enhances Cellular Infiltration Compared to Sacrificial Microfiber." *Journal of Biomaterials Applications* 37, no. 1: 77–88. https://doi.org/10.1177/08853282221075890.

Hofer, M., and M. P. Lutolf. 2021. "Engineering organoids." *Nature Reviews Materials* 6, no. 5: 402–420. https://doi.org/10.1038/s41578-021-00279-y.

Homan, K. A., N. Gupta, K. T. Kroll, et al. 2019. "Flow-Enhanced Vascularization and Maturation of Kidney Organoids In Vitro." *Nature Methods* 16, no. 3: 255–262. https://doi.org/10.1038/s41592-019-0325-y.

Hosseini, F. S., A. A. Abedini, F. Chen, T. Whitfield, C. C. Ude, and C. T. Laurencin. 2023. "Oxygen-Generating Biomaterials for Translational Bone Regenerative Engineering." *American Chemical Society Applied Materials & Interfaces* 15, no. 44: 50721–50741. https://doi.org/10.1021/acsami.2c20715.

Hrynevich, A., B. Elçi, J. N. Haigh, et al. 2018. "Dimension-Based Design of Melt Electrowritten Scaffolds." *Small* 14, no. 22: 1–6. https://doi.org/10.1002/smll.201800232.

Hsu, T. W., Y. J. Lu, Y. J. Lin, et al. 2021. "Transplantation of 3D MSC/HUVEC Spheroids With Neuroprotective and Proangiogenic Potentials Ameliorates Ischemic Stroke Brain Injury." *Biomaterials* 272: 1–12. https://doi.org/10.1016/j.biomaterials.2021.120765.

Huang, J., L. Zhang, A. Lu, and C. Liang. 2023. "Organoids as Innovative Models for Bone and Joint Diseases." *Cells* 12, no. 12: 1–22. https://doi.org/10.3390/cells12121590.

Huang, Y., M. Zhan, M. Shen, L. Zhang, and X. Shi. 2023. "Electrospun Short Fibers: A New Platform for Cancer Nanomedicine Applications." *Exploration of Drug Science* 1: 454–467. https://doi.org/10.37349/eds.2023.00030.

Jiang, J., S. Chen, H. Wang, M. A. Carlson, A. F. Gombart, and J. Xie. 2018. "CO_2-Expanded Nanofiber Scaffolds Maintain Activity of Encapsulated Bioactive Materials and Promote Cellular Infiltration and Positive Host Response." *Acta Biomaterialia* 68: 237–248. https://doi.org/10.1016/j.actbio.2017.12.018.

Jiménez-Beltrán, M. A., A. J. Gómez-Calderón, R. E. Quintanar-Zúñiga, et al. 2022. "Electrospinning-Generated Nanofiber Scaffolds Suitable for Integration of Primary Human Circulating Endothelial Progenitor Cells." *Polymers* 14, no. 12: 1–13. https://doi.org/10.3390/polym14122448.

Joddar, B., S. L. Natividad-Diaz, A. E. Padilla, et al. 2022. "Engineering Approaches for Cardiac Organoid Formation and Their Characterization." *Translational Research* 250: 46–67. https://doi.org/10.1016/j.trsl.2022.08.009.

Kamaraj, M., N. Moghimi, J. Chen, et al. 2023. "New Dimensions of Electrospun Nanofiber Material Designs for Biotechnological Uses." *Trends in Biotechnology*: 631–647. https://doi.org/10.1016/j.tibtech.2023.11.008.

Kang, L., W. Jia, M. Li, et al. 2019. "Hyaluronic Acid Oligosaccharide-Modified Collagen Nanofibers as Vascular Tissue-Engineered Scaffold for Promoting Endothelial Cell Proliferation." *Carbohydrate Polymers* 223, no. 115106: 1–14. https://doi.org/10.1016/j.carbpol.2019.115106.

Kang, L., T. Osire, L. Gorbacheva, and A. Arkhipova. 2024. "Fibroin-Based Porous Scaffolds for Bone Tissue Regeneration." *Microscopy and Microanalysis* 30, no. Suppl. 1: 868–870. https://doi.org/10.1093/mam/ozae044.425.

Kaniuk, Ł., A. Podborska, and U. Stachewicz. 2022. "Enhanced Mechanical Performance and Wettability of PHBV Fiber Blends With Evening Primrose Oil for Skin Patches Improving Hydration and Comfort." *Journal of Materials Chemistry B* 10, no. 11: 1763–1774. https://doi.org/10.1039/d1tb02805g.

Karbowniczek, J. E., K. Berniak, J. Knapczyk-Korczak, et al. 2023. "Strategies of Nanoparticles Integration in Polymer Fibers to Achieve Antibacterial Effect and Enhance Cell Proliferation With Collagen Production in Tissue Engineering Scaffolds." *Journal of Colloid and Interface Science* 650: 1371–1381. https://doi.org/10.1016/j.jcis.2023.07.066.

Karbowniczek, J. E., Ł. Kaniuk, K. Berniak, A. Gruszczyński, and U. Stachewicz. 2021. "Enhanced Cells Anchoring to Electrospun Hybrid Scaffolds With PHBV and HA Particles for Bone Tissue Regeneration." *Frontiers in Bioengineering and Biotechnology* 9: 1–13. https://doi.org/10.3389/fbioe.2021.632029.

Karbowniczek, J. E., D. P. Ura, and U. Stachewicz. 2022. "Nanoparticles Distribution and Agglomeration Analysis in Electrospun Fiber Based Composites for Desired Mechanical Performance of Poly(3-Hydroxybuty-Rate-co-3-Hydroxyvalerate) (PHBV) Scaffolds with Hydroxyapatite (HA) and Titanium Dioxide (TiO_2) Towards Medical Applications." *Composites Part B: Engineering* 241: 110011. https://doi.org/10.1016/j.compositesb.2022.110011.

Khajavi, R., M. Abbasipour, and A. Bahador. 2016. "Electrospun Biodegradable Nanofibers Scaffolds for Bone Tissue Engineering." *Journal of Applied Polymer Science* 133, no. 3: 1–19. https://doi.org/10.1002/app.42883.

Khorshidi, S., A. Solouk, H. Mirzadeh, et al. 2016. "A Review of Key Challenges of Electrospun Scaffolds for Tissue-Engineering Applications." *Journal of Tissue Engineering and Regenerative Medicine* 10, no. 9: 715–738. https://doi.org/10.1002/term.1978.

Kiessling, F., D. Razansky, and F. Alves. 2010. "Anatomical and Microstructural Imaging of Angiogenesis." *European Journal of Nuclear Medicine and Molecular Imaging* 37, no. Suppl. 1: S4–S19. https://doi.org/10.1007/s00259-010-1450-0.

Kim, D., J. Youn, J. Lee, H. Kim, and D. S. Kim. 2023. "Recent Progress in Fabrication of Electrospun Nanofiber Membranes for Developing Physiological In Vitro Organ/Tissue Models." *Macromolecular Bioscience* 23, no. 12: 1–25. https://doi.org/10.1002/mabi.202300244.

Kim, J., M. Chung, S. Kim, D. H. Jo, J. H. Kim, and N. L. Jeon. 2015. "Engineering of a Biomimetic Pericyte-Covered 3D Microvascular Network." *PLoS One* 10, no. 7: 1–15. https://doi.org/10.1371/journal.pone.0133880.

Klumpp, D., M. Rudisile, R. I. Kühnle, et al. 2012. "Three-Dimensional Vascularization of Electrospun PCL/Collagen-Blend Nanofibrous Scaffolds In Vivo." *Journal of Biomedical Materials Research.Part A* 100, no. 9: 2302–2311. https://doi.org/10.1002/jbm.a.34172.

Knapczyk-Korczak, J., J. Zhu, D. P. Ura, et al. 2021. "Enhanced Water Harvesting System and Mechanical Performance From Janus Fibers With Polystyrene and Cellulose Acetate." *American Chemical Society Sustainable Chemistry and Engineering* 9, no. 1: 180–188. https://doi.org/10.1021/acssuschemeng.0c06480.

Kontogianni, G. I., A. F. Bonatti, C. De Maria, et al. 2024. "Cell Instructive Behavior of Composite Scaffolds in a Co-Culture of Human Mesenchymal Stem Cells and Peripheral Blood Mononuclear Cells." *Journal of Functional Biomaterials* 15, no. 5: 1–21. https://doi.org/10.3390/jfb15050116.

Kontogianni, G. I., K. Loukelis, A. F. Bonatti, et al. 2023. "Effect of Uniaxial Compression Frequency on Osteogenic Cell Responses in Dynamic 3D Cultures." *Bioengineering* 10, no. 5: 1–16. https://doi.org/10.3390/bioengineering10050532.

Koohzad, F., and A. Asoodeh. 2024. "Development of a Highly Porous Bioscaffold by the Combination of Bubble Entrapping and Freezing-Thawing Techniques to Fabricate Hyaluronic Acid/Gelatin Tri-Layer Wound Dressing." *International Journal of Biological Macromolecules* 260: 1–11. https://doi.org/10.1016/j.ijbiomac.2024.129206.

Kook, M. G., S. E. Lee, N. Shin, et al. 2022. "Generation of Cortical Brain Organoid With Vascularization by Assembling With Vascular Spheroid." *International Journal of Stem Cells* 15, no. 1: 85–94. https://doi.org/10.15283/IJSC21157.

Kosyakova, N., D. D. Kao, M. Figetakis, et al. 2020. "Differential Functional Roles of Fibroblasts and Pericytes in the Formation of Tissue-Engineered Microvascular Networks In Vitro." *npj Regenerative Medicine* 5, no. 1: 1–12. https://doi.org/10.1038/s41536-019-0086-3.

Krock, B. L., N. Skuli, and M. C. Simon. 2011. "Hypoxia-Induced Angiogenesis: Good and Evil." *Genes & Cancer* 2, no. 12: 1117–1133. https://doi.org/10.1177/1947601911423654.

Krysiak, Z. J., and U. Stachewicz. 2022. "Urea-Based Patches With Controlled Release for Potential Atopic Dermatitis Treatment." *Pharmaceutics* 14, no. 7: 1494. https://doi.org/10.3390/pharmaceutics14071494.

Krysiak, Z. J., and U. Stachewicz. 2023. "Electrospun Fibers as Carriers for Topical Drug Delivery and Release in Skin Bandages and Patches for Atopic Dermatitis Treatment." *Wiley Interdisciplinary Reviews: Nanomedicine and Nanobiotechnology* 15, no. 1: 1–35. https://doi.org/10.1002/wnan.1829.

Lai, G. J., K. T. Shalumon, S. H. Chen, and J. P. Chen. 2014. "Composite Chitosan/Silk Fibroin Nanofibers for Modulation of Osteogenic Differentiation and Proliferation of Human Mesenchymal Stem Cells." *Carbohydrate Polymers* 111: 288–297. https://doi.org/10.1016/j.carbpol.2014.04.094.

Lapenna, A., M. De Palma, and C. E. Lewis. 2018. "Perivascular Macrophages in Health and Disease." *Nature Reviews Immunology* 18, no. 11: 689–702. https://doi.org/10.1038/s41577-018-0056-9.

Laschke, M. W., M. Rücker, G. Jensen, et al. 2008. "Incorporation of Growth Factor Containing Matrigel Promotes Vascularization of Porous PLGA Scaffolds." *Journal of Biomedical Materials Research. Part A* 85, no. 2: 397–407. https://doi.org/10.1002/jbm.a.31503.

Lavielle, N., A. Hébraud, G. Schlatter, L. Thöny-Meyer, R. M. Rossi, and A. M. Popa. 2013. "Simultaneous Electrospinning and Electrospraying: A Straightforward Approach for Fabricating Hierarchically Structured Composite Membranes." *American Chemical Society Applied Materials & Interfaces* 5, no. 20: 10090–10097. https://doi.org/10.1021/am402676m.

Lee, J. H., Y. S. Han, and S. H. Lee. 2016. "Long-Duration Three-Dimensional Spheroid Culture Promotes Angiogenic Activities of Adipose-Derived Mesenchymal Stem Cells." *Biomolecules & Therapeutics* 24, no. 3: 260–267. https://doi.org/10.4062/biomolther.2015.146.

Lefèvre, E., D. Farlay, Y. Bala, et al. 2019. "Compositional and Mechanical Properties of Growing Cortical Bone Tissue: A Study of the Human Fibula." *Scientific Reports* 9, no. 1: 1–16. https://doi.org/10.1038/s41598-019-54016-1.

Leong, M. F., M. Z. Rasheed, T. C. Lim, and K. S. Chian. 2009. "In Vitro Cell Infiltration and In Vivo Cell Infiltration and Vascularization in a Fibrous, Highly Porous Poly(d,l-Lactide) Scaffold Fabricated by Cryogenic Electrospinning Technique." *Journal of Biomedical Materials Research. Part A* 91, no. 1: 231–240. https://doi.org/10.1002/jbm.a.32208.

Li, C., Y. Zhang, Y. Du, et al. 2023. "A Review of Advanced Biomaterials and Cells for the Production of Bone Organoid." *Small Science* 3, no. 8: 1–23. https://doi.org/10.1002/smsc.202300027.

Li, M., M. J. Mondrinos, M. R. Gandhi, F. K. Ko, A. S. Weiss, and P. I. Lelkes. 2005. "Electrospun Protein Fibers as Matrices for Tissue Engineering." *Biomaterials* 26, no. 30: 5999–6008. https://doi.org/10.1016/j.biomaterials.2005.03.030.

Li, X., Z. Li, L. Wang, et al. 2016. "Low-Voltage Continuous Electrospinning Patterning." *American Chemical Society Applied Materials & Interfaces* 8, no. 47: 32120–32131. https://doi.org/10.1021/acsami.6b07797.

Li, Y., J. Zhu, H. Cheng, et al. 2021. "Developments of Advanced Electrospinning Techniques: A Critical Review." *Advanced Materials Technologies* 6, no. 11: 1–29. https://doi.org/10.1002/admt.202100410.

Liashenko, I., A. Ramon, J. Rosell-Llompart, and A. Cabot. 2022. "Patterning With Aligned Electrospun Nanofibers by Electrostatic Deflection of Fast Jets." *Advanced Engineering Materials* 24, no. 9: 1–8. https://doi.org/10.1002/adem.202101804.

Liashenko, I., J. Rosell-Llompart, and A. Cabot. 2020. "Ultrafast 3D Printing With Submicrometer Features Using Electrostatic Jet Deflection." *Nature Communications* 11, no. 1: 1–9. https://doi.org/10.1038/s41467-020-14557-w.

Liekens, S., E. De Clercq, and J. Neyts. 2001. "Angiogenesis: Regulators and Clinical Applications." *Biochemical Pharmacology* 61, no. 3: 253–270.

Lin, R. Z., and J. M. Melero-Martin. 2012. "Fibroblast Growth Factor-2 Facilitates Rapid Anastomosis Formation Between Bioengineered Human Vascular Networks and Living Vasculature." *Methods* 56, no. 3: 440–451. https://doi.org/10.1016/j.ymeth.2012.01.006.

Liu, E., M. D. Treiser, P. A. Johnson, et al. 2007. "Quantitative Biorelevant Profiling of Material Microstructure Within 3D Porous Scaffolds via Multiphoton Fluorescence Microscopy." *Journal of Biomedical Materials Research Part B: Applied Biomaterials* 82, no. 2: 284–297. https://doi.org/10.1002/jbm.b.30732.

Liu, H., X. Zhang, J. Liu, and J. Qin. 2023. "Vascularization of Engineered Organoids." *BMEMat* 1, no. 3: 1–22. https://doi.org/10.1002/bmm2.12031.

Liu, H., W. Wen, S. Chen, C. Zhou, and B. Luo. 2018. "Preparation of Icariin and Deferoxamine Functionalized Poly(l-lactide)/Chitosan Micro/Nanofibrous Membranes with Synergistic Enhanced Osteogenesis and Angiogenesis." *ACS Applied Bio Materials* 1, no. 2: 389–402. https://doi.org/10.1021/acsabm.8b00129.

Liu, Y., X. Chen, X. Lin, et al. 2024. "Electrospun Multi-Chamber Core–Shell Nanofibers and Their Controlled Release Behaviors: A Review." *WIREs Nanomedicine and Nanobiotechnology* 16, no. 2: e1954. https://doi.org/10.1002/wnan.1954.

Liu, X., Y. Yang, D. G. Yu, M. J. Zhu, M. Zhao, and G. R. Williams. 2019. "Tunable Zero-Order Drug Delivery Systems Created by Modified Triaxial Electrospinning." *Chemical Engineering Journal* 356: 886–894. https://doi.org/10.1016/j.cej.2018.09.096.

Loh, Q. L., and C. Choong. 2013. "Three-Dimensional Scaffolds for Tissue Engineering Applications: Role of Porosity and Pore Size." *Tissue Engineering. Part B: Reviews* 19, no. 6: 485–502. https://doi.org/10.1089/ten.teb.2012.0437.

Lowen, J. M., and J. K. Leach. 2020. "Functionally Graded Biomaterials for Use as Model Systems and Replacement Tissues." *Advanced Functional Materials* 30, no. 44: 1–16. https://doi.org/10.1002/adfm.201909089.

Maes, C., G. Carmeliet, and E. Schipani. 2012. "Hypoxia-Driven Pathways in Bone Development, Regeneration and Disease." *Nature Reviews Rheumatology* 8: 358–366. https://doi.org/10.1038/nrrheum.2012.36.

Mapanao, A. K., and V. Voliani. 2020. "Three-Dimensional Tumor Models: Promoting Breakthroughs in Nanotheranostics Translational Research." *Applied Materials Today* 19: 1–21. https://doi.org/10.1016/j.apmt.2019.100552.

Marquez, A. L., I. E. Gareis, F. J. Dias, C. Gerhard, and M. F. Lezcano. 2022. "Methods to Characterize Electrospun Scaffold Morphology: A Critical Review." *Polymers* 14, no. 3: 1–22. https://doi.org/10.3390/polym14030467.

Martine, L. C., B. M. Holzapfel, J. A. McGovern, et al. 2017. "Engineering a Humanized Bone Organ Model in Mice to Study Bone Metastases." *Nature Protocols* 12, no. 4: 639–663. https://doi.org/10.1038/nprot.2017.002.

Mastrullo, V., W. Cathery, E. Velliou, P. Madeddu, and P. Campagnolo. 2020. "Angiogenesis in Tissue Engineering: As Nature Intended?" *Frontiers in Bioengineering and Biotechnology* 8: 1–13. https://doi.org/10.3389/fbioe.2020.00188.

Mayoral, I., E. Bevilacqua, G. Gómez, et al. 2022. "Tissue Engineered In-Vitro Vascular Patch Fabrication Using Hybrid 3D Printing and Electrospinning." *Materials Today Bio* 14: 1–12. https://doi.org/10.1016/j.mtbio.2022.100252.

McClure, M. J., P. S. Wolfe, D. G. Simpson, S. A. Sell, and G. L. Bowlin. 2012. "The Use of Air-Flow Impedance to Control Fiber Deposition Patterns During Electrospinning." *Biomaterials* 33, no. 3: 771–779. https://doi.org/10.1016/j.biomaterials.2011.10.011.

Metwally, S., J. E. Karbowniczek, P. K. Szewczyk, et al. 2019. "Single-Step Approach to Tailor Surface Chemistry and Potential on Electrospun PCL Fibers for Tissue Engineering Application." *Advanced Materials Interfaces* 6, no. 2: 1–12. https://doi.org/10.1002/admi.201801211.

Metwally, S., and U. Stachewicz. 2019. "Surface Potential and Charges Impact on Cell Responses on Biomaterials Interfaces for Medical Applications." *Materials Science and Engineering C* 104: 1–27. https://doi.org/10.1016/j.msec.2019.109883.

Metwally, S., and U. Stachewicz. 2020. "Teeth Resorption at Cement—Enamel Junction (CEJ)—Microscopy Analysis." *Micron* 137: 1–6. https://doi.org/10.1016/j.micron.2020.102913.

Metwally, S., D. P. Ura, Z. J. Krysiak, Ł. Kaniuk, P. K. Szewczyk, and U. Stachewicz. 2021. "Electrospun PCL Patches With Controlled Fiber Morphology and Mechanical Performance for Skin Moisturization via Long-Term Release of Hemp Oil for Atopic Dermatitis." *Membranes* 11, no. 1: 1–13. https://doi.org/10.3390/membranes11010026.

Middleton, R., X. Li, J. Shepherd, et al. 2018. "Near-Field Electrospinning Patterning Polycaprolactone and Polycaprolactone/Collagen Interconnected Fiber Membrane." *Macromolecular Materials and Engineering* 303, no. 2: 1–6. https://doi.org/10.1002/mame.201700463.

Mukherjee, S., S. Darzi, K. Paul, F. L. Cousins, J. A. Werkmeister, and C. E. Gargett. 2020. "Electrospun Nanofiber Meshes With Endometrial MSCs Modulate Foreign Body Response by Increased Angiogenesis, Matrix Synthesis, and Anti-Inflammatory Gene Expression in Mice: Implication in Pelvic Floor." *Frontiers in Pharmacology* 11, no. 353: 1–18. https://doi.org/10.3389/fphar.2020.00353.

Muerza-Cascante, M. L., D. Haylock, D. W. Hutmacher, and P. D. Dalton. 2015. "Melt Electrospinning and Its Technologization in Tissue Engineering." *Tissue Engineering. Part B: Reviews* 21, no. 2: 187–202. https://doi.org/10.1089/ten.teb.2014.0347.

Näf, L., I. Miescher, L. Pfuderer, et al. 2024. "Pro-Angiogenic and Antibacterial Copper Containing Nanoparticles in PLGA/Amorphous Calcium Phosphate Bone Nanocomposites." *Heliyon* 10, no. 5: 1–15. https://doi.org/10.1016/j.heliyon.2024.e27267.

Nazarnezhad, S., F. Baino, H. W. Kim, T. J. Webster, and S. Kargozar. 2020. "Electrospun Nanofibers for Improved Angiogenesis: Promises for Tissue Engineering Applications." *Nanomaterials* 10, no. 8: 1–35. https://doi.org/10.3390/nano10081609.

Nazemi, M. M., A. Khodabandeh, and A. Hadjizadeh. 2022. "Near-Field Electrospinning: Crucial Parameters, Challenges, and Applications." *American Chemical Society Applied Bio Materials* 5, no. 2: 394–412. https://doi.org/10.1021/acsabm.1c00944.

Neal, R. A., S. G. Mcclugage, M. C. Link, L. S. Sefcik, R. C. Ogle, and E. A. Botchwey. 2009. "Laminin Nanofiber Meshes That Mimic Morphological Properties and Bioactivity of Basement Membranes." *Tissue Engineering. Part C, Methods* 15, no. 1: 11–21.

Niemczyk-Soczynska, B., D. Kolbuk, G. Mikulowski, I. A. Ciechomska, and P. Sajkiewicz. 2023. "Methylcellulose/Agarose Hydrogel Loaded With Short Electrospun PLLA/Laminin Fibers as an Injectable Scaffold for Tissue Engineering/3D Cell Culture Model for Tumour Therapies." *Royal Society of Chemistry Advances* 13, no. 18: 11889–11902. https://doi.org/10.1039/d3ra00851g.

Ning, X., N. Liu, T. Sun, et al. 2023. "Promotion of Adipose Stem Cell Transplantation Using GelMA Hydrogel Reinforced by PLCL/ADM Short Nanofibers." *Biomedical Materials* 18, no. 6: 1–15. https://doi.org/10.1088/1748-605X/acf551.

Oliinyk, D., A. Eigenberger, O. Felthaus, S. Haerteis, and L. Prantl. 2023. "Chorioallantoic Membrane Assay at the Cross-Roads of Adipose-Tissue-Derived Stem Cell Research." *Cells* 12, no. 4: 1–23. https://doi.org/10.3390/cells12040592.

Palomares, D., K. R. Ammann, J. J. Saldana Perez, et al. 2021. "Patterned Electrospinning: A Method of Generating Defined Fibrous Constructs Influencing Cell Adhesion and Retention." *American Chemical Society Applied Bio Materials* 4, no. 5: 4084–4093. https://doi.org/10.1021/acsabm.0c01311.

Pamu, D., K. K. Garikapati, G. Kuppusamy, et al. 2024. "Electrospun Statin-Loaded Nanofibers for Treating Diabetic Wounds." *Polymer Engineering and Science* 64: 1715–1730. https://doi.org/10.1002/pen.26639.

Park, S., W. Shou, L. Makatura, W. Matusik, and K. Fu. 2022. "3D Printing of Polymer Composites: Materials, Processes, and Applications." *Matter* 5, no. 1: 43–76. https://doi.org/10.1016/j.matt.2021.10.018.

Park, S. M., K. P. Lee, M. I. Huh, et al. 2019. "Development of an In Vitro 3D Choroidal Neovascularization Model Using Chemically Induced Hypoxia Through an Ultra-Thin, Free-Standing Nanofiber Membrane." *Materials Science & Engineering. C, Materials for Biological Applications* 104, no. 109964: 1–11. https://doi.org/10.1016/j.msec.2019.109964.

Park, Y., E. Cheong, J.-G. Kwak, R. Carpenter, J.-H. Shim, and J. Lee. 2021. "Trabecular bone organoid model for studying the regulation of localized bone remodeling." *Applied Sciences and Engineering* 7, no. 4: eabd6495.

Park, Y. S., J. Kim, J. M. Oh, et al. 2020. "Near-Field Electrospinning for Three-Dimensional Stacked Nanoarchitectures With High Aspect Ratios." *Nano Letters* 20, no. 1: 441–448. https://doi.org/10.1021/acs.nanolett.9b04162.

Passaniti, A., H. K. Kleinman, and G. R. Martin. 2022. "Matrigel: History/Background, Uses, and Future Applications." *Journal of Cell Communication and Signaling* 16, no. 4: 621–626. https://doi.org/10.1007/s12079-021-00643-1.

Patole, V., P. Bhosale, G. Ingavle, et al. 2024. "In Vitro and In Vivo Assessment of Gallic Acid-Chitosan/Polycaprolactone Conjugate Electrospun Nanofibers for Wound Healing." *Journal of Drug Delivery Science and Technology* 95: 105569. https://doi.org/10.1016/j.jddst.2024.105569.

Pesaran Afsharian, Y., M. Rahimnejad, S. Mahmood Rabiee, and F. Feizi. 2023. "Osteogenic and Osseointegration Responses of Electrospun-Based Composites in the Light of the Bone Regeneration Problems." *Composite Structures* 321: 1–21. https://doi.org/10.1016/j.compstruct.2023.117236.

Pitaktong, I., C. Lui, J. Lowenthal, et al. 2020. "Early Vascular Cells Improve Microvascularization Within 3D Cardiac Spheroids." *Tissue Engineering. Part C: Methods* 26, no. 2: 80–90. https://doi.org/10.1089/ten.tec.2019.0228.

Podgórski, R., M. Wojasiński, A. Małolepszy, J. Jaroszewicz, and T. Ciach. 2024. "Fabrication of 3D-Printed Scaffolds With Multiscale Porosity." *American Chemical Society Omega* 9, no. 27: 29186–29204. https://doi.org/10.1021/acsomega.3c09035.

Polak, M., K. Berniak, P. K. Szewczyk, J. E. Karbowniczek, M. M. Marzec, and U. Stachewicz. 2023. "PLLA Scaffolds With Controlled Surface Potential and Piezoelectricity for Enhancing Cell Adhesion in Tissue Engineering." *Applied Surface Science* 621: 1–11. https://doi.org/10.1016/j.apsusc.2023.156835.

Polak, M., D. P. Ura, K. Berniak, P. K. Szewczyk, M. M. Marzec, and U. Stachewicz. 2024. "Interfacial Blending in Co-Axially Electrospun Polymer Core-Shell Fibers and Their Interaction With Cells via Focal Adhesion Point Analysis." *Colloids and Surfaces B: Biointerfaces* 237: 113864. https://doi.org/10.1016/j.colsurfb.2024.113864.

Poling, H. M., A. Singh, M. Krutko, et al. 2024. "Promoting Human Intestinal Organoid Formation and Stimulation Using Piezoelectric Nanofiber Matrices." *bioRxiv*: 1–31. https://doi.org/10.1101/2024.06.12.598673.

Potier, E., E. Ferreira, R. Andriamanalijaona, et al. 2007. "Hypoxia Affects Mesenchymal Stromal Cell Osteogenic Differentiation and Angiogenic Factor Expression." *Bone* 40, no. 4: 1078–1087. https://doi.org/10.1016/j.bone.2006.11.024.

Preethi Soundarya, S., A. Haritha Menon, S. Viji Chandran, and N. Selvamurugan. 2018. "Bone Tissue Engineering: Scaffold Preparation Using Chitosan and Other Biomaterials With Different Design and Fabrication Techniques." *International Journal of Biological Macromolecules* 119: 1228–1239. https://doi.org/10.1016/j.ijbiomac.2018.08.056.

Putti, M., M. Simonet, R. Solberg, and G. W. M. Peters. 2015. "Electrospinning Poly(ε-Caprolactone) Under Controlled Environmental Conditions: Influence on Fiber Morphology and Orientation." *Polymer* 63: 189–195. https://doi.org/10.1016/j.polymer.2015.03.006.

Qian, C., T. Xin, W. Xiao, et al. 2020. "Vascularized Silk Electrospun Fiber for Promoting Oral Mucosa Regeneration." *NPG Asia Materials* 12, no. 1: 1–16. https://doi.org/10.1038/s41427-020-0221-z.

Qian, S., J. Wang, Z. Liu, et al. 2022. "Secretory Fluid-Aggregated Janus Electrospun Short Fiber Scaffold for Wound Healing." *Small* 18, no. 36: 1–12. https://doi.org/10.1002/smll.202200799.

Rafique, M., T. Wei, Q. Sun, et al. 2021. "The Effect of Hypoxia-Mimicking Responses on Improving the Regeneration of Artificial Vascular Grafts." *Biomaterials* 271: 1–16. https://doi.org/10.1016/j.biomaterials.2021.120746.

Rahmani, A., S. Hashemi-Najafabadi, M. B. Eslaminejad, F. Bagheri, and F. A. Sayahpour. 2019. "The Effect of Modified Electrospun PCL-nHA-nZnO Scaffolds on Osteogenesis and Angiogenesis." *Journal of Biomedical Materials Research. Part A* 107, no. 9: 2040–2052. https://doi.org/10.1002/jbm.a.36717.

Raja, C. R., M. Sawawi, S. K. Sahari, M. Andrew, and C. S. Fun. 2023. "A Review on Electrospun Short Fiber Production." *International Journal of Integrated Engineering* 15, no. 5: 28–34. https://doi.org/10.30880/ijie.2023.15.05.004.

Rajzer, I., A. Kurowska, A. Jabłoński, et al. 2018. "Layered Gelatin/PLLA Scaffolds Fabricated by Electrospinning and 3D Printing- For Nasal Cartilages and Subchondral Bone Reconstruction." *Materials and Design* 155: 297–306. https://doi.org/10.1016/j.matdes.2018.06.012.

Rambøl, M. H., E. Han, and L. E. Niklason. 2020. "Microvessel Network Formation and Interactions With Pancreatic Islets in Three-Dimensional Chip Cultures." *Tissue Engineering. Part A* 26, no. 9–10: 556–568. https://doi.org/10.1089/ten.tea.2019.0186.

Ribot, E. J., C. Tournier, R. Aid-Launais, et al. 2017. "3D Anatomical and Perfusion MRI for Longitudinal Evaluation of Biomaterials for Bone Regeneration of Femoral Bone Defect in Rats." *Scientific Reports* 7, no. 1: 1–11. https://doi.org/10.1038/s41598-017-06258-0.

Ritzau-Reid, K. I., S. J. P. Callens, R. Xie, et al. 2023. "Microfibrous Scaffolds Guide Stem Cell Lumenogenesis and Brain Organoid Engineering." *Advanced Materials* 35, no. 41: 1–14. https://doi.org/10.1002/adma.202300305.

Rnjak-Kovacina, J., and A. S. Weiss. 2011. "Increasing the Pore Size of Electrospun Scaffolds." *Tissue Engineering. Part B: Reviews* 17, no. 5: 365–372. https://doi.org/10.1089/ten.teb.2011.0235.

Rohde, F., K. Danz, N. Jung, S. Wagner, and M. Windbergs. 2022. "Electrospun Scaffolds as Cell Culture Substrates for the Cultivation of an In Vitro Blood–Brain Barrier Model Using Human Induced Pluripotent Stem Cells." *Pharmaceutics* 14, no. 6: 1–22. https://doi.org/10.3390/pharmaceutics14061308.

Rosell-Llompart, J., J. Grifoll, and I. G. Loscertales. 2018. "Electrosprays in the Cone-Jet Mode: From Taylor Cone Formation to Spray Development." *Journal of Aerosol Science* 125: 2–31. https://doi.org/10.1016/j.jaerosci.2018.04.008.

Rubenstein, D. A., V. K. Greene, and W. Yin. 2020. "Electrospun Scaffold Fiber Orientation Regulates Endothelial Cell and Platelet Properties Associated With Angiogenesis and Hemocompatibility." *Materialia* 14: 1–9. https://doi.org/10.1016/j.mtla.2020.100942.

Rutledge, G. C., and S. V. Fridrikh. 2007. "Formation of Fibers by Electrospinning." *Advanced Drug Delivery Reviews* 59, no. 14: 1384–1391. https://doi.org/10.1016/j.addr.2007.04.020.

Saberianpour, S., M. Heidarzadeh, M. H. Geranmayeh, H. Hosseinkhani, R. Rahbarghazi, and M. Nouri. 2018. "Tissue Engineering Strategies for the Induction of Angiogenesis Using Biomaterials." *Journal of Biological Engineering* 12, no. 1: 1–15. https://doi.org/10.1186/s13036-018-0133-4.

Safari, Z., S. S. Aghili, S. Hassantash, et al. 2024. "Recent Approaches to Enhance Osteogenesis of Dental Pulp Stem Cells on Electrospun Scaffolds." *Current Stem Cell Research & Therapy* 19, no. 5: 712–724. https://doi.org/10.2174/1574888X18666230530153521.

Santos, M. I., K. Tuzlakoglu, S. Fuchs, et al. 2008. "Endothelial Cell Colonization and Angiogenic Potential of Combined Nano- and Micro-Fibrous Scaffolds for Bone Tissue Engineering." *Biomaterials* 29, no. 32: 4306–4313. https://doi.org/10.1016/j.biomaterials.2008.07.033.

Sarogni, P., A. K. Mapanao, S. Marchetti, C. Kusmic, and V. Voliani. 2021. "A Standard Protocol for the Production and Bioevaluation of Ethical In Vivo Models of HPV-Negative Head and Neck Squamous Cell Carcinoma." *American Chemical Society Pharmacology and Translational Science* 4, no. 3: 1227–1234. https://doi.org/10.1021/acsptsci.1c00083.

Satapathy, Y., V. Nikitin, J. Hana, et al. 2024. "Multiscale Porosity Characterization in Additively Manufactured Polymer Nanocomposites Using Micro-Computed Tomography." *Additive Manufacturing* 86: 1–14. https://doi.org/10.1016/j.addma.2024.104199.

Sato, T., R. G. Vries, H. J. Snippert, et al. 2009. "Single Lgr5 Stem Cells Build Crypt-Villus Structures In Vitro Without a Mesenchymal Niche." *Nature* 459, no. 7244: 262–265. https://doi.org/10.1038/nature07935.

Scaglione, S., L. Ceseracciu, M. Aiello, et al. 2014. "A Novel Scaffold Geometry for Chondral Applications: Theoretical Model and In Vivo Validation." *Biotechnology and Bioengineering* 111: 2107–2119. https://doi.org/10.1002/bit.25255/abstract.

Schemitsch, E. H. 2017. "Size Matters: Defining Critical in Bone Defect Size!" *Journal of Orthopaedic Trauma* 31: S20–S22. https://doi.org/10.1097/BOT.0000000000000978.

Schmidt, A. H. 2021. "Autologous Bone Graft: Is It Still the Gold Standard?" *Injury* 52: S18–S22. https://doi.org/10.1016/j.injury.2021.01.043.

Selders, G. S., A. E. Fetz, S. L. Speer, and G. L. Bowlin. 2016. "Fabrication and Characterization of Air-Impedance Electrospun Polydioxanone Templates." *Electrospinning* 1, no. 1: 20–30. https://doi.org/10.1515/esp-2016-0003.

Seppänen-Kaijansinkko, R. 2019. *Tissue Engineering in Oral and Maxillofacial Surgery*. Cham, Switzerland: Springer International Publishing. https://doi.org/10.1007/978-3-030-24517-7.

Shafiee, A., and A. Atala. 2017. "Tissue Engineering: Toward a New Era of Medicine." *Annual Review of Medicine* 68: 29–40. https://doi.org/10.1146/annurev-med-102715-092331.

Shamosi, A., D. Mehrabani, M. Azami, et al. 2017. "Differentiation of Human Endometrial Stem Cells into Endothelial-Like Cells on Gelatin/Chitosan/Bioglass Nanofibrous Scaffolds." *Artificial Cells, Nanomedicine, and Biotechnology* 45, no. 1: 163–173. https://doi.org/10.3109/21691401.2016.1138493.

Sharifi, F., S. M. Atyabi, D. Norouzian, M. Zandi, S. Irani, and H. Bakhshi. 2018. "Polycaprolactone/Carboxymethyl Chitosan Nanofibrous Scaffolds for Bone Tissue Engineering Application." *International Journal of Biological Macromolecules* 115: 243–248. https://doi.org/10.1016/j.ijbiomac.2018.04.045.

Shimazaki, T., N. Noro, K. Hagikura, T. Matsumoto, and C. Yoshida-Noro. 2021. "Quantitative Analysis of Factors Regulating Angiogenesis for Stem Cell Therapy." *Biology* 10, no. 11: 1–16. https://doi.org/10.3390/biology10111212.

Shoulders, M. D., and R. T. Raines. 2009. "Collagen Structure and Stability." *Annual Review of Biochemistry* 78: 929–958. https://doi.org/10.1146/annurev.biochem.77.032207.120833.

Simonet, M., O. D. Schneider, P. Neuenschwander, and W. J. Stark. 2007. "Ultraporous 3D Polymer Meshes by Low-Temperature Electrospinning: Use of Ice Crystals as a Removable Void Template." *Polymer Engineering and Science* 47, no. 12: 2020–2026. https://doi.org/10.1002/pen.20914.

Simonet, M., N. Stingelin, J. G. F. Wismans, C. W. J. Oomens, A. Driessen-Mol, and F. P. T. Baaijens. 2014. "Tailoring the Void Space and Mechanical Properties in Electrospun Scaffolds Towards Physiological Ranges." *Journal of Materials Chemistry B* 2, no. 3: 305–313. https://doi.org/10.1039/c3tb20995d.

Simunovic, F., and G. Finkenzeller. 2021. "Vascularization Strategies in Bone Tissue Engineering." *Cells* 10, no. 7: 1–17. https://doi.org/10.3390/cells10071749.

Skedros, J. G., G. C. Clark, S. M. Sorenson, K. W. Taylor, and S. Qiu. 2011. "Analysis of the Effect of Osteon Diameter on the Potential Relationship of Osteocyte Lacuna Density and Osteon Wall Thickness." *Anatomical Record* 294, no. 9: 1472–1485. https://doi.org/10.1002/ar.21452.

Solanki, A. K., F. V. Lali, H. Autefage, et al. 2021. "Bioactive Glasses and Electrospun Composites That Release Cobalt to Stimulate the HIF Pathway for Wound Healing Applications." *Biomaterials Research* 25, no. 1: 1–16. https://doi.org/10.1186/s40824-020-00202-6.

Stachewicz, U., J. F. Dijksman, D. Burdinski, C. U. Yurteri, and J. C. M. Marijnissen. 2009. "Relaxation Times in Single Event Electrospraying Controlled by Nozzle Front Surface Modification." *Langmuir* 25, no. 4: 2540–2549. https://doi.org/10.1021/la8021408.

Stachewicz, U., J. F. Dijksman, C. U. Yurteri, and J. C. M. Marijnissen. 2007. "Experiments on Single Event Electrospraying." *Applied Physics Letters* 91, no. 25: 1–3. https://doi.org/10.1063/1.2826279.

Stachewicz, U., T. Qiao, S. C. F. Rawlinson, et al. 2015. "3D Imaging of Cell Interactions With Electrospun PLGA Nanofiber Membranes for Bone Regeneration." *Acta Biomaterialia* 27: 88–100. https://doi.org/10.1016/j.actbio.2015.09.003.

Stachewicz, U., C. A. Stone, C. R. Willis, and A. H. Barber. 2012. "Charge Assisted Tailoring of Chemical Functionality at Electrospun Nanofiber Surfaces." *Journal of Materials Chemistry* 22, no. 43: 22935–22941. https://doi.org/10.1039/c2jm33807f.

Stachewicz, U., P. K. Szewczyk, A. Kruk, A. H. Barber, and A. Czyrska-Filemonowicz. 2019. "Pore Shape and Size Dependence on Cell Growth Into Electrospun Fiber Scaffolds for Tissue Engineering: 2D and 3D Analyses Using SEM and FIB-SEM Tomography." *Materials Science and Engineering C* 95: 397–408. https://doi.org/10.1016/j.msec.2017.08.076.

Stoddard, R. J., A. L. Steger, A. K. Blakney, and K. A. Woodrow. 2016. "In Pursuit of Functional Electrospun Materials for Clinical Applications in Humans." *Therapeutic Delivery* 7, no. 6: 387–409. https://doi.org/10.4155/tde-2016-0017.

Stoiljkovic, A., and S. Agarwal. 2008. "Short Electrospun Fibers by UV Cutting Method." *Macromolecular Materials and Engineering* 293, no. 11: 895–899. https://doi.org/10.1002/mame.200800171.

Strobel, H. A., T. Gerton, and J. B. Hoying. 2021. "Vascularized Adipocyte Organoid Model Using Isolated Human Microvessel Fragments." *Biofabrication* 13, no. 3: 1–15. https://doi.org/10.1088/1758-5090/abe187.

Strobel, H. A., S. M. Moss, and J. B. Hoying. 2023. "Vascularized Tissue Organoids." *Bioengineering* 10, no. 2: 1–26. https://doi.org/10.3390/bioengineering10020124.

Sun, D., C. Chang, S. Li, and L. Lin. 2006. "Near-Field Electrospinning." *Nano Letters* 6, no. 4: 839–842. https://doi.org/10.1021/nl0602701.

Sun, Z., E. Zussman, A. L. Yarin, J. H. Wendorff, and A. Greiner. 2003. "Compound Core-Shell Polymer Nanofibers by co-Electrospinning." *Advanced Materials* 15, no. 22: 1929–1932. https://doi.org/10.1002/adma.200305136.

Szewczyk, P. K., S. Metwally, J. E. Karbowniczek, et al. 2019. "Surface-Potential-Controlled Cell Proliferation and Collagen Mineralization on Electrospun Polyvinylidene Fluoride (PVDF) Fiber Scaffolds for Bone Regeneration." *American Chemical Society Biomaterials Science and Engineering* 5, no. 2: 582–593. https://doi.org/10.1021/acsbiomaterials.8b01108.

Szewczyk, P. K., and U. Stachewicz. 2020. "The Impact of Relative Humidity on Electrospun Polymer Fibers: From Structural Changes to Fiber Morphology." *Advances in Colloid and Interface Science* 286: 1–23. https://doi.org/10.1016/j.cis.2020.102315.

Szewczyk, P. K., A. E. Taşlı, J. Knapczyk-Korczak, and U. Stachewicz. 2023. "Steering Triboelectric and Mechanical Properties of Polymer Fibers With Carbon Black." *Composites Science and Technology* 243: 1–11. https://doi.org/10.1016/j.compscitech.2023.110247.

Ura, D. P., K. Berniak, and U. Stachewicz. 2021. "Critical Length Reinforcement in Core-Shell Electrospun Fibers Using Composite Strategies." *Composites Science and Technology* 211: 1–9. https://doi.org/10.1016/j.compscitech.2021.108867.

Ura, D. P., J. E. Karbowniczek, P. K. Szewczyk, S. Metwally, M. Kopyściański, and U. Stachewicz. 2019. "Cell Integration With Electrospun PMMA Nanofibers, Microfibers, Ribbons, and Films: A Microscopy Study." *Bioengineering* 6, no. 2: 41. https://doi.org/10.3390/bioengineering6020041.

Ura, D. P., and U. Stachewicz. 2022. "The Significance of Electrical Polarity in Electrospinning: A Nanoscale Approach for the Enhancement of the Polymer Fibers' Properties." *Macromolecular Materials and Engineering* 307, no. 5: 1–23. https://doi.org/10.1002/mame.202100843.

Ura, D. P., and U. Stachewicz. 2024. "Direct Electrospinning of Short Polymer Fibers: Factors Affecting Size and Quality." *Composites Part A: Applied Science and Manufacturing* 181: 1–14. https://doi.org/10.1016/j.compositesa.2024.108138.

Vimalraj, S., S. Renugaa, and A. Dhanasekaran. 2023. "Chick Embryo Chorioallantoic Membrane: A Biomaterial Testing Platform for Tissue Engineering Applications." *Process Biochemistry* 124: 81–91. https://doi.org/10.1016/j.procbio.2022.11.007.

Walther, M., F. Rohde, T. Kielholz, and M. Windbergs. 2022. "Physico-Chemical Analysis of Electrospun Fibers—A Systematic Approach." *European Journal of Pharmaceutics and Biopharmaceutics* 171: 60–71. https://doi.org/10.1016/j.ejpb.2022.01.001.

Wang, C., W. W. Lu, and M. Wang. 2020. "Multifunctional Fibrous Scaffolds for Bone Regeneration With Enhanced Vascularization." *Journal of Materials Chemistry B* 8, no. 4: 636–647. https://doi.org/10.1039/c9tb01520e.

Wang, J., J. Lin, L. Chen, L. Deng, and W. Cui. 2022. "Endogenous Electric-Field-Coupled Electrospun Short Fiber via Collecting Wound Exudation." *Advanced Materials* 34, no. 9: 1–15. https://doi.org/10.1002/adma.202108325.

Wang, Y., M. Keshavarz, P. Barhouse, and Q. Smith. 2022. "Strategies for Regenerative Vascular Tissue Engineering." *Advanced Biology*: 1–15. https://doi.org/10.1002/adbi.202200050.

Watanabe, H., N. Maishi, M. Hoshi-Numahata, et al. 2023. "Skeletal-Vascular Interactions in Bone Development, Homeostasis, and Pathological Destruction." *International Journal of Molecular Sciences* 24, no. 13: 1–17. https://doi.org/10.3390/ijms241310912.

Wenger, A., A. Stahl, H. Weber, et al. 2004. "Modulation of In Vitro Angiogenesis in a Three-Dimensional Spheroidal Coculture Model for Bone Tissue Engineering." *Tissue Engineering* 10, no. 9: 1536–1547.

Williams, G. R., B. T. Raimi-Abraham, and C. J. Luo. 2018. *Nanofibers in Drug Delivery*. London: UCL Press.

Wilson, J., V. G. Rahul, L. V. Thomas, and P. D. Nair. 2022. "Three-Dimensional Wet Electrospun Scaffold System for the Differentiation of Adipose-Derived Mesenchymal Stem Cells to Islet-Like Clusters." *Journal of Tissue Engineering and Regenerative Medicine* 16, no. 12: 1276–1283. https://doi.org/10.1002/term.3366.

Wittmer, C. R., A. Hébraud, S. Nedjari, and G. Schlatter. 2014. "Well-Organized 3D Nanofibrous Composite Constructs Using Cooperative Effects Between Electrospinning and Electrospraying." *Polymer* 55, no. 22: 5781–5787. https://doi.org/10.1016/j.polymer.2014.08.044.

Woloszyk, A., P. Wolint, A. S. Becker, et al. 2019. "Novel Multimodal MRI and MicroCT Imaging Approach to Quantify Angiogenesis and 3D Vascular Architecture of Biomaterials." *Scientific Reports* 9, no. 1: 1–14. https://doi.org/10.1038/s41598-019-55411-4.

Wu, J., C. Huang, W. Liu, et al. 2014. "Cell Infiltration and Vascularization in Porous Nanoyarn Scaffolds Prepared by Dynamic Liquid Electrospinning." *Journal of Biomedical Nanotechnology* 10, no. 4: 603–614. https://doi.org/10.1166/jbn.2014.1733.

Wu, L., Y. Gu, L. Liu, et al. 2020. "Hierarchical Micro/Nanofibrous Membranes of Sustained Releasing VEGF for Periosteal Regeneration." *Biomaterials* 227: 1–16. https://doi.org/10.1016/j.biomaterials.2019.119555.

Xi, K., Y. Gu, J. Tang, et al. 2020. "Microenvironment-Responsive Immunoregulatory Electrospun Fibers for Promoting Nerve Function Recovery." *Nature Communications* 11, no. 1: 1–18. https://doi.org/10.1038/s41467-020-18265-3.

Xie, X., J. Cai, D. Li, et al. 2024. "Multiphasic Bone-Ligament-Bone Integrated Scaffold Enhances Ligamentization and Graft-Bone Integration After Anterior Cruciate Ligament Reconstruction." *Bioactive Materials* 31: 178–191. https://doi.org/10.1016/j.bioactmat.2023.08.004.

Xu, H., S. Fujiwara, L. Du, I. Liashenko, S. Luposchainsky, and P. D. Dalton. 2024. "Accessible Melt Electrowriting Three-Dimensional Printer for Fabricating High-Precision Scaffolds." *Polymer* 309: 1–11. https://doi.org/10.1016/j.polymer.2024.127466.

Yan, X., H. Yao, J. Luo, Z. Li, and J. Wei. 2022. "Functionalization of Electrospun Nanofiber for Bone Tissue Engineering." *Polymers* 14, no. 14: 1–18. https://doi.org/10.3390/polym14142940.

Yang, G., B. Mahadik, J. Y. Choi, and J. P. Fisher. 2020. "Vascularization in Tissue Engineering: Fundamentals and State-of-Art." *Progress in Biomedical Engineering* 2, no. 1: 1–18. https://doi.org/10.1088/2516-1091/ab5637.

Yang, R., Y. Zheng, Y. Zhang, et al. 2022. "Bipolar Metal Flexible Electrospun Fibrous Membrane Based on Metal–Organic Framework for Gradient Healing of Tendon-to-Bone Interface Regeneration." *Advanced Healthcare Materials* 11, no. 12: 1–14. https://doi.org/10.1002/adhm.202200072.

Yang, C., D. G. Yu, D. Pan, et al. 2016. "Electrospun pH-Sensitive Core–Shell Polymer Nanocomposites Fabricated Using a Tri-Axial Process." *Acta Biomaterialia* 35: 77–86. https://doi.org/10.1016/j.actbio.2016.02.029.

Yang, Y., M. Sun, W. Jia, et al. 2024. "An Osteoporosis Bone Defect Regeneration Strategy via Three-Dimension Short Fibers Loaded With Alendronate Modified Hydroxyapatite." *Colloids and Surfaces B: Biointerfaces* 233: 113659. https://doi.org/10.1016/J.COLSURFB.2023.113659.

Yao, T., H. Chen, R. Wang, et al. 2023. "Thiol-Ene Conjugation of VEGF Peptide to Electrospun Scaffolds as Potential Application for Angiogenesis." *Bioactive Materials* 20: 306–317. https://doi.org/10.1016/j.bioactmat.2022.05.029.

Yao, Z., H. Liu, M. Yang, et al. 2020. "Bone Marrow Mesenchymal Stem Cell-Derived Endothelial Cells Increase Capillary Density and Accelerate Angiogenesis in Mouse Hindlimb Ischemia Model." *Stem Cell Research & Therapy* 11, no. 1: 1–11. https://doi.org/10.1186/s13287-020-01710-x.

Yarin, A. L. 2011. "Coaxial Electrospinning and Emulsion Electrospinning of Core-Shell Fibers." *Polymers for Advanced Technologies* 22, no. 3: 310–317. https://doi.org/10.1002/pat.1781.

Ye, H., J. Zhu, D. Deng, S. Jin, J. Li, and Y. Man. 2019. "Enhanced Osteogenesis and Angiogenesis by PCL/Chitosan/Sr-Doped Calcium Phosphate Electrospun Nanocomposite Membrane for Guided Bone Regeneration." *Journal of Biomaterials Science* 30, no. 16: 1505–1522. https://doi.org/10.1080/09205063.2019.1646628.

Yokoyama, Y., S. Hattori, C. Yoshikawa, et al. 2009. "Novel Wet Electrospinning System for Fabrication of Spongiform Nanofiber 3-Dimensional Fabric." *Materials Letters* 63, no. 9–10: 754–756. https://doi.org/10.1016/j.matlet.2008.12.042.

Yu, H., Y. Li, Y. Pan, et al. 2023. "Multifunctional Porous Poly(L-Lactic Acid) Nanofiber Membranes With Enhanced Anti-Inflammation, Angiogenesis and Antibacterial Properties for Diabetic Wound Healing." *Journal of Nanobiotechnology* 21, no. 1: 1–14. https://doi.org/10.1186/s12951-023-01847-w.

Yu, Y., S. Hua, M. Yang, et al. 2016. "Fabrication and Characterization of Electrospinning/3D Printing Bone Tissue Engineering Scaffold." *Royal Society of Chemistry Advances* 6, no. 112: 110557–110565. https://doi.org/10.1039/C6RA17718B.

Zawadzki, P., R. Talar, K. Grochalski, and M. Dąbrowski. 2023. "The Influence of Osteon Orientation on Surface Topography Parameters After Machining of Cortical Bone Tissue." *Materials* 16, no. 12: 1–13. https://doi.org/10.3390/ma16124293.

Zhan, Y., B. Deng, H. Wu, et al. 2021. "Biomineralized Composite Liquid Crystal Fiber Scaffold Promotes Bone Regeneration by Enhancement of Osteogenesis and Angiogenesis." *Frontiers in Pharmacology* 12: 1–16. https://doi.org/10.3389/fphar.2021.736301.

Zhang, B., J. He, X. Li, F. Xu, and D. Li. 2016. "Micro/Nanoscale Electrohydrodynamic Printing: From 2D to 3D." *Nanoscale* 8, no. 34: 15376–15388. https://doi.org/10.1039/c6nr04106j.

Zhang, H., J. L. Liesveld, L. M. Calvi, et al. 2023. "The Roles of Bone Remodeling in Normal Hematopoiesis and Age-Related Hematological Malignancies." *Bone Research* 11, no. 1: 1–19. https://doi.org/10.1038/s41413-023-00249-w.

Zhang, K., S. Wang, C. Zhou, et al. 2018. "Advanced Smart Biomaterials and Constructs for Hard Tissue Engineering and Regeneration." *Bone Research* 6, no. 1: 1–15. https://doi.org/10.1038/s41413-018-0032-9.

Zhang, Y., Y. Zhou, Y. Jia, T. Wang, and D. Meng. 2023. "Adverse Effects of Hyperbaric Oxygen Therapy: A Systematic Review and Meta-Analysis." *Frontiers in Medicine* 10: 1–13. https://doi.org/10.3389/fmed.2023.1160774.

Zhang, Z., Y. Zhang, Y. Guo, et al. 2024. "Preparing Gelatin-Containing Polycaprolactone/Polylactic Acid Nanofibrous Membranes for Periodontal Tissue Regeneration Using Side-by-Side Electrospinning Technology." *Journal of Biomaterials Applications*: 48–57. https://doi.org/10.1177/08853282241248778.

Zhao, D., Q. Saiding, Y. Li, Y. Tang, and W. Cui. 2024. "Bone Organoids: Recent Advances and Future Challenges." *Advanced Healthcare Materials* 13, no. 5: 1–22. https://doi.org/10.1002/adhm.202302088.

Zhao, T., J. Zhang, X. Gao, D. Yuan, Z. Gu, and Y. Xu. 2022. "Electrospun Nanofibers for Bone Regeneration: From Biomimetic Composition, Structure to Function." *Journal of Materials Chemistry B* 10, no. 32: 6078–6106. https://doi.org/10.1039/d2tb01182d.

Zheng, G., W. Li, X. Wang, D. Wu, D. Sun, and L. Lin. 2010. "Precision Deposition of a Nanofibre by Near-Field Electrospinning." *Journal of Physics D: Applied Physics* 43, no. 41: 1–6. https://doi.org/10.1088/0022-3727/43/41/415501.

Zheng, W., Z. Bai, S. Huang, K. Jiang, L. Liu, and X. Wang. 2022. "The Effect of Angiogenesis-Based Scaffold of Mesoporous Bioactive Glass Nanofiber on Osteogenesis." *International Journal of Molecular Sciences* 23, no. 20: 1–23. https://doi.org/10.3390/ijms232012670.

Zhou, M., J. Hou, Y. Li, et al. 2019. "The Pro-Angiogenic Role of Hypoxia Inducible Factor Stabilizer FG-4592 and Its Application in an In Vivo Tissue Engineering Chamber Model." *Scientific Reports* 9, no. 1: 1–12. https://doi.org/10.1038/s41598-019-41924-5.

Zhou, R., Q. Guo, Y. Xiao, et al. 2021. "Endocrine Role of Bone in the Regulation of Energy Metabolism." *Bone Research* 9, no. 1: 1–19. https://doi.org/10.1038/s41413-021-00142-4.

Applied Surface Science 621 (2023) 156835

Contents lists available at ScienceDirect

Applied Surface Science

journal homepage: www.elsevier.com/locate/apsusc

Full Length Article

PLLA scaffolds with controlled surface potential and piezoelectricity for enhancing cell adhesion in tissue engineering

Martyna Polak [a], Krzysztof Berniak [a], Piotr K. Szewczyk [a], Joanna E. Karbowniczek [a], Mateusz M. Marzec [b], Urszula Stachewicz [a,*]

[a] Faculty of Metals Engineering and Industrial Computer Science, AGH University of Science and Technology, Al. A. Mickiewicza 30, Kraków 30-059, Poland
[b] Academic Centre for Materials and Nanotechnology, AGH University of Science and Technology, Al. A. Mickiewicza 30, Kraków 30-059, Poland

ARTICLE INFO

Keywords:
Cell Adhesion
Bone Regeneration
Osteoblasts
Surface Charge
Collagen Formation

ABSTRACT

The effect of the surface potential of biomaterials on cell attachment and development in regenerative medicine is still an unexplored area driving many regeneration processes, especially in piezoelectric bone tissue. Within this study, we electrospun poly(L-lactide) scaffolds constructed of fibers with either higher (−600 mV) or lower (−300 mV) surface potential, which is controlled by applied voltage polarity during their production. Interestingly, this way, the piezoelectric performance of PLLA fibers can be enhanced. The direct measurement of the PLLA fiber surface potential using Kelvin probe force microscopy (KPFM) showed a good correlation with the zeta potential analysis. The piezoelectricity of PLLA fibers was verified with piezoresponse force microscopy (PFM), indicating that it can be enhanced by applying the positive voltage polarity to the nozzle during electrospinning. Importantly, the cell adhesion assay showed a significant effect of the higher surface potential of PLLA fibers on osteoblasts behavior and creating a favorable bioelectric microenvironment. We observed enhanced initial adhesion of cells in the first 5 h with no additional effect of surface potential on proliferation, morphology, or collagen production. It was demonstrated that electrospun PLLA fibers with tunable surface potential and piezoelectricity are excellent for constructing bone tissue engineering scaffolds.

1. Introduction

Striving for the best possible imitation of the extracellular matrix (ECM) conditions in biomaterials application is one of the main goals of tissue engineering [1,2] to enhance the regeneration processes [3] and reduce bacterial infections [4]. Favorable bioelectric microenvironments for cell proliferation and adhesion vary depending on the cell type. Hence, the research focuses on combining cells' specific preferences with designing material properties for use as a tissue scaffold [5]. The typical surface modification approach in polymer fibers for tissue engineering includes adding bioactive molecules to control cellular attachment [1,6]. However, current knowledge on the stability of bioactive molecules on the surfaces of polymer fibers is limited; therefore, attempts to eliminate interference with the chemistry of the fiber surface are needed. Alternatively, manipulating physical material properties can have a stable and long-term positive impact on cells' responses [7,8].

The surface charges and electrostatic interactions in biological tissues are natural phenomena that occur due to ion-based physiological processes [9]. A characteristic feature of all types of cells is negatively charged cell membrane. The electric potential of cell membranes varies between −10 to −90 mV, depending on cell type. Moreover, the electrostatic forces play an essential role in the relationship of the negatively charged cell membrane and opposite charges accumulated on biomaterial surfaces. Here, the positively charged surfaces are beneficial for cells adhesion, proliferation and spreading [10]. In tissue regeneration, charges guide the signaling process and further cell behavior leading to tissue repair [11,12]. Osteoblast cells are responsible for rebuilding bone tissue by producing collagen fibrils that create a bone matrix [13]. The piezoelectric effect in tissues, such as bone and tendons, is ascribed to the crystalline fibrillar structure of collagen or elastin [14,15]. Collagen is the most abundant protein in the human body and the dominant element of ECM, which plays an essential role in tissue growth and regeneration [9]. Thus, one of the most critical aspects of bone tissue engineering includes collagen formation by interacting cells with biomaterials [16,17]. Electrospun polymer fibers properties, including

* Corresponding author.
E-mail address: ustachew@agh.edu.pl (U. Stachewicz).

https://doi.org/10.1016/j.apsusc.2023.156835
Received 19 January 2023; Received in revised form 12 February 2023; Accepted 20 February 2023
Available online 24 February 2023

morphology, and mechanical or electrical properties, can be tuned during the production process by a wide variety of changeable electrospinning parameters but also by properties of the polymer solution itself [18–22]. Voltage polarity effect in electrospinning is one of the options which allows controlling the surface and the mechanical properties of fibers [23]. Varying between positive and negative polarity leads to the accumulation of different charges on the polymer jet, inducing molecular reorientation, which is quenched in produced fibers [24]. This molecular reorientation results in a change in both the structural and surface properties of fibers [25,26].

As mentioned above, the biologically important aspect of enhancing cell responses and tissue regeneration is the effect of electric charges generated by biomaterial. These charges can result from the material's piezoelectric properties, leading to a relationship with the surface potential [17,27–29]. Cellular interactions with the piezoelectric material and vibrations are the mechanisms responsible for the generation of surface charges [30]. Cells exert enough stress during attachment and migration on scaffolds to generate electrical signals [14]. Notably, the increased cell activity can also be attributed to charges present on piezoelectric materials. It allows miming the original conditions for cells by providing the physiological electrical micro-environment [31]. Induction of charges due to the piezoelectric effect was explored for poly (vinylidene fluoride) (PVDF) [32,33], poly(3-hydroxybutyric acid-*co*-3-hydrovaleric acid) (PHBV) [34], or poly(L-lactide) (PLLA) scaffolds and films [35,36].

PLLA is a widely researched and common biopolymer used in medicine, especially in tissue engineering, due to its biocompatibility, stability, and relatively slow degradation [37–40]. PLLA electrospun fibers show mechanical properties that meet the requirements of bone tissue engineering [41]. The mechanical properties of PLLA fibers can be controlled via electrospinning parameters, and solvents, and molecular weight of the polymer used to prepare the solution, which can contain particles too [42,43]. Electrospun PLLA fibers' crystallinity can also be enhanced after thermal annealing due to the presence of α-crystalline phase [44]. The piezoelectric effect in PLLA electrospun fibers for tissue engineering is well known [36]. However, to date, it is still unclear how the surface potential of PLLA electrospun fibers affects cell adhesion and collagen mineralization which is crucial for the bone regeneration process [45–47].

In this study, we controlled the piezoelectricity and surface potential of produced PLLA fiber by applying positive and negative voltage polarity to the nozzle during electrospinning. Applying positive voltage polarity led to a higher surface potential of PLLA fibers (PLLA+), and negative voltage polarity resulted in a lower surface potential of PLLA fibers (PLLA-). Additionally, the piezoelectric properties of the individual electrospun PLLA fibers have been measured using high voltage switching spectroscopy piezoresponse force microscopy (HVSS-PFM). Therefore, we were able to investigate both: piezoelectric and surface potential effects of PLLA fibers on osteoblasts behavior in scaffolds enhancing bone tissue regeneration. We studied the effect on osteoblast adhesion, proliferation, and later collagen formation. Notably, the PLLA scaffolds are manufactured with a single-step approach without any chemical modifications, showing the ability of applied voltage polarity to tune the surface properties of electrospun polymer fibers. Knowing the significance of surface potential in the biomaterials field, we have proved that controlled surface charges on PLLA scaffolds can guide and enhance osteoblast responses.

2. Materials and methods

2.1. Material

Poly(L-lactide) (PLLA, PURASORB PL18, M_w = 221, 000 g·mol^{-1}, Corbion, The Netherlands) was dried before solution preparation for 2 h at 30 °C in a drying oven (POL-EKO-APARATURA, Poland). A polymer solution of 9 wt% concentration was prepared by dissolving PLLA in a mixture of dichloromethane (DCM, analytical standard, Avantor, Poland) and dimethylformamide (DMF, analytical standard, Avantor, Poland) in the ratio of 7:3 w/w. The polymer was dissolved entirely after 3 h of stirring at 25 °C at a constant speed of 400 rpm using the magnetic stirrer (IKA, Germany).

2.2. Electrospinning

Two types of PLLA scaffolds were prepared by applying either positive (PLLA+) and negative voltage polarity (PLLA-) to the stainless-steel nozzle (hypodermic injection needle K_D Fine 0.8 × 40 mm 21 G × 1 1/2″ green, K_D Medical GmbH Hospital Products, Germany) while electrospinning with apparatus SKE E-FIBER EF 100 (SKE Research Equipment, Italy). PLLA fibers were electrospun by applying a voltage of + 13.5 kV or −13.5 kV to the nozzle, with a solution flow rate of 6 ml/h and a distance of 16 cm between the nozzle and the collector. The process was conducted in a climate-control chamber at a T = 25 ºC and RH = 30 %.

2.3. Scanning electron microscopy (SEM)

Sample preparation before imaging included coating with an 8 nm Au layer using rotary-pumped sputter coating (Q150RS, Quorum Technologies, UK). Samples were imaged with the SEM (Merlin Gemini II, Zeiss, Germany) using a SE detector, applying a current of 100 – 150 pA, a voltage of 3 kV, and a working distance of 3 – 9 mm. Diameters of the fibers D_f were analyzed from SEM images using Fiji software (ImageJ 2.1.0, USA). The average fiber diameter was calculated from 100 measurements taken from SEM images.

2.4. Contact angle measurement

Contact angle measurement consisted of deposition of deionized water droplets (Spring 5UV purification system, Hydrolab, Poland) with a volume of 3 μL onto the surface of PLLA scaffold and taking the images using a Canon EOS 700D camera with EF-S 60 mm f/2.8 Macro USM zoom lens. MB ruler software (version 5.3, USA) was used to measure the contact angles. The average water contact angle was obtained from measurements of ten droplets per sample.

2.5. Surface and bulk chemistry analysis

Characterization of the surface chemistry of fibers deposited onto silicon wafers was done with XPS. The Angle-Resolved XPS (ARXPS) analyses were carried out in a PHI VersaProbeII Scanning XPS system using monochromatic Al Kα (1486.6 eV) X-rays focused to a 100 μm spot. The photoelectron take-off angle varied at 15 ° and 30 °, and the pass energy in the analyzer was set to 46.95 eV (0.1 eV step) to obtain high energy resolution spectra for the O 1 s regions. A dual beam charge compensation with 7 eV Ar + ions and 1 eV electrons were used to maintain a constant sample surface potential regardless of the sample conductivity. All XPS spectra were charge referenced to the unfunctionalized, saturated carbon (C—C) C 1 s peak at 285.0 eV. The operating pressure in the analytical chamber was less than 2 × 10^{-9} mbar. Deconvolution of spectra was carried out using PHI MultiPak software (v.9.9.2). Spectrum background was subtracted using the Shirley method.

The bulk chemistry was investigated with Fourier transform infrared spectroscopy (FTIR, Nicolet iS5, Thermo Fisher, USA). The samples were scanned 2 h after electrospinning in a range of 400 to 4000 cm^{-1} in a total scan number of 64. Total crystallinity of the samples was estimated by calculation of the ratio of the peak area at 921 cm^{-1} and the summation of 921 cm^{-1} and 955 cm^{-1} using equation (1)[48]

$$X_{C(FTIR)} = \frac{I_{921}}{I_{955} + I_{921}} 100\% \quad (1)$$

where I_{921} and I_{955} corresponds to the area of the crystalline and amorphous bands, respectively.

Differential scanning calorimetry (DSC) carried out using DSC (DSC 3, Mettler Toledo, Switzerland) allowed the analysis of thermal properties of PLLA+ and PLLA- fibers and PLLA pellets. Three independent examinations of each sample were performed, and the results present the average values. Samples were heated at a rate of 10 $Kmin^{-1}$ from 0 to 230 °C. DSC results allowed us to calculate the crystallinity using equation (2),

$$C = \frac{\Delta H_{measured}}{\Delta H_{100\%}} 100\% \quad (2)$$

where $\Delta H_{measured}$ is the heat of fusion of measured sample, $\Delta H_{100\%}$ is the heat of fusion of 100 % crystalline sample taken from literature, which is 96.3 Jg^{-1} [49].

2.6. Kelvin probe force microscopy and piezoresponse force microscopy

Atomic force microscopy (AFM), Kelvin probe force microscopy (KPFM), and high voltage switching spectroscopy piezoresponse force microscopy (HVSS-PFM) measurements were carried out using CoreAFM (Nanosurf, Switzerland). For KPFM, conductive HQ:NSC18/Pt (MikroMasch, Bulgaria) tips with force constant of 2.8 Nm^{-1} and a resonance frequency of 75 kHz were used. For HVSS-PFM, conductive ElectriCont-G (BudgetSensors, Bulgaria) tips with force constant of 0.2 Nm^{-1} and a resonance frequency of 13 kHz were used. Topography was obtained simultaneously with KPFM measurements. Depending on the measurement, areas of 15 × 15 and 50 × 50 μm were scanned.

KPFM data is an average of scan lines taken on the uppermost section of 7 different fibers measured on 4 separate scan regions. Gold was measured in tandem with PLLA fibers to serve as a control measurement of the KPFM signal. All measurements were carried out in one session to ensure similar room conditions and were carried out 24 h after electrospinning to control for the surface potential decay and to ensure that identical material conditions as applied in cell studies. The environmental conditions during the experiments were 50–65 % RH and 23 °C. The values for Au are an average of 10 separate lines on each of the 4 scans. Data were processed using Gwyddion (v2.56, gwyddion.net) and OriginPro (v9.7.0.188, OriginLab Corporation, USA) software.

HVSS-PFM data is an average of 3 separate measurements on the uppermost sections of the scanned fibers. The approach regarding the time of measurements, temperature, humidity, and data analysis were the same as for KPFM measurements except for the substrate for fibers, which for PFM measurement was glass with ITO coating. Spectroscopy was performed with a pulse time of 50 ms in 200 steps in the voltage range from −90 to 0 V, 0 to 90 V, and back from 90 to −90 V. The tip remained stationary on the material during the measurement. A complete method description has been reported previously [50] Using pulses instead of a continuous voltage ramp in this approach, the destructive contribution of surface potential is negated. HVSS-PFM allows determining the local piezoelectric response of the material in contact with the conductive tip of the AFM cantilever. The deflection amplitude (displacement) provides information on the strength of piezoelectric behavior. The phase of the deflection provides information on the polarization direction and its value, as well as the coercive bias of the material.

2.7. Zeta potential measurement

Streaming zeta potential analysis was conducted with a high-end electrokinetic analyzer (SurPASS 3, Anton Paar, Austria). The streaming potential was measured between two meshes with dimensions 20 × 10 mm placed in the cell with the adjustable gap set to 110 μm. The pH value was controlled in the range of 3.0–9.0 with pH steps of 0.3. The titrations were done by the progressive addition of 0.05 M HCl or 0.05 M NaOH to a 0.01 M KCl solution. The zeta potential was measured with four repetitions for each pH. The titration curves are shown as the average value with error bars calculated from these 4 tests.

2.8. Cell culture study

Human osteoblast-like cells (MG-63) (Sigma Aldrich, UK) were used for the cell culture study. Before cell seeding, which took place 24 h after scaffold electrospinning, samples of PLLA fibers were cut into 15 mm diameter circles, placed in 24-well plates, and sterilized with UV light for 30 min. Glass was used as a control. For cell seeding, an equal cell density of 2×10^4 cells per 1 ml in culture media was used for each cell culture study. Incubation was provided at 37 °C and humidity of 95 % in a 5 % CO_2 atmosphere in the incubator (Memmert GmbH + Co.KG, Inc 108med, Schwabach, Germany). The cellular medium consisted of Dulbecco's modified Eagle Medium (DMEM with 4.5 g/LD - glucose, Biological Industries, Israel), supplemented with 10 % of fetal bovine serum (FBS, Biological Industries, Israel), 2 % of antibiotics (penicillin − streptomycin, Biological Industries, Israel), 1 % of L-glutamine solution (Biological Industries, Israel), and 1 % of amino acids (mem nonessential amino acid solution 100×, Sigma-Aldrich, USA).

2.8.1. Cell adhesion and viability

For the adhesion test in three-time points 1 h, 3 h, and 5 h, cells were seeded on PLLA+ and PLLA- samples and on the glass as a control. After the required time from cell seeding for each time point, samples were washed in phosphate-buffered saline (PBS, Biomed Lublin, Poland) to remove unattached cells. In the next step, scaffolds and the control sample were fixed with 4 % paraformaldehyde for 15 min and rinsed with PBS. For nuclear staining 4′,6-diamidino-2-phenylindole dye (DAPI, Sigma-Aldrich, UK) incubation was performed for 15 min, followed by rinsing with PBS. Imaging was done by confocal laser scanning microscopy (Zeiss LSM 900, Germany). Quantitative cell analysis was carried out using macros in the Fiji software (ImageJ 2.1.0, USA).

The cell viability was evaluated using the CellTiter-BlueR©Assay (GloMax Discover plate Reader, Promega, USA) after 1, 3, and 7 days of incubation. At each time point media was replaced with 1 ml of media containing 20 % of CellTiter-BlueR© reagent (Promega, USA) and incubated for 4 h at 37 °C. From each well, 100 μm of reagent was transferred to a 96-well plate in triplicates, and fluorescence was read at 560/590 nm using the microplate reader GloMaxR©DiscoverSystem (Promega, USA). For the cell culture study, tests were conducted on two repetitions for each type of PLLA sample and glass. The statistical analysis was performed in OriginPro (ver. 2022 9.9 USA).

2.8.2. Confocal microscopy: Focal adhesion staining

Cells were seeded on each PLLA+ and PLLA- sample and glass and cultured for 1, 3, and 7 days. Further, scaffolds were fixed with 4 % paraformaldehyde (Sigma-Aldrich, UK) for 15 min. After fixation, the samples were washed with PBS. Afterward, incubation was carried out in 0.1 % Triton X-100 (Sigma-Aldrich, UK) for 10 min and followed by rinsing in PBS. The blocking step included incubation in 3 % bovine serum albumin (BSA, Sigma-Aldrich, UK) in PBS for 60 min. For overnight staining with primary antibodies, monoclonal anti-paxillin antibodies were used (ab32084, Abcam, UK) to stain paxillin in the focal adhesion complex. After staining, samples were rinsed in PBS for 15 min. Further, cells were incubated with an anti-rabbit secondary antibody conjugated with Alexa Fluor Plus 555 (A32732, Thermo Fisher, USA) for 1 h. Next, cells were incubated for 1 h at 23 °C with Alexa Fluor™ 488 Phalloidin (Thermo Fisher, USA) for actin staining. The last step was nuclear staining with DAPI for 15 min. The images were acquired using the confocal microscope (Zeiss LSM 900, Germany). During experiments, the Plan-Apochromat 10x/0.45 M27, 20x/0.8 M27, 40x/1.30 Oil DIC M27 and 63x/1.4 Oil DIC M27 objectives were used. Imaging was possible using the 405 nm or 488 nm, or 555 nm laser lines for exciting DAPI, Alexa Fluor™ 488 Phalloidin, Alexa Fluor Plus 555,

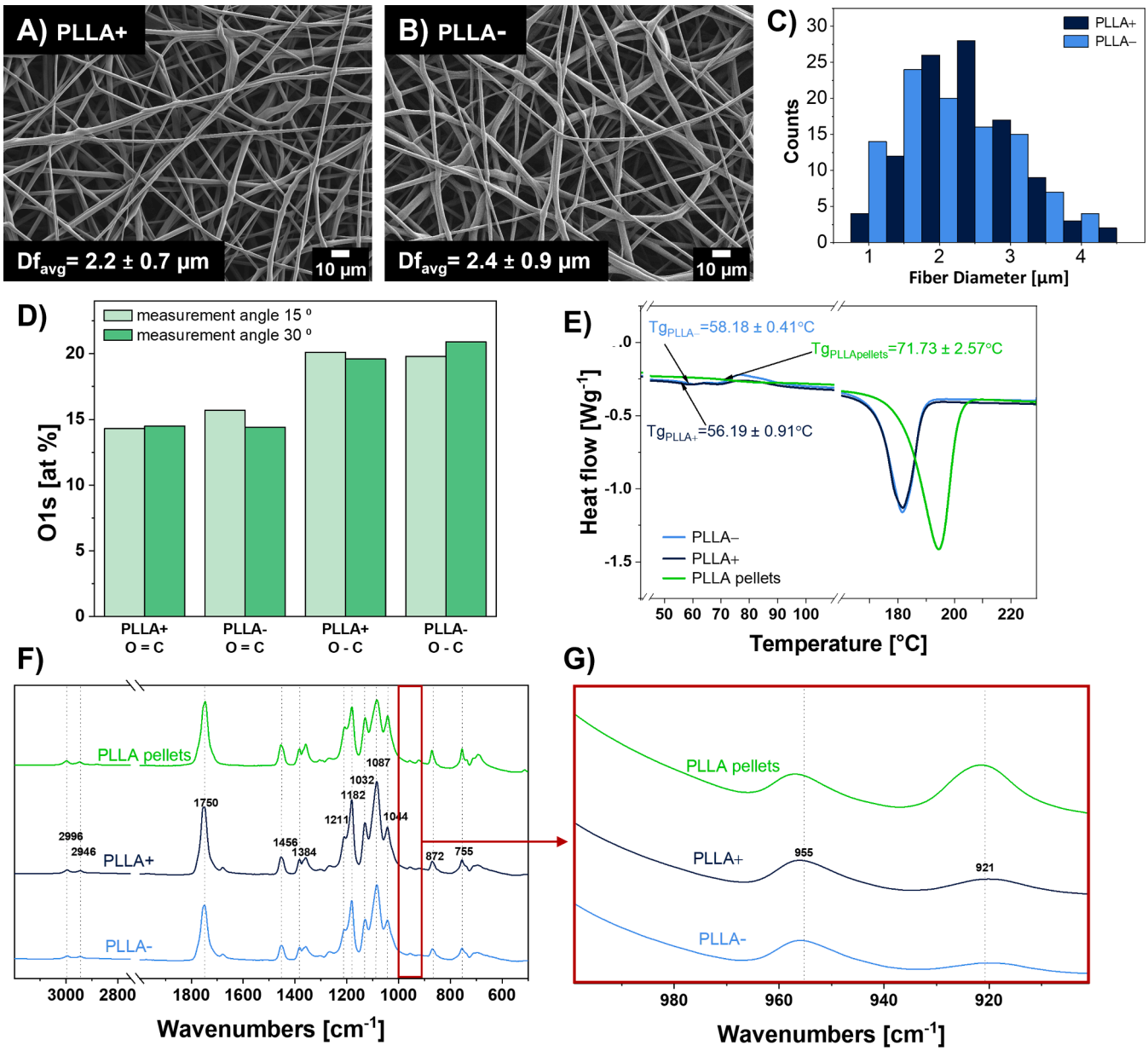

Fig. 1. SEM micrographs of electrospun of A) PLLA+ and B) PLLA- fibers, C) histogram of fiber diameter distribution with the average fiber diameter (Df$_{avg}$) of 2.2 µm for PLLA+ and 2.4 µm for PLLA-, D) XPS results of surface chemistry of PLLA+ and PLLA- fibers, E) DSC for PLLA+ and PLLA- fibers, and PLLA pellets, F) FTIR results, and G) FTIR results with focus on 921 and 955 cm^{-1} peaks, zoom of the spectra region marked in F).

respectively.

2.8.3. Confocal microscopy: Collagen staining

The extracellular collagen was immunofluorescently stained on days 14 and 21 after cells seeding on PLLA+ and PLLA- fibers. Cells were incubated for 1 h with monoclonal anti-collagen, type I antibody (C2456, Merck, USA) at 37 °C. Afterward, the cells were rinsed with 5 % FBS in PBS and then were fixed with 4 % formaldehyde in PBS for 15 min at 23 °C and rinsed two times with PBS. Cells were permeabilized with 0.1 % Triton X-100 in PBS for 10 °min at 23 °C and further incubated in a blocking solution (3 % BSA in PBS) for 1 h. Next, the cells were incubated with anti-mouse secondary antibody conjugated Alexa Fluor Plus 555 (A32727, Thermo Fisher, USA) for 1 h. For visualization of actin filaments, cells were incubated for 1 h at T = 23 °C with Alexa Fluor™ 488 Phalloidin (Thermo Fisher, USA) and then rinsed three times in PBS. Nuclear DNA was counterstained with DAPI (Sigma-Aldrich, UK) for 10 min. After staining, samples were rinsed with PBS three times (15 min each). The same laser parameters were used for focal adhesion imaging with the confocal microscope.

2.8.4. SEM imaging of cells

SEM imaging of cells on PLLA scaffolds was done after 7 and 14 days of culture. Cells were fixed with 2.5 % glutaraldehyde (Sigma-Aldrich, UK) for 1 h at 25 °C. Next, samples were rinsed three times with PBS and dehydrated in alcohol solution series (Avantor, Poland) with increasing ethanol concentrations (50 %, 70 %, 80 %, 90 %, 100 %). The scaffold incubation lasted 7 min for each solution and was repeated twice for 100 % ethanol solution. Further, samples were incubated in hexamethyldisilazane (HDMS, Sigma-Aldrich, UK). After complete evaporation of HDMS, samples were coated with an 8 nm thick gold layer and imaged with the same SEM parameters mentioned above for fibers characterization.

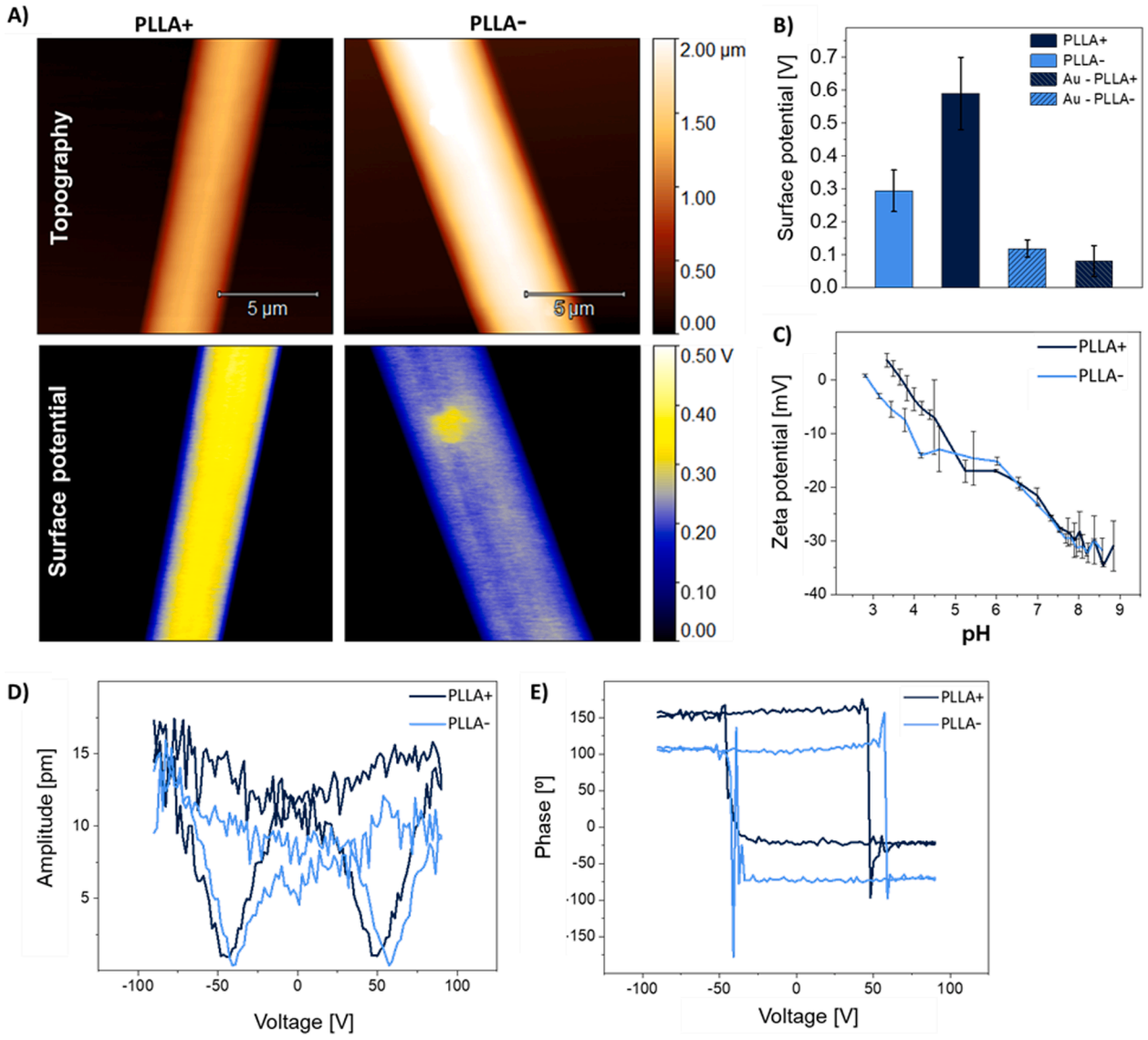

Fig. 2. A) Topography images with corresponding surface potential maps of PLLA+ and PLLA- fibers, B) plot of average values of surface potential with accompanying data for Au, C) zeta potential measurement results for PLLA+ and PLLA-. PFM measurement PLLA+ and PLLA- fibers: the exemplary plot of D) displacement versus voltage, and E) phase versus voltage. Errors are based on standard deviation.

3. Results and discussion

3.1. PLLA fibers morphology and wetting properties

The SEM micrographs show a smooth PLLA fiber surface in both cases without any pores or beads. The average fiber diameter was 2.2 µm ± 0.7 µm for PLLA+ and 2.4 µm ± 0.9 µm for PLLA-; see SEM images and histogram of the fiber diameter in Fig. 1 A) – C). To evaluate the wetting properties, water contact angles were measured and resulted in 120° depicting the hydrophobic nature of PLLA fibers (see Supplementary Information Fig. S1 A) and B)). The scaffold topography and wettability are essential in regulating the initial cell behavior, such as cell adhesion and proliferation. It is noteworthy that the porosity of electrospun scaffolds is in the range of 70 % – 90 %. Both PLLA scaffolds provide similar structural support and geometry for cells [51–54]. The representative image of scaffold is presented in Supplementary Information Fig. S1 C).

3.2. Chemistry and surface potential

The effect of the voltage polarity applied to the nozzle during the electrospinning of polymer fibers has already been described [23,52]. The applied charges at the liquid interface of a polymer solution affect the surface chemistry of electrospun fibers. Owing to the repulsion or attraction of electronegative functional groups with double-bonded oxygen, polymer chains in PLLA fibers can be reoriented toward the fiber surface [52]. Here, the surface chemistry of the PLLA fibers was examined with ARXPS to verify the presence of double and single-bonded oxygen for both PLLA+ and PLLA-, see Fig. 1 D) and Supplementary Information Fig. S2. The XPS study suggests that the reorientation of oxygen in PLLA molecules occurs due to a change in polarity, which is confirmed by the different intensity of O1s region at the 15 ° angle measurement for PLLA+ and PLLA-. Additionally, the DSC results showed 2 °C higher T_g for PLLA- fibers, indicating the structural changes in PLLA due to applied voltage polarity in electrospinning, see Fig. 1 E).

DSC results showed the highest crystallinity for the PLLA pellets 88.9 ± 0.5 %, and comparable crystallinity within borders of error for PLLA+

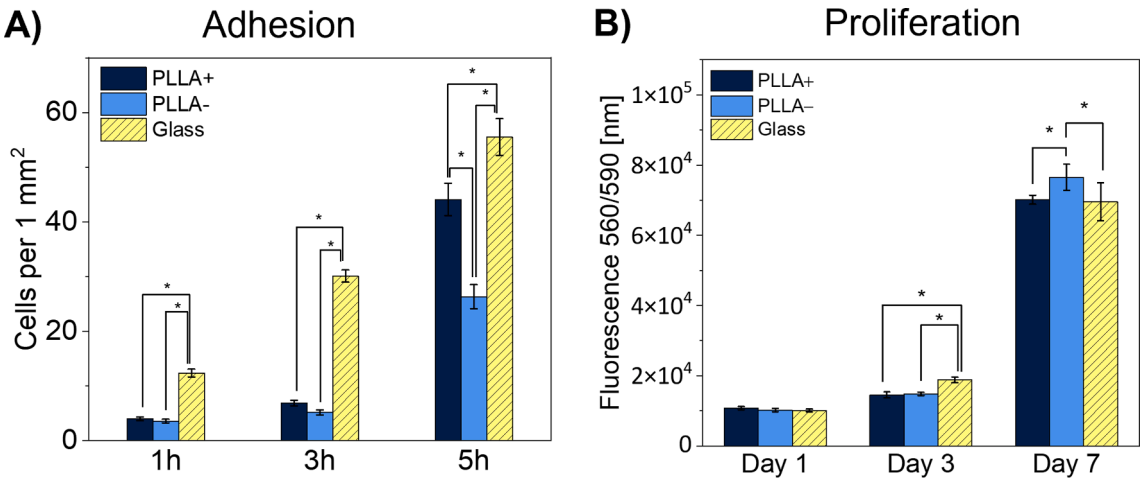

Fig. 3. Graphs of A) adhesion and B) proliferation assays of osteoblasts cells (MG – 63 cell line) on PLLA+ and PLLA- fibers, glass as the control. * Statistical significance calculated with ANOVA, followed by Tukey's post-hock test, $p < 0.05$; error bars are based on standard errors.

and PLLA-, 53.43 ± 0.94 %, and 55.84 ± 1.72 %, respectively. The similar bulk chemistry of PLLA+ and PLLA- samples was confirmed via FTIR, see Fig. 1 F). The main characteristic peaks of PLLA are located at 1750 cm^{-1}, corresponding to the C═O stretching mode of ester group [55,56]; 1211 and 1182 cm^{-1} are assigned to C—O—C and CH_3 groups [56] Bands at 1044 cm^{-1}, 1087 cm^{-1}, 1132 cm^{-1}, 1456 cm^{-1} are attributed to asymmetric deformation of C-CH_3, C—O—C, C-CH_3, CH_3, respectively. Stretching of CH_3 group is also shown by peaks at 2946 and 2996 cm^{-1} [44]. The peak at 1384 cm^{-1} is assigned to the stretching of C—H.[55] Weaker peaks at 872 and 921 cm^{-1} indicate the existence of α-crystals [44]. The band at 755 cm^{-1} is correlated with C═O bending. [49]. Importantly, we can obtain information about the crystallinity from the area of the amorphous band at 955 cm^{-1} by observing its changes compared to the area of the band of the crystalline phase at 921 cm^{-1}. Calculation of total crystallinity using eq. (1) showed the crystallinity of 60.8 % for the PLLA pellets, 28.06 % and 25.74 % for PLLA+ and PLLA- samples, respectively. Analysis of FTIR results, presented in Fig. 1 G), let us conclude that analog to DSC results, the PLLA pellets showed the highest crystallinity, whereas PLLA+ fibers are slightly more crystalline than PLLA-. Decreased crystallinity of PLLA fibers comparing to pellets is ascribed to the electrospinning parameters. During the solidification and stretching of fibers, polymer chains are limited in time to organize into crystal structure prior to their solidification [57].

The results for PLLA fibers from AFM topography scans with accompanying surface potential maps are shown in Fig. 2 A). The results demonstrate a significantly higher average surface potential of 589 ± 109 mV when electrospinning with positive voltage polarity (PLLA+), as compared to PLLA- fibers with a surface potential of 294 ± 62 mV when applying negative polarity. The values for Au used as control and background of the fibers samples were similar being 118 ± 25 mV and 80 ± 47 mV for PLLA- and PLLA+ samples, respectively, see Fig. 2 B). Voltage polarity during electrospinning affecting surface chemistry has a significant impact on the surface potential of PLLA fibers, where the potential is almost doubled for PLLA produced with positive voltage polarity. To further study – fiber surface potential, the zeta potential of PLLA fibers was measured as a function of pH in the range from pH 3.0 to 9.0 in a standard KCl solution. Zeta potential is key information on the behavior of the functional groups from the surface of the fibers in contact with acidic or base fluids that can represent the pH of the biological fluids. Therefore, this parameter is essential for understanding cellular interactions with the scaffold in the biological environment. [58]. Previously, it was presented that PCL, PHBV, and PC fibers electrospun with different voltage polarity exhibit zeta potential varying in pH function [17,59,60]. In Fig. 2 C) we show titration curves of zeta potential disparity in the PLLA samples in the pH between 3.0 and 9.0. Notwithstanding, zeta potential is comparable for both scaffolds reaching values from 3.7 to −30.94 mV for PLLA+ and from 0.86 to −31.73 mV for PLLA-. The largest difference in the value between the PLLA samples was observed in the 3 to 4.5 range of pH, where the zeta potential varies by about 5 mV. However, at pH 7, which is in the range of the biological fluids, the results of the zeta potential for PLLA fibers with high and low surface potential are similar, indicating that the initial surface potential is stabilized for both PLLA scaffolds.

Lately, the discovery of the piezoelectricity of PLLA caused a growing interest in exploring this biodegradable polymer as a substitute structure in bone regeneration [14,61]. The piezo activity of PLLA polymer was proved with a piezoelectric constant d_{14} of ~ 10 pC/N [49]. The electrospinning process can induce a piezoelectric response through stretching polymer chains of PLLA in an electric field which allows the transformation of the stable α-crystalline form into the β-crystalline form in which chains are aligned along the stretching direction, increasing polarization and piezoelectricity [62]. In this study, the incidence of β-crystalline form was not verified due to the lack of presence of the characteristic peak 908 cm^{-1} in FTIR spectrum [44]. The piezoelectric response of electrospun PLLA single fibers was measured using PFM [45,49,61].

Here, the piezoelectric properties in PLLA electrospun fibers were verified using HVSS-PFM, see Fig. 2 D), E). We observed the piezoelectric response in d_{33} orientation, confirming previous reports for fibers [63]. On average, we observe 35 % difference in displacement between samples, with PLLA+ being more piezoelectric. At the highest, PLLA+ provided a 107 % stronger displacement than its PLLA- counterpart. The shift of the hysteresis loops centers from 0 V indicates the possible existence of permanent change in the material caused by material processing [64] The average diameter of studied fibers was 1699 ± 42 nm and 1263 ± 6 nm for PLLA- and PLLA+, respectively, what can affect the d_{33} coefficient [36]. For both materials, we observed phase switching for similar voltages, namely −40 and 60 V showing hysteretic behavior, see Fig. 2 E). PLLA scaffolds electrospun with positive voltage polarity to show significantly higher surface potential and piezoelectric response, which is confirmed with the increased content of crystalline phase in PLLA+ verified by FTIR results.

3.3. Cell responses to material properties

3.3.1. Cell adhesion and proliferation

The initial cell adhesion, thus the first stage of attachment to the substrate, is a crucial factor affecting cell growth, differentiation, viability, and spreading[65]. Specific properties of polymer scaffolds, such as the geometry of fibers, stiffness, or surface charge, can promote

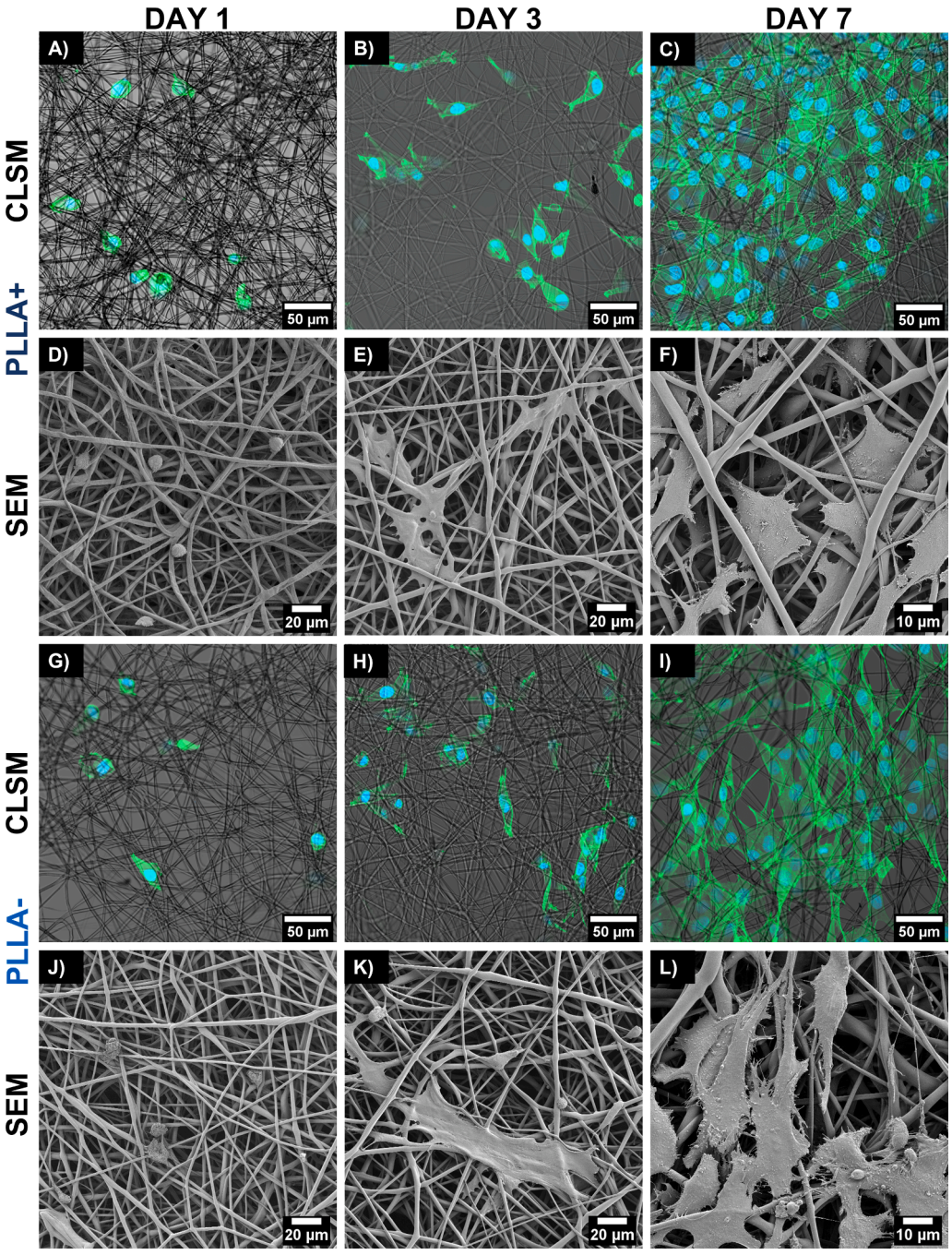

Fig. 4. CLSM and corresponding SEM images of MG – 63 cells A) - F) on PLLA+, and G)– L) on PLLA- fibers after 1,3,7 days of culture. The nuclei were stained with DAPI (blue), and the actin filaments with Alexa Fluor™ 488 Phalloidin (green). (For interpretation of the references to colour in this figure legend, the reader is referred to the web version of this article.)

particular cell responses [10]. In this study, we analyzed osteoblast adhesion to electrospun PLLA+ and PLLA- fibers after 1, 3, and 5 h from seeding, see Fig. 3 A). Clearly, the higher surface potential of fibers in PLLA+ increases cell adhesion. The number of cells on PLLA+ per 1 mm^2 of the sample after 5 h was approximately 40 % higher than on PLLA-. The cell viability tested with MTS assay after 1,3, and 7 days of incubation was similar in the margin of error for both samples of PLLA fibers, see Fig. 3 B). As the geometry and morphology of the scaffolds was similar, the main difference between PLLA scaffolds was the surface potential and piezoelectricity. The higher surface charge stimulates cells to attach to the preferable surfaces, which affects the very early stage of cell development. It is worth mentioning that zeta potential values around pH 7 was also stabilized for both types of scaffolds at similar values, suggesting that in the cell culture medium, the initial difference surface charge measured with KPFM was neutralized in a basic environment at higher temperature reaching 37 °C from the 23 °C used or the dry condition measurement [66].

3.3.2. *Cell morphology*

Microscopy investigation of osteoblast's response to PLLA fiber is indicated by the morphology of cells presented in Fig. 4. This study showed that cells were developing their cytoskeleton parallel in both samples of PLLA scaffolds. SEM micrographs of the 1st day show only nuclei and inchoate actin filaments. On the 3rd and 7th day, actin filaments were nicely stretched along the PLLA fibers. After 7 days, cells were distributed throughout the volume of the samples with many

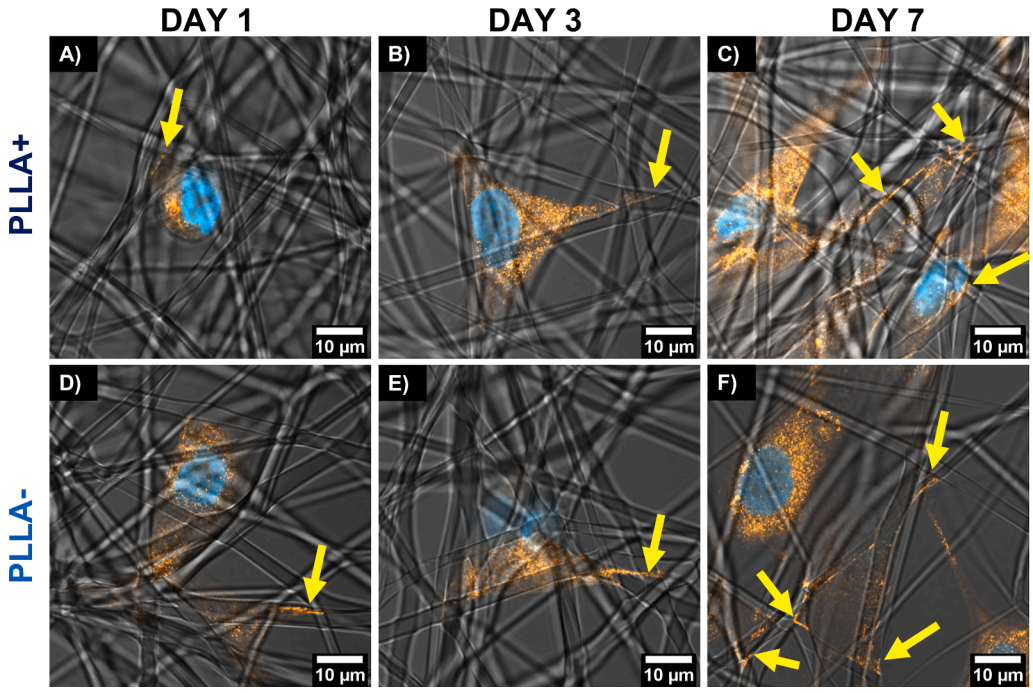

Fig. 5. CLSM images of MG – 63 cells on PLLA+ and PLLA- fibers after 1,3,7 days of culture. The nuclei were stained with DAPI (blue), and the focal adhesions (paxillin) Alexa Fluor™ Plus 555 (orange) indicated with yellow arrows. (For interpretation of the references to colour in this figure legend, the reader is referred to the web version of this article.)

visible filopodia attached to the fibers (Fig. 4 C), F)). Also, focal adhesions, marked with yellow arrows in Fig. 5, were already present after one day of cell incubation on both PLLA samples. A large amount of visible focal adhesions on day 7 (Fig. 5 C) and F)) is a strong hint about proper cell–material interaction without any significant effect of high or low surface potential PLLA scaffolds. The osteoblasts' shape and distribution together with the actin formation, were very similar for both PLLA scaffolds. Importantly, we start with the huge differences in the surface potential between the fibers in PLLA scaffolds initiating the differences in cell adhesion. However, the zeta potential indicates no differences at pH 7, which is a typical environment during cell culture studies. Therefore, cell proliferation up to 7 days is similar for both PLLA scaffolds. Zeta potential gives information about the surface charge of material in the physiological environment, which is crucial considering the adhesion of proteins affected by this surface potential and further tissue regeneration process [30]. However, not only the surface charge for PLLA scaffolds is important for investigating the osteoblasts responses, but also piezoelectricity should be considered [29] We observed a higher piezo response for PLLA+, which can be related to the higher surface charge of fibers and better adhesion of cells. Simply, the piezoelectric materials generate surface charges of fibers due to cellular motion on the scaffolds [30]. Here, the morphology of osteoblasts up to 7 days was similar for both types of PLLA scaffolds. Interestingly, we observe enhanced initial adhesion of osteoblast-like cells caused by the higher surface potential of material without a strong influence on the proliferation or morphology of cells. Previously a similar observation was in the context of the surface roughness effect on initial osteoblast adhesion, which was related to strengthening expressions of osteogenic genes that can improve osteoblastic differentiation [67]. The enhanced initial adhesion is shown to be associated with higher osteogenic gene expressions without differences in proliferation up to 5 days and morphology of cells in 24 h after seeding.

3.3.3. Collagen

Engineering of biomaterials imitating bone tissue focuses on designing and producing 3D structures that reflect the properties of ECM to the greatest possible extent. ECM is a highly organized structure, predominantly built of collagen fibrils and networks. It surrounds and supports cells, being a flexible substance that guides cellular behavior, tissue structure properties, and regeneration. So far, 28 collagen types have been identified [68]. Still, bone tissue consists mainly of type I collagen and a small quantity of type V [68]. Our investigation leads to the study of the relationship between the surface potential of PLLA fibrous scaffolds and type I collagen formation in the 14 and 21 days of culturing osteoblast cells. CLSM images (Fig. 6) demonstrate highly advanced 3D, fibrous collagen structures in each time point for PLLA+ and PLLA- fibers samples. The collagen networks showed a similar pattern for both types of PLLA scaffolds. SEM micrographs showing the surface of cells growing on PLLA fibers indicate that continuous biological processes took place between 14 and 21 days, leading to a change in their morphology. For both PLLA+ and PLLA- scaffolds, cells on day 21 form a more dense and solid structure that on day 14, with increasing collagen and actin formations, see Fig. 6. Previous studies of the relation between the surface potential of PCL fibers in the range of 550 and 700 mV and collagen formation of osteoblast cells showed that increased surface potential favored better collagen formation [17]. The results for PLLA scaffolds indicate their excellent biomimicking environment for enhanced cell development and regeneration process of bone tissue. Still, quantitative analysis of collagen formation in further studies is needed to verify surface potential role in PLLA fibers.

4. Conclusions

This work was focused on creating a favorable bioelectric environment using PLLA scaffolds. Within this study, we proved the great possibility of tuning surface potential as well as piezoelectricity of PLLA fibers by applying positive or negative voltage polarity during the electrospinning process. We successfully produced PLLA scaffolds with higher surface potential and piezoelectric responses. We proved that enhanced PLLA scaffolds' surface and structural properties cause significantly higher adhesion of osteoblast cells, especially in the first 5 h. Further studies indicated a similar proliferation of up to 7 days for

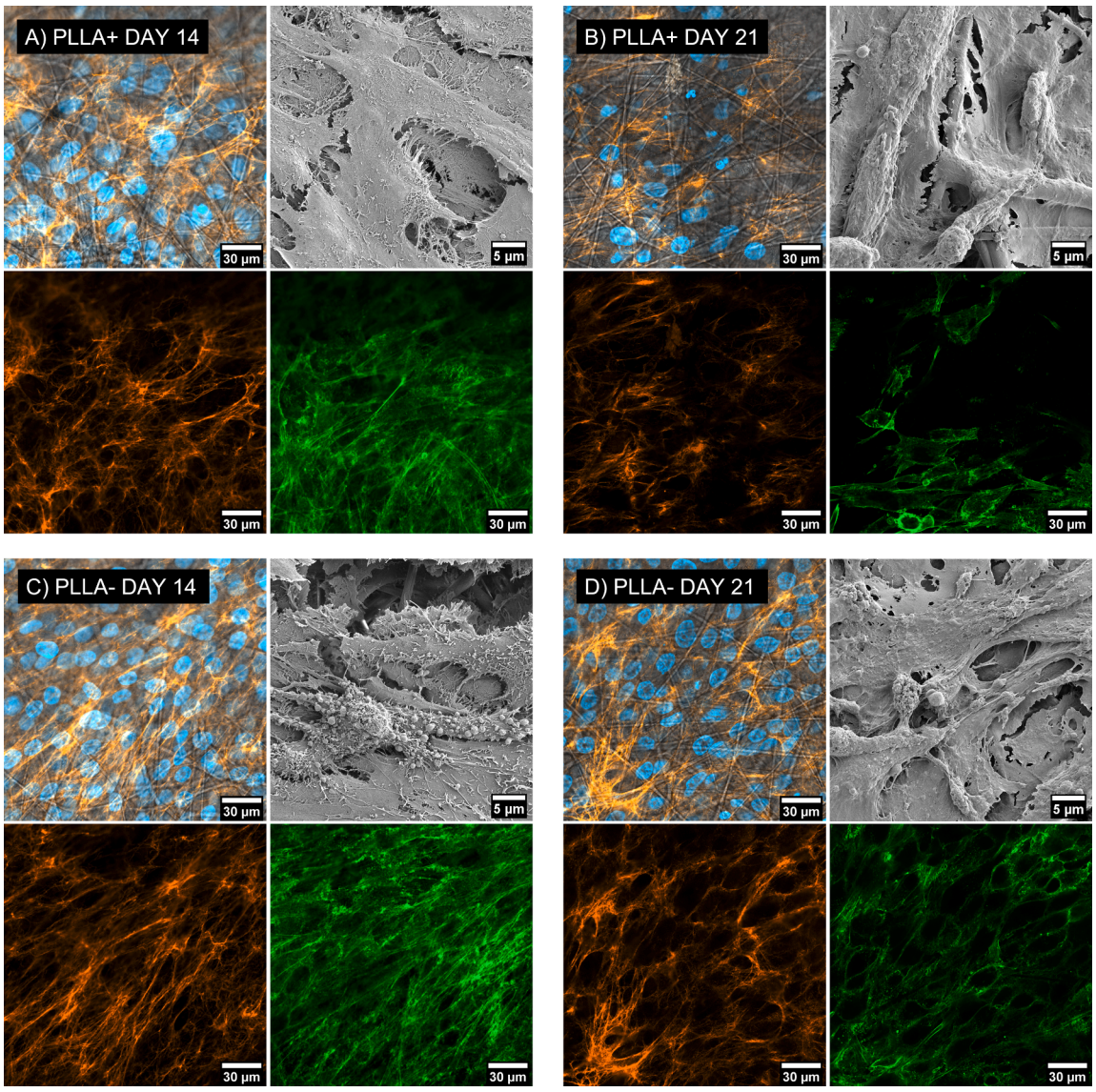

Fig. 6. CLSM and SEM images of MG – 63 cells A) and B) on PLLA+, and C) and D) PLLA- fibers after 14 and 21 days of culturing. Confocal imaging micrographs show collagen (orange), actin filaments (green), and nuclei (blue) stained with Alexa Fluor™ Plus 555, Alexa Fluor™ 488 Phalloidin, DAPI, respectively. (For interpretation of the references to colour in this figure legend, the reader is referred to the web version of this article.)

both scaffolds. Confocal microscopy analysis confirmed that cytoskeleton, filopodia, and focal adhesions were developing at the same high level, without surface potential effect causing any abnormalities in cells. Moreover, collagen formation was observed, showing 3D structure of collagen for both PLLA scaffolds. Generally, PLLA fibers are the favorable material in the form of electrospun scaffolds for osteoblasts, as indicated by numerous adhesion focal points and collagen production. Importantly, surface charges of PLLA fibers affected cell response resulting in enhanced adhesion due to the electrostatic interaction between negatively charged cells. These significant results will be investigated further in gene expression tests to understand the mechanism of cell adhesion and attachment process in early contact of cells with the PLLA scaffolds.

CRediT authorship contribution statement

Martyna Polak: Methodology, Investigation and experiments, Data curation, Writing - Original Draft preparation, Writing - Review and editing, Cells culture. **Krzysztof Berniak:** Methodology, Investigation and experiments, Data curation, Cells culture. **Piotr K. Szewczyk:** Investigation and experiments, Data curation. **Joanna E. Karbowniczek:** Methodology, Investigation and experiments, Writing - Review and editing, Cells culture. **Mateusz M. Marzec:** Investigation and experiments, Data curation. **Urszula Stachewicz:** Conceptualization, Methodology, Formal analysis, Data curation, Writing - Original Draft preparation, Writing - Review and editing, Supervision, Project administration, Funding acquisition. All authors provided critical feedback and helped shape the research, analysis, and manuscript.

Declaration of Competing Interest

The authors declare that they have no known competing financial interests or personal relationships that could have appeared to influence the work reported in this paper.

Data availability

Data will be made available on request.

Acknowledgment

This study was conducted with funding from the OPUS 17 project grant provided by the National Science Centre in Poland. No 2019/33/B/ST5/01311. The confocal microscopy studies were performed by Krzysztof Berniak in the project "Nanofiber-based sponges for atopic skin treatment" carried out within the First TEAM program of the Foundation for Polish Science co-financed by the European Union under the European Regional Development Fund, No POIR.04.04.00-00-4571/17-00.

Appendix A. Supplementary material

Supplementary data to this article can be found online at https://doi.org/10.1016/j.apsusc.2023.156835.

References

[1] S. Cai, C. Wu, W. Yang, W. Liang, H. Yu, L. Liu, Recent advance in surface modification for regulating cell adhesion and behaviors, Nanotechnol. Rev. 9 (2020) 971–989, https://doi.org/10.1515/ntrev-2020-0076.
[2] J. Nicolas, S. Magli, L. Rabbachin, S. Sampaolesi, F. Nicotra, L. Russo, 3D Extracellular Matrix Mimics: Fundamental Concepts and Role of Materials Chemistry to Influence Stem Cell Fate, Biomacromolecules 21 (2020) 1968–1994, https://doi.org/10.1021/acs.biomac.0c00045.
[3] L. Cai, D. Xu, H. Chen, L. Wang, Y. Zhao, Designing bioactive micro-/nanomotors for engineered regeneration, Engineered Regeneration. 2 (2021) 109–115, https://doi.org/10.1016/j.engreg.2021.09.003.
[4] Y. Gao, Q. Ma, Bacterial infection microenvironment-responsive porous microspheres by microfluidics for promoting anti-infective therapy, Smart Med. 1 (2022), https://doi.org/10.1002/smmd.20220012.
[5] B. Holmes, N.J. Castro, L.G. Zhang, E. Zussman, Electrospun fibrous scaffolds for bone and cartilage tissue generation: Recent progress and future developments, Tissue Eng. B Rev. 18 (2012) 478–486, https://doi.org/10.1089/ten.teb.2012.0096.
[6] M.B. Taskin, T. Ahmad, L. Wistlich, L. Meinel, M. Schmitz, A. Rossi, J. Groll, Bioactive Electrospun Fibers: Fabrication Strategies and a Critical Review of Surface-Sensitive Characterization and Quantification, Chem. Rev. 121 (2021) 11194–11237, https://doi.org/10.1021/acs.chemrev.0c00816.
[7] M. Nikkhah, F. Edalat, S. Manoucheri, A. Khademhosseini, Engineering microscale topographies to control the cell-substrate interface, Biomaterials 33 (2012) 5230–5246, https://doi.org/10.1016/j.biomaterials.2012.03.079.
[8] S. di Cio, J.E. Gautrot, Cell sensing of physical properties at the nanoscale: Mechanisms and control of cell adhesion and phenotype, Acta Biomater. 30 (2016) 26–48, https://doi.org/10.1016/j.actbio.2015.11.027.
[9] N.A. Kamel, Bio-piezoelectricity: fundamentals and applications in tissue engineering and regenerative medicine, Biophys. Rev. 14 (2022) 717–733, https://doi.org/10.1007/s12551-022-00969-z.
[10] S. Metwally, U. Stachewicz, Surface potential and charges impact on cell responses on biomaterials interfaces for medical applications, Mater. Sci. Eng. C 104 (2019), https://doi.org/10.1016/j.msec.2019.109883.
[11] M. Levin, Bioelectric mechanisms in regeneration: Unique aspects and future perspectives, Semin. Cell Dev. Biol. 20 (2009) 543–556, https://doi.org/10.1016/j.semcdb.2009.04.013.
[12] M.P. Harris, Bioelectric signaling as a unique regulator of development and regeneration, Development (Cambridge). 148 (2021), https://doi.org/10.1242/DEV.180794.
[13] R. Hosaki-Takamiya, M. Hashimoto, Y. Imai, T. Nishida, N. Yamada, H. Mori, T. Tanaka, N. Kawanabe, T. Yamashiro, H. Kamioka, Collagen production of osteoblasts revealed by ultra-high voltage electron microscopy, J. Bone Miner. Metab. 34 (2016) 491–499, https://doi.org/10.1007/s00774-015-0692-0.
[14] A. Zaszczynska, P. Sajkiewicz, A. Gradys, Piezoelectric scaffolds as smart materials for neural tissue engineering, Polymers (Basel). 12 (2020), https://doi.org/10.3390/polym12010161.
[15] S. Guerin, S.A.M. Tofail, D. Thompson, Longitudinal piezoelectricity in natural calcite materials: Preliminary studies, IEEE Trans. Dielectr. Electr. Insul. 25 (2018) 803–807, https://doi.org/10.1109/TDEI.2017.007045.
[16] A. Owczarzy, R. Kurasiński, K. Kulig, W. Rogóż, A. Szkudlarek, M. Maciążek-Jurczyk, COLLAGEN-STRUCTURE, PROPERTIES AND APPLICATION, (n.d.). https://doi.org/10.34821/eng.biomat.156.2020.17-23.
[17] S. Metwally, S. Ferraris, S. Spriano, Z.J. Krysiak, Ł. Kaniuk, M.M. Marzec, S.K. Kim, P.K. Szewczyk, A. Gruszczyński, M. Wytrwal-Sarna, J.E. Karbowniczek, A. Bernasik, S. Kar-Narayan, U. Stachewicz, Surface potential and roughness controlled cell adhesion and collagen formation in electrospun PCL fibers for bone regeneration, Mater. Des. 194 (2020), https://doi.org/10.1016/j.matdes.2020.108915.
[18] Y. Yan, V. Sencadas, T. Jin, X. Huang, J. Chen, D. Wei, Z. Jiang, Tailoring the wettability and mechanical properties of electrospun poly(L-lactic acid)-poly (glycerol sebacate) core-shell membranes for biomedical applications, J. Colloid Interface Sci. 508 (2017) 87–94, https://doi.org/10.1016/j.jcis.2017.08.033.
[19] N.D. Wanasekara, S. Ghosh, M. Chen, V.B. Chalivendra, S. Bhowmick, Effect of stiffness of micron/sub-micron electrospun fibers in cell seeding, J. Biomed. Mater. Res. A 103 (2015) 2289–2299, https://doi.org/10.1002/jbm.a.35362.
[20] I. Greenfeld, X. Sui, H.D. Wagner, Stiffness, Strength, and Toughness of Electrospun Nanofibers: Effect of Flow-Induced Molecular Orientation, Macromolecules 49 (2016) 6518–6530, https://doi.org/10.1021/acs.macromol.6b01204.
[21] S.C. Wong, A. Baji, S. Leng, Effect of fiber diameter on tensile properties of electrospun poly(ε-caprolactone), Polymer (Guildf). 49 (2008) 4713–4722, https://doi.org/10.1016/j.polymer.2008.08.022.
[22] A. Arinstein, M. Burman, O. Gendelman, E. Zussman, Effect of supramolecular structure on polymer nanofibre elasticity, Nat. Nanotechnol. 2 (2007) 59–62, https://doi.org/10.1038/nnano.2006.172.
[23] D.P. Ura, U. Stachewicz, The Significance of Electrical Polarity in Electrospinning: A Nanoscale Approach for the Enhancement of the Polymer Fibers' Properties, Macromol. Mater. Eng. 307 (2022), https://doi.org/10.1002/mame.202100843.
[24] G.C. Rutledge, S. v. Fridrikh, Formation of fibers by electrospinning, Adv Drug Deliv Rev. 59 (2007) 1384–1391. https://doi.org/10.1016/j.addr.2007.04.020.
[25] O. Urbanek, P. Sajkiewicz, F. Pierini, The effect of polarity in the electrospinning process on PCL/chitosan nanofibres' structure, properties and efficiency of surface modification, Polymer (Guildf). 124 (2017) 168–175, https://doi.org/10.1016/j.polymer.2017.07.064.
[26] D.P. Ura, J. Rosell-Llompart, A. Zaszczyńska, G. Vasilyev, A. Gradys, P. K. Szewczyk, J. Knapczyk-Korczak, R. Avrahami, A.O. Šišková, A. Arinstein, P. Sajkiewicz, E. Zussman, U. Stachewicz, The role of electrical polarity in electrospinning and on the mechanical and structural properties of as-spun fibers, Materials. 13 (2020), https://doi.org/10.3390/ma13184169.
[27] Y. Li, C. Liao, S.C. Tjong, Electrospun polyvinylidene fluoride-based fibrous scaffolds with piezoelectric characteristics for bone and neural tissue engineering, Nanomaterials 9 (2019), https://doi.org/10.3390/nano9070952.
[28] D. Khare, B. Basu, A.K. Dubey, Electrical stimulation and piezoelectric biomaterials for bone tissue engineering applications, Biomaterials 258 (2020), https://doi.org/10.1016/j.biomaterials.2020.120280.
[29] C. Ribeiro, V. Sencadas, D.M. Correia, S. Lanceros-Méndez, Piezoelectric polymers as biomaterials for tissue engineering applications, Colloids Surf. B Biointerfaces 136 (2015) 46–55, https://doi.org/10.1016/j.colsurfb.2015.08.043.
[30] B. Tandon, J.J. Blaker, S.H. Cartmell, Piezoelectric materials as stimulatory biomedical materials and scaffolds for bone repair, Acta Biomater. 73 (2018) 1–20, https://doi.org/10.1016/j.actbio.2018.04.026.
[31] Piotr K. Szewczyk, Krzysztof Berniak, Joanna Knapczyk-Korczak, Joanna E. Karbowniczek, Mateusz M. Marzec, Andrzej Bernasik, and Urszula Stachewicz, Mimicking natural electrical environment with cellulose acetate scaffolds enhances collagen formation of osteoblasts, Nanoscale. (2023). https://doi.org/DOI: 10.1039/d3nr00014a.
[32] Y. Cheng, Y. Xu, Y. Qian, X. Chen, Y. Ouyang, W.E. Yuan, 3D structured self-powered PVDF/PCL scaffolds for peripheral nerve regeneration, Nano Energy 69 (2020), https://doi.org/10.1016/j.nanoen.2019.104411.
[33] P.K. Szewczyk, A. Gradys, S.K. Kim, L. Persano, M. Marzec, A. Kryshtal, T. Busolo, A. Toncelli, D. Pisignano, A. Bernasik, S. Kar-Narayan, P. Sajkiewicz, U. Stachewicz, Enhanced Piezoelectricity of Electrospun Polyvinylidene Fluoride Fibers for Energy Harvesting, ACS Appl. Mater. Interfaces 12 (2020) 13575–13583, https://doi.org/10.1021/acsami.0c02578.
[34] Ł. Kaniuk, U. Stachewicz, Development and Advantages of Biodegradable PHA Polymers Based on Electrospun PHBV Fibers for Tissue Engineering and Other Biomedical Applications, ACS Biomater Sci. Eng. 7 (2021) 5339–5362, https://doi.org/10.1021/acsbiomaterials.1c00757.
[35] T. Zheng, Z. Yue, G.G. Wallace, Y. Du, M.J. Higgins, Nanoscale piezoelectric effect of biodegradable PLA-based composite fibers by piezoresponse force microscopy, Nanotechnology 31 (2020), https://doi.org/10.1088/1361-6528/ab96e3.
[36] Y. Tai, S. Yang, S. Yu, A. Banerjee, N. v. Myung, J. Nam, Modulation of piezoelectric properties in electrospun PLLA nanofibers for application-specific self-powered stem cell culture platforms, Nano Energy. 89 (2021). https://doi.org/10.1016/j.nanoen.2021.106444.
[37] S. Farah, D.G. Anderson, R. Langer, Physical and mechanical properties of PLA, and their functions in widespread applications — A comprehensive review, Adv. Drug Deliv. Rev. 107 (2016) 367–392, https://doi.org/10.1016/j.addr.2016.06.012.
[38] A.M. Tryba, M. Krok-Borkowicz, M. Kula, N. Piergies, M. Marzec, E. Wegener, J. Fraczyk, R. Jordan, B. Kolesińska, D. Scharnweber, C. Paluszkiewicz, E. Pamuła, Surface Functionalization of Poly(L-lactide-co-glycolide) Membranes with RGD-Grafted Poly(2-oxazoline) for Periodontal Tissue Engineering, J Funct Biomater. 13 (2022), https://doi.org/10.3390/jfb13010004.
[39] P. Muniyandi, V. Palaninathan, S. Veeranarayanan, T. Ukai, T. Maekawa, T. Hanajiri, M.S. Mohamed, ECM mimetic electrospun porous poly (l-lactic acid) (PLLA) scaffolds as potential substrates for cardiac tissue engineering, Polymers (Basel). 12 (2020), https://doi.org/10.3390/polym12020451.
[40] P. Feng, P. Wu, C. Gao, Y. Yang, W. Guo, W. Yang, C. Shuai, A Multimaterial Scaffold With Tunable Properties: Toward Bone Tissue Repair, Adv. Sci. 5 (2018), https://doi.org/10.1002/advs.201700817.
[41] J.H. Lee, Y.J. Lee, H.J. Cho, H. Shin, Guidance of in vitro migration of human mesenchymal stem cells and in vivo guided bone regeneration using aligned electrospun fibers, Tissue Eng. A 20 (2014) 2031–2042, https://doi.org/10.1089/ten.tea.2013.0282.
[42] X. Zhang, R. Nakagawa, K.H.K. Chan, M. Kotaki, Mechanical property enhancement of polylactide nanofibers through optimization of molecular weight, electrospinning conditions, and stereocomplexation, Macromolecules 45 (2012) 5494–5500, https://doi.org/10.1021/ma300289z.

[43] P. Feng, J. Jia, S. Peng, Y. Shuai, H. Pan, X. Bai, C. Shuai, Transcrystalline growth of PLLA on carbon fiber grafted with nano-SiO2 towards boosting interfacial bonding in bone scaffold, Biomater Res. 26 (2022), https://doi.org/10.1186/s40824-021-00248-0.
[44] C. Ribeiro, V. Sencadas, C.M. Costa, J.L. Gómez Ribelles, S. Lanceros-Méndez, Tailoring the morphology and crystallinity of poly(L-lactide acid) electrospun membranes, Sci Technol, Adv. Mater. 12 (2011), https://doi.org/10.1088/1468-6996/12/1/015001.
[45] V. Sencadas, C. Ribeiro, A. Heredia, I.K. Bdikin, A.L. Kholkin, S. Lanceros-Mendez, Local piezoelectric activity of single poly(L-lactic acid) (PLLA) microfibers, Appl. Phys. A Mater. Sci. Process. 109 (2012) 51–55, https://doi.org/10.1007/s00339-012-7095-z.
[46] R. Inai, M. Kotaki, S. Ramakrishna, Structure and properties of electrospun PLLA single nanofibres, Nanotechnology 16 (2005) 208–213, https://doi.org/10.1088/0957-4484/16/2/005.
[47] N.T. Cuong, S. Barrau, M. Dufay, N. Tabary, A. da Costa, A. Ferri, R. Lazzaroni, J. M. Raquez, P. Leclère, On the nanoscale mapping of the mechanical and piezoelectric properties of poly (L-lactic acid) electrospun nanofibers, Applied Sciences (Switzerland). 10 (2020), https://doi.org/10.3390/app10020652.
[48] M. Radjabian, M.H. Kish, N. Mohammadi, Characterization of poly(lactic acid) multifilament yarns. I. The structure and thermal behavior, J. Appl. Polym. Sci. 117 (2010) 1516–1525, https://doi.org/10.1002/app.32046.
[49] I.O. Pariy, R. v. Chernozem, P. v. Chernozem, Y.R. Mukhortova, A.G. Skirtach, V. v. Shvartsman, D.C. Lupascu, M.A. Surmeneva, S. Mathur, R.A. Surmenev, Hybrid biodegradable electrospun scaffolds based on poly(l-lactic acid) and reduced graphene oxide with improved piezoelectric response, Polym J. (2022). https://doi.org/10.1038/s41428-022-00669-1.
[50] S. Jesse, A.P. Baddorf, S. v. Kalinin, Switching spectroscopy piezoresponse force microscopy of ferroelectric materials, Appl Phys Lett. 88 (2006). https://doi.org/10.1063/1.2172216.
[51] R. Tzoneva, N. Faucheux, T. Groth, Wettability of substrata controls cell-substrate and cell-cell adhesions, Biochim. Biophys. Acta Gen. Subj. 1770 (2007) 1538–1547, https://doi.org/10.1016/j.bbagen.2007.07.008.
[52] S. Metwally, J.E. Karbowniczek, P.K. Szewczyk, M.M. Marzec, A. Gruszczyński, A. Bernasik, U. Stachewicz, Single-Step Approach to Tailor Surface Chemistry and Potential on Electrospun PCL Fibers for Tissue Engineering Application, Adv. Mater. Interfaces 6 (2019), https://doi.org/10.1002/admi.201801211.
[53] U. Stachewicz, P.K. Szewczyk, A. Kruk, A.H. Barber, A. Czyrska-Filemonowicz, Pore shape and size dependence on cell growth into electrospun fiber scaffolds for tissue engineering: 2D and 3D analyses using SEM and FIB-SEM tomography, Mater. Sci. Eng. C 95 (2019) 397–408, https://doi.org/10.1016/j.msec.2017.08.076.
[54] F. Croisier, A.S. Duwez, C. Jérôme, A.F. Léonard, K.O. van der Werf, P.J. Dijkstra, M.L. Bennink, Mechanical testing of electrospun PCL fibers, Acta Biomater. 8 (2012) 218–224, https://doi.org/10.1016/j.actbio.2011.08.015.
[55] F. Nazir, M. Iqbal, A.N. Khan, M. Mazhar, Z. Hussain, Fabrication of robust poly L-lactic acid/cyclic olefinic copolymer (PLLA/COC) blends: study of physical properties, structure, and cytocompatibility for bone tissue engineering, J. Mater. Res. Technol. 13 (2021) 1732–1751, https://doi.org/10.1016/j.jmrt.2021.05.073.
[56] A. Leroy, S. Ribeiro, C. Grossiord, A. Alves, R.H. Vestberg, V. Salles, C. Brunon, K. Gritsch, B. Grosgogeat, Y. Bayon, FTIR microscopy contribution for comprehension of degradation mechanisms in PLA-based implantable medical devices, J. Mater. Sci. - Mater. Med. 28 (2017), https://doi.org/10.1007/s10856-017-5894-7.
[57] X. Zong, K. Kim, D. Fang, S. Ran, B.S. Hsiao, B. Chu, Structure and process relationship of electrospun bioabsorbable nanofiber membranes, n.d. www.elsevier.com/locate/polymer.
[58] E.A. Sroczyk, J.A. Bryant, F. de Cogan, J. Knapczyk-Korczak, M.M. Marzec, P. K. Szewczyk, M. Banzhaf, U. Stachewicz, Modification of electrospun PI membranes with active chlorine for antimicrobial skin patches applications, Appl. Surf. Sci. 592 (2022), https://doi.org/10.1016/j.apsusc.2022.153302.
[59] D.P. Ura, J. Knapczyk-Korczak, P.K. Szewczyk, E.A. Sroczyk, T. Busolo, M. M. Marzec, A. Bernasik, S. Kar-Narayan, U. Stachewicz, Surface Potential Driven Water Harvesting from Fog, ACS Nano 15 (2021) 8848–8859, https://doi.org/10.1021/acsnano.1c01437.
[60] Ł. Kaniuk, S. Ferraris, S. Spriano, T. Luxbacher, Z. Krysiak, K. Berniak, A. Zaszczynska, M.M. Marzec, A. Bernasik, P. Sajkiewicz, U. Stachewicz, Time-dependent effects on physicochemical and surface properties of PHBV fibers and films in relation to their interactions with fibroblasts, Appl. Surf. Sci. 545 (2021), https://doi.org/10.1016/j.apsusc.2021.148983.
[61] A.H. Rajabi, M. Jaffe, T.L. Arinzeh, Piezoelectric materials for tissue regeneration: A review, Acta Biomater. 24 (2015) 12–23, https://doi.org/10.1016/j.actbio.2015.07.010.
[62] E. Capuana, F. Lopresti, M. Ceraulo, V. la Carrubba, Poly-L-Lactic Acid (PLLA)-Based Biomaterials for Regenerative Medicine: A Review on Processing and Applications, Polymers (Basel). 14 (2022), https://doi.org/10.3390/polym14061153.
[63] M. Smith, Y. Calahorra, Q. Jing, S. Kar-Narayan, Direct observation of shear piezoelectricity in poly-l-lactic acid nanowires, APL Mater. 5 (2017), https://doi.org/10.1063/1.4979547.
[64] Q. Li, Y. Liu, D. Wang, R.L. Withers, Z. Li, H. Luo, Z. Xu, Switching spectroscopic measurement of surface potentials on ferroelectric surfaces via an open-loop Kelvin probe force microscopy method, Appl. Phys. Lett. 101 (2012), https://doi.org/10.1063/1.4772511.
[65] F. Zamani, M. Amani-Tehran, M. Latifi, M.A. Shokrgozar, The influence of surface nanoroughness of electrospun PLGA nanofibrous scaffold on nerve cell adhesion and proliferation, J. Mater. Sci. - Mater. Med. 24 (2013) 1551–1560, https://doi.org/10.1007/s10856-013-4905-6.
[66] J. Michl, K.C. Park, P. Swietach, Evidence-based guidelines for controlling pH in mammalian live-cell culture systems, Commun Biol. 2 (2019), https://doi.org/10.1038/s42003-019-0393-7.
[67] X. feng Yang, Y. Chen, F. Yang, F.M. He, S. fang Zhao, Enhanced initial adhesion of osteoblast-like cells on an anatase-structured titania surface formed by H2O2/HCl solution and heat treatment, Dental Materials. 25 (2009) 473–480. https://doi.org/10.1016/j.dental.2008.09.007.
[68] Y. Li, Y. Liu, R. Li, H. Bai, Z. Zhu, L. Zhu, C. Zhu, Z. Che, H. Liu, J. Wang, L. Huang, Collagen-based biomaterials for bone tissue engineering, Mater. Des. 210 (2021), https://doi.org/10.1016/j.matdes.2021.110049.

PLLA scaffolds with controlled surface potential and piezoelectricity for enhancing cell adhesion in tissue engineering

Martyna Polak[1], Krzysztof Berniak[1], Piotr K. Szewczyk[1], Joanna E. Karbowniczek[1], Mateusz M. Marzec[2], Urszula Stachewicz[1,]*

[1]Faculty of Metals Engineering and Industrial Computer Science, [2]Academic Centre for Materials and Nanotechnology, AGH University of Science and Technology, Al. A. Mickiewicza 30, Kraków 30-059, Poland

*E-mail: ustachew@agh.edu.pl

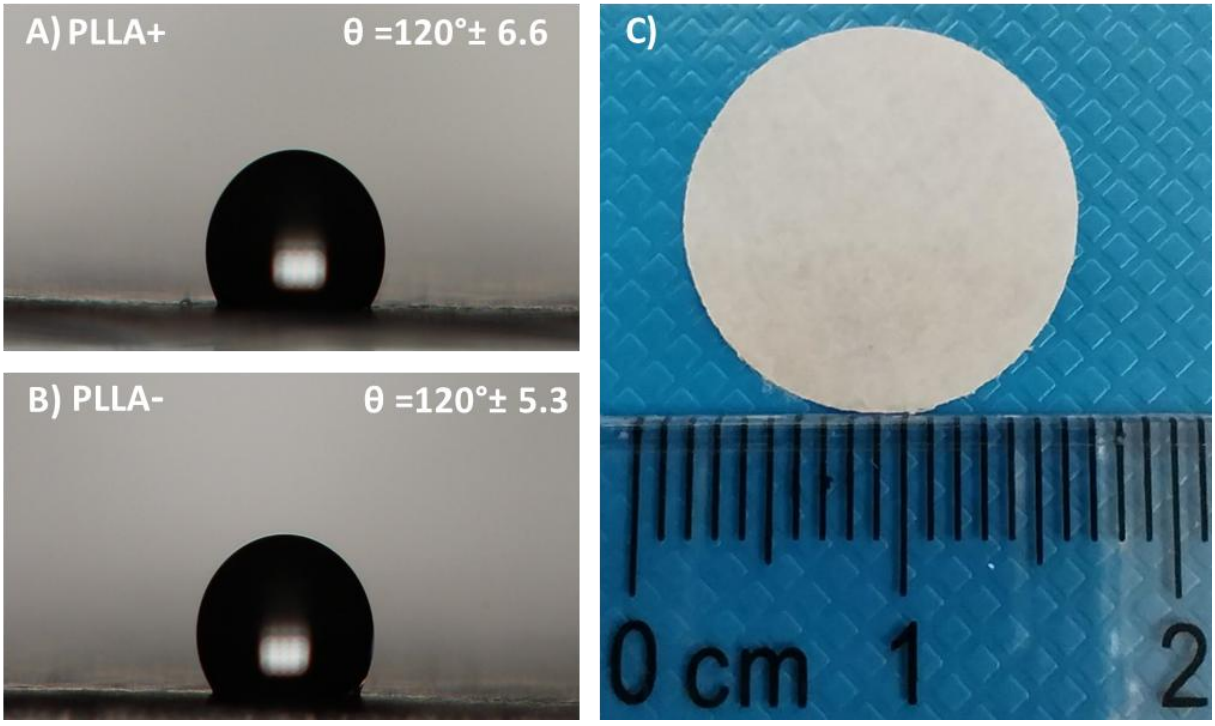

Figure S1. The exemplary images of the water droplets on A) PLLA(HSP), B) PLLA(LSP) for contact angle measurement and C) image of PLLA scaffold.

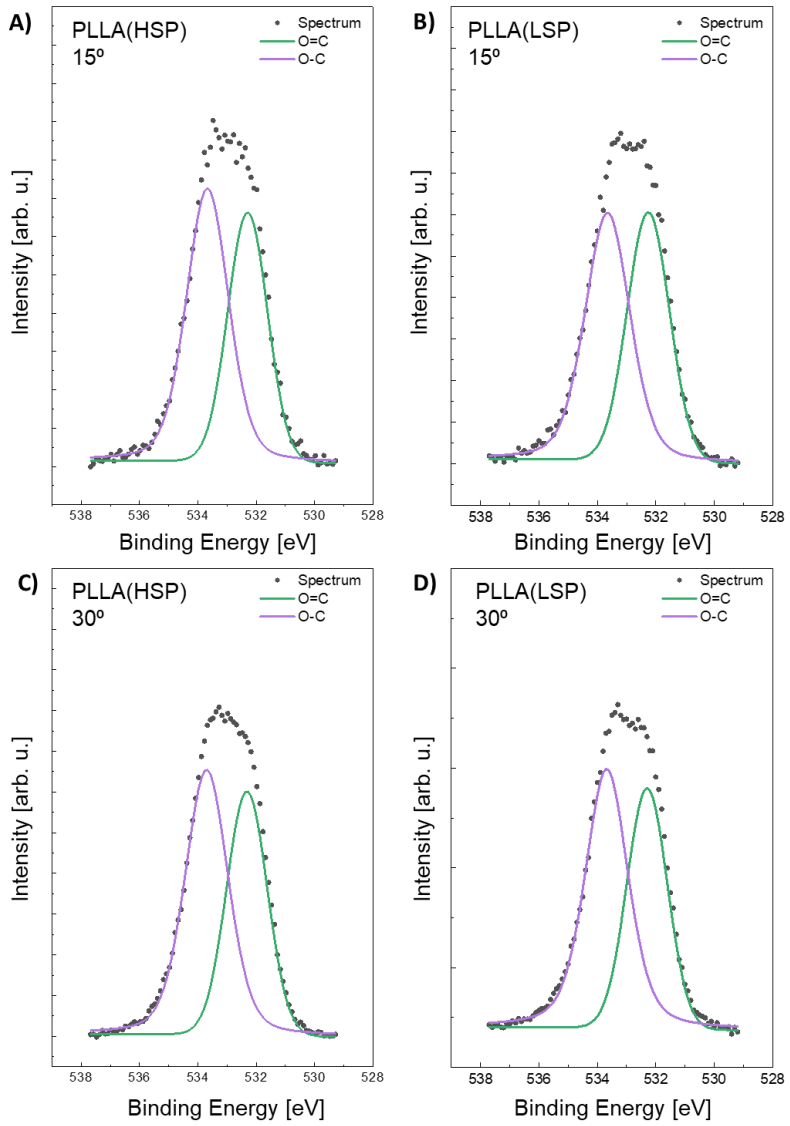

Figure S2. ARXPS spectra of O 1s region: A, C) for PLLA(HSP) and B, D) for PLLA(LSP) taken at 15° (information depth ≈2.1 nm) and 30° (information depth ≈4.0 nm), respectively. For all spectra, two lines were fitted corresponding to oxygen in O-C (533.5 eV, purple) and O=C (531.9 eV, green) bonds.

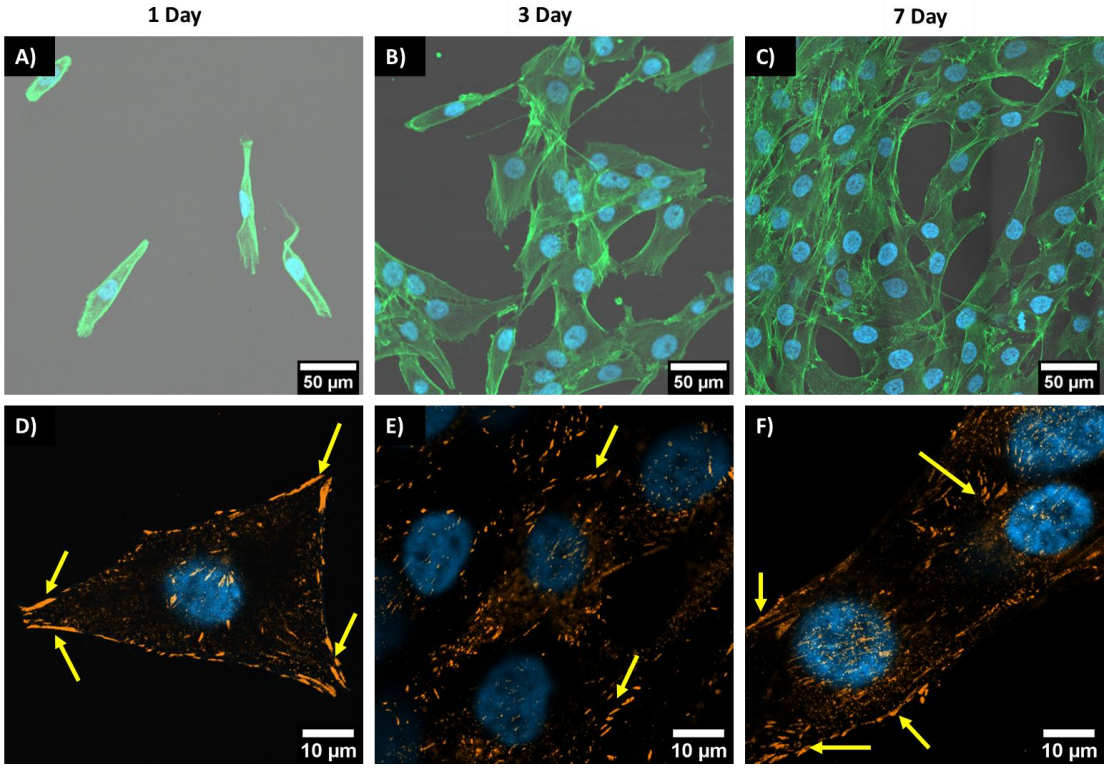

Figure S3. Confocal microscopy images of MG – 63 cells on glass after 1,3,7 days of culturing, showing A) - C) cytoskeleton and spreading of cells, D) - F) stained focal adhesions. The nuclei were stained with DAPI (blue) and the actin filaments with Alexa Fluor 488 Phalloidin (green)).

Colloids and Surfaces B: Biointerfaces 237 (2024) 113864

Contents lists available at ScienceDirect

Colloids and Surfaces B: Biointerfaces

journal homepage: www.elsevier.com/locate/colsurfb

Interfacial blending in co-axially electrospun polymer core-shell fibers and their interaction with cells via focal adhesion point analysis

Martyna Polak [a], Daniel P. Ura [a], Krzysztof Berniak [a], Piotr K. Szewczyk [a], Mateusz M. Marzec [b], Urszula Stachewicz [a,*]

[a] Faculty of Metals Engineering and Industrial Computer Science, AGH University of Krakow, Al. A. Mickiewicza 30, Kraków 30-059, Poland
[b] Academic Centre for Materials and Nanotechnology, AGH University of Krakow, Al. A. Mickiewicza 30, Kraków 30-059, Poland

ARTICLE INFO

Keywords:
Osteoblasts
Cell-material interaction
Focal adhesion
Co-axial electrospinning
Blend polymers
Core-shell fibers

ABSTRACT

Electrospun polymer scaffolds have gained prominence in biomedical applications, including tissue engineering, drug delivery, and wound dressings, due to their customizable properties. As the interplay between cells and materials assumes fundamental significance in biomaterials research, understanding the relationship between fiber properties and cell behaviour is imperative. Nevertheless, altering fiber properties introduces complexity by intertwining mechanical and surface chemistry effects, challenging the differentiation of their individual impacts on cell behaviour. Core-shell fibers present an appealing solution, enabling the control of mechanical properties of scaffolds, flexibility in material and drug selection, efficient encapsulation, strong protection of bioactive drugs against harsh environments, and controlled, prolonged drug release. This study addresses a key challenge in core-shell fiber design related to the blending effect between core and shell polymers. Two types of fibers, PMMA and core-shell PC-PMMA, were electrospun, and thorough analyses confirmed the desired core-shell structure in PC-PMMA fibers. Surface chemistry analysis revealed PC diffusion to the PMMA shell of the core-shell fiber during electrospinning, subsequently prompting an investigation of the fiber's surface potential. Conducting cellular studies on osteoblasts by super-resolution confocal microscopy provided insights into the direct influence of interfacial polymer blending and, consequently, altered fiber surface and mechanical properties on cell focal adhesion points, bridging the gap between material attributes and cell responses in core-shell fibers.

1. Introduction

Electrospun polymer scaffolds are widely used in biomedical applications such as tissue engineering, drug delivery systems, or wound dressings due to the tunability of their properties [1–5]. As the interaction between cells and materials represents a crucial and fundamental area of study in biomaterials research, the relationship between fiber properties and cell behaviour needs to be investigated [6–8]. Electrospinning, due to a wide variety of changeable processing parameters, allows the manipulation of the surface, mechanical or geometrical properties of fibers directly affecting the proliferation, differentiation, or attachment of cells [9–11]. Electrospun scaffolds are designed to mimic the extracellular matrix (ECM), which is a network consisting of minerals, proteins, and enzymes that provide structural and biochemical support for cells [12,13].

One drawback of modifying fiber's mechanics using techniques like photopolymerization and blending is the introduction of interdependence between mechanics and surface chemistry, making it challenging to distinguish their individual effects on cell behaviour. For example, polymer blends can alter the surface roughness and hydrophilicity of fibers, consequently affecting cell attachment and their mechanical interactions within the environment [14,15]. However, blend electrospun fibers are an attractive method of drug encapsulation for drug delivery systems and tissue engineering [15–19]. In contrast, core-shell fibers provide an appealing alternative, allowing independent control of mechanical properties without influencing surface chemistry and scaffold geometry [20,21]. Numerous drug delivery methods have been thoroughly explored, encompassing polymer micelles, liposomes, gels, complexes, and co-axially electrospun fibers [22]. Among these, core-shell fibers offer distinct advantages such as flexibility in material and drug selection, efficient encapsulation, strong protection of bioactive drugs against harsh environments, cost-effectiveness, ease of

* Corresponding author.
E-mail address: ustachew@agh.edu.pl (U. Stachewicz).

https://doi.org/10.1016/j.colsurfb.2024.113864
Received 14 November 2023; Received in revised form 8 March 2024; Accepted 19 March 2024
Available online 20 March 2024

operation, and controlled, prolonged drug release. This makes core-shell fibers an attractive appealing option for drug delivery [23]. Moreover, many studies show the successful incorporation of bioactive substances in the shell of fibers to increase their effects due to exposure at the surface of fibers and induce cellular responses [24–26]. In this study, we introduce a challenge in core-shell fibers design related to the occurrence of a blending effect between core and shell polymers. While highly porous scaffolds made of electrospun fibers can successfully emulate significant characteristics of the extracellular matrix in tissue engineering, they face a limitation in their inability to safely incorporate and release biocompounds such as drugs and growth factors in a controlled manner [27]. Here, the interfacial blending effect in core-shell fibers, such as drug delivery systems, should be considered.

In our research, we produced two types of fibers, PMMA (polymethyl methacrylate) and core-shell PC-PMMA (polycarbonate – polymethyl methacrylate), by electrospinning. We analyzed the morphology of the fibers, bulk and surface chemistry, thermal properties, and finally, mechanical properties, proving the formation of the correct core-shell structure in PC-PMMA fibers. The surface chemistry, crucial from the point of view of interactions with cells, showed the occurrence of PC in the surface of PC-PMMA fibers, which consequently led us to the analysis of the surface potential of the fibers using Kelvin probe force microscopy (KPFM). Further, the surface chemistry analysis helped to investigate PC diffusion to the surface of core-shell fibers that occurred during the co-axial electrospinning. As the next step, we performed a series of cellular studies on osteoblasts, including unique super-resolution confocal microscopy, which allowed us to investigate the direct effect of changes in fiber properties on cell adhesion points [28]. How cells adhere to substrate materials significantly impacts cell function and tissue development. Cell adhesion sets off signaling cascades that possess the capacity to govern a range of processes, encompassing embryogenesis, tissue differentiation, and cell migration. While focal adhesion size and assembly can be considered a critical cue for the correlation between cellular behaviour, functions, and substrate properties, we investigated this relation [29,30].

2. Materials and methods

2.1. Materials

Polycarbonate granulate (PC, Makrolon 3108, Goodfellow GmbH, Germany) was dissolved in a mixture of N, N-dimethylformamide (DMF, Sigma Aldrich, UK) and N, N-dimethyloacetamide (DMAC, Thermo Fisher Scientific, USA) at 1:1 wt. ratio in the concentration of 24 wt%. The second solution was produced by dissolving 14 wt% of polymethyl methacrylate (PMMA, 350 000 g mol^{-1}, Sigma Aldrich, UK) in DMF. Solutions were stirred at 1000 rpm for 3 h on a hot plate set at 60 °C (IKA RCT basic, Staufen, Germany).

2.2. Electrospinning

Both types of fibers were electrospun (EC-DIG apparatus with climate control, IME Technologies, the Netherlands) at 25 °C and relative humidity of 40%. Fabrication of PMMA fibers required using a stainless-steel nozzle (0.51 mm inner (ID) and 0.82 mm outer diameter (OD), 21 G x 1 ½"). PC-PMMA core-shell fibers were produced using a coaxial nozzle (IME Technologies, the Netherlands) with an ID of 0.4 mm and a shell nozzle diameter of 1.2 mm. For PMMA fibers the distance between the nozzle and the collector was 15 cm, and the voltage applied to the nozzle of 14 kV, while for PC-PMMA core-shell fibers it was 25 cm, and 13 kV, respectively. The flow rate for electrospinning PMMA fibers was 4 ml/h^{-1}, and for PC-PMMA core-shell fibers 2.8 ml/h^{-1} of PC solution and 3.2 ml/h^{-1} of PMMA solution.

2.3. Scanning electron microscopy (SEM)

Prior to SEM imaging, samples were coated with an 8 nm Au layer using rotary-pumped sputter coating (Q150RS, Quorum Technologies, UK). Then, samples were imaged with the SEM (Merlin Gemini II, Zeiss, Germany) using a SE detector, applying a current of 100 – 150 pA, a voltage of 3 kV, and a working distance of 3 – 9 mm. Diameters of the fibers D_f were analyzed from SEM images using ImageJ software (ImageJ 2.1.0, USA), and the average value was calculated from 100 measurements taken from SEM micrographs and presented in Fig. 1 using Gaussian fit. For cross-section investigation fibers were immersed in liquid N_2 for 5 min and cut using a scalpel.

2.4. Contact angle measurement

Deionized water (Spring 5UV purification system, Hydrolab, Poland) droplets of 3 μL volume were deposited onto the surface of electrospun PMMA and PC-PMMA membranes. Images were taken using the camera with the macro lens (EOS 700D camera with EF-S 60 mm f/2.8 Macro USM, Canon, Japan) in the first 3 s from droplet deposition. Contact angles were measured using ImageJ software (ImageJ 2.1.0, USA). The average water contact angle was obtained from measurements of ten droplets per sample.

2.5. Bulk chemistry and structure analysis

The bulk chemistry of PMMA powder, PC granules, PMMA, and PC-PMMA fibers was investigated with Fourier transform infrared spectroscopy (FTIR, Nicolet iS5, Thermo Fisher, USA). The samples were scanned in a range of 400–4000 cm^{-1} in a total scan number of 64.

Differential scanning calorimetry (DSC) carried out using DSC 3 (Mettler Toledo, Switzerland) allowed the analysis of thermal properties of PMMA powder, PC granules, and both PMMA and PC-PMMA electrospun fibers. The results present the average values taken from the three independent measurements of each sample. Samples were heated at a rate of 10 $K{\cdot}min^{-1}$ from −20 °C to 300 °C.

2.6. Mechanical tests

Fibrous mats were laser-cut into rectangular samples with a size of 130×70 mm, which were later tested using a tensile machine (20 N cell, Kammrath & Weiss, Germany) at T=24 °C and RH=40%, with an extension rate 25 μms^{-1}. The stress was determined by dividing the force measured by the machine by the initial cross-section of the electrospun mats. The thickness of the samples was measured using a light microscope (Axio Imager M1m, ZEISS, Germany) in the z-direction at 5 different points on each sample. To obtain the average values for toughness (W), maximum stress (R_m), elongation at maximum stress (ε_{max}), and elongation at failure (ε_f), five separate measurements were taken and then calculated using the Integrate function in the OriginPro software (ver. 2022 9.9 USA).

For tensile tests of single and two fibers, fibers were deposited directly onto the paper frames, with an inside hole size of 1×2 mm, during the electrospinning. The presence of fibers on the frames and their alignment along the stretching direction was verified with a light microscope (Primo Star 1, ZEISS, Germany). Analogical characteristic values were calculated as it was done for fibrous mats. Additionally, using the slope value of linear fitting in the OriginPro software (ver. 2022 9.9 USA), it was possible to calculate the value of Young's Modulus. The diameter of fibers required for calculations was determined as the average diameter measured from SEM images as mentioned above.

2.7. Surface properties investigation

The surface chemistry analysis of fibers deposited onto silicon wafers

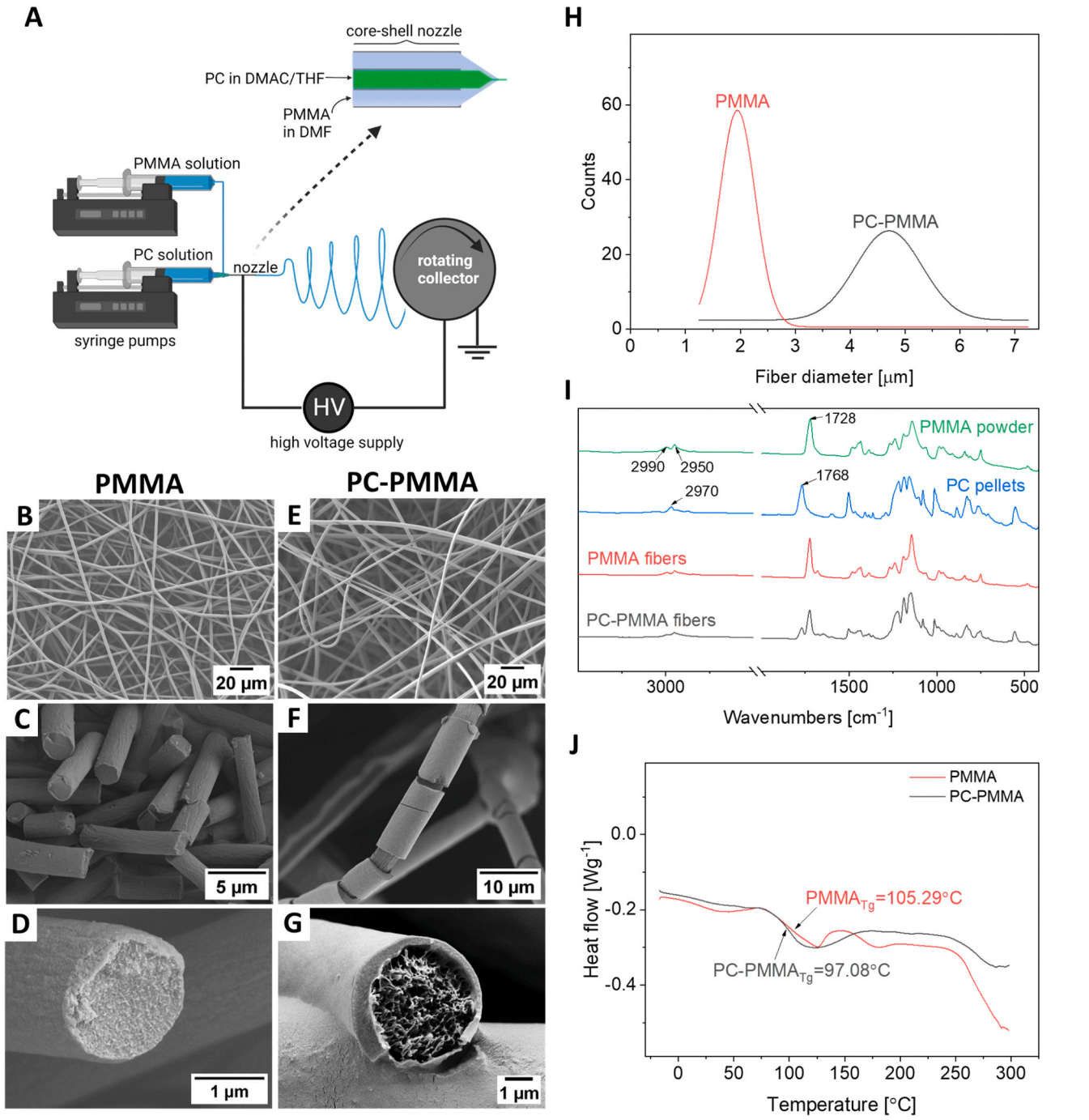

Fig. 1. A) Scheme of core-shell electrospinning with a focus on the core-shell nozzle. SEM micrographs of B)-D) PMMA, and E)-G) PC-PMMA fibers. H) Fiber diameter distribution graph (Gaussian fit), I) FTIR results of PMMA powder, PC pellets, PMMA, and PC-PMMA fibers. J) DSC of PMMA and PC-PMMA scaffolds.

was conducted using the Angle-Resolved XPS (ARXPS PHI VersaProbeII Scanning XPS) system. Monochromatic Al Kα (1486.6 eV) X-rays were used, focused to a 100 µm spot. To achieve high energy resolution spectra for the C 1 s and O 1 s regions, the photoelectron take-off angles were varied at 10° and 90°. The analyzer's pass energy was set to 46.95 eV with a 0.1 eV step. Dual beam charge compensation was employed using 7 eV Ar+ ions and 1 eV electrons, irrespective of the sample conductivity to maintain a constant sample surface potential. All XPS spectra were charge referenced to the unfunctionalized, saturated carbon (C–C) C1s peak at 285.0 eV. The operating pressure in the analytical chamber was kept below 2×10^{-9} mbar. For data analysis, spectra deconvolution was performed using PHI MultiPak software (v.9.9.3), and the Shirley method was used for spectrum background subtraction.

Kelvin probe force microscopy (KPFM) measurements were conducted using the CoreAFM system (Nanosurf, Switzerland). For KPFM measurements, conductive HQ:NSC18/Pt tips (MikroMasch, Bulgaria), with a force constant of 2.8 Nm^{-1} and a resonance frequency of 75 kHz were utilized. During the measurements, topography data was obtained simultaneously with KPFM, and scanning areas of 15 × 15 μm^2 and 50 × 50 μm^2 were used depending on the specific measurement. KPFM data was generated by averaging scan lines taken from the apex of 7 different fibers measured on 4 separate scan regions. To serve as a control measurement of the KPFM signal, measurements from the ITO layer of the

glass were taken alongside fibers. All measurements were performed in a single session to ensure consistent environmental conditions of RH at 50–65% and 23 °C. The values for ITO represent an average of 10 separate lines on each of the 4 scans. Data was processed using Gwyddion (v2.56, gwyddion.net) and OriginPro (v9.7.0.188, OriginLab Corporation, USA) software.

2.8. Cell culture study

2.8.1. Cell proliferation

The cell culture study was performed using human osteoblast-like cells (MG-63) (Sigma Aldrich, UK). Before cell seeding, scaffolds were cut into 15 mm diameter circles, placed in 24-well plates, and sterilized with UV light for 30 min. Tissue culture polystyrene (TCPS) was used as a control. The cell density of 2×10^4 cells per 1 ml in culture media was used for the proliferation assay. Incubation was provided at 37 °C and RH of 95% in a 5% CO_2 atmosphere in the incubator (Memmert GmbH Co.KG, INC 108med, Schwabach, Germany). The cellular medium consisted of Dulbecco's modified Eagle Medium (DMEM with 4.5 g/LD – glucose, Biological Industries, Israel), supplemented with 10% of fetal bovine serum (FBS, Biological Industries, Israel), 2% of antibiotics (penicillin−streptomycin, Biological Industries, Israel), 1% of L-glutamine solution (Biological Industries, Israel), and 1% of amino acids (mem nonessential amino acid solution 100×, Sigma-Aldrich, USA).

Proliferation tests were done using the CellTiter-BlueR Assay (GloMax Discover plate Reader, Promega, USA). Cell viability was evaluated after 1, 3, and 7 days of incubation. After each time point, the media was replaced with 1 ml of media containing 20% of CellTiter-BlueR© reagent (Promega, USA), and incubated for 4 h at 37 °C. From each well, 100 μm of reagent was transferred to a 96-well plate in triplicates, and fluorescence was read at 560/590 nm using the microplate reader GloMaxR©DiscoverSystem (Promega, USA). For the cell culture study, tests were conducted on two repetitions for each type of fibers and control. The statistical analysis was performed in OriginPro (ver. 2022 9.9 USA) using a one-way Analysis of variance (ANOVA) and Tukey's *post hoc* test. Differences were considered statistically significant when $p < 0.05$.

2.8.2. Confocal microscopy imaging: nuclei, actin, and focal adhesion staining

For proliferation study, cells were seeded on samples as well as on glass and cultured for 1, 3, and 7 days. In the case of focal adhesion investigation, cells were seeded and cultured on samples for 3 days. Further procedure was similar for all immunofluorescent staining experiments. The scaffolds were fixed using a 4% paraformaldehyde solution (Sigma-Aldrich, UK) for 15 min. Following fixation, the samples were washed with PBS and then incubated in a 0.1% Triton X-100 solution (Sigma-Aldrich, UK) for 10 min, followed by rinsing with PBS. To prevent nonspecific binding, a blocking step was performed by incubating the samples in a 3% bovine serum albumin (BSA, Sigma-Aldrich, UK) solution in PBS for 60 min. Monoclonal anti-paxillin antibodies (ab32084, Abcam, UK) were used to stain the focal adhesion complex, and the samples were incubated with these antibodies overnight. After staining, the samples were rinsed with PBS for 15 min. Subsequently, the cells were incubated with an anti-rabbit secondary antibody conjugated with Alexa Fluor Plus 555 (A32732, Thermo Fisher, USA) for 1 h. To visualize actin, cells were incubated with Alexa Fluor™ 488 Phalloidin (Thermo Fisher, USA) for 1 h at 23 °C. The last step involved nuclear staining using DAPI for 15 min.

Confocal microscopy (Zeiss LSM 900, Germany) was used to acquire the images. Different objectives, including Plan-Apochromat 10x/0.45 M27, 20x/0.8 M27, 40x/1.30 Oil DIC M27, and 63×/1.4 Oil DIC M27, were utilized during the experiments. For the excitation of DAPI, Alexa Fluor™ 488 Phalloidin, and Alexa Fluor Plus 555, laser lines at 405 nm, 488 nm, and 555 nm were used, respectively [31]. The following parameters were used for Airyscan confocal superresolution microscopy: Plan-Apochromat 63×/1.4 Oil DIC M27, excitation 488 nm, 561 nm, emission detection bands 500 – 550 nm for Alexa Fluor 488 coupled with Phalloidin, 560 – 700 nm for Alexa Fluor 555 [28]. Registration was performed in sequential mode, 16-bit dynamic range.

2.8.3. SEM imaging of cells

Cells were fixed after 1, 3, and 7 days of culture with 2.5% glutaraldehyde (Sigma-Aldrich, UK) for 1 h at 25 °C. In the next step, samples were rinsed three times with PBS for further dehydration in ethanol solution series (Avantor, Poland) (50%, 70%, 80%, 90%, 100%). Incubation in each ethanol solution lasted 7 min and was repeated twice for 100% solution, followed by incubation in hexamethyldisilazane (HDMS, Sigma-Aldrich, UK) under a fume hood until complete evaporation of HDMS. SEM imaging and Au coating of cells on scaffolds were done using the same parameters for the fiber characterization mentioned above.

3. Results and discussion

3.1. Scaffold characterization

PMMA fibers were electrospun using a single nozzle, contrary to PC-PMMA core-shell fibers produced using coaxial multichannel spinneret, schematically shown in Fig. 1A). In core-shell electrospinning, a droplet emerges at the exit point of the core-shell nozzle, which takes on a shape resembling a Taylor cone due to the attractive influence of electric Maxwell stresses exerted on the liquid [32]. Within the cone, the liquid experiences an electric field, leading to the formation of a compound jet. This jet then undergoes the bending instability propelled by electrical forces, similar to the typical electrospinning process. This instability-induced stretching of the jet is accompanied by significant thinning and rapid solvent evaporation. Consequently, the core-shell jet solidifies, and the resulting core-shell fibers are deposited onto a collector [32,33]. Performed SEM of randomly electrospun PMMA and core-shell PC-PMMA fibers shows smooth, beads-free morphology, Fig. 1B), E), which proves obtained stable process of electrospinning [34]. The average fiber diameter (D_f) for PMMA fibers reached 2 ± 0.35 μm, while for core-shell PC-PMMA increased to 4.94 ± 0.88 μm. The histograms of fiber diameter for both samples show unimodal distribution, Fig. 1H). Samples were manually stretched and imaged using SEM to observe the mechanical behaviour of materials. PMMA fibers demonstrated a brittle character, while core-shell fibers present a more elastic PC core and brittle PMMA shell damaged by mechanical deformation, Fig. 1C), F). Additionally, freeze fractures were done to present proper solid PMMA fibers and core-shell PC-PMMA formation, Fig. 1D), G). Contact angle measurement led to a comparison of wetting properties of scaffolds, where for PMMA, the average contact angle was 120.94 ± 4.21 °, and for PC-PMMA, 124.75 ± 3.86 °, indicating a similar hydrophobic nature of both types of fibers. Examples of images used for measurements are presented in **SI** Figure S1. Verification of bulk chemistry was performed using FTIR and allowed to prove the existence of PC in core-shell fibers, Fig. 1I). The presence of PMMA in core-shell fibers was confirmed by peaks at 2950 and 2990 cm^{-1}, observed for PMMA powder, PMMA fibers, and PC-PMMA fibers, which correspond to α-methyl, ester – methyl, and methylene C-H stretching [35]. Furthermore, for all samples consisting of PMMA was observed peak at 1728 cm^{-1} responsible for the C═O group stretching mode belonging to PMMA polymer [35,36]. Identification of PC in core-shell fibers was verified by the characteristic peak at 1768 cm^{-1} associated with the carbonyl group, present for both PC pellets and PC-PMMA fibers [37]. The thermal properties of the two types of fibers were analyzed using DSC, and results show differences in glass transition temperature (T_g), Fig. 1J). PMMA fibers exhibit an average T_g = 105.29 °C, around 8 ° higher than the average T_g of PC-PMMA core-shell fibers.

3.2. Mechanical testing

The distinctive mechanical behaviour of pure PMMA fibers and core-shell PC-PMMA fibers was observed after manual stretching fibrous mats and SEM imaging. It confirms the possibility of manipulating the mechanical properties of PMMA fibers via co-axial processing [38]. PMMA fibers showed brittleness in opposition to core-shell fibers in which PC core tends to elongate, while the rigid shell cracked, Fig. 1C), F). This observation was verified with the mechanical testing of fibrous scaffolds. In Fig. 2A), B), stress–strain curves are shown after tensile testing of PMMA and PC-PMMA scaffolds. Both curves show sharp stress peaks, which are characteristic for PMMA because for both samples strain at maximum stress is similar, 1.81 ± 0.52% for PMMA fibers, and 2.15 ± 0.46% for PC-PMMA, see Table 1. PC-PMMA fibers obtained a maximum stress value of more than two times higher, as well as an elongation of 200%, which is 10 times higher compared to PMMA fibers. Moreover,

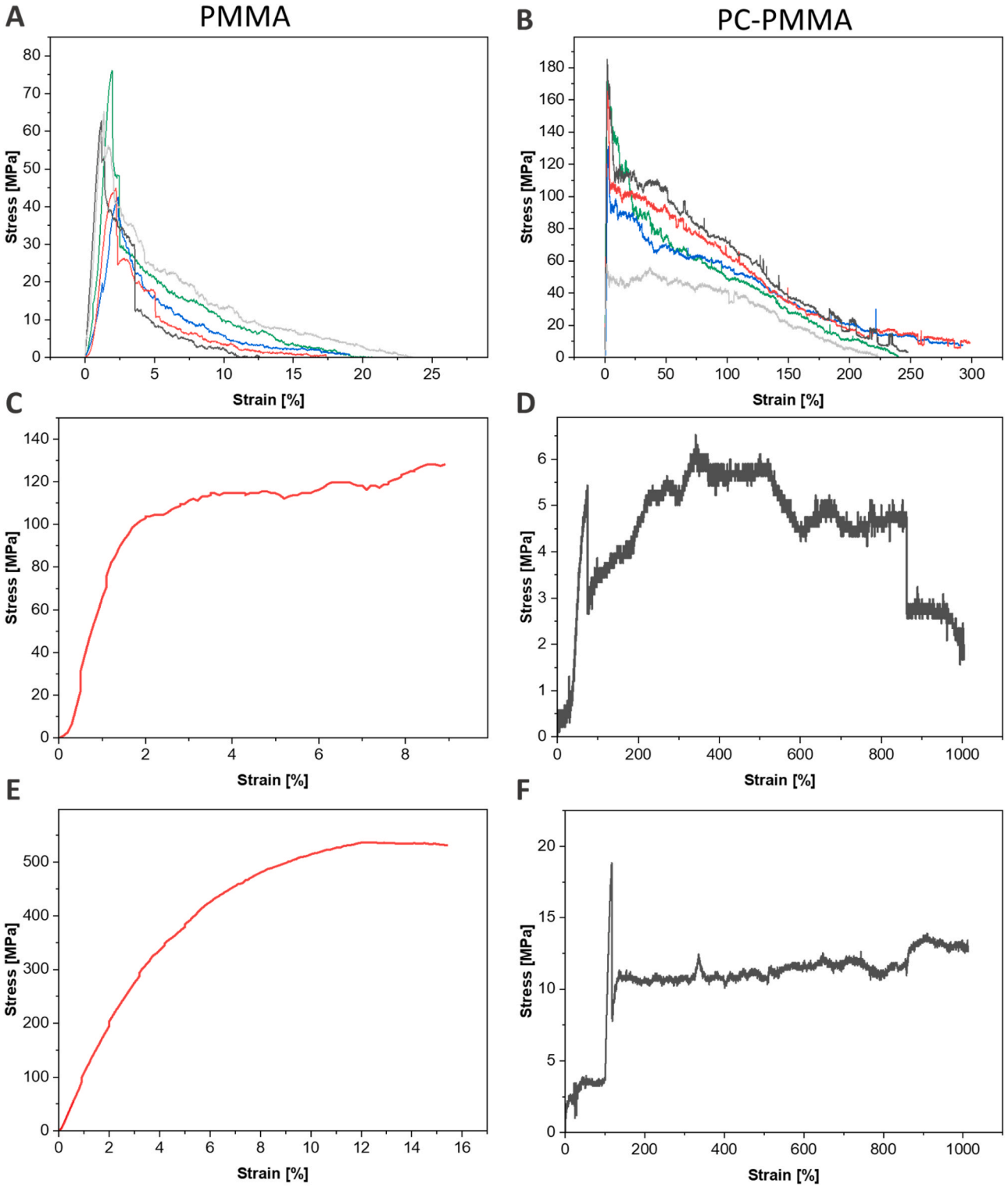

Fig. 2. Stress-strain curves of A) PMMA and B) PC-PMMA mats; C) PMMA and D) PC-PMMA single fibers; E) PMMA and F) PC-PMMA two fibers.

Table 1
Tensile test results for PMMA and PC-PMMA mats, single fiber and two fibers. With the characteristics values of elongation at failure (Ɛf), maximum stress (Rm), toughness (W), elongation at maximum stress (Ɛmax), and Young's Modulus E. Errors are based on standard deviation, with N = 5, where N is the tensile test of one mat sample.

Sample	$Ɛ_f$ [%]	R_m [MPa]	W [MJ·m^{-3}]	$Ɛ_{max}$ [%]	E [MPa]
PMMA mat	19.41 ± 4.52	58.31 ± 14.24	2.25 ± 0.82	1.81 ± 0.53	
PC-PMMA mat	260.39 ± 33.09	142.89 ± 51.64	117.71 ± 29.91	2.15 ± 0.46	
PMMA 1 fiber	8.9	128.03	9.2	8.5	58.20 ± 7.98
PMMA 2 fibers	15.4	537.26	62.92	12.2	98.83 ± 4.31
PC-PMMA 1 fiber	1003.7	6.53	40.21	341.2	0.51 ± 0.27
PC-PMMA 2 fibers	1012.9	18.84	108.11	117.2	0.61 ± 0.17

the resulting toughness is 50 times higher for PC-PMMA fibers, demonstrating a significant trend of higher mechanical properties for core-shell fibrous mats, which was also previously reported for aligned PMMA and PC-PMMA fibers [38].

Additionally, the tensile tests of individual PMMA and core-shell PC-PMMA fibers were performed indicating much higher maximum tensile stress and elastic modulus for PMMA fibers. This trend is similar for both single and two fibers measurements. However, the elongation at failure for core-shell PC-PMMA single fiber (Fig. 2D)) is more than 100 times higher compared to PMMA (Fig. 2C)). Furthermore, the stress-strain curves of individual PC-PMMA fibers show sharp peaks around the strain of 100%, which can be assigned to the characteristic brittle behaviour of PMMA. The Young's modulus for PMMA is also two orders of magnitude higher for individual fibers than for core-shell PC-PMM, indicating higher stiffness of PMMA than PC. Basically, our results confirm that PMMA is intrinsically brittle and PC is more ductile [39].

3.3. Surface properties of scaffolds

The differences in the surface chemistry investigated via XPS analysis of PMMA fibers and PC-PMMA core-shell fibers are caused by diffusion of core material toward fiber surface, which is schematically shown in Fig. 3A). Identification of PC in the surface of the core-shell fibers using XPS showed the presence of carbonate group (-O-(C═O)-O-) in our electrospun fibers. XPS spectra of PMMA and PC-PMMA from the measurement depth of 1.4 nm are shown in Fig. 3B), C). Additionally, all the XPS spectra obtained at depths of 1.4 and 8 nm, performed at different measurement angles, are included in Supplementary Information, Figure S2. We observed increased intensity of peak energy at 289 eV, characterizing the O-C═O group present in PMMA. Carbon from this group marked as C4 in Fig. 3D) and Table 2, is present in both PMMA and PC-PMMA fibers, regardless of measurement depth. Carbon from the carbonate group of PC found at a binding energy of 291 eV (C5 in Fig. 3D) and Table 2) was present in PC-PMMA fibers in both 1.4 and 8 nm depth of measurement in similar concentrations, proving diffusion of PC from the core to the surface of the fiber, see Table 2. Herein, we assume that interdiffusion between two miscible solutions was possible before the ejection of the compound jet, which occurred as the two solutions first met in the cone formed at the end of the coaxial nozzle [40, 41]. Moreover, it was reported that this interdiffusion during the co-electrospinning process can lead to partial or complete mixing of core and shell layers [41–43]. Further, as the surface chemistry of our

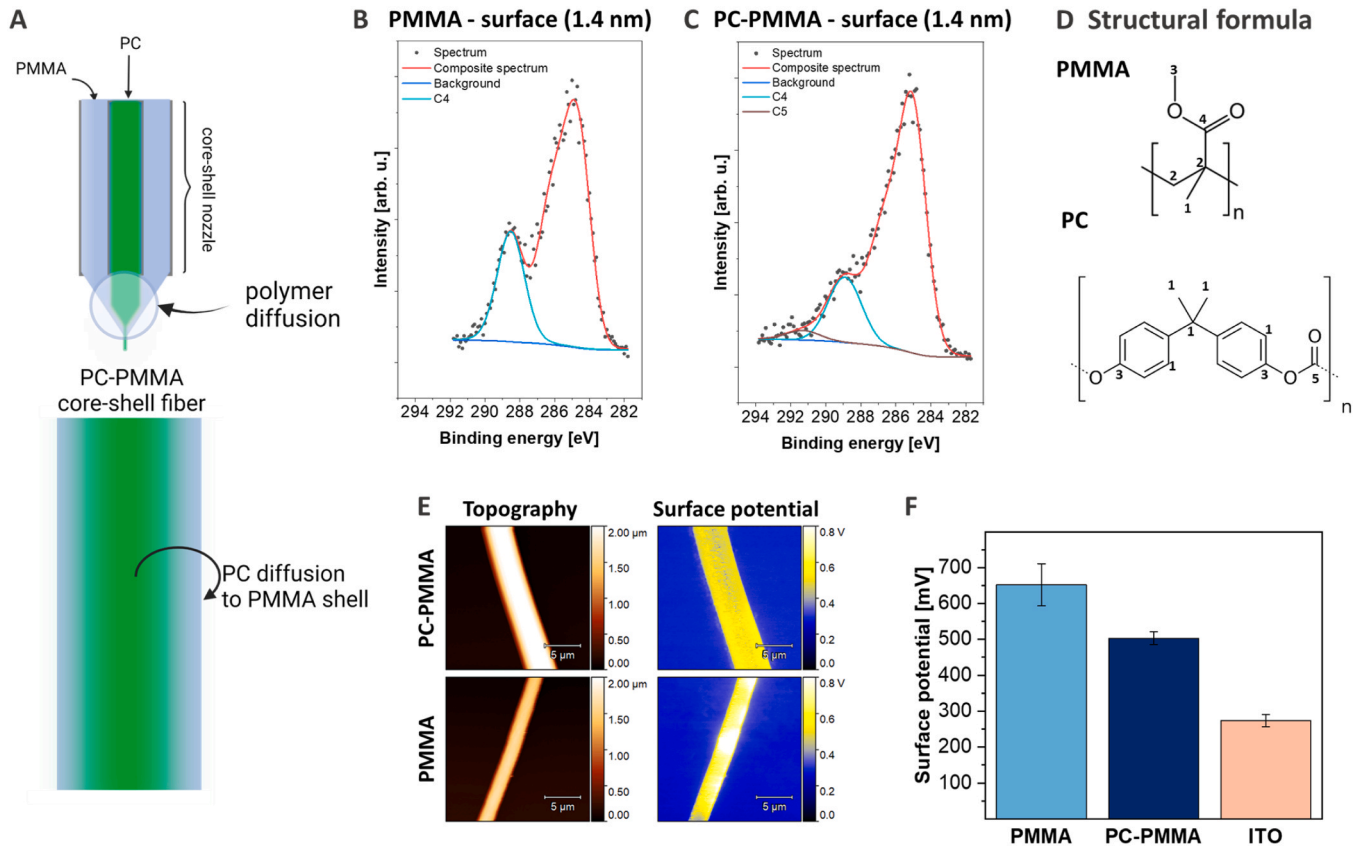

Fig. 3. A) Scheme of core polymer diffusion in core-shell fiber. XPS spectra of B) PMMA, and C) PC-PMMA. D) Structural formula of PMMA and PC. E) KPFM maps of fibers topography and surface potential, and F) calculated values of surface potential (error bars present standard deviation calculated for N = 7, where N is the surface potential value for one fiber scan or scan of the ITO reference).

Table 2
XPS results for PMMA and PC-PMMA samples at two angles, 10 and 90 °, corresponding to 1.4 and 8 nm measurement depth, respectively. The full spectra are presented in **SI,** Figure S2.

Measurement depth [nm]	PMMA				PC-PMMA				
	C1 [%]	C2	C3	C4	C1 [%]	C2	C3	C4	C5
1.4	25.9	14.3	14.2	18.8	36.9	11.2	16.1	13.7	2.2
8	26.6	16.8	15.3	14.2	40.1	12.3	14.2	9.4	2.0

core-shell fibers is not pure PMMA, we performed additional surface analysis related to the surface potential of electrospun fibers used as scaffolds in tissue engineering. Charges at the surface of polymer fibers can be controlled by electrospinning parameters, especially via applied voltage polarity [44,45] It has a significant effect on the surface free energy of polymers [46,47], and their triboelectric performance [48] and follows with the cell interactions once placed in cell culture studies [3,49]. Higher surface potential can improve the adhesion of cells to fibers; thus, this effect should also be considered in later cell culture studies [50–53]. Therefore, in Fig. 3E) we present KPFM maps of fibers topography and surface potential. Measurements show around 150 mV higher surface potential of PMMA fibers, where the values were ~650 mV for PMMA, and ~500 mV for PC-PMMA fibers, see Fig. 3F).

3.4. Cellular behaviour to material properties

3.4.1. Cell proliferation

The proliferation assay, see Fig. 4A), was performed to analyze the viability of cells on polymer scaffolds after 1, 3 and 7 days of culture. Results for both samples show a continuously increased number of osteoblasts with cell culture time. However, a significant difference in proliferation between the samples was observed after 7 days, indicating 28% better viability of cells on PMMA fibers. In the standard confocal microscopy, we used a low-magnification lens with a large depth of field, as presented in the scheme in Fig. 4B), which gave us the ability to image cells on scaffolds and obtain comparable information about cell morphology as from SEM micrographs. As a control, cells were seeded and cultured on glass and further imaged with the confocal microscope, see **SI,** Figure S3. Notably, the proliferation results are consistent with the recorded SEM and CLSM images. Higher proliferation was observed on PMMA fibers after 7 days of cell culture, clearly visible contrasting PMMA scaffold after day 7, Fig. 4H), and PC-PMMA sample, Fig. 4N). Studies show that increased replicative activity of immortalized cell lines is observed only after 3 and even after 5 days of incubation. Hence, differentiated cell proliferation in response to the properties of electrospun fibers are observed after this time [4]. The further examination indicates that cells on the PMMA fibers tend to create solid and dense structures, which is a different behaviour than on PC-PMMA fibers, where cells were more distributed and less numerous. Additionally, cells on core-shell fibers were stretched more with longer filopodia. These morphological differences can be caused by different mechanical properties of fibers or surface properties like surface potential, higher for PMMA fibers which can promote better proliferation and adhesion of cells [53]. Generally, the diameter of fibers constructing scaffolds influences cell morphology [4,54]; however, PMMA and PC-PMMA fiber diameters are in the same order of magnitude. It was already reported that PCL electrospun scaffolds with a fiber diameter range of 1 μm to 8 μm did not affect the proliferation of stem cells [55]. Consequently, this aspect was neglected. In the context of tissue engineering, the mechanical properties of scaffolds play a vital role at the cellular scale related to mechanotransduction. It pertains to the intricate molecular pathways through which cells perceive external forces and exert forces onto a substrate [56,57]. Throughout all stages of tissue development, cells, ranging from stem cells to mature cells, possess mechanoreceptors on their cell surface, enabling them to perceive their mechanical surroundings. Upon initial contact with the extracellular matrix, integrins, which are adhesive molecules on the cell surface, bind with ligands present on the matrix surface. This interaction leads to the formation of significant protein complexes known as focal adhesions, which anchor the cell cytoskeleton to the matrix. These intricate nanoscale processes are crucial in determining the cell's attachment points, morphology, and, ultimately, their function [58]. While core-shell fibers hold the potential for independently regulating cell-matrix mechanical interaction regardless of surface chemistry, none of the studies have conducted measurements of the micromechanics of these fibers at the cell-sensing scale [14,59]. Furthermore, we show the inseparable impact of core material on surface potential and surface chemistry, which strongly affects cellular responses [50,53,60].

3.4.2. Morphology and focal adhesion analysis

To investigate cell morphology and adhesion, single fibers of the analyzed samples were deposited on glass, and in the next step, cells were seeded and incubated for 3 days. After actin and paxillin were stained, confocal microscopy imaging was performed. This approach allowed us to obtain information about cell adhesion to glass and fiber from the same focal plane. The imaging parameters were identical regardless of the type of adhesion and the type of sample, which makes it possible to correlate the intensity of the signal with the amount of protein molecules accumulating at the cell-material contact sites. Actin provides insight into the cell's morphology and shape, whereas paxillin functions as one of the focal adhesion proteins. Focal adhesions are complex structures containing integrins and multiple proteins, which create mechanical connections between the intracellular actin bundles and the extracellular substrate in various cell types. These focal adhesions are sizeable and dynamic protein complexes consisting, among other proteins, of paxillin, vinculin, talin, or zyxin that enable the cell's cytoskeleton to link with the ECM [61,62]. Here, we use paxillin as an immunofluorescent marker to label the distribution of cell adhesion sites. For imaging the focal adhesion sides localization, the Airyscan confocal superresolution method was used [28]. For both samples, cells created advanced actin structure, which confirms accurate morphology, see Fig. 5C), G). Focal adhesions of osteoblasts to glass for PMMA (**SI** Figure S4 **I), II), III)**) as well as PC-PMMA (**SI** Figure S4 **IV), V), VI)**) samples show characteristic patterns and similar intensity compared to each other [62]. Interestingly, we observed completely different adhesion of cells to PMMA and PC-PMMA fibers. Adhesion to PMMA is intensive, and the amount of proteins is enormous (Fig. 5 **I, II, III**), while adhesion to PC-PMMA fiber is hardly seen (Fig. 5 **IV, V, VI**). For more precise results in the difference in focal adhesion to both types of fibers, we analyzed signal intensity profiles based on Airyscan images.

To analyze the intensity of the signal coming from paxillin, actin filaments, which allow detection of the cell body, were also stained, see Fig. 6A), C). The cells show stretching along the fiber for both samples. Areas of paxillin in contact between the cell and the fiber were determined from which signal intensity analysis was performed for PMMA (Fig. 6B)) and for PC-PMMA sample (Fig. 6D)). Despite the difference in paxillin distribution and signal intensity being confirmed, paxillin in PC-PMMA sample does not form as numerous adhesion sites as when interacting with PMMA. Local accumulation foci are very few, Fig. 6D). The signal intensity of focal points is about 7–8 times lower (Fig. 6G), H)) than for paxillin at sites of adhesion to PMMA (Fig. 6E), F)). This indicates that the number of paxillin molecules involved in the adhesion

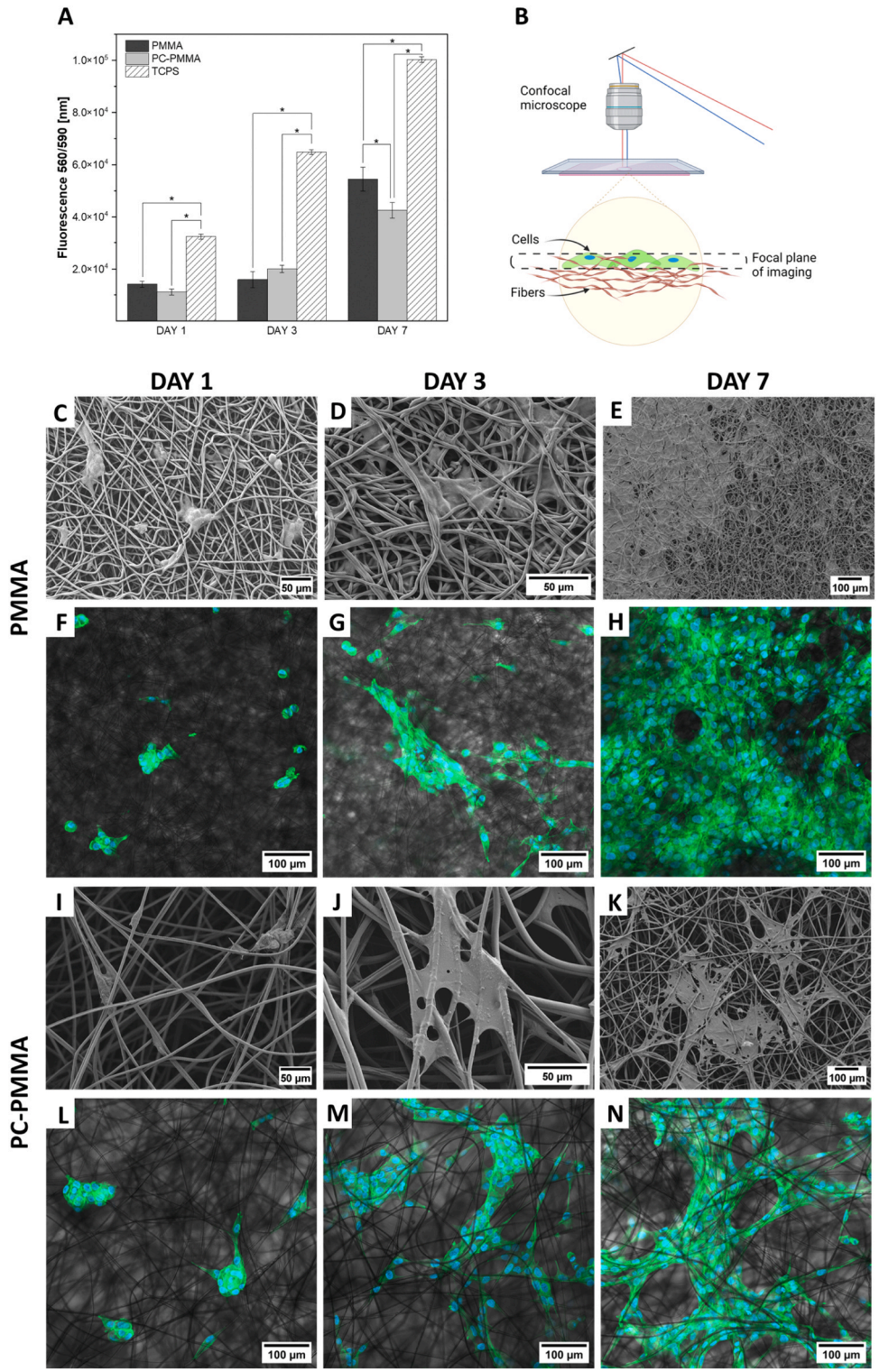

Fig. 4. Results from cell culture studies showing A) proliferation assay of osteoblasts on PMMA and PC-PMMA scaffolds. B) Scheme of the focal plane of imaging in confocal microscope investigation of scaffolds. SEM micrographs of cell culture after 1, 3, and 7 days on C) – E) PMMA, and F) – H) PC-PMMA scaffolds with corresponding CLSM images of F) – H) PMMA and L) – N) PC-PMMA scaffolds. Actin (green) stained with Alexa Fluor™ 488 Phalloidin and nuclei (blue) with DAPI. *Statistical significance is calculated with ANOVA, followed by Tukey's post-hock test, $p < 0.05$; error bars are based on standard deviation.

process to PC-PMMA fibers is many times lower, making the strength and efficiency of adhesion to PC-PMMA fibers much lower. Weaker cell adhesion to PC-PMMA fibers correlates with inferior proliferation on PC-PMMA scaffolds compared to PMMA. While PMMA is a well-studied polymer with high biocompatibility tested on osteoblast cell cultures [63,64], we assume that diffused PC in core-shell fibers is responsible for decreased proliferation and adhesion due to the possible presence of residual xenohormone Bisphenol A (BPA) [65]. This study indicates that even infinitesimal diffusion of core polymer toward the surface of the core-shell fiber alters a number of fiber surface property parameters conditioning cell behaviour and, in this particular example, lowers the biocompatibility of PMMA shell.

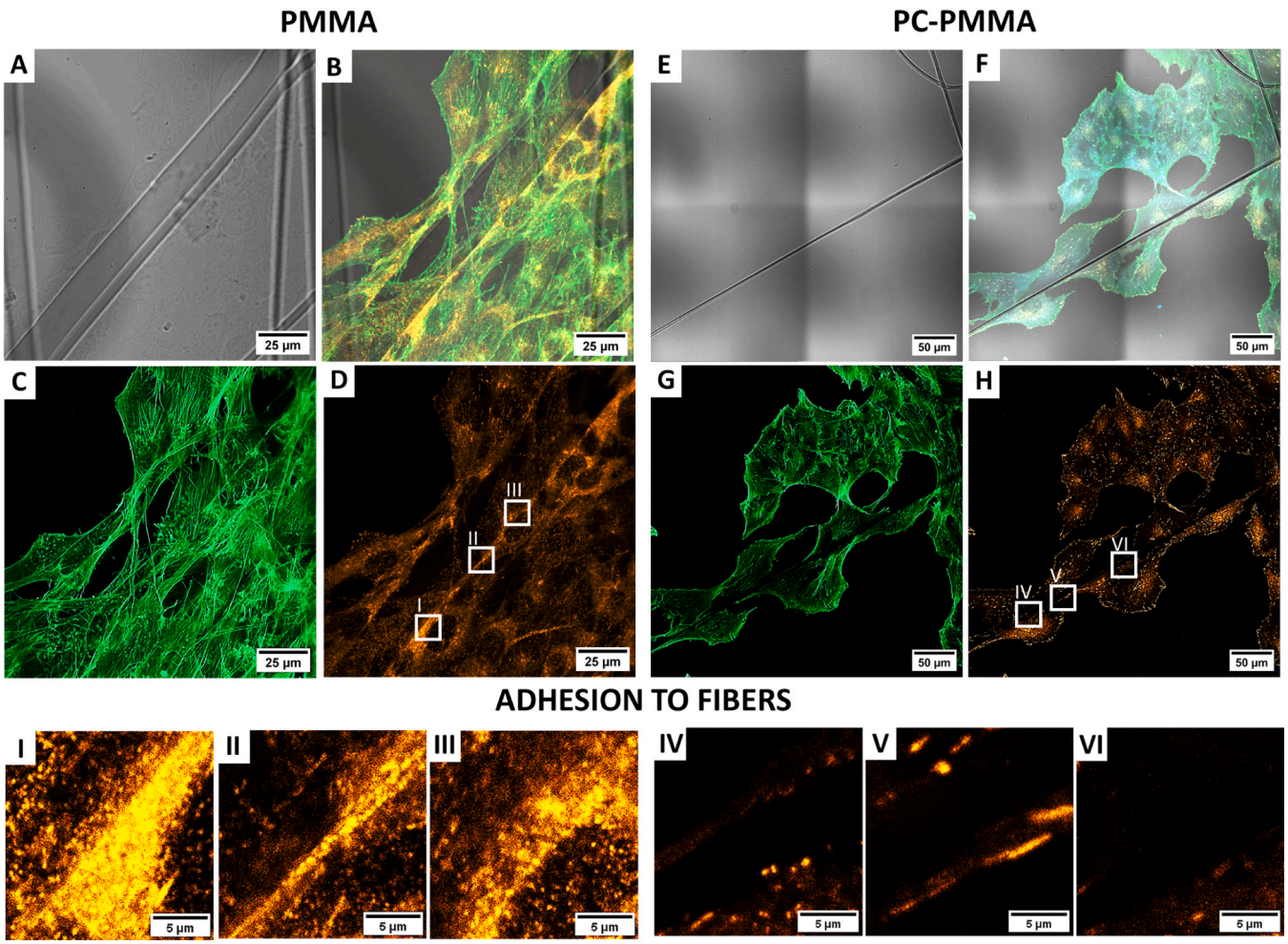

Fig. 5. Focal adhesions analysis on PMMA fibers: A) in transmitted light channel, B) merged channels, C) stained actin (green), D) stained paxillin (orange). Zoom on paxillin from the cell adhesion to PMMA fiber images I) – III). Focal adhesions analysis on PC-PMMA fibers: E) in transmitted light channel, F) merged channels, G) stained actin (green), H) stained paxillin (orange). Zoom on paxillin from the cell adhesion to PC-PMMA fiber images IV) – VI). Paxillin and actin stained with Alexa Fluor™ Plus 555, Alexa Fluor™ 488 Phalloidin, respectively.

4. Conclusions

Co-axial electrospinning is a challenging process used to produce core-shell fibers combining properties of two different materials. It is possible to provide unique fiber features due to the variations in chemical composition and mechanical properties between core and shell, which is attractive in biomaterial applications. For the first time, our study shows the complexity of polymer interfacial blending occurring during co-axial electrospinning for further surface chemistry, surface potential, and mechanical properties of fibers. We conducted a cell culture study to verify if diffusion of core polymer is significant in affecting cell responses. Notably, after 7 days of cell culture, we observed 28% higher cell viability on PMMA than on PC-PMMA fibers. Additionally, with around 7 times stronger signal intensity, the focal adhesion point analysis indicated much stronger osteoblasts adhesion to the PMMA fibers. These favorable cellular responses to PMMA fibers were attributed to preferable surface properties, which were different in core-shell fibers because of the interfacial blending of polymers during co-axial electrospinning, resulting in the occurrence of PC in the fiber surface. The proliferation assay and the focal adhesion point analysis clearly show decreased biocompatibility of core-shell fibers caused by the diffusion of the less biocompatible core material toward the fiber surface. By using focal adhesion point analysis, we demonstrate the necessity to consider the influence of diffusion phenomena in co-axial electrospinning on the design of core-shell fiber surface properties for applications in tissue engineering or drug delivery systems.

CRediT authorship contribution statement

Mateusz M. Marzec: Writing – review & editing, Visualization, Methodology, Investigation. **Urszula Stachewicz:** Writing – review & editing, Writing – original draft, Supervision, Resources, Project administration, Methodology, Funding acquisition, Formal analysis, Conceptualization. **Krzysztof Berniak:** Writing – review & editing, Writing – original draft, Visualization, Validation, Supervision, Methodology, Investigation, Formal analysis. **Piotr K. Szewczyk:** Writing – review & editing, Writing – original draft, Methodology, Investigation, Formal analysis, Data curation. **Martyna Polak:** Writing – review & editing, Writing – original draft, Visualization, Validation, Methodology, Investigation, Formal analysis, Data curation. **Daniel P. Ura:** Writing – review & editing, Visualization, Methodology, Investigation, Formal analysis.

Declaration of Competing Interest

The authors declare that they have no known competing financial interests or personal relationships that could have appeared to influence the work reported in this paper.

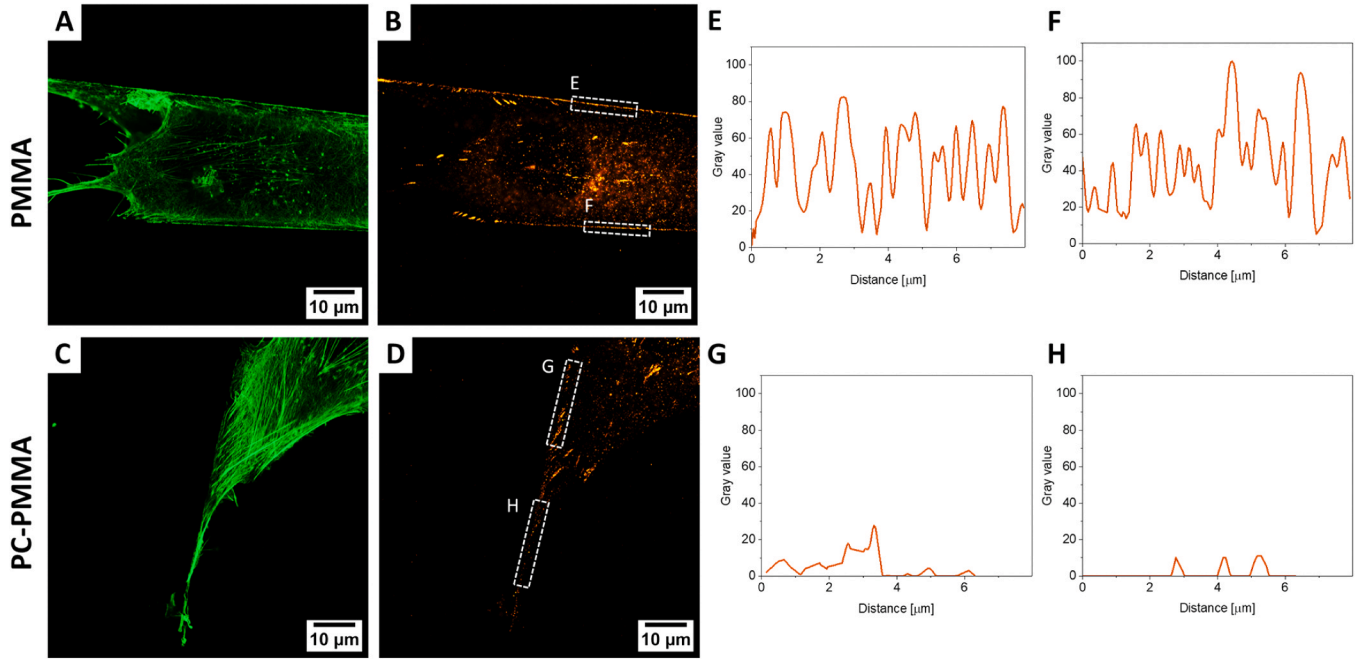

Fig. 6. Airyscan images of stained actin (green) A) and paxillin (orange) B) for PMMA sample with signal intensity profiles of paxillin from marked regions E), F). Analogously, images of stained actin (green) C) and paxillin (orange) D) for PC-PMMA sample with signal intensity profiles of paxillin from marked regions G), H).

Data Availability

Data will be made available on request.

Acknowledgments

This study was conducted with funding from the OPUS 17 project grant provided by the National Science Centre in Poland. No 2019/33/B/ST5/01311. The confocal microscopy studies were supported by the project "Nanofiber-based sponges for atopic skin treatment" carried out within the First TEAM program of the Foundation for Polish Science co-financed by the European Union under the European Regional Development Fund, No POIR.04.04.00-00-4571/17-00. DSC and FTIR measurements were performed within the BioCom4SavEn project funded by the European Research Council under the European Union's Horizon 2020 Framework Programme for Research and Innovation (ERC grant agreement no. 948840).

Schemes were created using BioRender.com.

Appendix A. Supporting information

Supplementary data associated with this article can be found in the online version at doi:10.1016/j.colsurfb.2024.113864.

References

[1] Z.J. Krysiak, U. Stachewicz, Urea-based patches with controlled release for potential atopic dermatitis treatment, Pharmaceutics 14 (2022) 1494, https://doi.org/10.3390/pharmaceutics14071494.

[2] S. Metwally, D.P. Ura, Z.J. Krysiak, Ł. Kaniuk, P.K. Szewczyk, U. Stachewicz, Electrospun PCL patches with controlled fiber morphology and mechanical performance for skin moisturization via long-term release of hemp oil for atopic dermatitis, Membr. (Basel) 11 (2021) 1–13, https://doi.org/10.3390/membranes11010026.

[3] Ł. Kaniuk, S. Ferraris, S. Spriano, T. Luxbacher, Z. Krysiak, K. Berniak, A. Zaszczynska, M.M. Marzec, A. Bernasik, P. Sajkiewicz, U. Stachewicz, Time-dependent effects on physicochemical and surface properties of PHBV fibers and films in relation to their interactions with fibroblasts, Appl. Surf. Sci. 545 (2021), https://doi.org/10.1016/j.apsusc.2021.148983.

[4] Z.J. Krysiak, P.K. Szewczyk, K. Berniak, E.A. Sroczyk, E. Boratyn, U. Stachewicz, Stretchable skin hydrating PVB patches with controlled pores' size and shape for deliberate evening primrose oil spreading, transport and release, Biomater. Adv. 136 (2022), https://doi.org/10.1016/j.bioadv.2022.212786.

[5] B. Azimi, H. Maleki, L. Zavagna, J.G. de la Ossa, S. Linari, A. Lazzeri, S. Danti, Bio-based electrospun fibers for wound healing, J. Funct. Biomater. 11 (2020), https://doi.org/10.3390/JFB11030067.

[6] J. Lin, W. Zhou, S. Han, V. Bunpetch, K. Zhao, C. Liu, Z. Yin, H. Ouyang, Cell-material interactions in tendon tissue engineering, Acta Biomater. 70 (2018) 1–11, https://doi.org/10.1016/j.actbio.2018.01.012.

[7] D. Grafahrend, J.L. Calvet, K. Klinkhammer, J. Salber, P.D. Dalton, M. Möller, D. Klee, Control of protein adsorption on functionalized electrospun fibers, Biotechnol. Bioeng. 101 (2008) 609–621, https://doi.org/10.1002/bit.21928.

[8] N. Su, P.L. Gao, K. Wang, J.Y. Wang, Y. Zhong, Y. Luo, Fibrous scaffolds potentiate the paracrine function of mesenchymal stem cells: a new dimension in cell-material interaction, Biomaterials 141 (2017) 74–85, https://doi.org/10.1016/j.biomaterials.2017.06.028.

[9] S. Sankar, C.S. Sharma, S.N. Rath, S. Ramakrishna, Electrospun fibers for recruitment and differentiation of stem cells in regenerative medicine, Biotechnol. J. 12 (2017), https://doi.org/10.1002/biot.201700263.

[10] M.C. Amores de Sousa, C.A.V. Rodrigues, I.A.F. Ferreira, M.M. Diogo, R. J. Linhardt, J.M.S. Cabral, F.C. Ferreira, Functionalization of electrospun nanofibers and fiber alignment enhance neural stem cell proliferation and neuronal differentiation, Front. Bioeng. Biotechnol. 8 (2020), https://doi.org/10.3389/fbioe.2020.580135.

[11] A. Saudi, S. Amini, N. Amirpour, M. Kazemi, A. Zargar Kharazi, H. Salehi, M. Rafienia, Promoting neural cell proliferation and differentiation by incorporating lignin into electrospun poly(vinyl alcohol) and poly(glycerol sebacate) fibers, Mater. Sci. Eng. C 104 (2019), https://doi.org/10.1016/j.msec.2019.110005.

[12] M. Abedin, N. King, Diverse evolutionary paths to cell adhesion, Trends Cell Biol. 20 (2010) 734–742, https://doi.org/10.1016/j.tcb.2010.08.002.

[13] J. Hao, C. Qin, C. Wu, Three-dimensional multicellular biomaterial platforms for biomedical application, Interdiscip. Mater. 2 (2023) 714–734, https://doi.org/10.1002/idm2.12122.

[14] K.M. Kennedy, A. Bhaw-Luximon, D. Jhurry, Cell-matrix mechanical interaction in electrospun polymeric scaffolds for tissue engineering: implications for scaffold design and performance, Acta Biomater. 50 (2017) 41–55, https://doi.org/10.1016/j.actbio.2016.12.034.

[15] J.E. Karbowniczek, D.P. Ura, U. Stachewicz, Nanoparticles distribution and agglomeration analysis in electrospun fiber based composites for desired mechanical performance of poly(3-hydroxybuty-rate-co-3-hydroxyvalerate (PHBV) scaffolds with hydroxyapatite (HA) and titanium dioxide (TiO2) towards medical applications, Compos B Eng. 241 (2022) 110011, https://doi.org/10.1016/j.compositesb.2022.110011.

[16] Z.J. Krysiak, U. Stachewicz, Electrospun fibers as carriers for topical drug delivery and release in skin bandages and patches for atopic dermatitis treatment, Wiley Inter. Rev. Nanomed. Nanobiotechnol. 15 (2023), https://doi.org/10.1002/wnan.1829.

[17] J. Wu, Z. Zhang, J. Gu, W. Zhou, X. Liang, G. Zhou, C.C. Han, S. Xu, Y. Liu, Mechanism of a long-term controlled drug release system based on simple blended

electrospun fibers, J. Control. Release 320 (2020) 337–346, https://doi.org/10.1016/j.jconrel.2020.01.020.
[18] B. Ghafoor, A. Aleem, M. Najabat Ali, M. Mir, Review of the fabrication techniques and applications of polymeric electrospun nanofibers for drug delivery systems, J. Drug Deliv. Sci. Technol. 48 (2018) 82–87, https://doi.org/10.1016/j.jddst.2018.09.005.
[19] G.R.R.-A.B.T.L.C.J. Williams. Nanofibres in Drug Delivery, UCL Press, 2018, https://doi.org/10.14324/111.9781787350182.
[20] R.A. Perez, H.W. Kim, Core-shell designed scaffolds for drug delivery and tissue engineering, Acta Biomater. 21 (2015) 2–19, https://doi.org/10.1016/j.actbio.2015.03.013.
[21] J.W. Drexler, H.M. Powell, Regulation of electrospun scaffold stiffness via coaxial core diameter, Acta Biomater. 7 (2011) 1133–1139, https://doi.org/10.1016/j.actbio.2010.10.025.
[22] D. Rybak, C. Rinoldi, P. Nakielski, J. Du, M.A. Haghighat Bayan, S.S. Zargarian, M. Pruchniewski, X. Li, B. Strojny-Cieslak, B. Ding, F. Pierini, Injectable and self-healable nano-architectured hydrogel for NIR-light responsive chemo- and photothermal bacterial eradication, J. Mater. Chem. B (2024), https://doi.org/10.1039/d3tb02693k.
[23] Y. Lu, J. Huang, G. Yu, R. Cardenas, S. Wei, E.K. Wujcik, Z. Guo, Coaxial electrospun fibers: applications in drug delivery and tissue engineering, Wiley Inter. Rev. Nanomed. Nanobiotechnol. 8 (2016) 654–677, https://doi.org/10.1002/wnan.1391.
[24] M.M. Kareem, T. Hodgkinson, M.S. Sanchez, M.J. Dalby, K.E. Tanner, Hybrid core-shell scaffolds for bone tissue engineering, Biomed. Mater. (Bristol) 14 (2019), https://doi.org/10.1088/1748-605X/aafbf1.
[25] D. Ji, Y. Lin, X. Guo, B. Ramasubramanian, R. Wang, N. Radacsi, R. Jose, X. Qin, S. Ramakrishna, Electrospinning of nanofibres, Nat. Rev. Methods Prim. 4 (2024), https://doi.org/10.1038/s43586-023-00278-z.
[26] J.E. Karbowniczek, K. Berniak, J. Knapczyk-Korczak, G. Williams, J.A. Bryant, N. D. Nikoi, M. Banzhaf, F. de Cogan, U. Stachewicz, Strategies of nanoparticles integration in polymer fibers to achieve antibacterial effect and enhance cell proliferation with collagen production in tissue engineering scaffolds, J. Colloid Interface Sci. 650 (2023) 1371–1381, https://doi.org/10.1016/j.jcis.2023.07.066.
[27] L.E. Sperling, K.P. Reis, P. Pranke, J.H. Wendorff, Advantages and challenges offered by biofunctional core-shell fiber systems for tissue engineering and drug delivery, Drug Discov. Today 21 (2016) 1243–1256, https://doi.org/10.1016/j.drudis.2016.04.024.
[28] K. Berniak, D.P. Ura, A. Piórkowski, U. Stachewicz, Cell–material interplay in focal adhesion points, ACS Appl. Mater. Interfaces (2024), https://doi.org/10.1021/acsami.3c19035.
[29] S. Fusco, V. Panzetta, V. Embrione, P.A. Netti, Crosstalk between focal adhesions and material mechanical properties governs cell mechanics and functions, Acta Biomater. 23 (2015) 63–71, https://doi.org/10.1016/j.actbio.2015.05.008.
[30] B. Wehrle-Haller, Structure and function of focal adhesions, Curr. Opin. Cell Biol. 24 (2012) 116–124, https://doi.org/10.1016/j.ceb.2011.11.001.
[31] Ł. Kaniuk, K. Berniak, A. Lichawska-Cieślar, J. Jura, J.E. Karbowniczek, U. Stachewicz, Accelerated wound closure rate by hyaluronic acid release from coated PHBV electrospun fiber scaffolds, J. Drug Deliv. Sci. Technol. 77 (2022), https://doi.org/10.1016/j.jddst.2022.103855.
[32] Z. Sun, E. Zussman, A.L. Yarin, J.H. Wendorff, A. Greiner, Compound core-shell polymer nanofibers by co-electrospinning, Adv. Mater. 15 (2003) 1929–1932, https://doi.org/10.1002/adma.200305136.
[33] A.L. Yarin, Coaxial electrospinning and emulsion electrospinning of core-shell fibers, Polym. Adv. Technol. 22 (2011) 310–317, https://doi.org/10.1002/pat.1781.
[34] S. De Vrieze, P. Westbroek, T. Van Camp, K. De Clerck, Solvent system for steady state electrospinning of polyamide 6.6, J. Appl. Polym. Sci. 115 (2010) 837–842, https://doi.org/10.1002/app.30331.
[35] S. Sain, D. Ray, A. Mukhopadhyay, S. Sengupta, T. Kar, C.J. Ennis, P.K.S. M. Rahman, Synthesis and characterization of PMMA-cellulose nanocomposites by in situ polymerization technique, J. Appl. Polym. Sci. 126 (2012), https://doi.org/10.1002/app.36723.
[36] F.J. Tommasinia, L. da Cunha Ferreira, L.G.P. Tienne, V. de Oliveira Aguiar, M.H.P. da Silva, L.F. da Mota Rocha, M. de F.átima Vieira Marques, Poly (methyl methacrylate)-Sic nanocomposites prepared through in situ polymerization, Mater. Res. 21 (2018), https://doi.org/10.1590/1980-5373-mr-2018-0086.
[37] P.M. Gore, P. Gawali, M. Naebe, X. Wang, B. Kandasubramanian, Polycarbonate and activated charcoal-engineered electrospun nanofibers for selective recovery of oil/solvent from oily wastewater, SN Appl. Sci. 2 (2020), https://doi.org/10.1007/s42452-020-03609-x.
[38] D.P. Ura, K. Berniak, U. Stachewicz, Critical length reinforcement in core-shell electrospun fibers using composite strategies, Compos Sci. Technol. 211 (2021), https://doi.org/10.1016/j.compscitech.2021.108867.
[39] Z. Tang, K. Fujimoto, S. Okazaki, A comparison of the brittle PMMA with the ductile PC on the elasticity and yielding from a molecular dynamics perspective, Polym. (Guildf.) 226 (2021), https://doi.org/10.1016/j.polymer.2021.123809.
[40] K. Yan, Y. Le, H. Mengen, L. Zhongbo, H. Zhulin, Effect of solution miscibility on the morphology of coaxial electrospun cellulose acetate nanofibers, Polym. (Basel) 13 (2021), https://doi.org/10.3390/polym13244419.
[41] J.T. McCann, D. Li, Y. Xia, Electrospinning of nanofibers with core-sheath, hollow, or porous structures, J. Mater. Chem. 15 (2005) 735–738, https://doi.org/10.1039/b415094e.
[42] D. Li, Y. Xia, Direct fabrication of composite and ceramic hollow nanofibers by electrospinning, Nano Lett. 4 (2004) 933–938, https://doi.org/10.1021/nl049590f.
[43] Z. Kurban, A. Lovell, S.M. Bennington, D.W.K. Jenkins, K.R. Ryan, M.O. Jones, N. T. Skipper, W.I.F. David, A solution selection model for coaxial electrospinning and its application to nanostructured hydrogen storage materials, J. Phys. Chem. C 114 (2010) 21201–21213, https://doi.org/10.1021/jp107871v.
[44] D.P. Ura, U. Stachewicz, The significance of electrical polarity in electrospinning: a nanoscale approach for the enhancement of the polymer fibers' properties, Macromol. Mater. Eng. 307 (2022), https://doi.org/10.1002/mame.202100843.
[45] D.P. Ura, J. Knapczyk-Korczak, P.K. Szewczyk, E.A. Sroczyk, T. Busolo, M. M. Marzec, A. Bernasik, S. Kar-Narayan, U. Stachewicz, Surface potential driven water harvesting from fog, ACS Nano 15 (2021) 8848–8859, https://doi.org/10.1021/acsnano.1c01437.
[46] U. Stachewicz, A.H. Barber, Enhanced wetting behavior at electrospun polyamide nanofiber surfaces, Langmuir 27 (2011) 3024–3029, https://doi.org/10.1021/la1046645.
[47] U. Stachewicz, C.A. Stone, C.R. Willis, A.H. Barber, Charge assisted tailoring of chemical functionality at electrospun nanofiber surfaces, J. Mater. Chem. 22 (2012) 22935–22941, https://doi.org/10.1039/c2jm33807f.
[48] T. Busolo, D.P. Ura, S.K. Kim, M.M. Marzec, A. Bernasik, U. Stachewicz, S. Kar-Narayan, Surface potential tailoring of PMMA fibers by electrospinning for enhanced triboelectric performance, Nano Energy 57 (2019) 500–506, https://doi.org/10.1016/j.nanoen.2018.12.037.
[49] P.K. Szewczyk, K. Berniak, J. Knapczyk-Korczak, J.E. Karbowniczek, M.M. Marzec, A. Bernasik, U. Stachewicz, Mimicking natural electrical environment with cellulose acetate scaffolds enhances collagen formation of osteoblasts, Nanoscale 15 (2023) 6890–6900, https://doi.org/10.1039/d3nr00014a.
[50] S. Metwally, J.E. Karbowniczek, P.K. Szewczyk, M.M. Marzec, A. Gruszczyński, A. Bernasik, U. Stachewicz, Single-step approach to tailor surface chemistry and potential on electrospun PCL fibers for tissue engineering application, Adv. Mater. Interfaces 6 (2019), https://doi.org/10.1002/admi.201801211.
[51] P.K. Szewczyk, S. Metwally, J.E. Karbowniczek, M.M. Marzec, E. Stodolak-Zych, A. Gruszczyński, A. Bernasik, U. Stachewicz, Surface-potential-controlled cell proliferation and collagen mineralization on electrospun polyvinylidene fluoride (PVDF) fiber scaffolds for bone regeneration, ACS Biomater. Sci. Eng. 5 (2019) 582–593, https://doi.org/10.1021/acsbiomaterials.8b01108.
[52] S. Metwally, S. Ferraris, S. Spriano, Z.J. Krysiak, Ł. Kaniuk, M.M. Marzec, S.K. Kim, P.K. Szewczyk, A. Gruszczyński, M. Wytrwal-Sarna, J.E. Karbowniczek, A. Bernasik, S. Kar-Narayan, U. Stachewicz, Surface potential and roughness controlled cell adhesion and collagen formation in electrospun PCL fibers for bone regeneration, Mater. Des. 194 (2020), https://doi.org/10.1016/j.matdes.2020.108915.
[53] M. Polak, K. Berniak, P.K. Szewczyk, J.E. Karbowniczek, M.M. Marzec, U. Stachewicz, PLLA scaffolds with controlled surface potential and piezoelectricity for enhancing cell adhesion in tissue engineering, Appl. Surf. Sci. 621 (2023), https://doi.org/10.1016/j.apsusc.2023.156835.
[54] D.P. Ura, J.E. Karbowniczek, P.K. Szewczyk, S. Metwally, M. Kopyściański, U. Stachewicz, Cell integration with electrospun PMMA nanofibers, microfibers, ribbons, and films: a microscopy study, Bioengineering 6 (2019) 41, https://doi.org/10.3390/bioengineering6020041.
[55] Z. Gu, S. Fan, S.C. Kundu, X. Yao, Y. Zhang, Fiber diameters and parallel patterns: proliferation and osteogenesis of stem cells, Regen. Biomater. 10 (2023), https://doi.org/10.1093/rb/rbad001.
[56] T. Mammoto, A. Mammoto, D.E. Ingber, Mechanobiology and developmental control, Annu. Rev. Cell Dev. Biol. 29 (2013) 27–61, https://doi.org/10.1146/annurev-cellbio-101512-122340.
[57] E.K. Paluch, C.M. Nelson, N. Biais, B. Fabry, J. Moeller, B.L. Pruitt, C. Wollnik, G. Kudryasheva, F. Rehfeldt, W. Federle, Mechanotransduction: u.se the force(s), BMC Biol. 13 (2015), https://doi.org/10.1186/s12915-015-0150-4.
[58] A. Van der Flier, A. Sonnenberg, Function and interactions of integrins, Cell Tissue Res. 305 (2001) 285–298, https://doi.org/10.1007/s004410100417.
[59] M.A. Haghighat Bayan, Y.J. Dias, C. Rinoldi, P. Nakielski, D. Rybak, Y.B. Truong, A.L. Yarin, F. Pierini, Near-infrared light activated core-shell electrospun nanofibers decorated with photoactive plasmonic nanoparticles for on-demand smart drug delivery applications, J. Polym. Sci. 61 (2023) 521–533, https://doi.org/10.1002/pol.20220747.
[60] S. Metwally, U. Stachewicz, Surface potential and charges impact on cell responses on biomaterials interfaces for medical applications, Mater. Sci. Eng. C 104 (2019), https://doi.org/10.1016/j.msec.2019.109883.
[61] B. Geiger, J.P. Spatz, A.D. Bershadsky, Environmental sensing through focal adhesions, Nat. Rev. Mol. Cell Biol. 10 (2009) 21–33, https://doi.org/10.1038/nrm2593.
[62] P. Kanchanawong, G. Shtengel, A.M. Pasapera, E.B. Ramko, M.W. Davidson, H. F. Hess, C.M. Waterman, Nanoscale architecture of integrin-based cell adhesions, Nature 468 (2010) 580–584, https://doi.org/10.1038/nature09621.
[63] P. Torricelli, M. Fini, G. Giavaresi, R. Botter, D. Beruto, R. Giardino, Biomimetic PMMA-based bone substitutes: a comparative in vitro evaluation of the effects of pulsed electromagnetic field exposure, J. Biomed. Mater. Res. A 64 (2003) 182–188, https://doi.org/10.1002/jbm.a.10372.
[64] M. Jäger, A. Wilke, Comprehensive biocompatibility testing of a new PMMA-HA bone cement versus conventional PMMA cement in vitro, J. Biomater. Sci. Polym. Ed. 14 (2003) 1283–1298, https://doi.org/10.1163/156856203322553491.
[65] P. Wei, G.A. Bhat, D.J. Darensbourg, Enabling new approaches: recent advances in processing aliphatic polycarbonate-based materials, Angew. Chem. - Int. Ed. (2023), https://doi.org/10.1002/anie.202307507.

Supplementary Information to:

Interfacial blending in co-axially electrospun polymer core-shell fibers and their interaction with cells via focal adhesion point analysis

Martyna Polak[1], Daniel P. Ura[1], Krzysztof Berniak[1], Piotr K. Szewczyk[1], Mateusz M. Marzec[2], Urszula Stachewicz[1,]*

[1]Faculty of Metals Engineering and Industrial Computer Science, [2]Academic Centre for Materials and Nanotechnology, AGH University of Krakow, Al. A. Mickiewicza 30, Kraków 30-059, Poland

*E-mail: ustachew@agh.edu.pl

KEYWORDS

Osteoblasts, cell-material interaction, focal adhesion, co-axial electrospinning, blend polymers, core-shell fibers

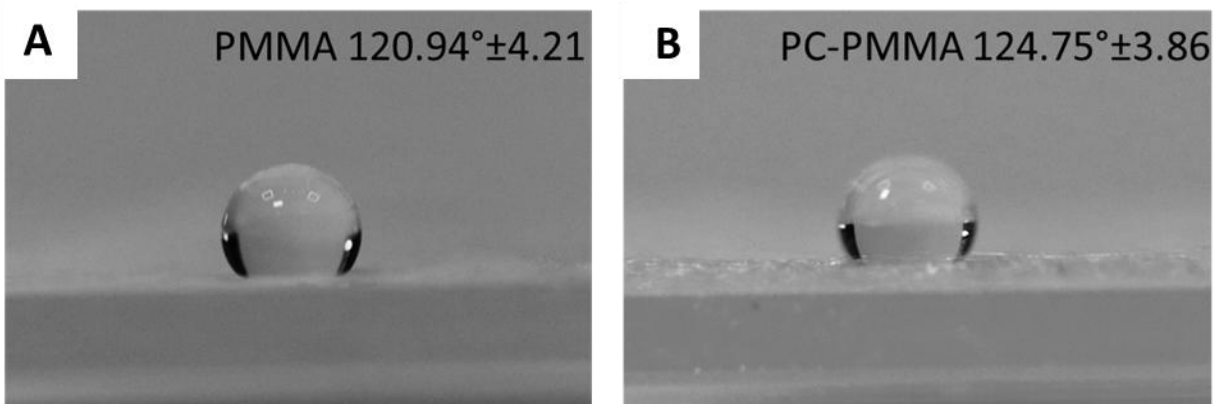

Figure S1. Water droplets on A) PMMA, B) PC-PMMA fiber mats for contact angle measurement with the average values indicated on the images. Error based on standard deviation where N = 10, and N is the angle measurement from one drop.

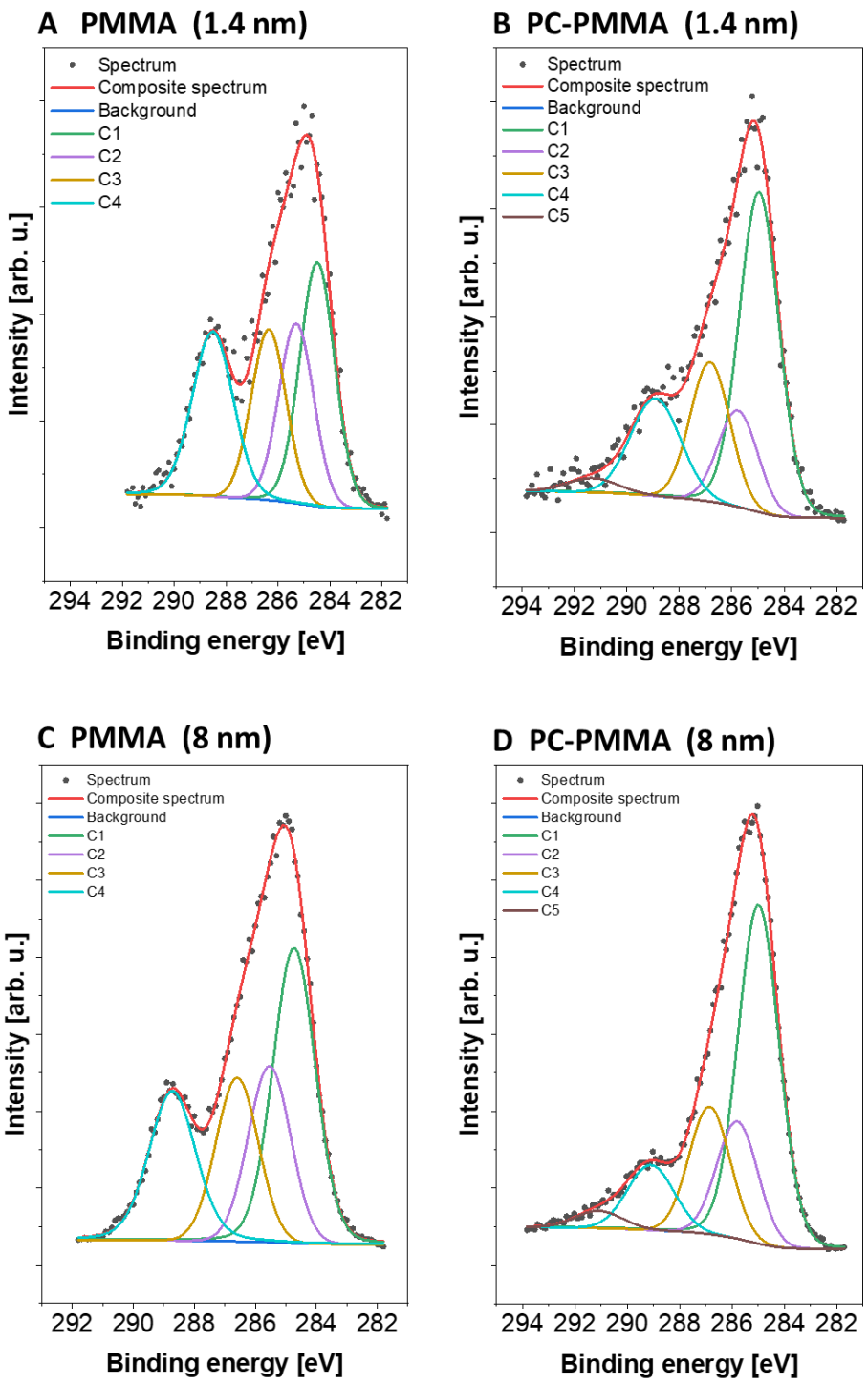

Figure S2. XPS spectra of C1 s for A), C) PMMA and B), D) PC-PMMA samples from 1.4 nm, and 8 nm measurement depth.

The C 1s spectra for PMMA only fibers were fitted with four peaks: first centered at 285.0 eV attributed to aliphatic carbon (C1), second found at 285.8 eV originating from secondary shift C*-

C-O (C2), third line positioned at 286.9 eV indicating C-O bonds (C3) and fourth line found at 289.0 eV from O-C=O group (C4). For PC-PMMA fibers additional fifth line was applied positioned at 291.0 eV indicating carbonate group (C5)[1,2].

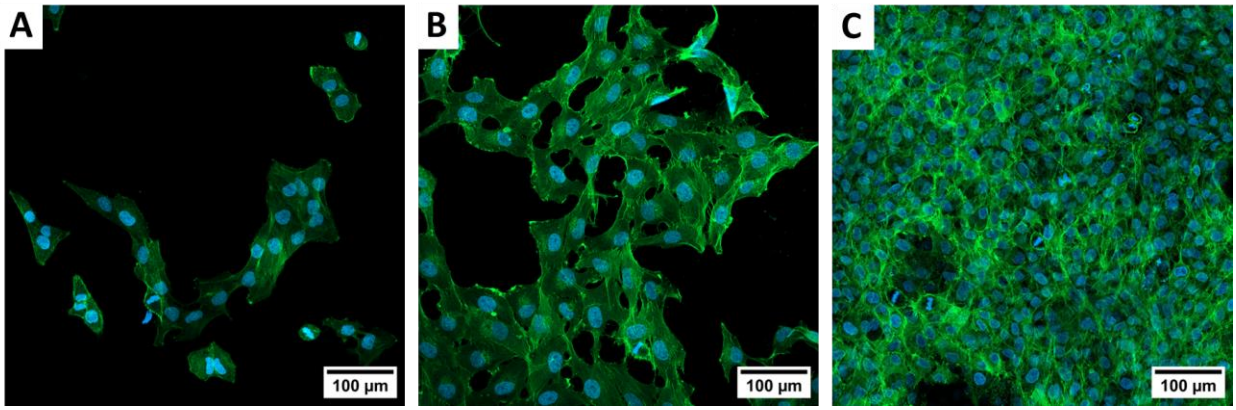

Figure S3. A) - C) Confocal microscopy images of MG – 63 cells on glass after 1,3,7 days of culture, showing cytoskeleton and spreading of cells. The nuclei were stained with DAPI (blue) and the actin filaments with Alexa Fluor 488 Phalloidin (green).

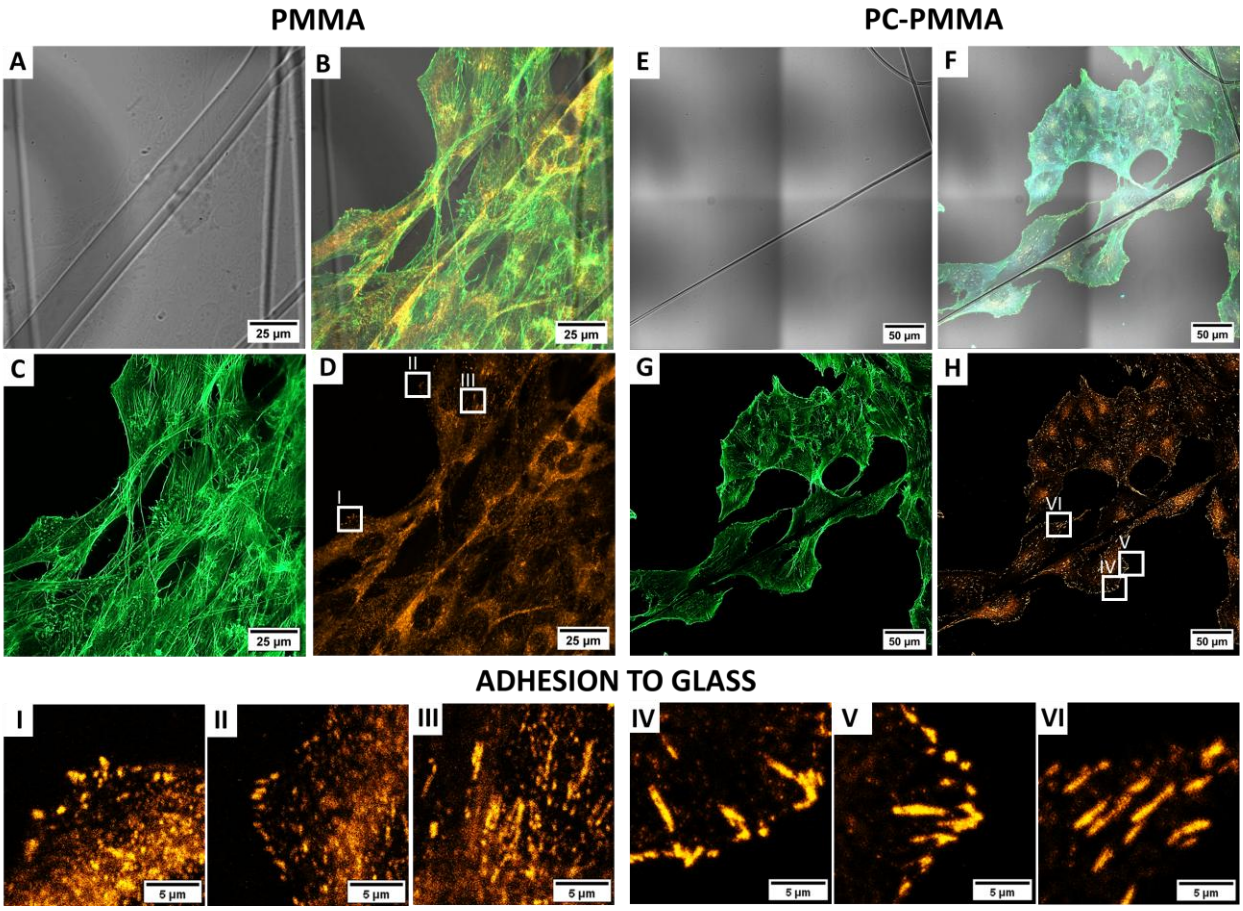

Figure S4. Focal adhesions analysis on PMMA fibers: A) in transmitted light channel, B) merged channels, C) stained actin (green), D) stained paxillin (orange). I) – III) Zoom on paxillin from the cell adhesion to glass for PMMA sample. Focal adhesions analysis on PC-PMMA fibers: E) in transmitted light channel, F) merged channels, G) stained actin (green), H) stained paxillin (orange). IV) – VI) Zoom on paxillin from the cell adhesion to glass for PC-PMMA sample. Paxillin and actin stained with Alexa Fluor™ Plus 555, Alexa Fluor™ 488 Phalloidin, respectively.

REFERENCES

(1) Briggs, D. *Surface Analysis of Polymers by XPS and Static SIMS*; Cambridge University Press: New York, 2005.

(2) Beamson, G.; Briggs, D. High Resolution XPS of Organic Polymers: The Scienta ESCA300 Database (Beamson, G.; Briggs, D.). *J Chem Educ* **1993**, *70* (1), A25. https://doi.org/10.1021/ed070pA25.5.

Materials Today Bio 32 (2025) 101785

Contents lists available at ScienceDirect

Materials Today Bio

journal homepage: www.journals.elsevier.com/materials-today-bio

Modulating cell adhesion and infiltration in advanced scaffold designs based on PLLA fibers with rGO and MXene ($Ti_3C_2T_x$)

Martyna Polak [a], Krzysztof Berniak [a], Piotr K. Szewczyk [a], Joanna Knapczyk-Korczak [a], Mateusz M. Marzec [b], Muhammad Abiyyu Kenichi Purbayanto [c], Agnieszka M. Jastrzębska [c], Urszula Stachewicz [a,*]

[a] Faculty of Metals Engineering and Industrial Computer Science, AGH University of Krakow, Al. A. Mickiewicza 30, Krakow, 30-059, Poland
[b] Academic Centre for Materials and Nanotechnology, AGH University of Krakow, Al. A. Mickiewicza 30, Krakow, 30-059, Poland
[c] Warsaw University of Technology, Faculty of Mechatronics, św. A. Boboli 8, Warsaw, 02-525, Poland

ARTICLE INFO

Keywords:
PLLA
MXenes
rGO
Osteoblast infiltration
Surface charge
Focal adhesions
Cluster analysis

ABSTRACT

The development of electrospun scaffolds that support cell adhesion and infiltration remains a critical challenge in tissue engineering. In this study, we investigate the influence of two-dimensional (2D) fillers—reduced graphene oxide (rGO) and MXene ($Ti_3C_2T_x$)—incorporated into poly(L-lactic acid) (PLLA) electrospun fibers on their properties and osteoblast responses. The presence of fillers modified fiber arrangement and created varying inter-fiber spacing due to surface charge repulsion and agglomeration. Importantly, surface potential measurements via Kelvin probe force microscopy (KPFM) of PLLA fibers show a significant shift caused by the incorporation of $Ti_3C_2T_x$ to ~400 mV compared to ~50 mV for rGO. *In vitro* tests indicate that rGO-modified scaffolds support osteoblast infiltration up to ~100 μm, unlike PLLA fibers, which limit cell infiltration to a maximum of ~70 μm. However, $Ti_3C_2T_x$ promotes even deeper (~120 μm) and more uniform cell's infiltration due to changes in scaffold architecture. High-resolution confocal imaging confirmed that PLLA-$Ti_3C_2T_x$ fosters larger, elongated adhesion site clusters of cells, whereas rGO increases cell's adhesion site density in relation to PLLA scaffolds without any filler. Our findings highlight the distinct roles of rGO and $Ti_3C_2T_x$ in modulating scaffold geometry, mechanical behavior, and cellular interactions. Tailoring the composition and distribution of conductive fillers in fibers offers a promising strategy for optimizing scaffold performance in tissue engineering applications.

1. Introduction

The design of advanced tissue engineering scaffolds focuses on developing materials mimicking the extracellular matrix (ECM) to create a supportive environment for tissue regeneration and expose cells to stimulating conditions. These highly complex materials, with properties defined during their fabrication, are not only intended to regenerate tissue by stimulating cells but are also utilized in other applications [1]. These include drug delivery, cancer treatment, the creation of organoids used as platforms to simulate specific organs, and studying and modeling diseases [2–4]. However, it is worth noting that fundamental studies on novel scaffolds often miss the direct distinction between the material's single property and the triggered biological response. For instance, research on electrospun fibers often emphasizes their structural and functional design for specific applications; while these studies highlight the benefits of fibers, they frequently do not discuss challenges like cell migration throughout the scaffolds [5,6]. Limited pore size, dense fiber packing, and insufficient spacing between fibers are common in electrospun scaffolds and significantly hinder cell migration, which is essential for tissue ingrowth, nutrient transport, and long-term scaffold integration [5]. Moreover, cellular adhesion remains the initial cell response to the material, which affects on later tissue development, especially considering signaling pathways essential for early osseointegration and long-term bone healing [7–9]. Focal adhesions, as protein complexes, answer how cells interact with biomaterials [10]. Their size, distribution, and dynamics influence adhesion strength, migration efficiency, and cascade of cellular responses critical for scaffold integration [11]. Therefore, cell adhesion and migration are closely connected. It was reported that cells on nanofiber scaffolds formed larger focal adhesion clusters, enhancing migration speed compared to

* Corresponding author.
E-mail address: ustachew@agh.edu.pl (U. Stachewicz).

https://doi.org/10.1016/j.mtbio.2025.101785
Received 4 March 2025; Received in revised form 6 April 2025; Accepted 21 April 2025
Available online 21 April 2025

cells on flat surfaces [12].

Despite numerous advances in scaffold fabrication, many current investigated scaffolds struggle to mimic the electroactive environment of ECM to support sufficient cell infiltration. These limitations hinder scaffold integration and functional tissue regeneration. Our study addresses this gap by exploring how conductive fillers can be used not only to adjust surface charge but also to influence fiber arrangement and inter-fiber spacing, ultimately improving cell-fiber interactions and cells infiltration deep into scaffolds. The key strategy to improve cell infiltration in the electrospun scaffolds is control over the scaffold porosity [5,13–15]. Among the various modifications in the electrospinning process to control scaffold geometry, we recognize the lack of research on composite fiber architecture and the fiber-fiber repellency effect caused by their charged surfaces [16–18]. Recently, we have observed increased interest in developing biomaterials biomimicking electrically active cell environments by incorporating conductive fillers [19,20]. Various cell behavior is influenced by local electric fields due to the usually negatively charged cell membrane [21]. Conductive fillers added to the scaffolds can create the favorable surface charges enhancing the electrostatic responses of cells to materials [22]. However, the effect of their incorporation in electrospun fibers on their architecture and later cell infiltration and adhesion was never addressed. Among the others, two-dimensional (2D) inorganic materials like graphene oxide (GO), reduced graphene oxide (rGO), and transition metal carbides, nitrides, or carbonitrides (MXenes) have lately been extensively studied [23–25]. GO and rGO are investigated graphene derivatives in biomedical applications, attributed to their superior mechanical strength, thermal stability, and flexibility [26]. GO is distinguished by abundant hydrophilic functional groups—hydroxyl, carboxyl, and epoxy—on its surface, whereas rGO exhibits a reduced presence of these groups, resulting in decreased hydrophilicity. The integration of graphene-based nanoparticles into soft biomedical polymers has emerged as a promising strategy in tissue engineering [27,28]. Recent studies have explored the incorporation of rGO into electrospun polymer fibers to develop scaffolds with improved properties for tissue engineering applications [26,29]. For instance, electrospun polyetherimide nanofibers integrated with rGO have shown enhanced conductivity and porosity, which are beneficial for electrochemical sensing electrodes [30]. Moreover, it was reported that rGO in polymer composite supported human mesenchymal stem cell (hMSC) proliferation and osteogenic differentiation. Additionally, these scaffolds showed antimicrobial properties [31,32]. On the other hand, MXenes, derived from MAX phases, invented by Naguib, Gogotsi, and Barsoum, are 2D materials possessing features like high electrical conductivity, large surface area, rich surface chemistry, hydrophilicity, and biocompatibility [33,34]. MXenes, due to their unique properties, have garnered significant attention and show great promise as functionalizing materials for electrospun fibers in various applications like energy storage and conversion, as well as biomedical [23,35–38]. Awasthi et al. showed that polycaprolactone-MXene composite electrospun fibers promoted protein adsorption and biomineralization for pre-osteoblast cells [39].

In response to the growing interest in rGO and MXenes due to their unique properties, we address the question of how 2D fillers, rGO, and MXenes – namely, $Ti_3C_2T_x$, influence the surface and mechanical properties of fibers and if it is possible to use the fillers to induce a repelling effect in fibers. Using Kelvin probe force microscopy (KPFM) to evaluate the surface potential, we verify the surface charges with nanoscale precision. Poly(L-lactic acid) (PLLA) was selected as the polymer matrix due to its established biocompatibility, biodegradability, and mechanical properties suitable for bone tissue engineering applications [40–42]. Compared to other biopolymers such as PCL (polycaprolactone) and PLGA (poly(lactic-co-glycolic) acid), PLLA offers higher mechanical strength and a slower degradation rate, making it particularly advantageous for applications requiring long-term structural support, such as bone regeneration [43]. For the first time, we correlate the incorporation of fillers with cell adhesion and infiltration. Our analysis uniquely examines focal adhesion points on fiber regions with 2D materials, revealing clear differences in adhesion patterns and density. We show that the problem of limited cell migration can be solved by incorporating fillers that can, in a controlled manner, change the surface potential of fibers, providing novel insights into scaffold design for biomedical applications. The concept of the study is presented in Fig. 1.

2. Materials and methods

2.1. Materials

Poly(L-lactide) (PLLA, PURASORB PL18, $M_w = 221,000$ g mol^{-1}, Corbion, The Netherlands) was dried before solution preparation for 2h at 30 °C in a drying oven (POL-EKO-APARATURA, Poland). A polymer solution of 9 wt% concentration was prepared by dissolving PLLA in a mixture of dichloromethane (DCM, analytical standard, Avantor, Poland) and dimethylformamide (DMF, analytical standard, Avantor, Poland) in the ratio of 7:3 w/w. The polymer was dissolved entirely after 3h of stirring at 25 °C, at a constant speed of 400 rpm, using the magnetic stirrer (IKA, Germany) in DCM. We prepared 3 solutions: PLLA, PLLA with reduced graphene oxide (PLLA-rGO), and PLLA with $Ti_3C_2T_x$ (PLLA- $Ti_3C_2T_x$). The synthesis of $Ti_3C_2T_x$ was performed from the Ti_3AlC_2 MAX phase (Carbon, Ukraine) by the classical acidic aluminum extraction method, as already reported [44]. The standard procedure of PLLA solution preparation requires first dissolving PLLA pellets in DCM, and when PLLA is dissolved, DMF is added. In the case of solutions with fillers, before adding DMF to the PLLA solution, it was used to prepare a homogenized suspension for two samples containing rGO and $Ti_3C_2T_x$. The fillers in the concentration of 16.7 wt% to polymer mass were ultrasonicated in DMF for 2 h using an ultrasonic bath (Sonorex Bandelin, Germany). Next, DMF suspensions were added to PLLA solutions and stirred for 1 h and later ultrasonicated for 1 h. Finally, all solutions were mixed using a vortex with the highest possible vibration frequency (Labnet VX-200 Vortex Mixer, Labnet International, USA) for 2 min before electrospinning. As mentioned, the filler concentration reached 16.7 wt% to ensure equal loading of rGO and $Ti_3C_2T_x$ while maintaining a stable and repeatable fiber formation during electrospinning. It was the highest achievable concentration without causing nozzle clogging or electrospinning discontinuity, ensuring reproducibility of produced scaffolds.

2.2. Electrospinning

Electrospinning of all samples was conducted using equipment with a climate control chamber (EC-DIG apparatus, IME Technologies, the Netherlands) at a constant temperature T = 25 °C and relative humidity RH = 40 %. The process required using a stainless-steel nozzle (0.51 mm inner (ID) and 0.82 mm outer diameter (OD), 21G × 1 1/2). The voltage, nozzle-collector distance, and flow rate values are presented in Table 1. The thickness of the mats was controlled by the time of deposition and flow rate to collect the same amount of material for each sample for all the experiments. The conductivity of polymer solutions was measured with a Mettler Toledo Conductometer (Seven Compact S210, Zurich, Switzerland). The conductivity value is an average value from 10 measurements; the error represents the standard deviation.

2.3. Scanning electron microscopy, energy dispersive spectroscopy (SEM, EDS-SEM)

The morphology of the produced samples was analyzed using scanning electron microscopy (SEM, Merlin Gemini II, ZEISS, Germany). Before imaging, samples were coated with an 8 nm Au layer using a sputter coater (Q150RS, Quorum Technologies, UK). Imaging was conducted at an accelerating voltage of 2–3 kV and a working distance ranging from 3 to 7 mm, using an SE detector. The average diameters (D_f) were determined by analyzing 100 randomly selected fibers from

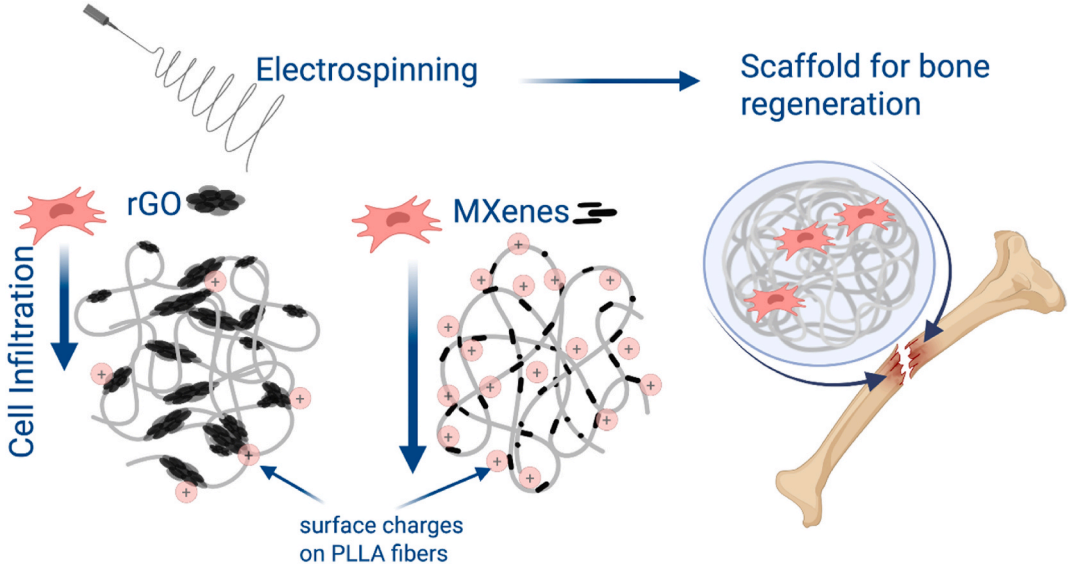

Fig. 1. Conceptual scheme of the study on conductive filler effect on scaffold performance and cell responses.

Table 1
Electrospinning parameters and polymer solution conductivity.

Sample	Voltage [kV]	Nozzle-collector distance [cm]	Flow rate [mL/h]	Conductivity [μS/cm]
PLLA	13.5	16	6	1.83 ± 0.1
PLLA-rGO	16.5	16	3.5	11.78 ± 0.22
PLLA-$Ti_3C_2T_x$	19	16	1.2	10.53 ± 0.12

SEM micrographs using ImageJ software (version 1.53d, USA). To prepare a graph, the kernel smooth distribution in Origin software was used (ver. 2022 9.9 USA). To investigate the distribution of $Ti_3C_2T_x$ in PLLA fibers, elemental mapping was performed using energy-dispersive X-ray spectroscopy (EDS, Brucker, Germany). Before EDS analysis, samples were coated with a thin layer of C (approximately 15 nm) using a carbon evaporator (K950 Emitech, Quorum Technologies, UK). Mapping was conducted utilizing a backscattered electron detector for 500 s at an accelerating voltage of 15 kV, a current of 550 pA, and a working distance ranging from 6 to 7 mm.

2.4. Contact angle measurement

Contact angle measurement was carried out by depositing 3 μL deionized water droplets (Spring 5UV purification system, Hydrolab, Poland) onto the surface of scaffolds. Images of droplets were captured after 3 s from the deposition, using a Canon camera (EOS 700D, EF-S 60 mm f/2.8 Macro USM zoom lens, Canon, Japan). ImageJ software (version 1.53d, USA) was used to measure contact angles from the images of ten droplets per sample.

2.5. Tensile test

Electrospun mats were cut into samples measuring 130 × 70 mm, which were subsequently tested using a tensile machine (20 N cell, Kammrath & Weiss, Germany) at T = 24 °C and RH = 40 %, with an extension rate of 50 μms^{-1}. The stress was calculated by dividing the force measured by the machine by the initial cross-sectional area of the electrospun mats. The thickness of the samples was measured in the z-direction at ten different points using a SEM (Phenom ProX Desktop SEM, Thermo Fisher Scientific, USA). To determine the average values for toughness (W), maximum stress (Rm), elongation at maximum stress (Ɛmax), and elongation at failure ($Ɛ_f$), five separate measurements were taken for each scaffold sample, and the data were processed using the Integrate function in OriginPro software (ver. 2022 9.9, USA). The curves presented on the graph are the averages of the five tensile tests of each type of sample. Errors are based on the standard deviation.

2.6. Filler agglomeration distribution analysis

For each sample, 20 images were captured in transmitted light across different fields of view (confocal laser scanning microscope, Zeiss LSM 900, Germany). The images for all samples were recorded using the same imaging parameters. Agglomeration size detection for $Ti_3C_2T_X$ and rGO was performed using macros written in ImageJ software (version 1.51, Fiji, USA). The first step of the process involved the detection of fibers. $Ti_3C_2T_x$ or rGO agglomerations were identified exclusively within the areas defined by the previously established fiber mask in the images. Morphological analysis of the identified agglomerates was conducted using ImageJ (version 1.53d, USA). Errors on the graph represent the standard deviation.

2.7. Thermal properties (DSC), surface and bulk chemistry analysis (XPS, FTIR)

Thermal properties were analyzed using differential scanning calorimetry (DSC) (DSC 3, Mettler Toledo, Switzerland). The DSC curves present the average values of three independent measurements per sample heated at a rate of 10 $Kmin^{-1}$ from 0 to 230 °C. To identify the functional groups in samples, Fourier transform infrared spectroscopy (FTIR) was used (FTIR, Nicolet iS5, Thermo Fisher, USA) in a range of 400–4000 cm^{-1} with a total number of 64 scans using Ge crystal plate.

Analysis of the surface chemistry of fibers deposited on silicon wafers was performed with X-ray photoelectron spectroscopy (XPS). The XPS analyses were carried out in a PHI VersaProbeII Scanning XPS system using monochromatic Al Kα (1486.6 eV) X-rays focused to a 100 μm spot and scanned over the area of 400 μm × 400 μm. The photoelectron take-off angle was 45° and the pass energy in the analyzer was set to 117.50 eV (0.5 eV step) for survey scans and 46.95 eV (0.1 eV step) to obtain high energy resolution spectra for the C 1s, and O 1s regions. A dual beam charge compensation with 7 eV Ar^+ ions and 1 eV electrons were used to maintain a constant sample surface potential regardless of the sample conductivity. All XPS spectra were charge referenced to the unfunctionalized, saturated carbon (C-C) C 1s peak at 285.0 eV. The

analytical chamber operating pressure was less than 3×10^{-9} mbar. Deconvolution of spectra was done using PHI MultiPak software (v.9.9.3). The Shirley method was used to correct the spectrum background.

2.8. Kelvin probe force microscopy (KPFM)

Atomic force microscopy (AFM) and KPFM were performed using a CoreAFM system (Nanosurf, Switzerland). For KPFM, conductive HQ: NSC18/Pt tips (MikroMasch, Bulgaria) with a force constant of 2.8 Nm^{-1} and a resonance frequency of 75 kHz were utilized. During KPFM measurements, topographical data were captured simultaneously. Scans covered areas of 100 μm^2. KPFM data represent the average of 6 separate scan lines taken on top of the fibers. To provide a control for the KPFM signal, measurements from the ITO glass were taken alongside fiber measurements. KPFM measurements were performed in tapping/lift mode with simultaneous topography acquisition, and all scans were conducted in a controlled environment during a single session (RH = 50–65 %, T = 23 °C) to minimize electrostatic artifacts and ensure reproducible surface potential mapping, following similar protocols reported in the literature [37]. Data was analyzed using Gwyddion (v2.56, gwyddion.net) and OriginPro (version 2022 9.9, USA) software.

2.9. Zeta potential measurement

Streaming zeta potential analysis was performed using a high-performance electrokinetic analyzer (SurPASS 3, Anton Paar, Austria). The streaming potential was measured between two meshes, each with dimensions of 20 × 10 mm, positioned in the cell with an adjustable gap set to 115 μm. The pH was controlled within the range of 5.5–9.0. The pH was controlled by gradually adding 0.05 M HCl or 0.05 M NaOH to a 0.01 M KCl solution. Zeta potential measurements were taken in four repetitions at each pH level, with the sample being replaced after each measurement. Results are presented as the average values, with error bars representing the standard deviation calculated from the four tests.

2.10. Cell culture studies

Human osteoblast-like cells (MG-63) (Sigma Aldrich, UK) were used for the cell culture study. Scaffolds were cut into 15 mm diameter circles, placed in 24-well plates, and sterilized under UV light for 30 min. Glass was used as a control. For each study, an equal cell density of 2×10^4 cells per 1 ml of culture medium was used. Incubation took place at 37 °C with 95 % humidity in a 5 % CO_2 atmosphere in an incubator (Memmert GmbH + Co. KG, Inc 108med, Schwabach, Germany). The cell culture medium consisted of Dulbecco's Modified Eagle Medium (DMEM with 4.5 g/L D-glucose, Biological Industries, Israel), supplemented with 10 % fetal bovine serum (FBS, Biological Industries, Israel), 2 % antibiotics (penicillin-streptomycin, Biological Industries, Israel), 1 % L-glutamine solution (Biological Industries, Israel), and 1 % non-essential amino acid solution (Sigma-Aldrich, USA).

2.11. Cell adhesion

Cells were seeded onto scaffolds for the cell adhesion evaluation and incubated for 5 h. After this time, samples were washed with phosphate-buffered saline (PBS, Biomed Lublin, Poland) to remove non-adherent cells. Subsequently, the scaffolds and control were fixed using 4 % paraformaldehyde for 15 min and then rinsed again with PBS. Nuclear staining was achieved by incubating the samples with 4′,6-diamidino-2-phenylindole (DAPI, Sigma-Aldrich, UK) for 15 min, followed by a final PBS rinse. The samples were investigated using a confocal laser scanning microscope (Zeiss LSM 900, Germany), and cell quantification was performed using 100 images per sample with CellProfiler 4.2.6 (Broad Institude, USA) software.

2.12. Confocal microscopy: nuclei, actin, focal adhesions

Cell actin was analyzed after 1, 3 and 7 days of incubation. Focal adhesions were visualized after 3 days. Staining protocols were similar to those previously reported [45]. Briefly, all immunofluorescence staining followed a procedure: scaffolds were fixed with 4 % paraformaldehyde (Sigma-Aldrich, UK) for 15 min, washed with PBS, and permeabilized with 0.1 % Triton X-100 (Sigma-Aldrich, UK) for 10 min. After blocking with 3 % BSA (Sigma-Aldrich, UK) in PBS for 60 min, focal adhesion complexes were stained with anti-paxillin antibodies (ab32084, Abcam, UK) overnight. Secondary staining with Alexa Fluor Plus 555 (A32732, Thermo Fisher, USA) and actin staining with Alexa Fluor 488 Phalloidin (Thermo Fisher, USA) were done for 1 h, followed by nuclear staining with DAPI (Sigma-Aldrich, UK) for 15 min.

Images were captured using a confocal microscope (Zeiss LSM 900, Germany) with objectives ranging from 10× to 63× . Excitation used laser lines at 405 nm, 488 nm, and 555 nm for DAPI, Alexa Fluor 488, and Alexa Fluor 555, respectively. Airyscan superresolution microscopy utilized a 63× oil objective with specific emission bands for fluorescence detection.

2.13. Confocal microscopy: cluster analysis

For each sample, images were captured in 15 different fields of view using both confocal and Airyscan modes. The confocal mode was used to capture transmitted light images of PLLA fibers, with visible $Ti_3C_2T_x$ and rGO agglomerates. The Airyscan mode was employed for high-resolution imaging of paxillin proteins, which are involved in cell adhesion processes. Confocal laser microscopy imaging parameters are presented in Table 2.

The distribution of paxillin at cell adhesion sites on PLLA fibers (both with and without $Ti_3C_2T_x$ or rGO) was imaged and analyzed using ImageJ software (version 1.51, Fiji, USA). Fluorescence images were normalized using the Statistical Dominance Algorithm (SDA) to reduce noise and correct uneven illumination. Cell adhesion regions were manually defined, and the analysis focused on these areas. ImageJ tools were used to identify local maxima of signal intensity, and nearest-neighbor (NN) analysis was conducted to determine the minimum distances between the local peaks of paxillin and the identified $Ti_3C_2T_x$ or rGO agglomerations, following the previously established protocols [10].

Clustering of these points was analyzed using the Density-Based Spatial Clustering of Applications with Noise (DBSCAN), which identifies clusters and outliers based on the proximity of points. DBSCAN parameters (epsilon and minimum points) were optimized using a set of 10 images and then applied to the remaining data. Statistical analysis of the results was performed using OriginPro software (version 2022 9.9, USA).

Table 2
The summary of all confocal laser microscopy imaging parameters.

Imaging mode	Objective	Laser wavelength	Detection wavelength	Pixel time	Pixel size
Confocal	Plan-apochromat 63x/1.4 Oil DIC M27	561 nm, 488 nm, and 405 nm for Alexa 555, Alexa 488, and DAPI, respectively	540–700 nm for Alexa 555, 450–545 nm for Alexa 488, and 400–600 nm for DAPI	1.91 μs	0.071 μm
Airyscan	Plan-apochromat 63x/1.4 Oil DIC M27	561 nm, 488 nm, and 405 nm for Alexa 555, Alexa 488, and DAPI, respectively	540–700 nm for Alexa 555, 450–545 nm for Alexa 488, and 400–600 nm for DAPI	3.82 μs	0.035 μm

2.14. Cell proliferation, replication and infiltration

Cell proliferation was measured using the CellTiter-Blue® Assay (GloMax Discover plate reader, Promega, USA) at 1, 3 and 7 days post-incubation. At each time point, the culture media was replaced with 1 ml of fresh media containing 20 % CellTiter-Blue® reagent (Promega, USA) and incubated for 4 h at 37 °C. After incubation, 100 μl of the reagent mixture was transferred from each well to a 96-well plate in triplicate, and fluorescence was recorded at 560/590 nm using the GloMax® Discover system (Promega, USA). Each type of scaffold and control glass was tested in duplicate. Statistical analysis of the data was carried out using OriginPro software (version 2022 9.9, USA).

For the replication assessment, cells grown on scaffolds and glass (as a control) were treated with 10 μM 5-ethynyl-2′-deoxyuridine (EdU) for 1 h after 1, 3 and 5 days of culture. Following treatment, the samples were washed with PBS, fixed with 4 % paraformaldehyde, and then permeabilized with 0.1 % Triton X-100 (Sigma-Aldrich, USA) and blocked in 3 % bovine serum albumin (Sigma-Aldrich, USA) at 25 °C. The incorporated EdU was detected using the ClickiT™ EdU AF488 imaging kit (Invitrogen/Molecular Probes, USA). Cells were stained with DAPI (Millipore, Germany) for 15 min. Fixed samples were imaged using a Zeiss LSM 900 confocal microscope (CLSM, Carl Zeiss Microscopy GmbH). For imaging, 405 nm and 488 nm laser lines were used for excitation, with emission detection bands of 410–500 nm for DAPI and 500–700 nm for Alexa Fluor™ 488 bound to the incorporated EdU. A Plan-Apochromat 20× /0.8 M27 objective was used for imaging. For each sample, over 60 images were captured from different fields of view. The images were recorded in two channels: the green channel, where the signal from Alexa 488-labeled EdU precursor incorporated into the cell was detected, and the blue channel, where the signal from labeled DNA in cell nuclei was captured. Nuclei detection in both channels was performed using the CellProfiler 4.2.6 software (Broad Institute, USA).

Cell infiltration into the scaffolds after 7 days of incubation was analyzed with CLSM. Parallel imaging of cell nuclei and actin was performed to provide a detailed evaluation of cellular distribution. All samples were fixed prior to imaging to preserve cellular morphology with DAPI and Alexa Fluor 488 Phalloidin. Imaging was conducted using Z-stacks, capturing the fluorescent signal. The imaging settings, including excitation light intensity, detection ranges, and detector gain, were kept consistent across all samples to ensure reliable and comparable results. Z-stacks were acquired with a step size of 1.7 μm. The acquisition range for each sample was individually adjusted, starting from the first in-focus layer where nuclei appeared and continuing deeper into the scaffold until the last visible labeled nuclei moved out of focus. From each layer within the Z-stack, the average pixel intensity was calculated. The depth corresponding to the maximum average pixel intensity in the Z-stack was identified as the plane with the highest density of in-focus nuclei, which was interpreted as the position of cells on the scaffold surface. In the resulting plots, the X axis represents the scanned depth for each sample, providing a visualization of cellular distribution and scaffold infiltration.

2.15. SEM of scaffolds with cells

SEM imaging of cells on PLLA scaffolds was carried out after 7 days of culture. The cells were fixed using 2.5 % glutaraldehyde (Sigma-Aldrich, UK) for 1 h at 25 °C. After fixation, the samples were rinsed three times with PBS and then dehydrated through a series of ethanol solutions (Avantor, Poland) with increasing concentrations (50 %, 60 %, 70 %, 80 %, 90 %, 100 %). The scaffolds were incubated in each ethanol solution for 7 min, repeating the process twice for the 100 % ethanol. Following dehydration, the samples were treated with hexamethyldisilazane (HMDS, Sigma-Aldrich, UK). Once the HMDS had fully evaporated, the samples were coated with an 8 nm layer of Au and imaged using the same SEM parameters as previously used for fiber characterization. Cell infiltration was assessed by visualizing cross-sections of scaffolds, which were cut through the middle of the sample using a scalpel and then coated with an Au layer using the protocol mentioned above.

3. Results and discussion

3.1. Scaffold's morphological, chemical, and mechanical characterization

Electrospinning is a straightforward technique for producing highly porous polymer scaffolds, with porosity exceeding 90 %, arranged in a random orientation. Thus, this method is widely used in tissue engineering, particularly for wound healing applications [46,47]. However, the interplay of the electric field and the surface tension in this electrohydrodynamic process is accompanied by many more parameters [48,49]. Importantly, whenever we start to create the hybrid scaffolds with rGO and MXene, one has to take into account the conductivity of the polymer solution. Following this essential line of thinking, we measured the conductivity for our three polymer solutions: PLLA, PLLA-rGO, and PLLA-$Ti_3C_2T_x$ [48,50,51]. As expected, 2D conductive materials rGO and $Ti_3C_2T_x$ enhanced the conductivity of the solution [52–54]. Results in Table 1 show that adding rGO increased the conductivity by approximately 11 μScm^{-1}, while adding $Ti_3C_2T_x$ increased it by 10 μScm^{-1}. Consequently, due to the increased conductivity of solutions, the applied voltage and flow rate had to be adjusted to conduct electrospinning of fibers in a stable cone-jet mode (see Table 1). A similar observation was made based on experiments with polylactide (PLA) with the addition of cellulose nanocrystals [55].

Fibers of PLLA-rGO and PLLA-$Ti_3C_2T_x$ samples differ compared to PLLA in many aspects. Firstly, we analyzed the morphology of fibers using scanning electron microscopy (SEM), see Fig. 2A. Material agglomeration is present for both samples containing fillers and looks similar to beads, contrary to smooth and uniform PLLA fibers. The average diameter of fibers for all the samples is similar, as presented in the histogram (Fig. 2B). It is 1.74 ± 0.42 μm for PLLA fibers, while for fibers with fillers, the value slightly decreased, resulting in 1.56 ± 0.51 μm for PLLA-rGO and 1.14 ± 0.26 μm for PLLA-$Ti_3C_2T_x$. It has been demonstrated previously that variations of ~0.5 μm in fiber diameter do not significantly affect cell proliferation or differentiation when the diameters remain within the same order of magnitude [56]. Differences between the scaffolds are visible not only microscopically but also macroscopically, as presented in SI Figure S1 A, where it is shown that fillers affect the color of the scaffold. Moreover, to gather complex characterization of samples, we provide static contact angle measurements done with water, showing no significant differences, resulting in 117.6 ± 4.1°, 118.3 ± 2.9°, and 120.1 ± 4.5° for PLLA, PLLA-rGO, and PLLA-$Ti_3C_2T_x$, respectively. Exemplary images of the water droplets on the scaffolds for this measurement are presented in SI Figure S1 B-D.

In terms of mechanical performance, the agglomeration of $Ti_3C_2T_x$ and rGO within PLLA fibers significantly impacts their tensile properties, as shown in stress-strain curves (Fig. 2C). Fig. 2C presents the average curves from 5 measurements per sample, while all the curves are presented in SI Figure S1 E-G. Table 3 summarizes mechanical properties, highlighting evident differences between all samples. The Young's modulus of randomly oriented electrospun fiber mats was not determined due to fiber slippage and non-linear deformation behavior during tensile testing. As already been indicated in several studies the obtained values of the Young's modulus from not aligned electrospun fibers mats can be misleading [57–59]. Pure PLLA fibers exhibit good mechanical properties, with an elongation at break (ε_f) of 42 ± 5.29 %, a tensile strength (σ) of 2.41 ± 0.18 MPa, strain at maximum stress (ε_{max}) of 21.86 ± 4.56 %, and a toughness (W) of 70.62 ± 15.26 MJ m^{-3}. The tensile test results for PLLA fibers are comparable to those reported in the literature for electrospun mats made of PLA and other polymers commonly used in tissue engineering [55,60,61]. Incorporating rGO into PLLA fibers results in a slight increase in ε_f to 43.43 ± 1.85 %, indicating that rGO has a minor effect on the flexibility of the composite. However, compared to PLLA fibers, the tensile strength of PLLA-rGO

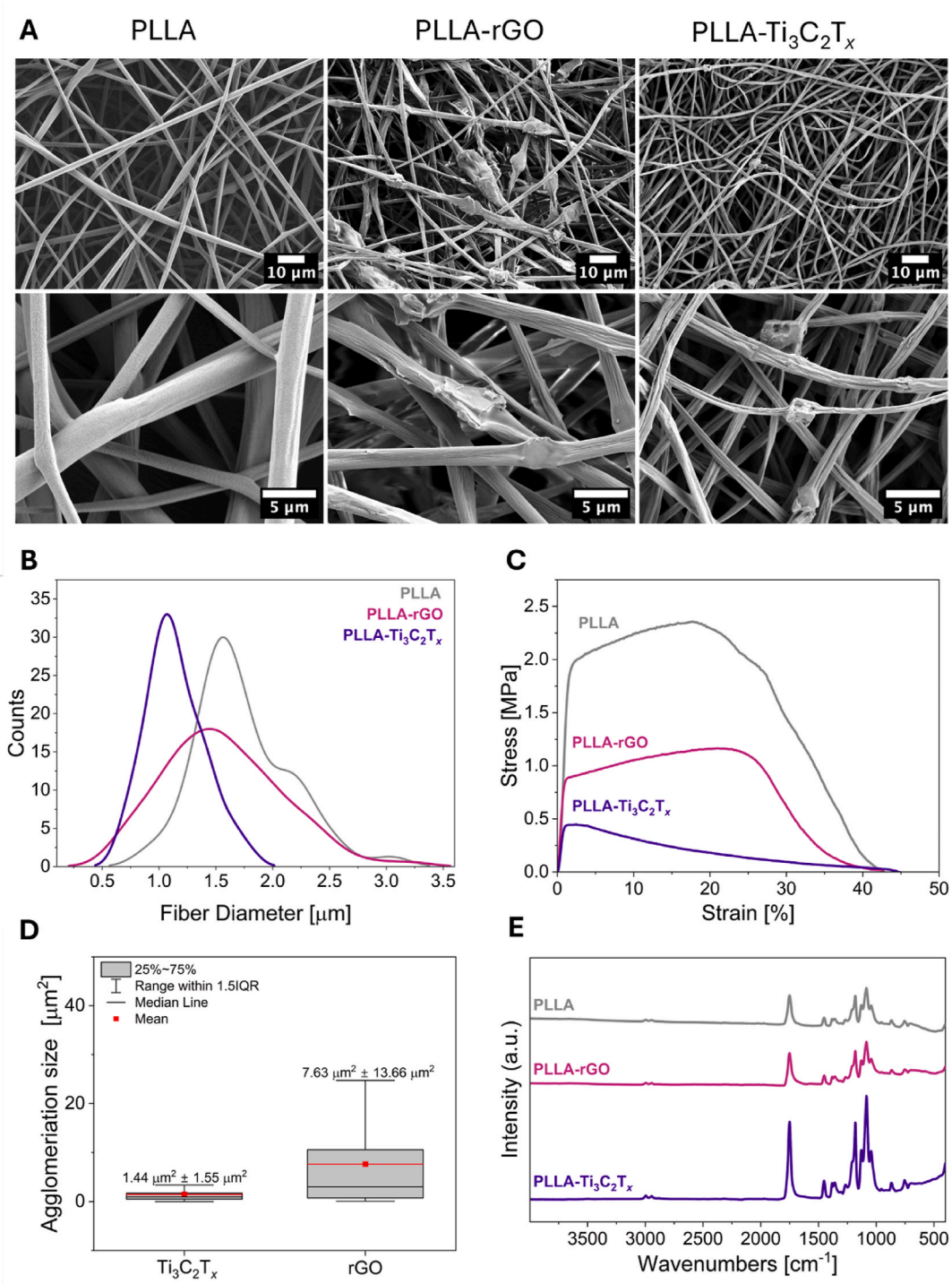

Fig. 2. A) SEM micrographs of PLLA, PLLA-rGO, PLLA-$Ti_3C_2T_x$ fibers. B) Fiber diameter distribution graph. C) Stress-strain curves from tensile tests of samples. D) Box chart of agglomeration size distribution within the fibers. E) FTIR results for fiber samples.

Table 3
Tensile test results with the characteristics values of elongation at failure (ε_f), tensile strength (σ), toughness (W), and elongation at maximum stress (ε_{max}). Errors are based on standard deviation, with N = 5, where N is the tensile test of one mat sample.

Sample	ε_f [%]	σ [MPa]	ε_{max} [%]	W [MJ·m^{-3}]
PLLA	42 ± 5.29	2.41 ± 0.18	21.86 ± 4.56	70.62 ± 15.26
PLLA-rGO	43.43 ± 1.85	1.08 ± 0.19	20.76 ± 0.65	30.37 ± 5.40
PLLA-$Ti_3C_2T_x$	45.16 ± 3.29	0.45 ± 0.10	2.17 ± 0.50	8.34 ± 1.43

fibers decreases significantly to 1.08 ± 0.19 MPa, while toughness drops to 30.37 ± 5.40 MJ m^{-3}. The large agglomeration sizes observed for rGO, contribute to this reduction in strength and toughness. These regions of high-stress act as initiation sites for crack propagation, diminishing the overall mechanical integrity of the fibers [62]. Moreover, PLLA-$Ti_3C_2T_x$ composite fibers exhibit an even more significant decrease in mechanical performance compared to PLLA and PLLA-rGO samples, with a lower tensile strength of 0.45 ± 0.10 MPa and a drastic reduction in ε_{max} to 2.17 ± 0.50 %. The toughness is also reduced to 8.34 ± 1.43 MJ m^{-3}, reflecting a substantial drop in the deformation energy the

composite can absorb before failure.

To investigate the role of filler agglomeration size and distribution on the fiber properties, we analyzed agglomeration patterns of $Ti_3C_2T_x$ and rGO within the fiber structures using confocal laser scanning microscopy (CLSM) and its transmitted light imaging. Consistent imaging parameters were applied across all samples, capturing 20 images per sample to ensure a comprehensive agglomerate distribution and size assessment. Agglomerations of $Ti_3C_2T_x$ and rGO were identified and analyzed within the fiber regions (SI Figure S1 H, J), delineated by the red mask (SI Figure S1 I, K).

Quantitative analysis revealed distinct differences in agglomeration size between the two fillers, as illustrated in the box plot in Fig. 2D. The average agglomeration size of rGO was significantly larger (7.63 ± 13.66 μm^2) compared to $Ti_3C_2T_x$ (1.44 ± 1.55 μm^2). rGO also exhibited greater variability, as indicated by a broader interquartile range and overall range in the box plot. In contrast, $Ti_3C_2T_x$ showed a narrower distribution and smaller agglomerates than rGO, suggesting better dispersion within the polymer matrix. These differences can be connected to distinct solvent-nanosheet interactions observed for $Ti_3C_2T_x$ and rGO when dispersed in DMF. $Ti_3C_2T_x$ is naturally terminated with surface functional groups (-OH, -F, -O) after the selective etching [63]. The presence of these polar functional groups renders its dispersion in polar solvents like DMF, as the polarity index of the solvent closely matches with the polarity of the material [64]. Here, the Hildebrand and Hansen models can be employed to predict the dispersion stability of nanomaterials in solvents. The Hildebrand solubility parameter (δ_T) is defined as the square root of the cohesive energy density, whereas the Hansen parameters refer to the contribution from dispersion, dipole, and hydrogen bonding interactions. According to these models, $Ti_3C_2T_x$ is stable in solvents with a δ_T close to 25.1 $MPA^{1/2}$ [65], which aligns well with DMF (δ_T of 24.9 $MPA^{1/2}$). Furthermore, the Hansen model describes that $Ti_3C_2T_x$ is stable in solvents with high polarity and high dispersion interaction strength, explaining their favorable dispersion in polar solvents [64]. In contrast, the reduction process of rGO removes oxygen-containing surface functional groups, leading to a loss of surface polarity. Consequently, rGO exhibits poor dispersibility in DMF compared to $Ti_3C_2T_x$. The δ_T of rGO is approximately 22 $MPA^{1/2}$ [66], but this value varies depending on the degree of reduction, indicating a lower compatibility with DMF.

Additionally, by energy-dispersive X-ray spectroscopy (EDS) we confirmed the presence of $Ti_3C_2T_x$ in the fibers, as shown by elemental mapping (SI Figure S1 L-N). Channels highlighting carbon (C), titanium (Ti), and fluorine (F) (SI Figure S1 N), as well as isolated Ti and F maps, verified the material's integration into fibers, appearing as agglomerates in beads-like features (SI Figure S1 L,M). The EDS spectrum for the PLLA-$Ti_3C_2T_x$ sample (SI Figure S1 O) confirmed the presence of Ti. In summary, both fillers influence fiber mechanical properties, with their agglomeration size and distribution playing a critical role. Despite the smaller and more uniform agglomerates of $Ti_3C_2T_x$, its presence in the PLLA matrix contributes to greater deterioration of tensile properties compared to rGO. This highlights the need to carefully consider filler dispersion and agglomeration characteristics in the design of composite materials.

As a necessary verification step, we performed Fourier-transform infrared spectroscopy (FTIR), see Fig. 2E. In the FTIR spectra of the composite fibers, characteristic peaks corresponding to the PLLA matrix were clearly visible. Although vibrations associated with $Ti_3C_2T_x$ —such as Ti–C stretching—are typically reported around 469 cm^{-1}, this peak was not clearly distinguishable in our samples. This is likely due to overlapping signals from the polymer and the relatively low filler content. As a result, identifying MXene-specific peaks using FTIR is challenging in this system, particularly in the 400–800 cm^{-1} region where such features are expected to appear [39,67]. Therefore, we acknowledge the limitations of FTIR in confirming the presence of MXenes in our composites and rely on additional characterization techniques (e.g., EDS, confocal imaging) to confirm their incorporation. The analysis of $Ti_3C_2T_x$ powder is presented in SI Figure S1 P. Characteristic peaks of rGO could not also be distinguished in PLLA-rGO fibers due to the overlapping of peaks with those coming from PLLA material. Analysis of pure rGO powder revealed increased intensity at 1715 cm^{-1} assigned to the stretching vibration of C=O moiety, and 1634 cm^{-1}, which can be attributed to the absorbed water molecules (SI Figure S1 P) [68]. The FTIR spectrum of all three samples of fibers reveals several distinctive peaks associated with PLLA chemical structure. A prominent peak at 1750 cm^{-1} corresponds to the C=O stretching mode of the ester group [69]. Peaks at 1211 and 1182 cm^{-1} are attributed to the C–O–C and CH_3 groups, respectively. Other characteristic bands appear at 1044, 1087, 1132, and 1456 cm^{-1}, linked to the asymmetric deformation of the C-CH_3, C–O–C, C-CH_3, and CH_3 groups, respectively [70]. Stretching vibrations of the CH_3 group are further indicated by peaks at 2946 and 2996 cm^{-1} [71]. The peak at 1384 cm^{-1} is also assigned to C–H stretching. Weaker bands at 872 and 921 cm^{-1} suggest the presence of α-crystal, while the band at 755 cm^{-1} is associated with C=O bending [71,72].

To complement the chemical verification provided by FTIR, differential scanning calorimetry (DSC) was performed to assess the thermal properties of the composite fibers and evaluate whether the incorporation of $Ti_3C_2T_x$ and rGO affected the thermal behavior of the fibers. The DSC analysis (SI Figure S1 R) revealed no significant variation in the glass transition temperature (T_g) among the samples. The measured T_g values were 60.44 ± 0.51 °C for neat PLLA, 60.02 ± 0.22 °C for PLLA-rGO, and 60.27 ± 0.59 °C for PLLA-$Ti_3C_2T_x$. These results indicate that the addition of $Ti_3C_2T_x$ and rGO did not alter the crystalline structure and further the thermal stability of the polymer matrix [73]. The consistency in T_g across all samples suggests limited interaction between the fillers and the polymer chains at a level that would significantly influence the thermal transitions. Comparing these findings with the literature is difficult because changes in the polymer structure are dependent on the composite fabrication process. However, similar results were reported with no change in T_g caused by incorporating rGO in polycaprolactone (PCL) or PLA matrix [73,74]. Although our thermal analysis did not reveal strong interactions between the polymer and fillers, previous studies suggest that conductive fillers within an insulating polymer matrix can still enhance charge transport, influencing the properties of composite fibers. For example, Wang et al. demonstrated that in polyethylene/graphene nanocomposites, improved conductivity was achieved through trap-modulated charge carrier transport, even with minimal polymer–filler interaction [75].

3.2. Surface properties of scaffolds

XPS analysis was performed to verify the surface chemistry of electrospun fibers. Table 4 lists the surface concentrations of chemical bonds obtained from fitting XPS data for all analyzed samples. The C 1s spectra were fitted with three components typical for PLLA polymer [76]. The first line centered at 285.0 eV indicates the presence of aliphatic carbon C-C, the second line at 286.9 eV indicates the presence of C-O groups, and the third line at 289.0 eV comes from O-C=O type bonds [76]. The O

Table 4
Atomic composition (%) of the surface of electrospun samples determined by fitting XPS data, see SI Figure S2.

	C			O			Si
Binding energy [eV]	285.0	286.9	289.0	532.2	533.6	535.0	100–103
Group	C-C	C-O	O-C=O	O=C	O-C O-Si	H_2O_{ads}	Si SiO_x
PLLA	22.5	16.7	23.9	16.4	17.0	2.6	0.9
PLLA-rGO	21.0	18.2	20.8	17.3	17.7	2.7	2.3
PLLA-$Ti_3C_2T_x$	18.1	16.4	21.6	15.0	17.5	4.4	6.9

1s spectra were fitted with three components: the first line centered at 532.2 eV, which points out the existence of O=C type bonds; the second line centered at 533.6 eV, indicating the presence of O-C type bonds, both typical for PLLA polymer and the last line centered at 535.0 eV comes from the presence of adsorbed water [76,77]. There is also a small amount of silicon in both metallic state and oxide form (from the substrate, which is a silicon wafer). High-resolution spectra are presented in SI Figure S2. The XPS analysis reveals that the surface chemistry of all samples is characterized only by bonds typical for PLLA, not the rGO and $Ti_3C_2T_x$. It suggests that most of the fillers are blended inside the fibers during electrospinning, as the XPS analysis depth is up to 5.7 nm from the fiber surface at a 45° measurement angle [78,79]. If the filler mixed with the PLLA solution were located at the surface, the XPS analysis would be able to detect that [80]. Similar surface chemistry of all the samples let us exclude this parameter from the possible effect on cell response.

As discussed in the literature, the changes in the surface chemistry of electrospun fibers can be correlated with the surface potential variation measured directly by KPFM or validated by zeta potential investigation, which highly affects cell integration with the scaffolds [81,82]. For instance, it was reported that the charges on the fibers can be tuned by changing voltage polarity during electrospinning, further improving cell adhesion [45,83]. Fig. 3A shows the KPFM maps illustrating the fiber topography and the corresponding surface potential. The KPFM measurements revealed that fibers with rGO exhibited an average surface potential shift of approximately 50 mV compared to pure PLLA fibers, as presented in Fig. 3B. Notably, fibers containing $Ti_3C_2T_x$ displayed an even greater surface potential shift, exceeding 400 mV relative to pure PLLA. The observed change in surface potential is likely due to a shift in the material's work function after blending PLLA with rGO and $Ti_3C_2T_x$ fillers. It is due to the relationship between work function and the contact potential difference obtained in the KPFM measurement as stated in the equation:

$$V_{CPD} = \frac{WF_{tip} - WF_{sample}}{e} \quad (1)$$

where WF_{tip} and WF_{sample} are the work functions of the tip and the sample, respectively, and *e* is the elementary charge [84]. In this work, we determined the work function (WF) of PLLA using highly ordered pyrolytic graphite (HOPG) as a reference, obtaining a value of 4.7 ± 0.1 eV. This estimated WF is consistent with previous findings, where, although the WF of PLLA was not directly reported, data suggested a similar range, allowing us to approximate a WF of 4.6 ± 0.1 eV [45]. Therefore, we estimate the WF of electrospun PLLA to be in the range of 4.6–4.7 eV. Thus, the relatively small shift in surface potential for the PLLA-rGO fibers is probably due to the similarity between the WF of PLLA and rGO, which is approximately 4.8 eV according to the literature, which results in minimal impact on the overall surface potential of

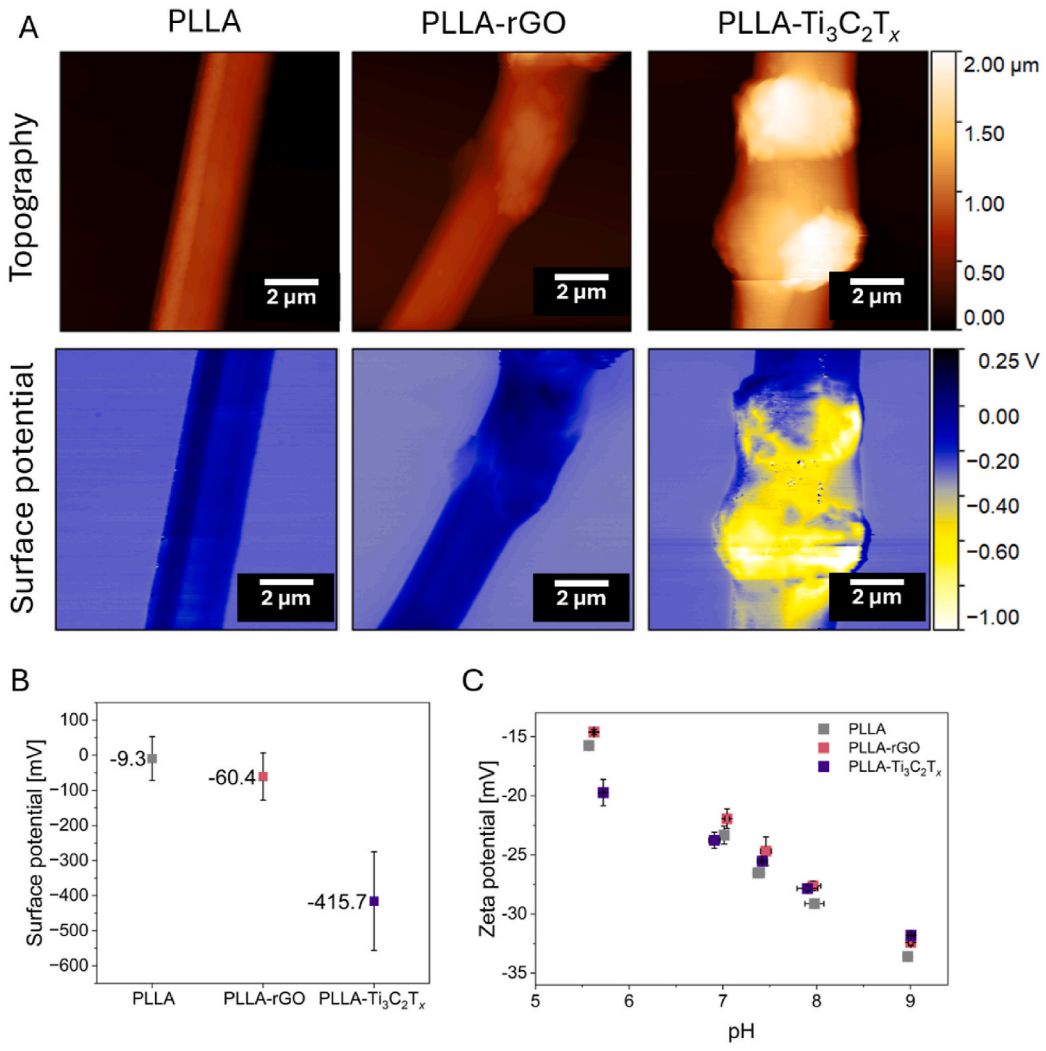

Fig. 3. Surface properties of fibers: A) topography images and surface potential maps (KPFM), B) surface potential of fibers (KPFM), and C) zeta potential results in the pH range of approximately 5.5–9.

PLLA-rGO fibers [85]. In contrast, PLLA-$Ti_3C_2T_x$ fibers showed a substantial increase in surface potential, likely due to the lower WF of $Ti_3C_2T_x$ (~4.2 eV) [86] The introduction of $Ti_3C_2T_x$ filler thus shifted the WF of the composite material, resulting in the observed change in surface potential. It is important to note that these measurements were conducted under ambient conditions, which may introduce variations and contribute to the observed standard deviation in WF calculations. While KPFM provides localized surface potential measurements on individual fibers, the consistent trends observed across multiple sites suggest these values are representative. The data demonstrate a clear correlation between the filler type and the resulting surface potential, highlighting the potential of rGO and MXene for tuning fiber surface properties in relevant applications.

Results given by XPS and KPFM prove that even if the incorporated particles are not exposed on the surface being covered with a layer of polymer thicker than 6 nm, they still affect the surface charge of fibers. As KPFM measures the local surface potential at the nanoscale, providing the data on the work function or contact potential difference, this is a direct reflection of surface charge density, but on a dry, solid surface in a controlled environment. In contrast, zeta potential indicates the electrostatic potential near the slipping plane in a liquid environment, reflecting the charge that can develop when the material is suspended in a solution [87]. We performed zeta potential measurements to give a more comprehensive view of the material behavior across different conditions (Fig. 3C). The results show no significant differences between the samples in zeta potential values in the pH range of 5.5–9. We have chosen this pH range to reflect conditions relevant to the human body, encompassing the physiological pH spectrum commonly observed in various biological systems. For pH around 7.5, zeta potential was −26.61 mV for PLLA, −24.7 mV for PLLA-rGO, and −25.52 mV for PLLA-$Ti_3C_2T_x$. Work published by Yin and Drelich discusses the role of electrokinetic effects and surface heterogeneity challenges in zeta potential measurements [88]. Their study highlights how zeta potential measurements can often average out the actual heterogeneity of surface charges, as traditional electrokinetic approaches do not provide localized information and only offer an overall potential across complex surfaces. Due to the complex composition of the cell culture media, the interpretation of the zeta potential data is challenging, however, it has been previously validated for the simulated body fluid [89].

3.3. Cell adhesion and focal adhesion point analysis

Cell adhesion after 5h of incubation, followed by scaffold rinsing to remove non-adhered cells, was measured as cell density per mm^2 of fibrous scaffold (see Fig. 4A). Here, PLLA and PLLA-$Ti_3C_2T_x$ demonstrated similar adhesion of osteoblasts. In contrast, PLLA-rGO showed significantly higher cell adhesion than pure PLLA fibers, reflected by the greater median cell density and a wider range of values, suggesting strong cell-fiber interactions. This suggests that rGO can enhance physical adhesion due to rGO agglomerates being much bigger in size (SI Figure S1 H-K), changing scaffold geometry, and creating supportive architecture. To the best of our knowledge, agglomerated fillers were never used to diversify the architecture of electrospun fibers for better cell-material interaction in tissue engineering. Interestingly, beaded electrospun fibers have similar morphology and have recently drawn attention in drug delivery systems [90–92]. A study by Santillan et al. presents that beads-on-string fibers benefit osteoblast attachment and filipodia formation, serving more attachment sites [93].

Since adhesion after 5 h is an initial cell response, we additionally provide a detailed analysis of focal adhesion points after 3 days of incubation. Here, we use the protocol of osteoblast's focal adhesion formation assessment that was already published for electrospun PMMA fibers [10]. Similarly, we verified cell-individual fiber interaction as presented in the scheme in Fig. 4B. In this study, paxillin, a key protein forming the multiprotein complex responsible for cell adhesion to the extracellular matrix, was labeled using immunofluorescence. Paxillin, visualized in orange in the images, enabled detailed analysis of adhesion sites. High-resolution CLSM (Airyscan) imaging provided high-quality images of paxillin distribution within cells, subsequently used for quantitative analysis of cell adhesion site distribution on different scaffolds. In Fig. 4: C, C_1, D, D_1, E, E_1 we present CLSM images of focal adhesions (stained paxillin - orange) and transmitted light channel for single fiber and single cell for PLLA, PLLA-rGO, and PLLA-$Ti_3C_2T_x$ fibers. The application of high-resolution CLSM imaging enabled precise visualization of the distribution of cell adhesion sites to the scaffold fibers (C_2, C_3, C_4). High-resolution CLSM imaging resulted in a higher signal-to-noise ratio, allowing for the identification of a greater number of distinguishable adhesion sites and structural features, which were not as clearly resolved with confocal imaging [10,94,95]. Agglomerations of rGO and $Ti_3C_2T_x$ are visibly seen in transmitted light Fig. 4: D_1, D_3, E_1, E_3, respectively.

The quantitative analysis involved binary processing and quantification of the labeled adhesion site signals, followed by cluster and morphological analyses. The cluster analysis, see Fig. 4: D_4, E_4, utilized the DBSCAN algorithm to identify and quantify the distribution of adhesion sites. Morphological analysis focused on determining fundamental parameters, including: area (the size of identified adhesion clusters, see Fig. 4F), density (the number of detected intensity maxima within each cluster area see Fig. 4G), Feret diameter (the maximum dimension of the adhesion clusters, see Fig. 4H), distance between clusters (the spatial arrangement and separation between adhesion clusters, see Fig. 4I). For regions where cells interacted with $Ti_3C_2T_x$ or rGO containing fibers, additional analysis was conducted. This involved measuring the distance from each detected local intensity maximum (adhesion site) to the centroid of the corresponding $Ti_3C_2T_x$ or rGO area. These measurements provided detailed insights into how scaffold properties influence the spatial organization of adhesion sites (Fig. 4J) [10].

The analysis of the area of cell adhesion clusters (Fig. 4F) revealed notable differences depending on the scaffold material. The average cluster size for cell adhesion to PLLA fibers was comparable to that observed for PLLA-rGO fibers, indicating similar interactions between cells and these scaffolds in terms of adhesion area. However, in the case of cells adhering to PLLA-$Ti_3C_2T_x$ fibers, the average cluster size was over 50 % larger than those observed for the other two materials. This significant increase suggests that the inclusion of $Ti_3C_2T_x$ in the scaffold composition enhances the development of larger adhesion sites. This could be attributed to the unique surface potential of PLLA-$Ti_3C_2T_x$ fibers, which may promote stronger or more extensive interactions between cells and the scaffold surface.

The density (Fig. 4G), representing the local maxima per millimeter within identified adhesion clusters, did not reveal significant differences between the tested scaffolds. However, a wider spread of values was observed for adhesion to PLLA-$Ti_3C_2T_x$ and PLLA-rGO fibers. For adhesion complexes on PLLA fibers, the variability in this parameter was approximately two times lower, suggesting a more uniform cell adhesion process. This can be explained by the cells interacting either directly with regions enriched with $Ti_3C_2T_x$ or rGO agglomerates or with areas of the scaffold lacking these additives.

The Feret diameter (Fig. 4H), defined as the maximum distance between two points on the outer contour of an object along a specific direction, provides insights into the elongation of adhesion clusters on different scaffolds. The results indicate that the most elongated adhesion clusters were observed in the interactions between cells and PLLA-$Ti_3C_2T_x$ fibers, with an average Feret diameter of 2.35 μm. Additionally, this scaffold type exhibited the highest variability in Feret diameter distribution among all tested scaffolds, suggesting diverse morphologies of adhesion clusters. In contrast, the least elongated adhesion clusters were associated with cell adhesion to PLLA-rGO fibers, with an average Feret diameter of 1.68 μm and the smallest variability in distribution. This observation implies that adhesion clusters on PLLA-rGO fibers are more compact and uniform in shape than those on PLLA-$Ti_3C_2T_x$ or pure

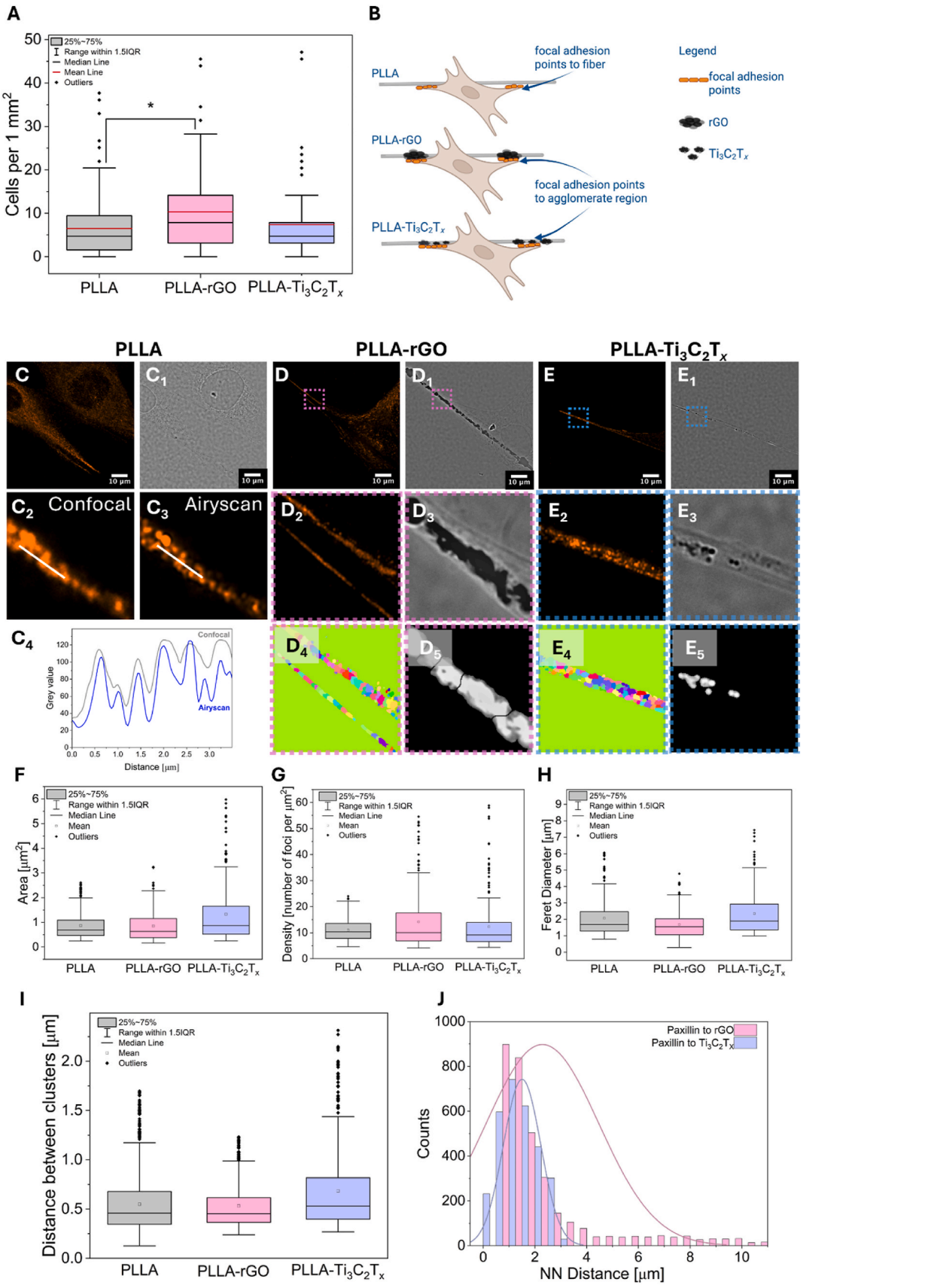

(caption on next page)

Fig. 4. A) Cell adhesion after 5 h of incubation. B) Scheme presenting the focal adhesion point analysis of cells to PLLA fibers, and fibers with filler enriched regions (rGO, and $Ti_3C_2T_x$), underlying single fiber – single cell interaction. High-resolution imaging and quantitative analysis of cellular interaction with different scaffolds: C) CLSM image of single cell and single PLLA fiber with stained paxillin (orange), and C_1) the same view in transmitted light. C_2), C_3) Graph displaying the differences in the resolution contrast between CLSM and high-resolution CLSM (Airyscan mode) imaging. C_4) Graph presenting the intensity profile, which demonstrates improved spatial resolution of Airyscan mode compared to confocal imaging. D) CLSM image of single cell and single PLLA-rGO fiber with stained paxillin (orange), and D_1) the same view in transmitted light. D_2), D_3) Zoomed images on selected areas from D) and D_1) marked with pink squares. D_4), D_5) Segmented paxillin and rGO agglomerations for quantitative analysis, respectively. E) CLSM image of single cell and single PLLA-$Ti_3C_2T_x$ fiber with stained paxillin (orange), and E_1) the same view in transmitted light. E_2), E_3) Zoomed images on selected areas from E) and E_1) marked with blue squares. E_4), E_5) Segmented paxillin and $Ti_3C_2T_x$ agglomerations for quantitative analysis, respectively. F) Box chart presenting cluster analysis of the area of focal adhesions. G) Graph showing foci density, and H) Feret diameter of focal adhesions. I) Box chart presenting the distance between the clusters, and J) graph of nearest-neighbor (NN) distance distribution between rGO and $Ti_3C_2T_x$ agglomerations and focal adhesions. Focal adhesions (paxillin) stained with Alexa Fluor Plus 555 (orange). (For interpretation of the references to color in this figure legend, the reader is referred to the Web version of this article.)

PLLA fibers.

The analysis of the distance between clusters (Fig. 4I) examined the spatial distribution of adhesion clusters on different scaffold types. The results revealed no statistically significant differences in the average distance between adhesion clusters on PLLA and PLLA-rGO fibers, indicating a similar spatial arrangement of adhesion sites on these materials. In contrast, interactions between cells and PLLA-$Ti_3C_2T_x$ fibers showed a broader spread in the measured distances between clusters. Additionally, the average distance between adhesion clusters on PLLA-$Ti_3C_2T_x$ was approximately 30 % greater than that observed for PLLA and PLLA-rGO fibers. This increased variability and larger average distance suggest that the incorporation of $Ti_3C_2T_X$ alters the spatial organization of adhesion clusters, potentially due to the unique surface properties or very good distribution of $Ti_3C_2T_x$ within the scaffold.

The histogram in Fig. 4J represents the distribution of measured distances between the center of intensity for each identified paxillin accumulation site (as a marker of cell adhesion) and the centroid of polymer fibers containing either $Ti_3C_2T_x$ or rGO. This analysis provides insight into how cells form adhesion sites relative to regions enriched with $Ti_3C_2T_x$ or rGO in PLLA fibers. The results presented in this histogram (Fig. 4J) indicate that for PLLA-rGO fibers, cells exhibit a stronger tendency to form adhesion sites in close proximity to or directly at fiber regions rich in rGO, compared to $Ti_3C_2T_x$. In both cases, the majority of identified adhesion sites are located near regions containing $Ti_3C_2T_x$ or rGO. However, a significant portion of adhesion sites associated with PLLA-$Ti_3C_2T_x$ fibers are found at greater distances from the "$Ti_3C_2T_x$-enriched" regions. This observation is somewhat counterintuitive. $Ti_3C_2T_x$-rich regions in fibers are smaller and more uniformly distributed compared to rGO-rich regions, theoretically giving cells more opportunities to form adhesion sites close to $Ti_3C_2T_x$ agglomerates. Conversely, rGO clusters within the fibers are significantly larger, making it expected that the measured distances between adhesion sites and the centroids of rGO-enriched regions would be greater, but surprisingly, this is not the case. This phenomenon can be explained by the differences in the accessibility and spatial distribution of rGO and $Ti_3C_2T_x$ within the PLLA fibers. Data from Fig. 2D and SI Figure S1 H-K highlight substantial differences in the distribution of $Ti_3C_2T_x$ and rGO within the fibers. Cells have relatively greater access to rGO-enriched regions within PLLA-rGO fibers, which encourages the formation of adhesion sites directly at these regions. In contrast, the smaller and more evenly dispersed $Ti_3C_2T_x$ agglomerates result in cells forming adhesion sites at varying distances from $Ti_3C_2T_x$ regions. The larger rGO agglomerates within fibers promote more consistent and closer adhesion, whereas the smaller, more uniform $Ti_3C_2T_x$ areas lead to a broader distribution of adhesion distances.

Summarizing, cluster and morphological analyses revealed significant differences in the architecture of cell adhesion sites formed on PLLA fibers compared to PLLA fibers with $Ti_3C_2T_x$ or rGO additives. Cell adhesion clusters on PLLA-$Ti_3C_2T_x$ fibers were observed to be longer, larger, and denser in terms of local maxima of adhesion sites compared to those on the other fiber types. This indicates that the addition of $Ti_3C_2T_x$ significantly alters the adhesion site architecture, promoting the formation of more extensive and dense adhesion clusters. In contrast, the adhesion clusters formed on PLLA and PLLA-rGO fibers exhibited similar morphological characteristics, including comparable sizes and elongation. However, cells interacting with PLLA-rGO fibers formed a denser network of local adhesion sites compared to those on pure PLLA. It is important to note that the initial cell adhesion measured after 5 h reflects early attachment dynamics, whereas the analysis of focal adhesion points via paxillin staining after 3 days provides insight into more mature and stabilized cell–material interactions, which follow different trends over time.

3.4. Cell proliferation, replication, and infiltration into the scaffold

Cell proliferation is the critical step of material biocompatibility assessment, which gives information on how well cells grow and multiply on the material, indicating the material's ability to support cellular functions vital for tissue regeneration and repair [96–101]. The surface properties of electrospun fibers, such as topography, porosity, architecture, surface chemistry, and surface charges, play a role in influencing cell proliferation by modulating cell adhesion, nutrient diffusion, and signaling pathways [21,45]. Hence, proliferation, replication, and adhesion provide complementary evaluations of cell behavior in response to fiber surface properties [12,102–104]. The replication test is used to detect new DNA synthesis during cell replication. This assay enables the measurement of DNA synthesis activity, accurately determining whether cells are undergoing division during the specific time window in which they were incubated with the precursor [105]. It offers high sensitivity and specificity, helping in the interpretation of the results of standard proliferation and adding information about its dynamics [102,106–109]. Fig. 5A presents results from the proliferation of cells on different substrates: PLLA, PLLA-rGO, and PLLA-$Ti_3C_2T_x$ fibers at days 1, 3, and 7 of incubation. On day 1, all materials showed similar cell proliferation, suggesting no significant difference in initial compatibility. Day 3 results indicate significantly the best proliferation for PLLA-rGO, slightly lower for PLLA, and lastly for PLLA-$Ti_3C_2T_x$. The last time point at day 7 presents significantly increased proliferation for all of the samples, with the highest fluorescence coming from PLLA fibers, followed by PLLA-rGO and PLLA--$Ti_3C_2T_x$. Replication activity, defined as the ratio of replicating to all cells, was relatively similar for all samples on days 1 and 3, see Fig. 5E. In contrast, at day 7, PLLA-$Ti_3C_2T_x$ displayed the highest replication activity, significantly higher than for PLLA-rGO. Exemplary CLSM images used for the replication study are shown in SI Figure S3, where green nuclei represent the replicating and blue non-replicating cells.

The confocal images in Fig. 5C_1-C_9 demonstrate the increased number of cells on all scaffolds over time, starting from day 1 (Fig. 5C_1-C_3), progressing through day 3 (Fig. 5C_4-C_6), and culminating at day 7 (Fig. 5C_7-C_9). During this period, the cell morphology remains consistent with standard cellular structures, indicating no adverse effects on cell morphology. By day 7, a monolayer of cells is evident on the surface of the PLLA fibers. In contrast, for the PLLA-rGO and PLLA-$Ti_3C_2T_x$ scaffolds, the cells appear less densely packed on the top surface of fibers.

Due to observed differences in the properties of scaffolds and varieties in cell responses, we provide a study on cell infiltration into the

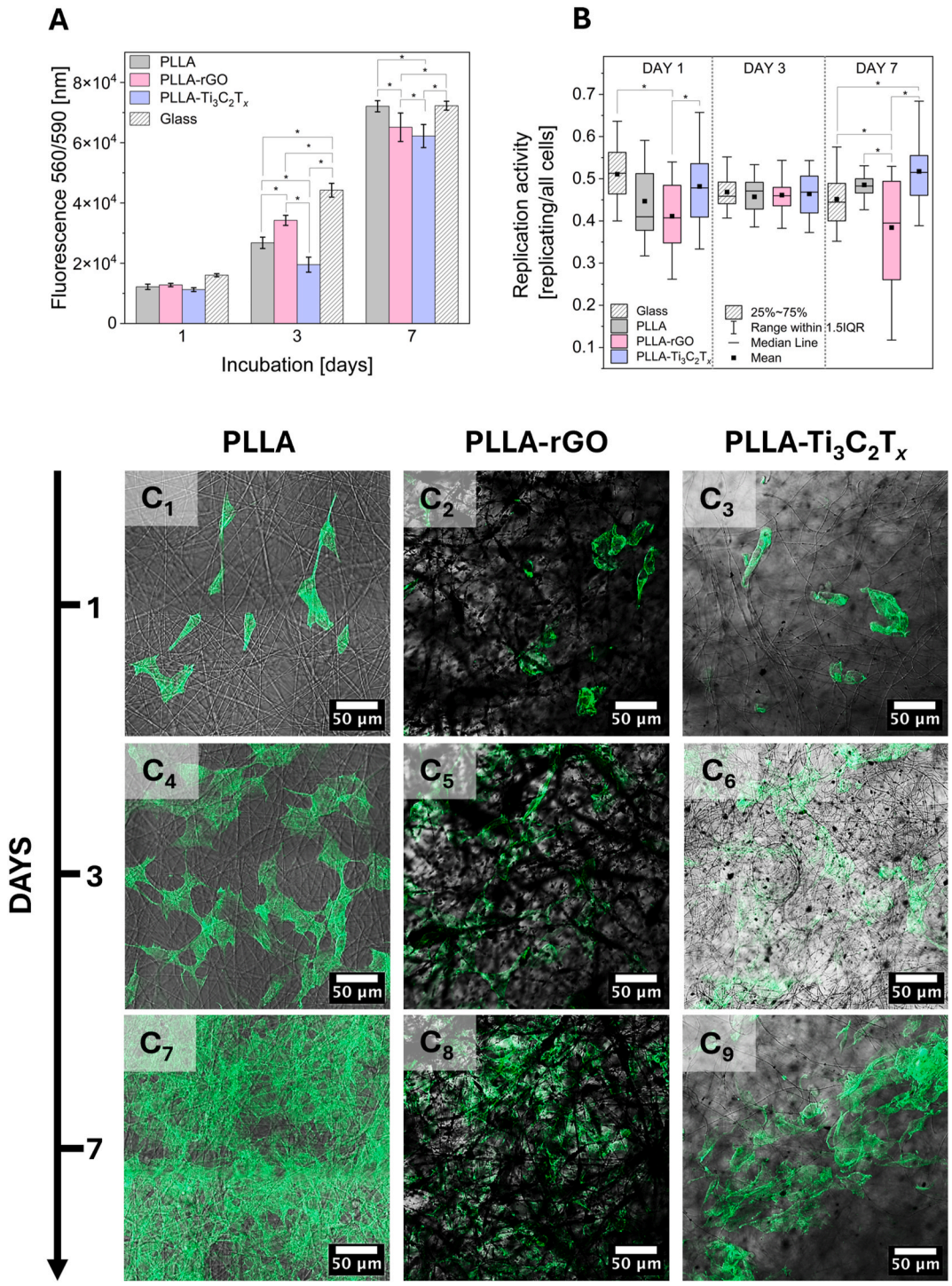

Fig. 5. A) Proliferation and B) replication assessment after 1, 3, and 7 days of cell incubation on three types of scaffolds and glass slide as a positive control. Morphology of cells on PLLA, PLLA-rGO, and PLLA-$Ti_3C_2T_x$ fibers at 1 (C_1-C_3), 3 (C_4-C_6), and 7 (C_7-C_9) days of culture visualized with CLSM. The actin filaments were stained with Alexa Fluor 488 Phalloidin (green). *statistical significance calculated with ANOVA followed by Tukey's post hock tests, $p < 0.05$. (For interpretation of the references to color in this figure legend, the reader is referred to the Web version of this article.)

fibrous structure. Cells are visibly growing into the scaffold structure, as evidenced by cell bodies extending out of the focal plane of the confocal images (Fig. 5C_7-C_9). This observation was further confirmed by 3D CLSM imaging (z-stack) and signal depth analysis, which captured signals from both actin filaments and nuclei presented in a digital movie (SI Movie S1). This technique confirms cellular penetration throughout the PLLA, PLLA-rGO and PLLA-$Ti_3C_2T_x$ scaffolds, and CLSM signal depth analysis gives insights into cell infiltration. The mean intensity profiles of nuclei (Fig. 6A) and actin (Fig. 6B) across the depth of the scaffolds PLLA, PLLA-rGO, and PLLA-$Ti_3C_2T_x$ highlight the variations in cellular behavior. The actin signal for PLLA scaffolds peaks with a full width at half maximum (FWHM) of 30.1 µm. This sharp and narrow peak indicates that cells predominantly reside near the scaffold's surface, with very limited migration into deeper layers. Similarly, the nuclei signal shows a maximum intensity of 10.9 with an FWHM of 29.7 µm, confirming restricted cellular penetration. The PLLA-rGO scaffold exhibits a

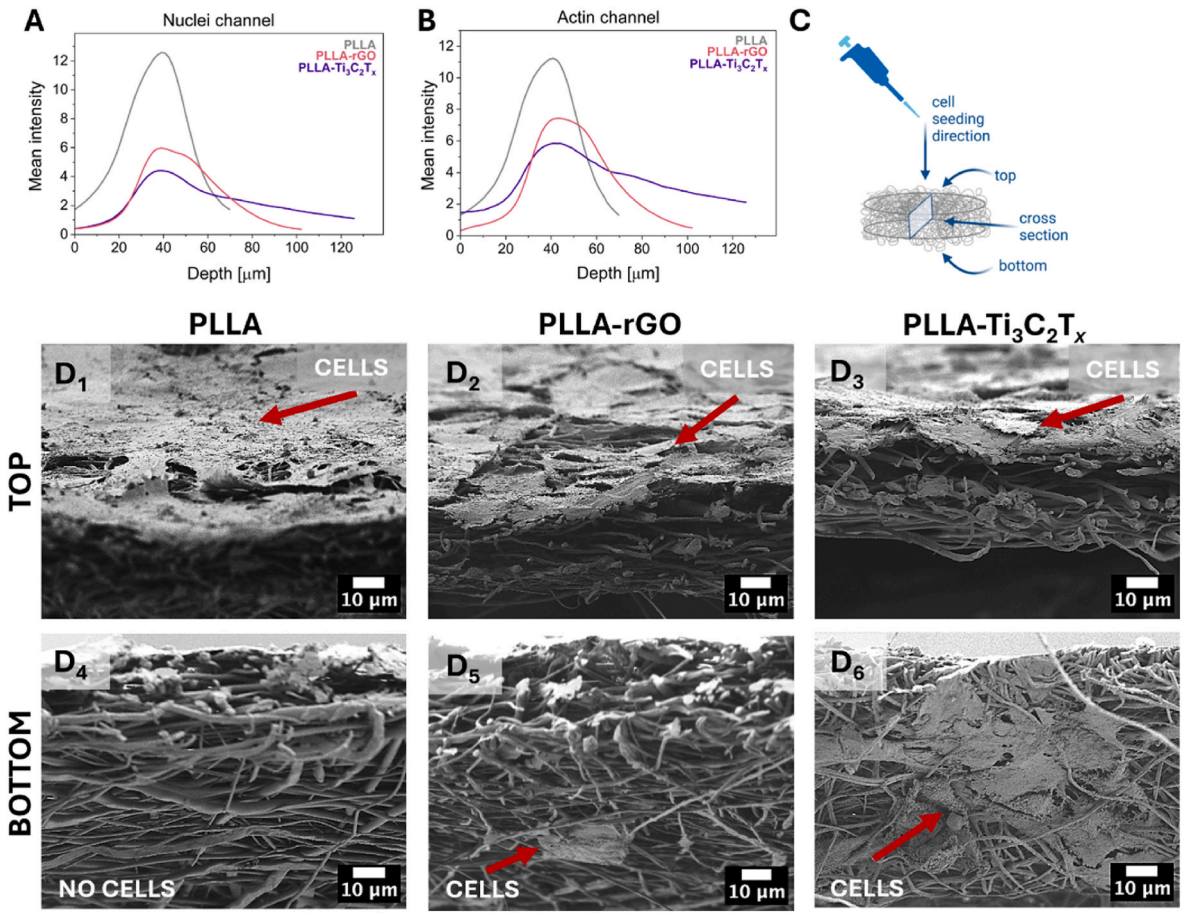

Fig. 6. Analysis of signal intensity from immunofluorescently stained actin and nuclei of osteoblasts on varying depths of z-stack imaging of PLLA, PLLA-rGO, and PLLA-$Ti_3C_2T_x$ scaffolds (7th day of incubation), with depth 0 μm being the top view of the sample. A) Graph with the signal intensity of nuclei channel (DAPI), and B) the actin channel (Alexa Fluor 488 Phalloidin). C) Scheme of cell seeding with indicated top and bottom view of sample observation. D_1-D_6) SEM micrographs of cells after 7 days of culture on PLLA, PLLA-rGO, and PLLA-$Ti_3C_2T_x$ fibers, taken at: D_1-D_3) top view, D_4-D_6) bottom view of the samples, allowing analysis of cell infiltration into the scaffolds.

broader actin signal profile, with a maximum intensity of 5.8 and an FWHM of 52.1 μm. This indicates enhanced cellular infiltration throughout the scaffold, with cells distributed over a wider depth range, reaching depths up to 100 μm. The nuclei signal also supports this observation, with a maximum intensity of 4.0 and an FWHM of 48.3 μm. The broader depth distribution in PLLA-rGO sample (up to ~100 μm) reflects improved scaffold properties, which promote cellular migration and integration compared to PLLA. The actin signal for the PLLA-$Ti_3C_2T_x$ scaffold shows a maximum intensity of 7.4 μm and an FWHM of 37.3 μm. This distribution suggests the best cellular infiltration, with cells extending deeper into the scaffold than for PLLA and PLLA-rGO. The cells penetrate to depths of approximately 120 μm. The nuclei signal mirrors this trend, with a maximum intensity of 5.6 μm and an FWHM of 38.0 μm. This suggests that PLLA-$Ti_3C_2T_x$ scaffolds provide the most preferable environment for cellular migration into deeper layers (up to ~120 μm), while the PLLA scaffold limits cellular penetration to surface layers, with cells concentrated within the first ~30 μm from the surface.

Supplementary data related to this article can be found online at https://doi.org/10.1016/j.mtbio.2025.101785

The scheme in Fig. 6C shows the methodology of seeding cells and choosing the plane for top and bottom observations of cell infiltration. In Fig. 6D_1-D_6**-D**, we present SEM micrographs of scaffolds after 7 days of cell incubation with a focus on the top (Fig. 6D_1-D_3), and the bottom (Fig. 6D_4-D_6) of the scaffold. In all scaffolds, cells were visibly growing on the top surfaces of the fibers. PLLA scaffolds show a dense layer of cells on the top, while no cell is on the bottom of the scaffold. Minimal or no cellular infiltration beyond the surface layer of PLLA fibers suggests a barrier effect likely caused by the structural density of the fibers limiting cell migration through the scaffold. In contrast, analyzing together results from CLSM cell morphology and SEM, we observe a less dense cell layer on the top of PLLA-rGO and PLLA-$Ti_3C_2T_x$ scaffolds. Still, there is a higher degree of cell infiltration demonstrated by the presence of cells at the bottom of these two samples, highlighted with red arrows (Fig. 6D_5, D_6). Definitely, the best infiltration was observed for PLLA-$Ti_3C_2T_x$ with the highest number of cells on the bottom side. It can be assumed that both rGO and $Ti_3C_2T_x$ incorporated in fibers affected the surface potential of fibers, which also led to changed scaffold geometry supporting better cellular penetration. rGO incorporated in fibers affected scaffold architecture due to large filler agglomerates. However, it must be noted that it is PLLA-$Ti_3C_2T_x$ that shows the highest surface potential measured with KPFM and the highest level of cell infiltration. The highly charged PLLA-$Ti_3C_2T_x$ fibers were repelling each other, increasing scaffold porosity and supporting better cell infiltration [110–112].

Previous studies have demonstrated that incorporating rGO into electrospun scaffolds can enhance cell proliferation, osteogenic differentiation, and even impart antimicrobial properties due to improved surface roughness and conductivity [113–115]. Similarly, MXene-containing scaffolds have shown potential for promoting protein adsorption, biomineralization, and supporting osteoblast activity, as reported by Awasthi et al. [39]. However, these studies did not directly evaluate or compare the impact of rGO and MXene fillers on local surface charge or correlate these effects with focal adhesion dynamics. Our

study uniquely addresses this gap by analysis of surface charges and zeta potential of scaffolds and cells responses. This is a unique comparative approach to investigation of rGO and MXenes fillers in fibrous PLLA scaffolds. A summary of the key findings of our studies and their relevance for tissue engineering applications is provided in Table 5.

4. Conclusions

This study demonstrates the consequences of the scaffold properties related to the incorporation of conductive fillers, such as rGO and $Ti_3C_2T_x$, into electrospun PLLA fibers. We identified two major findings. First, the correlation between cell adhesion to fibers and cell infiltration into scaffolds is not straightforward. Second, the conductivity of the polymer solution during electrospinning, along with the surface charge retained by the produced fibers, has a significant impact on cellular responses in tissue engineering.

In more detail, the morphological analysis of fibers using CLSM revealed distinct agglomeration patterns where rGO forms larger and more variable clusters, while $Ti_3C_2T_x$ produces smaller, more uniform agglomerates. These differences have significant implications for the mechanical performance of the fibers. Incorporating rGO and $Ti_3C_2T_x$ into PLLA significantly altered the tensile strength, which decreased by 55 % with rGO and 81 % with $Ti_3C_2T_x$ compared to neat PLLA. Toughness dropped substantially by 57 % with rGO and 88 % with $Ti_3C_2T_x$, reflecting a significant reduction in the material's ability to absorb deformation energy. Additionally, strain at maximum stress remained stable for PLLA-rGO but was reduced by 90 % for PLLA-$Ti_3C_2T_x$, indicating increased brittleness.

KPFM analysis revealed substantial shifts in surface potential, highlighting the impact of the fillers on fiber surface charge density. PLLA-rGO fibers exhibited a modest surface potential difference compared to PLLA (~50 mV), while PLLA-$Ti_3C_2T_x$ fibers showed a significant shift exceeding 400 mV. These surface potential changes correlate with the filler's influence on cellular interactions despite their sub-surface embedding, confirmed by the XPS analysis.

Cell studies showed that cell adhesion after 5 h of incubation is significantly better for PLLA-rGO than PLLA fibers. Later, cell focal adhesion points were verified, highlighting that the incorporation of rGO and $Ti_3C_2T_x$ altered adhesion site architecture. $Ti_3C_2T_x$ promoted the formation of larger, elongated, and denser adhesion clusters, while rGO enhanced the density of localized adhesion points. These results emphasize the role of filler type and distribution in modulating cell adhesion characteristics. Moreover, cell infiltration was affected by differences between scaffolds. Pure PLLA fibers support surface-level cell proliferation but exhibit limited cellular penetration, while the incorporation of rGO changes scaffold architecture and provides more cell anchoring spots, enabling deeper cell migration (~100 μm). $Ti_3C_2T_x$ also changes the geometry of the scaffold similarly to rGO but improves infiltration even better, allowing cells to penetrate uniformly to depths of ~120 μm.

Importantly, incorporating rGO and $Ti_3C_2T_x$ into electrospun PLLA fibers distinctly alters fiber morphology, mechanical properties, surface potential, and cellular behavior. While rGO creates the most diversified scaffold architecture and improves adhesion density, $Ti_3C_2T_x$ stands out for its ability to enhance cellular infiltration and support extensive adhesion cluster formation. Despite the promising results presented in this study, certain limitations should be acknowledged. While versatile and scalable, the electrospinning process still faces challenges in achieving precise control over filler dispersion and maintaining batch-to-batch consistency. Additionally, isolating the specific contribution of surface charge from other properties, such as topography and stiffness, remains complex. Using non-degradable conductive fillers like rGO and MXenes also raises questions about long-term biocompatibility and clearance, which require further investigation. Nevertheless, our study contributes to the fundamental understanding of how local surface properties of biomaterials affect cell adhesion and infiltration. These insights are relevant for scaffold design in tissue engineering and provide a broader framework for interpreting cell–material interactions across various biomedical applications.

Table 5
Summary of the key findings from this study and their implications for tissue engineering applications. The table highlights the effects of rGO and $Ti_3C_2T_x$ incorporation on scaffold properties and cell behavior.

Parameter Studied	Key Finding	Implications for Tissue Engineering
filler type (rGO vs $Ti_3C_2T_x$)	$Ti_3C_2T_x$ produced higher charged surfaces compared to rGO	filler selection affects bioelectric interactions with cells
fiber morphology	filler aggregates affected morphology and the mechanical performance of scaffolds	morphological and mechanical properties affect cell behavior and integration with scaffold
surface potential (KPFM)	PLLA-$Ti_3C_2T_x$ scaffolds showed highest surface potential	high surface potential promotes stronger/ enhanced cell-material interactions
early cell adhesion (up to 5 h *in vitro* studies)	addition of rGO promoted early adhesion; PLLA-$Ti_3C_2T_x$ showed comparable adhesion to pure PLLA	early cell adhesion can affect subsequent cell responses
focal adhesion cluster size analysis	addition of $Ti_3C_2T_x$ increased cluster size and density of focal adhesion sites of cells	enhanced adhesion clusters can promote better integration of cells with scaffold
cell infiltration depth	cell infiltration improved from ~70 μm (PLLA) to ~100 (PLLA-rGO) and ~125 μm (PLLA-$Ti_3C_2T_x$)	deep cells infiltration in the scaffolds improves and speeds up tissue regeneration
scaffold porosity and spacing between fibers	repelling effect and agglomeration of fillers led to more open structure of PLLA-$Ti_3C_2T_x$ scaffolds	scaffold 3D architecture can be tuned via surface charge effect on polymer fibers

CRediT authorship contribution statement

Martyna Polak: Writing – review & editing, Writing – original draft, Visualization, Validation, Methodology, Investigation, Formal analysis, Data curation, Conceptualization. **Krzysztof Berniak:** Writing – review & editing, Writing – original draft, Visualization, Methodology, Investigation. **Piotr K. Szewczyk:** Writing – review & editing, Writing – original draft, Visualization, Methodology, Investigation. **Joanna Knapczyk-Korczak:** Writing – review & editing, Visualization, Methodology, Investigation. **Mateusz M. Marzec:** Writing – review & editing, Visualization, Methodology, Investigation. **Muhammad Abiyyu Kenichi Purbayanto:** Writing – review & editing, Methodology, Investigation. **Agnieszka M. Jastrzębska:** Writing – review & editing, Supervision, Resources, Methodology. **Urszula Stachewicz:** Writing – review & editing, Writing – original draft, Visualization, Validation, Supervision, Resources, Project administration, Methodology, Funding acquisition, Formal analysis, Conceptualization.

Notes

The authors declare that they have no known competing financial interests or personal relationships that could have appeared to influence the work reported in this paper. The raw/processed data required to reproduce this finding are available on request.

Declaration of competing interest

The authors declare that they have no known competing financial interests or personal relationships that could have appeared to influence the work reported in this paper.

Acknowledgment

This study was conducted with OPUS 17 project granted by the National Science Centre in Poland, No 2019/33/B/ST5/01311 and supported by the ERC-2020-STG project (BioCom4SavEn), under ERC grant agreement no. 948840, funded by the European Research Council within the EU's Horizon 2020 Framework Programme and by the program „Excellence initiative – research university" for the AGH University of Krakow in Poland.

The schematics were prepared using Biorender.com.

Appendix A. Supplementary data

Supplementary data to this article can be found online at https://doi.org/10.1016/j.mtbio.2025.101785.

Data availability

Data will be made available on request.

References

[1] C. Shuai, X. Yuan, W. Yang, S. Peng, G. Qian, Z. Zhao, Synthesis of a mace-like cellulose nanocrystal@Ag nanosystem via in-situ growth for antibacterial activities of poly-L-lactide scaffold, Carbohydr. Polym. 262 (2021), https://doi.org/10.1016/j.carbpol.2021.117937.

[2] A. Gelmi, C.E. Schutt, Stimuli-responsive biomaterials: scaffolds for stem cell control, Adv. Healthcare Mater. 10 (2021), https://doi.org/10.1002/adhm.202001125.

[3] W. Yang, C. Zhou, C. He, Y. Yang, W. Aiyiti, L. Xu, C. Shuai, Defect engineering synergistically boosts the catalytic activity of Fe-MoOv for highly efficient breast mesh antitumor therapy, J. Colloid Interface Sci. 678 (2025) 260–271, https://doi.org/10.1016/j.jcis.2024.08.195.

[4] M. Rahman, M. Kabir, T. Islam, Y. Wang, Q. Meng, H. Liu, S. Chen, S. Wu, Curcumin-loaded ZIF-8 nanomaterials: exploring drug loading efficiency and biomedical performance, ACS Omega (2025), https://doi.org/10.1021/acsomega.4c09945.

[5] M. Polak, J.E. Karbowniczek, U. Stachewicz, Strategies in electrospun polymer and hybrid scaffolds for enhanced cell integration and vascularization for bone tissue engineering and organoids, Wiley Interdiscip. Rev. Nanomed. Nanobiotechnol. 16 (2024), https://doi.org/10.1002/wnan.2022.

[6] W. Mohammad, L. Chen, B. Wu, P. Dietz, T. Bou-Akl, W. Ren, D.C. Markel, Cell migration within porous electrospun nanofibrous scaffolds in a mouse subcuticular implantation model, J. Orthop. Res. (2024), https://doi.org/10.1002/jor.25979.

[7] S. Chen, Y. Guo, R. Liu, S. Wu, J. Fang, B. Huang, Z. Li, Z. Chen, Z. Chen, Tuning surface properties of bone biomaterials to manipulate osteoblastic cell adhesion and the signaling pathways for the enhancement of early osseointegration, Colloids Surf. B Biointerfaces 164 (2018) 58–69, https://doi.org/10.1016/j.colsurfb.2018.01.022.

[8] A.A. Khalili, M.R. Ahmad, A Review of cell adhesion studies for biomedical and biological applications, Int. J. Mol. Sci. 16 (2015) 18149–18184, https://doi.org/10.3390/ijms160818149.

[9] M. Bigerelle, K. Anselme, Bootstrap analysis of the relation between initial adhesive events and long-term cellular functions of human osteoblasts cultured on biocompatible metallic substrates, Acta Biomater. 1 (2005) 499–510, https://doi.org/10.1016/j.actbio.2005.06.001.

[10] K. Berniak, D.P. Ura, A. Piórkowski, U. Stachewicz, Cell–material interplay in focal adhesion points, ACS Appl. Mater. Interfaces (2024), https://doi.org/10.1021/acsami.3c19035.

[11] R. Kumari, K. Ven, M. Chastney, S.B. Kokate, J. Peränen, J. Aaron, K. Kogan, L. Almeida-Souza, E. Kremneva, R. Poincloux, T.L. Chew, P.W. Gunning, J. Ivaska, P. Lappalainen, Focal adhesions contain three specialized actin nanoscale layers, Nat. Commun. 15 (2024), https://doi.org/10.1038/s41467-024-46868-7.

[12] K. Sheets, S. Wunsch, C. Ng, A.S. Nain, Shape-dependent cell migration and focal adhesion organization on suspended and aligned nanofiber scaffolds, Acta Biomater. 9 (2013) 7169–7177, https://doi.org/10.1016/j.actbio.2013.03.042.

[13] S. Soliman, S. Sant, J.W. Nichol, M. Khabiry, E. Traversa, A. Khademhosseini, Controlling the porosity of fibrous scaffolds by modulating the fiber diameter and packing density, J. Biomed. Mater. Res. 96 A (2011) 566–574, https://doi.org/10.1002/jbm.a.33010.

[14] M. Simonet, N. Stingelin, J.G.F. Wismans, C.W.J. Oomens, A. Driessen-Mol, F.P. T. Baaijens, Tailoring the void space and mechanical properties in electrospun scaffolds towards physiological ranges, J. Mater. Chem. B 2 (2014) 305–313, https://doi.org/10.1039/c3tb20995d.

[15] S.J. Eichhorn, W.W. Sampson, Relationships between specific surface area and pore size in electrospun polymer fibre networks, J. R. Soc. Interface 7 (2010) 641–649, https://doi.org/10.1098/rsif.2009.0374.

[16] G. Collins, J. Federici, Y. Imura, L.H. Catalani, Charge generation, charge transport, and residual charge in the electrospinning of polymers: a review of issues and complications, J. Appl. Phys. 111 (2012), https://doi.org/10.1063/1.3682464.

[17] C.A. Bonino, K. Efimenko, S.I. Jeong, M.D. Krebs, E. Alsberg, S.A. Khan, Three-dimensional electrospun alginate nanofiber mats via tailored charge repulsions, Small 8 (2012) 1928–1936, https://doi.org/10.1002/smll.201101791.

[18] S.I. Jeong, N.A. Burns, C.A. Bonino, I.K. Kwon, S.A. Khan, E. Alsberg, Improved cell infiltration of highly porous 3D nanofibrous scaffolds formed by combined fiber-fiber charge repulsions and ultra-sonication, J. Mater. Chem. B 2 (2014) 8116–8122, https://doi.org/10.1039/c4tb01487a.

[19] S. Luo, C. Zhang, W. Xiong, Y. Song, Q. Wang, H. Zhang, S. Guo, S. Yang, H. Liu, Advances in electroactive biomaterials: through the lens of electrical stimulation promoting bone regeneration strategy, J. Orthop. Translat. 47 (2024) 191–206, https://doi.org/10.1016/j.jot.2024.06.009.

[20] H.-S. Kim, T. Baby, J.-H. Lee, U.S. Shin, H.-W. Kim, Biomaterials-enabled electrical stimulation for tissue healing and regeneration, Méd. Sur X 2 (2024), https://doi.org/10.1007/s44258-024-00020-8.

[21] S. Metwally, U. Stachewicz, Surface potential and charges impact on cell responses on biomaterials interfaces for medical applications, Mater. Sci. Eng. C 104 (2019), https://doi.org/10.1016/j.msec.2019.109883.

[22] H. Nekounam, S. Gholizadeh, Z. Allahyari, H. Samadian, N. Nazeri, M. A. Shokrgozar, R. Faridi-Majidi, Electroconductive scaffolds for tissue regeneration: current opportunities, pitfalls, and potential solutions, Mater. Res. Bull. 134 (2021), https://doi.org/10.1016/j.materresbull.2020.111083.

[23] S. Iravani, A. Zarepour, E. Nazarzadeh Zare, P. Makvandi, A. Khosravi, A. Zarrabi, Synergistic advancements: exploring MXene/graphene oxide and MXene/reduced graphene oxide composites for next-generation applications, Flat Chem. 48 (2024), https://doi.org/10.1016/j.flatc.2024.100759.

[24] P. Kumbhakar, J.S. Jayan, A.S. Madhavikutty, P.R. Sreeram, A. Saritha, T. Ito, C. S. Tiwary, Prospective applications of two-dimensional materials beyond laboratory frontiers: A review, (n.d.). https://doi.org/10.1016/j.isci.

[25] A. Zarepour, Ç. Karasu, Y. Mir, M.H. Nematollahi, S. Iravani, A. Zarrabi, Graphene- and MXene-based materials for neuroscience: diagnostic and therapeutic applications, Biomater. Sci. 11 (2023) 6687–6710, https://doi.org/10.1039/d3bm01114c.

[26] J.J. Grant, S.C. Pillai, S. Hehir, M. McAfee, A. Breen, Biomedical applications of electrospun graphene oxide, ACS Biomater. Sci. Eng. 7 (2021) 1278–1301, https://doi.org/10.1021/acsbiomaterials.0c01663.

[27] S. Kumar, D. Azam, S. Raj, E. Kolanthai, K.S. Vasu, A.K. Sood, K. Chatterjee, 3D scaffold alters cellular response to graphene in a polymer composite for orthopedic applications, in: J Biomed Mater Res B Appl Biomater, John Wiley and Sons Inc., 2016, pp. 732–749, https://doi.org/10.1002/jbm.b.33549.

[28] Y. Shen, J. Cui, X. Yu, J. Song, P. Cai, W. Guo, Y. Zhao, J. Wu, H. Gu, B. Sun, X. Mo, Recent advances in three-dimensional printing in cardiovascular devices: bench and bedside applications, Smart Mater. Med. 5 (2024) 36–51, https://doi.org/10.1016/j.smaim.2023.07.001.

[29] L. Wei, S. Wang, M. Shan, Y. Li, Y. Wang, F. Wang, L. Wang, J. Mao, Conductive fibers for biomedical applications, Bioact. Mater. 22 (2023) 343–364, https://doi.org/10.1016/j.bioactmat.2022.10.014.

[30] M.H. Hussain, N.F. Abu Bakar, M. Chung, N.F.N. Khalid, N.H. Othman, H.L. Tan, M.S. Osman, Z. Lockman, N. Radacsi, Electrospun polyetherimide nanofibers with reduced graphene oxide-zeolitic imidazolate framework for conductivity improvement, Emergent. Mater. 6 (2023) 271–281, https://doi.org/10.1007/s42247-022-00410-x.

[31] M. Cámara-Torres, R. Sinha, S. Eqtesadi, R. Wendelbo, M. Scatto, P. Scopece, A. Sanchez, S. Villanueva, A. Egizabal, N. Álvarez, A. Patelli, C. Mota, L. Moroni, Effect of the reduced graphene oxide (rGO) compaction degree and concentration on rGO-polymer composite printability and cell interactions, Nanoscale 13 (2021) 14382–14398, https://doi.org/10.1039/d1nr02927d.

[32] A. Ivanoska-dacikj, P. Makreski, N. Geskovski, J. Karbowniczek, U. Stachewicz, N. Novkovski, J. Tanasić, I. Ristić, G. Bogoeva-gaceva, Electrospun PEO/rGO scaffolds: the influence of the concentration of rGO on overall properties and cytotoxicity, Int. J. Mol. Sci. 23 (2022), https://doi.org/10.3390/ijms23020988.

[33] B. Pant, M. Park, A.A. Kim, MXene-embedded electrospun polymeric nanofibers for biomedical applications: recent advances, Micromachines 14 (2023), https://doi.org/10.3390/mi14071477.

[34] M. Naguib, M. Kurtoglu, V. Presser, J. Lu, J. Niu, M. Heon, L. Hultman, Y. Gogotsi, M.W. Barsoum, Two-dimensional nanocrystals produced by exfoliation of Ti 3AlC 2, Adv. Mater. 23 (2011) 4248–4253, https://doi.org/10.1002/adma.201102306.

[35] X. Li, S. Wang, M. Zheng, Z. Ma, Y. Chen, L. Deng, W. Xu, G. Fan, S. Khademolqorani, S.N. Banitaba, A.I. Osman, Synergistic integration of MXene nanostructures into electrospun fibers for advanced biomedical engineering applications, Nanoscale Horiz. (2024), https://doi.org/10.1039/d4nh00209a.

[36] K. Li, M. Liang, H. Wang, X. Wang, Y. Huang, J. Coelho, S. Pinilla, Y. Zhang, F. Qi, V. Nicolosi, Y. Xu, 3D MXene architectures for efficient energy storage and conversion, Adv. Funct. Mater. 30 (2020), https://doi.org/10.1002/adfm.202000842.

[37] P. Iravani, S. Iravani, R.S. Varma, MXene-chitosan composites and their biomedical potentials, Micromachines 13 (2022), https://doi.org/10.3390/mi13091383.

[38] M. Rafiq, S. ullah Rather, T.U. Wani, A.H. Rather, R.S. Khan, A.E. Khan, I. Hamid, H.A. Khan, A.S. Alhomida, F.A. Sheikh, Recent progress in MXenes incorporated into electrospun nanofibers for biomedical application: study focusing from 2017

to 2022, Chin. Chem. Lett. 34 (2023), https://doi.org/10.1016/j.cclet.2023.108463.
[39] G.P. Awasthi, B. Maharjan, S. Shrestha, D.P. Bhattarai, D. Yoon, C.H. Park, C. S. Kim, Synthesis, characterizations, and biocompatibility evaluation of polycaprolactone–MXene electrospun fibers, Colloids Surf. A Physicochem. Eng. Asp. 586 (2020), https://doi.org/10.1016/j.colsurfa.2019.124282.
[40] C. Shuai, W. Yang, P. Feng, S. Peng, H. Pan, Accelerated degradation of HAP/PLLA bone scaffold by PGA blending facilitates bioactivity and osteoconductivity, Bioact. Mater. 6 (2021) 490–502, https://doi.org/10.1016/j.bioactmat.2020.09.001.
[41] P. Feng, P. Wu, C. Gao, Y. Yang, W. Guo, W. Yang, C. Shuai, A multimaterial scaffold with tunable properties: toward bone tissue repair, Adv. Sci. 5 (2018), https://doi.org/10.1002/advs.201700817.
[42] X. Liu, J. Jiang, H. Liu, F. Liu, H. Shao, S. Chen, S. Wu, Adjusting morphology, structure, and mechanical properties of electrospun high-molecular-weight poly (l-lactic-acid) nanofibrous yarns through hot stretching treatment, Macromol. Biosci. (2025), https://doi.org/10.1002/mabi.202400656.
[43] S. Pramanik, S. Kharche, N. More, D. Ranglani, G. Singh, G. Kapusetti, Natural biopolymers for bone tissue engineering: a brief review, Eng. Regen. 4 (2023) 193–204, https://doi.org/10.1016/j.engreg.2022.12.002.
[44] A.M. Jastrzębska, E. Karwowska, T. Wojciechowski, W. Ziemkowska, A. Rozmysłowska, L. Chlubny, A. Olszyna, The atomic structure of Ti 2 C and Ti 3 C 2 MXenes is responsible for their antibacterial activity toward E. coli bacteria, J. Mater. Eng. Perform. 28 (2019) 1272–1277, https://doi.org/10.1007/s11665-018-3223-z.
[45] M. Polak, K. Berniak, P.K. Szewczyk, J.E. Karbowniczek, M.M. Marzec, U. Stachewicz, PLLA scaffolds with controlled surface potential and piezoelectricity for enhancing cell adhesion in tissue engineering, Appl. Surf. Sci. 621 (2023), https://doi.org/10.1016/j.apsusc.2023.156835.
[46] Ł. Kaniuk, K. Berniak, A. Lichawska-Cieślar, J. Jura, J.E. Karbowniczek, U. Stachewicz, Accelerated wound closure rate by hyaluronic acid release from coated PHBV electrospun fiber scaffolds, J. Drug Deliv. Sci. Technol. 77 (2022), https://doi.org/10.1016/j.jddst.2022.103855.
[47] U. Stachewicz, T. Qiao, S.C.F. Rawlinson, F.V. Almeida, W.Q. Li, M. Cattell, A. H. Barber, 3D imaging of cell interactions with electrospun PLGA nanofiber membranes for bone regeneration, Acta Biomater. 27 (2015) 88–100, https://doi.org/10.1016/j.actbio.2015.09.003.
[48] J. Fernandez De La Mora A N D, I.G. Loscertales, The Current Emitted by Highly Conducting Taylor Cones, 1994.
[49] U. Stachewicz, J.F. Dijksman, C.U. Yurteri, J.C.M. Marijnissen, Experiments on single event electrospraying, Appl. Phys. Lett. 91 (2007), https://doi.org/10.1063/1.2826279.
[50] Y. Xin, D.H. Reneker, Garland formation process in electrospinning, Polymer 53 (2012) 3629–3635, https://doi.org/10.1016/j.polymer.2012.05.060.
[51] C.J. Angammana, S.H. Jayaram, Analysis of the effects of solution conductivity on electrospinning process and fiber morphology, IEEE Trans. Ind. Appl. 47 (2011) 1109–1117, https://doi.org/10.1109/TIA.2011.2127431.
[52] K. Gong, K. Zhou, X. Qian, C. Shi, B. Yu, MXene as emerging nanofillers for high-performance polymer composites: a review, Compos. B Eng. 217 (2021), https://doi.org/10.1016/j.compositesb.2021.108867.
[53] M. Jakubczak, D. Bury, A. Wojciechowska, J. Mitrzak, K. Budnik, D. Moszczyńska, A.M. Jastrzębska, The 2D Ti3C2Tx MXene-enabled self-cleaning and self-sterilizing lacquer coatings for offset printing, J. Alloys Compd. 976 (2024), https://doi.org/10.1016/j.jallcom.2023.173318.
[54] A. Malas, A. Bharati, O. Verkinderen, B. Goderis, P. Moldenaers, R. Cardinaels, Effect of the GO reduction method on the dielectric properties, electrical conductivity and crystalline behavior of PEO/rGO nanocomposites, Polymers 9 (2017), https://doi.org/10.3390/polym9110613.
[55] T.U. Rashid, R.E. Gorga, W.E. Krause, Mechanical properties of electrospun fibers—a critical review, Adv. Eng. Mater. 23 (2021), https://doi.org/10.1002/adem.202100153.
[56] Z. Gu, S. Fan, S.C. Kundu, X. Yao, Y. Zhang, Fiber diameters and parallel patterns: proliferation and osteogenesis of stem cells, Regen. Biomater. 10 (2023), https://doi.org/10.1093/rb/rbad001.
[57] J.V. Sanchaniya, I. Lasenko, V. Gobins, A. Kobeissi, D. Goljandin, A finite element method for determining the mechanical properties of electrospun nanofibrous mats, Polymers 16 (2024), https://doi.org/10.3390/polym16060852.
[58] P. Chavoshnejad, M.J. Razavi, Effect of the interfiber bonding on the mechanical behavior of electrospun fibrous mats, Sci. Rep. 10 (2020), https://doi.org/10.1038/s41598-020-64735-5.
[59] L.Y. Wan, H. Wang, W. Gao, F. Ko, An analysis of the tensile properties of nanofiber mats, Polymer 73 (2015) 62–67, https://doi.org/10.1016/j.polymer.2015.07.018.
[60] C. Liu, H.M. Wong, K.W.K. Yeung, S.C. Tjong, Novel electrospun polylactic acid nanocomposite fiber mats with hybrid graphene oxide and nanohydroxyapatite reinforcements having enhanced biocompatibility, Polymers 8 (2016), https://doi.org/10.3390/polym8080287.
[61] D. Jiang, H. Zou, H. Zhang, W. Zhao, Y. Lan, M. Yuan, Preparation and properties of electrospun PLLA/PTMC scaffolds, Polymers 14 (2022), https://doi.org/10.3390/polym14204406.
[62] J.E. Karbowniczek, D.P. Ura, U. Stachewicz, Nanoparticles distribution and agglomeration analysis in electrospun fiber based composites for desired mechanical performance of poly(3-hydroxybuty-rate-co-3-hydroxyvalerate (PHBV) scaffolds with hydroxyapatite (HA) and titanium dioxide (TiO2) towards medical applications, Compos. B Eng. 241 (2022) 110011, https://doi.org/10.1016/j.compositesb.2022.110011.
[63] M.A.K. Purbayanto, M. Chandel, M. Birowska, A. Rosenkranz, A.M. Jastrzębska, Optically Active MXenes in Van der Waals Heterostructures, Adv. Mater. 35 (2023), https://doi.org/10.1002/adma.202301850.
[64] K. Maleski, V.N. Mochalin, Y. Gogotsi, Dispersions of two-dimensional titanium carbide MXene in organic solvents, Chem. Mater. 29 (2017) 1632–1640, https://doi.org/10.1021/acs.chemmater.6b04830.
[65] Q. Zhang, H. Lai, R. Fan, P. Ji, X. Fu, H. Li, High concentration of Ti3C2TxMXene in organic solvent, ACS Nano 15 (2021) 5249–5262, https://doi.org/10.1021/acsnano.0c10671.
[66] D. Konios, M.M. Stylianakis, E. Stratakis, E. Kymakis, Dispersion behaviour of graphene oxide and reduced graphene oxide, J. Colloid Interface Sci. 430 (2014) 108–112, https://doi.org/10.1016/j.jcis.2014.05.033.
[67] T. Parker, D. Zhang, D. Bugallo, K. Shevchuk, M. Downes, G. Valurouthu, A. Inman, B. Chacon, T. Zhang, C.E. Shuck, Y.J. Hu, Y. Gogotsi, Fourier-transform infrared spectral library of MXenes, Chem. Mater. (2024), https://doi.org/10.1021/acs.chemmater.4c01536.
[68] S. Pu, D. Long, Z. Liu, F. Yang, J. Zhu, Preparation of RGO-P25 nanocomposites for the photocatalytic degradation of ammonia in livestock farms, Catalysts 8 (2018), https://doi.org/10.3390/catal8050189.
[69] F. Nazir, M. Iqbal, A.N. Khan, M. Mazhar, Z. Hussain, Fabrication of robust poly L-lactic acid/cyclic olefinic copolymer (PLLA/COC) blends: study of physical properties, structure, and cytocompatibility for bone tissue engineering, J. Mater. Res. Technol. 13 (2021) 1732–1751, https://doi.org/10.1016/j.jmrt.2021.05.073.
[70] A. Leroy, S. Ribeiro, C. Grossiord, A. Alves, R.H. Vestberg, V. Salles, C. Brunon, K. Gritsch, B. Grosgogeat, Y. Bayon, FTIR microscopy contribution for comprehension of degradation mechanisms in PLA-based implantable medical devices, J. Mater. Sci. Mater. Med. 28 (2017), https://doi.org/10.1007/s10856-017-5894-7.
[71] C. Ribeiro, V. Sencadas, C.M. Costa, J.L. Gómez Ribelles, S. Lanceros-Méndez, Tailoring the morphology and crystallinity of poly(L-lactide acid) electrospun membranes, Sci. Technol. Adv. Mater. 12 (2011), https://doi.org/10.1088/1468-6996/12/1/015001.
[72] I.O. Pariy, R.V. Chernozem, P.V. Chernozem, Y.R. Mukhortova, A.G. Skirtach, V. V. Shvartsman, D.C. Lupascu, M.A. Surmeneva, S. Mathur, R.A. Surmenev, Hybrid biodegradable electrospun scaffolds based on poly(l-lactic acid) and reduced graphene oxide with improved piezoelectric response, Polym. J. 54 (2022) 1237–1252, https://doi.org/10.1038/s41428-022-00669-1.
[73] A.F. Ghanem, M.A. Yassin, R. Cosquer, F. Gouanvé, E. Espuche, M.H. Abdel Rehim, Polycaprolactone composite films infused with hyperbranched polyester/reduced graphene oxide: influence on biodegradability, gas/water transport and antimicrobial properties for sustainable packaging, RSC Adv. 14 (2024) 5740–5753, https://doi.org/10.1039/d3ra08948g.
[74] C. Sánchez-rodríguez, M.D. Avilés, R. Pamies, F.J. Carrión-vilches, J. Sanes, M. D. Bermúdez, Extruded pla nanocomposites modified by graphene oxide and ionic liquid, Polymers 13 (2021) 1–15, https://doi.org/10.3390/polym13040655.
[75] Z. Li, B. Du, C. Han, H. Xu, Trap modulated charge carrier transport in polyethylene/graphene nanocomposites, Sci. Rep. 7 (2017), https://doi.org/10.1038/s41598-017-04196-5.
[76] G. Beamson, D. Briggs, High resolution XPS of organic polymers: the scienta ESCA300 database (Beamson, G.; Briggs, D.), J. Chem. Educ. 70 (1993) A25, https://doi.org/10.1021/ed070pA25.5.
[77] C.D. Wagner, NIST X-Ray Photoelectron Spectroscopy (XPS) Database, 1990, https://doi.org/10.6028/NIST.TN.1289. Gaithersburg, MD.
[78] P.J. Cumpson, Angle-resolved XPS depth-profiling strategies, Appl. Surf. Sci. 144–145 (1999) 16–20, https://doi.org/10.1016/S0169-4332(98)00752-1.
[79] G. Tasneem, W.S.M. Werner, W. Smekal, C.J. Powell, Interlaboratory study comparing analyses of simulated angle-resolved X-ray photoelectron spectroscopy data, Surf. Interface Anal. 46 (2014) 321–332, https://doi.org/10.1002/sia.5482.
[80] M. Polak, D.P. Ura, K. Berniak, P.K. Szewczyk, M.M. Marzec, U. Stachewicz, Interfacial blending in co-axially electrospun polymer core-shell fibers and their interaction with cells via focal adhesion point analysis, Colloids Surf. B Biointerfaces 237 (2024) 113864, https://doi.org/10.1016/j.colsurfb.2024.113864.
[81] T. Busolo, D.P. Ura, S.K. Kim, M.M. Marzec, A. Bernasik, U. Stachewicz, S. Kar-Narayan, Surface potential tailoring of PMMA fibers by electrospinning for enhanced triboelectric performance, Nano Energy 57 (2019) 500–506, https://doi.org/10.1016/j.nanoen.2018.12.037.
[82] Ł. Kaniuk, S. Ferraris, S. Spriano, T. Luxbacher, Z. Krysiak, K. Berniak, A. Zaszczynska, M.M. Marzec, A. Bernasik, P. Sajkiewicz, U. Stachewicz, Time-dependent effects on physicochemical and surface properties of PHBV fibers and films in relation to their interactions with fibroblasts, Appl. Surf. Sci. 545 (2021), https://doi.org/10.1016/j.apsusc.2021.148983.
[83] D.P. Ura, U. Stachewicz, The significance of electrical polarity in electrospinning: a nanoscale approach for the enhancement of the polymer fibers' properties, Macromol. Mater. Eng. 307 (2022), https://doi.org/10.1002/mame.202100843.
[84] S. Chen, H. Dong, J. Yang, Surface potential/charge sensing techniques and applications, Sensors 20 (2020), https://doi.org/10.3390/s20061690.
[85] G.H. Jun, S.H. Jin, B. Lee, B.H. Kim, W.S. Chae, S.H. Hong, S. Jeon, Enhanced conduction and charge-selectivity by N-doped graphene flakes in the active layer of bulk-heterojunction organic solar cells, Energy Environ. Sci. 6 (2013) 3000–3006, https://doi.org/10.1039/c3ee40963e.
[86] Q. Hao, L. Chen, W. Wang, G. Li, Modulate the work function of MXene in MXene/InGaN heterojunction for visible light photodetector, Appl. Phys. Lett. 125 (2024), https://doi.org/10.1063/5.0217557.

[87] S. Kamble, S. Agrawal, S. Cherumukkil, V. Sharma, R.V. Jasra, P. Munshi, Revisiting zeta potential, the key feature of interfacial phenomena, with applications and recent advancements, ChemistrySelect 7 (2022), https://doi.org/10.1002/slct.202103084.
[88] X. Yin, J. Drelich, Surface charge microscopy: novel technique for mapping charge-mosaic surfaces in electrolyte solutions, Langmuir 24 (2008) 8013–8020, https://doi.org/10.1021/la801269z.
[89] S. Metwally, S. Ferraris, S. Spriano, Z.J. Krysiak, Ł. Kaniuk, M.M. Marzec, S. K. Kim, P.K. Szewczyk, A. Gruszczyński, M. Wytrwal-Sarna, J.E. Karbowniczek, A. Bernasik, S. Kar-Narayan, U. Stachewicz, Surface potential and roughness controlled cell adhesion and collagen formation in electrospun PCL fibers for bone regeneration, Mater. Des. 194 (2020), https://doi.org/10.1016/j.matdes.2020.108915.
[90] H. Zhao, H. Chi, Electrospun bead-on-string fibers: useless or something of value?, in: Novel Aspects of Nanofibers InTech, 2018 https://doi.org/10.5772/intechopen.74661.
[91] Y. Yang, W. Chen, M. Wang, J. Shen, Z. Tang, Y. Qin, D.G. Yu, Engineered shellac beads-on-the-string fibers using triaxial electrospinning for improved colon-targeted drug delivery, Polymers 15 (2023), https://doi.org/10.3390/polym15102237.
[92] S. Somvipart, S. Kanokpanont, R. Rangkupan, J. Ratanavaraporn, S. Damrongsakkul, Development of electrospun beaded fibers from Thai silk fibroin and gelatin for controlled release application, Int. J. Biol. Macromol. 55 (2013) 176–184, https://doi.org/10.1016/j.ijbiomac.2013.01.006.
[93] J. Santillán, E.A. Dwomoh, Y.G. Rodríguez-Avilés, S.A. Bello, E. Nicolau, Fabrication and evaluation of polycaprolactone beads-on-string membranes for applications in bone tissue regeneration, ACS Appl. Bio Mater. 2 (2019) 1031–1040, https://doi.org/10.1021/acsabm.8b00628.
[94] J. Huff, The Airyscan detector from ZEISS: confocal imaging with improved signal-to-noise ratio and super-resolution, Nat. Methods 12 (2015), https://doi.org/10.1038/NMETH.F.388 ii.
[95] V.L. Kolossov, M. Sivaguru, J. Huff, K. Luby, K. Kanakaraju, H.R. Gaskins, Airyscan super-resolution microscopy of mitochondrial morphology and dynamics in living tumor cells, Microsc. Res. Tech. 81 (2018) 115–128, https://doi.org/10.1002/jemt.22968.
[96] J.E. Karbowniczek, Ł. Kaniuk, K. Berniak, A. Gruszczyński, U. Stachewicz, Enhanced cells anchoring to electrospun hybrid scaffolds with PHBV and HA particles for bone tissue regeneration, Front. Bioeng. Biotechnol. 9 (2021), https://doi.org/10.3389/fbioe.2021.632029.
[97] A. Lopez Marquez, I.E. Gareis, F.J. Dias, C. Gerhard, M.F. Lezcano, How fiber surface topography affects interactions between cells and electrospun scaffolds: a systematic review, Polymers 14 (2022), https://doi.org/10.3390/polym14010209.
[98] X. Liu, Q. Ouyang, X. Yao, Y. Zhang, A facile nanopattern modification of silk fibroin electrospun scaffold and corresponding impact on cell proliferation and osteogenesis, (n.d.). https://doi.org/10.1093/rb/rbae117/7801222.
[99] R. Yaseri, M. Fadaie, E. Mirzaei, H. Samadian, A. Ebrahiminezhad, Surface modification of polycaprolactone nanofibers through hydrolysis and aminolysis: a comparative study on structural characteristics, mechanical properties, and cellular performance, Sci. Rep. 13 (2023), https://doi.org/10.1038/s41598-023-36563-w.
[100] A.M. Yessuf, M. Bahri, T.S. Kassa, B.P. Sharma, A.M. Salama, C. Xing, Q. Zhang, Y. Liu, Electrospun polymeric nanofibers: current trends in synthesis, surface modification, and biomedical applications, ACS Appl. Bio Mater. 7 (2024) 4231–4253, https://doi.org/10.1021/acsabm.4c00307.
[101] F.F.R. Damanik, G. Spadolini, J. Rotmans, S. Farè, L. Moroni, Biological activity of human mesenchymal stromal cells on polymeric electrospun scaffolds, Biomater. Sci. 7 (2019) 1088–1100, https://doi.org/10.1039/c8bm00693h.
[102] P.K. Szewczyk, S. Metwally, J.E. Karbowniczek, M.M. Marzec, E. Stodolak-Zych, A. Gruszczyński, A. Bernasik, U. Stachewicz, Surface-potential-controlled cell proliferation and collagen mineralization on electrospun polyvinylidene fluoride (PVDF) fiber scaffolds for bone regeneration, ACS Biomater. Sci. Eng. 5 (2019) 582–593, https://doi.org/10.1021/acsbiomaterials.8b01108.
[103] M. Chen, P.K. Patra, S.B. Warner, S. Bhowmick, Role of fiber diameter in adhesion and proliferation of NIH 3T3 fibroblast on electrospun polycaprolactone scaffolds, Tissue Eng. 13 (2007) 579–587, https://doi.org/10.1089/ten.2006.0205.
[104] F. Tian, H. Hosseinkhani, M. Hosseinkhani, A. Khademhosseini, Y. Yokoyama, G. G. Estrada, H. Kobayashi, Quantitative analysis of cell adhesion on aligned micro- and nanofibers, J. Biomed. Mater. Res. 84 (2008) 291–299, https://doi.org/10.1002/jbm.a.31304.
[105] K. Yadav, N. Singhal, V. Rishi, H. Yadav, Cell proliferation assays, in: Encyclopedia of Life Sciences, Wiley, 2014, https://doi.org/10.1002/9780470015902.a0002566.
[106] D. Zhang, N. Ni, J. Chen, Q. Yao, B. Shen, Y. Zhang, M. Zhu, Z. Wang, J. Ruan, J. Wang, X. Mo, W. Shi, J. Ji, X. Fan, P. Gu, Electrospun SF/PLCL nanofibrous membrane: a potential scaffold for retinal progenitor cell proliferation and differentiation, Sci. Rep. 5 (2015), https://doi.org/10.1038/srep14326.
[107] Y. Nikakhtar, S.S. Shafiei, M. Fathi-roudsari, M. Asadi-Eydivand, F. ShiraliPour, Preparation and characterization of electrospun polycaprolactone/brushite scaffolds to promote osteogenic differentiation of mesenchymal stem cells, J. Biomater. Sci. Polym. Ed. 33 (2022) 1102–1122, https://doi.org/10.1080/09205063.2022.2041786.
[108] Z.J. Krysiak, P.K. Szewczyk, K. Berniak, E.A. Sroczyk, E. Boratyn, U. Stachewicz, Stretchable skin hydrating PVB patches with controlled pores' size and shape for deliberate evening primrose oil spreading, transport and release, Biomater. Adv. 136 (2022), https://doi.org/10.1016/j.bioadv.2022.212786.
[109] U. Stachewicz, P.K. Szewczyk, A. Kruk, A.H. Barber, A. Czyrska-Filemonowicz, Pore shape and size dependence on cell growth into electrospun fiber scaffolds for tissue engineering: 2D and 3D analyses using SEM and FIB-SEM tomography, Mater. Sci. Eng. C 95 (2019) 397–408, https://doi.org/10.1016/j.msec.2017.08.076.
[110] N. Lavielle, A. Hébraud, G. Schlatter, L. Thöny-Meyer, R.M. Rossi, A.M. Popa, Simultaneous electrospinning and electrospraying: a straightforward approach for fabricating hierarchically structured composite membranes, ACS Appl. Mater. Interfaces 5 (2013) 10090–10097, https://doi.org/10.1021/am402676m.
[111] K.P. Feltz, E.A. Growney Kalaf, C. Chen, R.S. Martin, S.A. Sell, A review of electrospinning manipulation techniques to direct fiber deposition and maximize pore size, Electrospinning 2 (2017) 46–61, https://doi.org/10.1515/esp-2017-0002.
[112] B. Fromager, E. Marhuenda, B. Louis, N. Bakalara, J. Cambedouzou, D. Cornu, Recent advances in electrospun fibers for biological applications, Macromolecules (Washington, DC, U. S.) 3 (2023) 569–613, https://doi.org/10.3390/macromol3030033.
[113] Y. Luo, H. Shen, Y. Fang, Y. Cao, J. Huang, M. Zhang, J. Dai, X. Shi, Z. Zhang, Enhanced proliferation and osteogenic differentiation of mesenchymal stem cells on graphene oxide-incorporated electrospun poly(lactic-co-glycolic acid) nanofibrous mats, ACS Appl. Mater. Interfaces 7 (2015) 6331–6339, https://doi.org/10.1021/acsami.5b00862.
[114] M.H. Norahan, M. Amroon, R. Ghahremanzadeh, N. Rabiee, N. Baheiraei, Reduced graphene oxide: osteogenic potential for bone tissue engineering, IET Nanobiotechnol. 13 (2019) 720–725, https://doi.org/10.1049/iet-nbt.2019.0125.
[115] M. Wu, L. Zou, L. Jiang, Z. Zhao, J. Liu, Osteoinductive and antimicrobial mechanisms of graphene-based materials for enhancing bone tissue engineering, J. Tissue. Eng. Regen. Med. 15 (2021) 915–935, https://doi.org/10.1002/term.3239.

Supporting Information to:

Modulating Cell Adhesion and Infiltration in Advanced Scaffold Designs based on PLLA Fibers with rGO and MXene ($Ti_3C_2T_x$)

Martyna Polak[1], Krzysztof Berniak[1], Piotr K. Szewczyk[1], Joanna Knapczyk-Korczak[1], Mateusz M. Marzec[2], Muhammad Abiyyu Kenichi Purbayanto[3], Agnieszka M. Jastrzębska[3], Urszula Stachewicz[1,*]

[1]Faculty of Metals Engineering and Industrial Computer Science, AGH University of Krakow, Al. A. Mickiewicza 30, 30-059 Krakow, Poland

[2]Academic Centre for Materials and Nanotechnology, AGH University of Krakow, Al. A. Mickiewicza 30, 30-059 Krakow, Poland

[3]Warsaw University of Technology, Faculty of Mechatronics, św. A. Boboli 8, 02-525 Warsaw, Poland

*E-mail: ustachew@agh.edu.pl

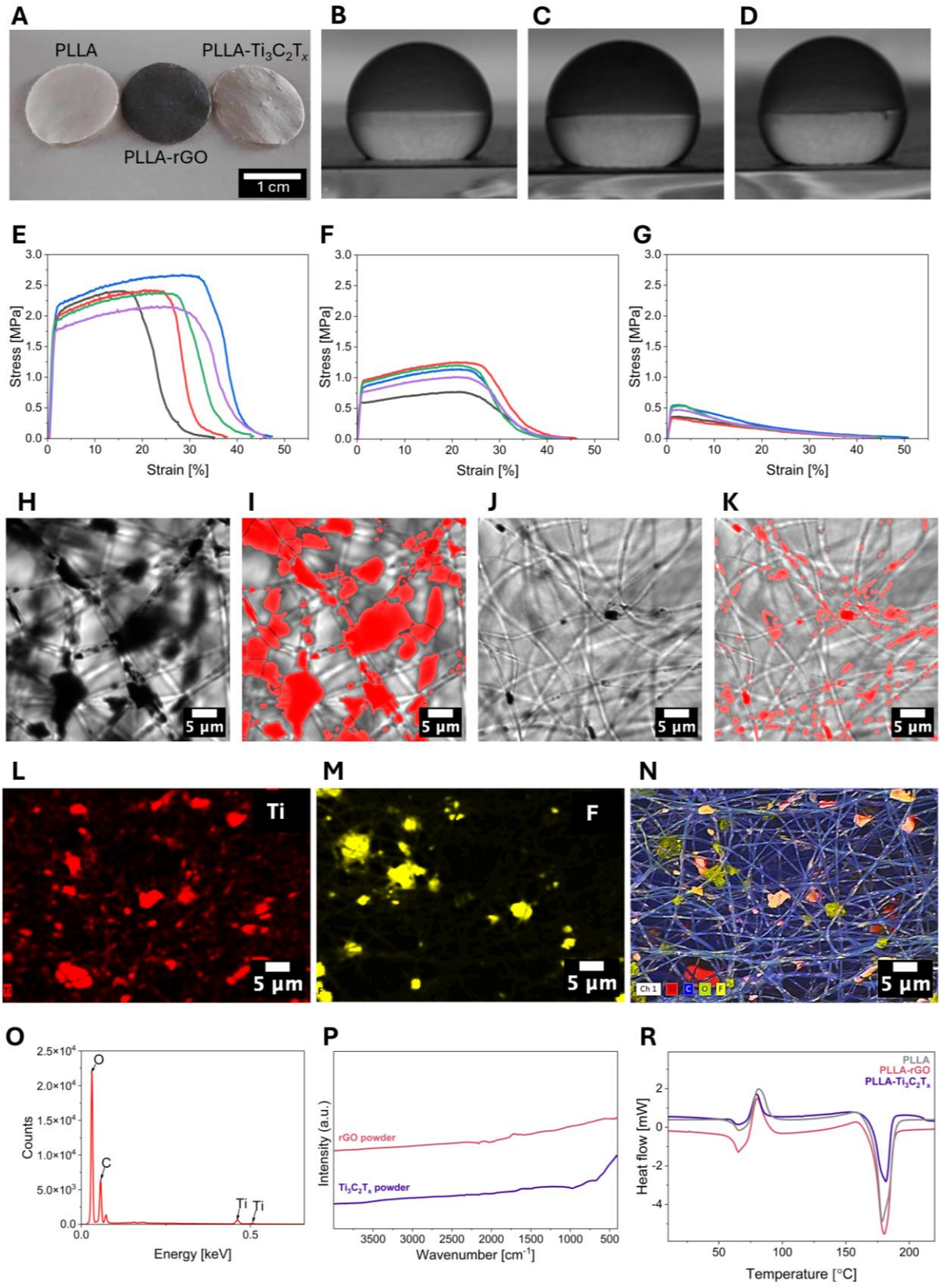

Figure S1. A) Macroscopic images of scaffolds deposited on baking paper. Exemplary images of 3 µL water droplets deposited on B) PLLA, C) PLLA-rGO, and D) PLLA-$Ti_3C_2T_x$ scaffolds for

static contact angle measurements. Stress-strain curves for F) PLLA, G) PLLA-rGO, and H) PLLA-$Ti_3C_2T_x$. H) CLSM (ESID) representative image of PLLA-rGO for identification of rGO agglomerations, and I) accompanying images with a red mask indicating rGO agglomerations. Similarly, J) CLSM (ESID) representative images of PLLA-$Ti_3C_2T_x$, and K) images with a red mask indicating $Ti_3C_2T_x$ agglomerations. SEM EDS maps of L) titanium, M) fluorine, and N) merged channels for the PLLA-$Ti_3C_2T_x$ fibers. O) SEM EDS spectrum for PLLA-$Ti_3C_2T_x$ fibers. E) FTIR spectrum for rGO and $Ti_3C_2T_x$ powders. F) DSC curve for all scaffolds.

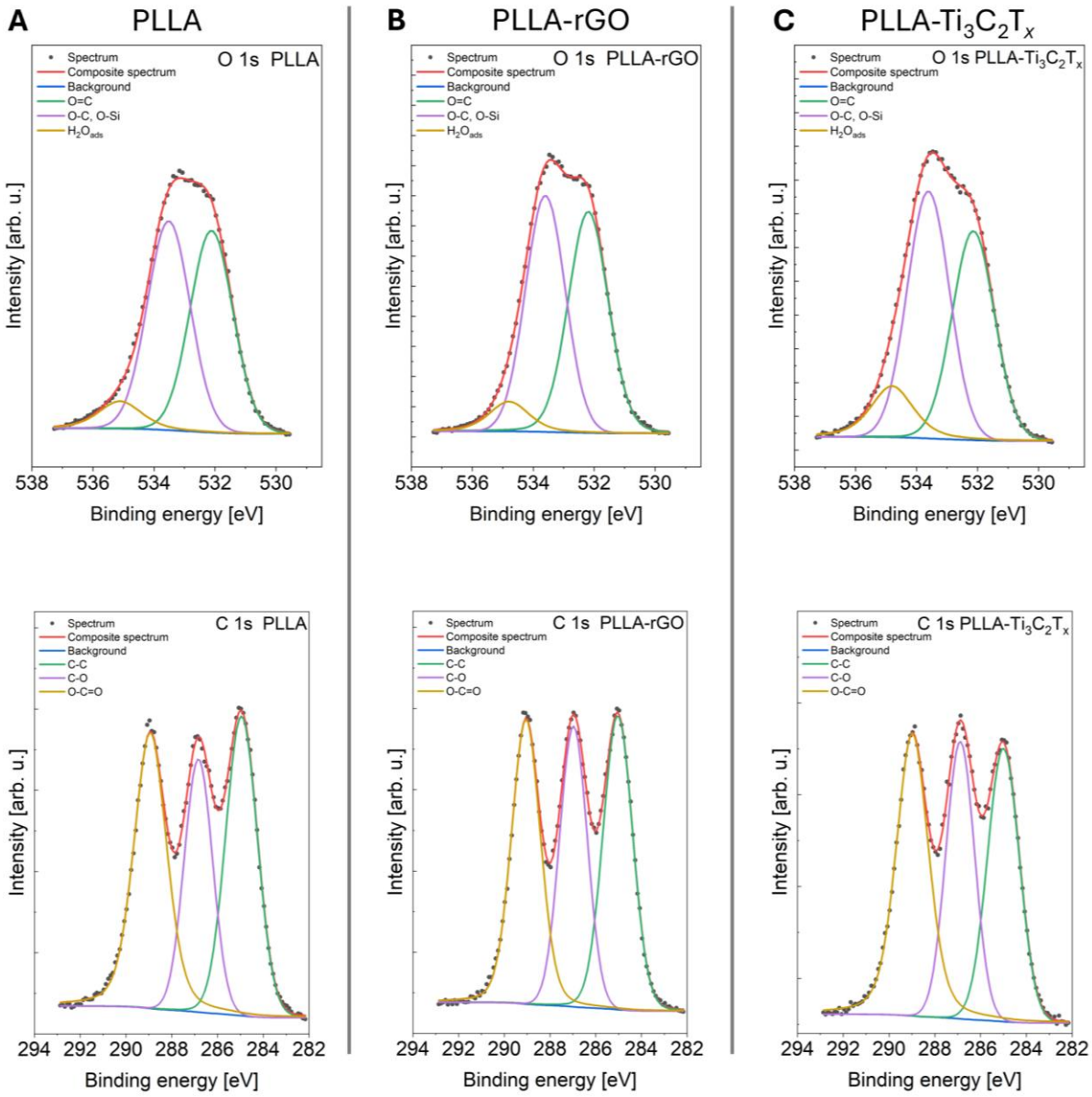

Figure S2. High-resolution XPS spectra of A) PLLA, B) PLLA-rGO, and C) PLLA-$Ti_3C_2T_x$ scaffolds.

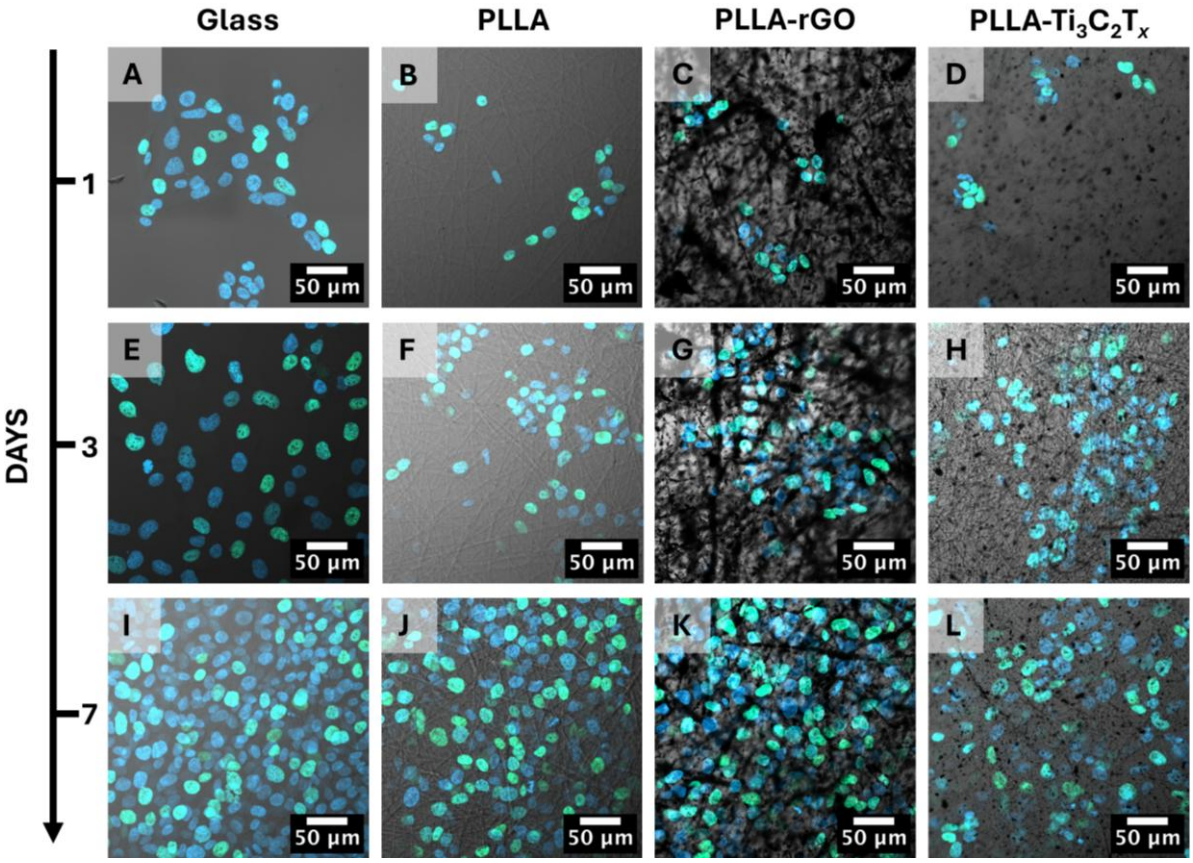

Figure S3. CLSM micrographs representing osteoblasts on glass, PLLA, PLLA-rGO, and PLLA-$Ti_3C_2T_x$ scaffolds on day 1 (A–D), day 3 (E-H), and day 7 (I-L). Nuclei were stained with DAPI (blue); additionally, EdU incorporated during replication was stained with Alexa Fluor™ 488 (green).

Movie S1. Visualization of z-stack recorded with CLSM for PLLA, PLLA-rGO, and PLLA-$Ti_3C_2T_x$ scaffolds on the 7th day of cell culture, presenting infiltration of cells starting from the top of the scaffold (defined as 0 µm imaging depth).